

**AFRL-RI-RS-TR-2009-184**  
**Final Technical Report**  
**July 2009**



# **QUANTUM ENHANCED IMAGING BY ENTANGLED STATES**

Northrop Grumman Systems Corp.

Sponsored by  
Defense Advanced Research Projects Agency  
DARPA Order No. AJ12/00

*APPROVED FOR PUBLIC RELEASE; DISTRIBUTION UNLIMITED.*

**STINFO COPY**

**AIR FORCE RESEARCH LABORATORY  
INFORMATION DIRECTORATE  
ROME RESEARCH SITE  
ROME, NEW YORK**

## **NOTICE AND SIGNATURE PAGE**

Using Government drawings, specifications, or other data included in this document for any purpose other than Government procurement does not in any way obligate the U.S. Government. The fact that the Government formulated or supplied the drawings, specifications, or other data does not license the holder or any other person or corporation; or convey any rights or permission to manufacture, use, or sell any patented invention that may relate to them.

This report was cleared for public release by the 88<sup>th</sup> ABW, Wright-Patterson AFB Public Affairs Office and is available to the general public, including foreign nationals. Copies may be obtained from the Defense Technical Information Center (DTIC) (<http://www.dtic.mil>).

AFRL-RI-RS-TR-2009-184 HAS BEEN REVIEWED AND IS APPROVED FOR PUBLICATION IN ACCORDANCE WITH ASSIGNED DISTRIBUTION STATEMENT.

FOR THE DIRECTOR:

/s/  
DONALD J. NICHOLSON  
Work Unit Manager

/s/  
EDWARD J. JONES, Deputy Chief  
Advanced Computing Division  
Information Directorate

This report is published in the interest of scientific and technical information exchange, and its publication does not constitute the Government's approval or disapproval of its ideas or findings.

**REPORT DOCUMENTATION PAGE***Form Approved*  
**OMB No. 0704-0188**

Public reporting burden for this collection of information is estimated to average 1 hour per response, including the time for reviewing instructions, searching data sources, gathering and maintaining the data needed, and completing and reviewing the collection of information. Send comments regarding this burden estimate or any other aspect of this collection of information, including suggestions for reducing this burden to Washington Headquarters Service, Directorate for Information Operations and Reports, 1215 Jefferson Davis Highway, Suite 1204, Arlington, VA 22202-4302, and to the Office of Management and Budget, Paperwork Reduction Project (0704-0188) Washington, DC 20503.

**PLEASE DO NOT RETURN YOUR FORM TO THE ABOVE ADDRESS.****1. REPORT DATE (DD-MM-YYYY)**  
JULY 2009**2. REPORT TYPE**  
Final**3. DATES COVERED (From - To)**  
August 2007 – March 2009**4. TITLE AND SUBTITLE**

QUANTUM ENHANCED IMAGING BY ENTANGLED STATES

**5a. CONTRACT NUMBER**

FA8750-07-C-0201

**5b. GRANT NUMBER**

N/A

**5c. PROGRAM ELEMENT NUMBER**

61101E

**6. AUTHOR(S)**

Doyle Nichols

**5d. PROJECT NUMBER**

AJ12

**5e. TASK NUMBER**

QU

**5f. WORK UNIT NUMBER**

EN

**7. PERFORMING ORGANIZATION NAME(S) AND ADDRESS(ES)**Northrop Grumman Systems Corporation  
1580A Nursery Road  
Linthicum Heights, MD 21090-2202**8. PERFORMING ORGANIZATION  
REPORT NUMBER**

N/A

**9. SPONSORING/MONITORING AGENCY NAME(S) AND ADDRESS(ES)**AFRL/RITC  
525 Brooks Rd.  
Rome NY 13441-4505**10. SPONSOR/MONITOR'S ACRONYM(S)**

N/A

**11. SPONSORING/MONITORING  
AGENCY REPORT NUMBER**  
AFRL-RI-RS-TR-2009-184**12. DISTRIBUTION AVAILABILITY STATEMENT**

APPROVED FOR PUBLIC RELEASE; DISTRIBUTION UNLIMITED. PA# 88ABW-2009-3355 Date Cleared: 22-July-2009

**13. SUPPLEMENTARY NOTES****14. ABSTRACT**

The use of entangled states in a prospective standoff imaging sensor has been explored. Specifically, the question of whether enhanced performance (in terms of achievable resolution, in particular) may be obtained through the use of entangled states in a ghost imaging configuration has been investigated. The resiliency of such a system in the presence of transmission impairments that necessarily accompany sensors in a tactical environment, such as large optical loss, atmospheric turbulence and scattering has been considered. The prospective imaging sensor based on quantum entangled states has been compared with respect to a similar sensor based on classical states in terms of its expected performance. Experiments concerned with the generation of ghost images with nondegenerate pulsed sources of entangled photons as well as with tri-photons have been carried out. Prospects for multiple photon absorption by coupled quantum wells have also been studied.

**15. SUBJECT TERMS**

REMOTE SENSING; LIDAR; RADAR; SYNTHETIC APERTURE RADAR (SAR); SENSORS USING PHOTONS IN A NON-CLASSICAL STATE; EG SQUEEZED, ENTANGLED

**16. SECURITY CLASSIFICATION OF:****a. REPORT**  
U**b. ABSTRACT**  
U**c. THIS PAGE**  
U**17. LIMITATION OF  
ABSTRACT**

UU

**18. NUMBER  
OF PAGES**

124

**19a. NAME OF RESPONSIBLE PERSON**

Donald J. Nicholson

**19b. TELEPHONE NUMBER (Include area code)**

N/A

## ABSTRACT

The use of entangled states in a prospective standoff imaging sensor has been explored. Specifically, the question of whether enhanced performance (in terms of achievable resolution, in particular) may be obtained through the use of entangled states in a ghost imaging configuration has been investigated. The resiliency of such a system in the presence of transmission impairments that necessarily accompany sensors in a tactical environment, such as large optical loss, atmospheric turbulence and scattering has been considered. The prospective imaging sensor based on quantum entangled states has been compared with respect to a similar sensor based on classical states in terms of its expected performance. Experiments concerned with the generation of ghost images with nondegenerate pulsed sources of entangled photons as well as with tri-photons have been carried out. Prospects for multiple photon absorption by coupled quantum wells have also been studied.

It has been found that entangled states in general can maintain their entanglement in the face of scattering and optical loss. Also, propagation of the individual photons is also governed by Maxwell's equations, just as with classical light so that the energy propagates at the wavelength of the individual photons. States configurations have been found that offer enhanced resolution. States have also been found that suffer impairments no more egregiously than classical light. However, no entangled states and sensor configurations have been found that satisfy both of these crucial criteria simultaneously. Quantum ghost imaging sensors have been found to give advantages in principle in resolution and signal to noise ratio when compared to their classical analogs. However, the conditions required to make use of these advantages will be very difficult to realize in practice. We have formulated suggested structures for multiple photon detectors based on coupled quantum wells as well as tri-photon sources based on aperiodic gratings. Experimentally, we have made what we believe to be the first measurements of correlation peaks as well as a ghost image utilizing a pulsed nondegenerate source of entangled photons. We have also generated entangled tri-photons (using hexagonally poled lithium tantalate) which will be required for the realization of enhanced resolution in an imaging sensor.

# TABLE OF CONTENTS

<b>1</b>	<b><i>Summary .....</i></b>	<b><i>1</i></b>
<b>2</b>	<b><i>Introduction.....</i></b>	<b><i>4</i></b>
<b>3</b>	<b><i>System Analysis.....</i></b>	<b><i>7</i></b>
<b>3.1</b>	<b>Resolution .....</b>	<b>7</b>
3.1.1	Modulation Transfer Function.....	7
3.1.2	Real Space Description of Resolution: Rayleigh Diffraction Limit .....	9
3.1.3	Resolution of Quantum versus Classical Ghost Imaging .....	11
<b>3.2</b>	<b>SNR Analysis .....</b>	<b>14</b>
3.2.1	General Quantum versus Classical Considerations .....	14
3.2.2	SNR and CAR of Classical and Quantum Systems .....	16
3.2.3	Atmospheric Effects .....	21
3.2.4	Ghost Imaging SNR Model .....	23
3.2.5	Ghost Imaging SNR: Intensity Interferometer Approach.....	25
<b>4</b>	<b><i>Quantum Imaging Experiments.....</i></b>	<b><i>33</i></b>
<b>4.1</b>	<b>SHG System Setup and Diagnostics .....</b>	<b>33</b>
4.1.1	Nonlinear Optics.....	33
4.1.2	Coincidence Detectors and Electronics .....	35
<b>4.2</b>	<b>Experimental Issues .....</b>	<b>36</b>
4.2.1	Background light .....	36
4.2.2	Spurious Effects of InGaAs APD.....	36
4.2.3	Spatial overlap of correlated photons .....	38
<b>4.3</b>	<b>Observation of a Correlation Peak.....</b>	<b>38</b>
<b>4.4</b>	<b>Performance Comparison Between Correlation Peak and Ghost Imaging.....</b>	<b>39</b>
<b>4.5</b>	<b>Ghost Imaging with a Diffusive Target.....</b>	<b>40</b>
<b>4.6</b>	<b>Ghost Imaging with Nondegenerate Source → Post QSP Activity Following Immediately from QSP Efforts .....</b>	<b>41</b>
<b>5</b>	<b><i>Triphoton Source Development.....</i></b>	<b><i>45</i></b>
<b>6</b>	<b><i>Quantum Well Multiple Photon Absorbers .....</i></b>	<b><i>47</i></b>
<b>6.1</b>	<b>Introduction.....</b>	<b>47</b>
<b>6.2</b>	<b>Asymmetric Coupled Quantum Well Absorption Structure .....</b>	<b>48</b>
<b>6.3</b>	<b>Proposed Semiconductor Quantum-Well Test Structure.....</b>	<b>55</b>
<b>6.4</b>	<b>Conclusions → Quantum Well Multiple Photon Absorbers .....</b>	<b>57</b>
<b>7</b>	<b><i>Theoretical Analysis of Imaging with Entangled States .....</i></b>	<b><i>58</i></b>
<b>7.1</b>	<b>Interaction with the Target .....</b>	<b>58</b>
<b>7.2</b>	<b>Resolution and Energy Propagation .....</b>	<b>58</b>
<b>7.3</b>	<b>Impact of Transmission Impairments.....</b>	<b>61</b>
<b>8</b>	<b><i>Experimental Study on Entangled Triphoton Beams.....</i></b>	<b><i>64</i></b>
<b>9</b>	<b><i>Suggestions for Further Work.....</i></b>	<b><i>72</i></b>

<i>References</i> .....	74
<i>List of Acronyms</i> .....	76
<i>Appendix A Effect of Scattering on Ghost Imaging</i> .....	78
<i>Appendix B Imaging with Non-Degenerate Bi-Photons</i> .....	84
<i>Appendix C Spatial Resolution Enhancement in Quantum Imaging beyond the Diffraction Limit Using Entangled Photon-Number State</i> .....	92
<i>Appendix D Three-Photon Entangled Beams</i> .....	104
<i>Appendix E</i> .....	111
<i>Appendix F</i> .....	112

## LIST OF FIGURES

FIGURE 1 DIFFRACTION LIMITED MTF (BLUE CURVE) AND TURBULENCE-INDUCED MTF FOR $C_n^2 = 5 \times 10^{-16} m^{-2/3}$ AND $C_n^2 = 5 \times 10^{-15} m^{-2/3}$ (YELLOW AND MAGENTA CURVES, RESPECTIVELY). THE RANGE TO TARGET WAS 20 KFT. ....	9
FIGURE 2 ERROR PROBABILITY ( $P_{ERROR}$ ) VERSUS SEPARATION OF TWO POINT SOURCES RELATIVE TO THE RAYLEIGH DIFFRACTION LIMIT FOR $N = 10$ PHOTONS INCIDENT ON A DETECTOR OF UNIT QUANTUM EFFICIENCY. ....	10
FIGURE 3 RESOLUTION VERSUS $SNR$ FOR PROBABILITY OF ERROR, $P_{ERROR}$ , OF $10^{-2}$ .....	11
FIGURE 4 MINIMUM SEPARATION BETWEEN POINT SOURCES CORRESPONDING TO GIVEN $SNR$ FOR A CLASSICAL SENSOR.....	11
FIGURE 5 RESOLUTION VERSUS $SNR$ FOR DIFFERENT RANGES OF THE BASELINE AND QUANTUM GHOST IMAGERS. ....	13
FIGURE 6 UNFOLDED VERSION OF SETUP FOR PSEUDO-THERMAL GHOST IMAGING. ....	13
FIGURE 7 SYSTEM ARCHITECTURES: CLASSICAL VERSUS QUANTUM IMAGING.....	15
FIGURE 8 COMPARISON OF $CAR$ OF QUANTUM SENSOR TO $SNR$ OF CLASSICAL ONE.....	17
FIGURE 9 $CAR^2$ VERSUS FRACTION OF CORRELATED PHOTONS.....	19
FIGURE 10 $CAR^2$ VERSUS SOURCE FLUX (PHOTONS PER SECOND).....	20
FIGURE 11 $C_n^2$ VS. ALTITUDE.....	21
FIGURE 12 (A) – (C) SPATIAL PROFILES OF BEAM ALONG ATMOSPHERIC PATH. (D)-(E) FFTS OF STARTING AND FINAL DISTRIBUTIONS OF BEAM. ABSCISSA IS IN CYCLES PER METER. ....	22
FIGURE 13 VARIANCE IN ARRIVAL TIME AS A FUNCTION OF INITIAL COINCIDENCE WIDTH AFTER PROPAGATION THROUGH 40 KM IN ATMOSPHERE. ....	23
FIGURE 14 $SNR$ VERSUS DETECTOR EFFICIENCY FOR $F = 0.9$ AND UNITY BUCKET DETECTOR EFFICIENCY (LEFT), AND $SNR$ VERSUS $F$ FOR UNITY SOURCE AND DETECTOR EFFICIENCIES (RIGHT).....	25
FIGURE 15 COMPARISON OF RATE OF PHOTONS INCIDENT ON DETECTOR FOR BASELINE AND ENTANGLED PHOTON SOURCES AGAINST THAT DUE TO SOLAR PHOTONS AND DARK COUNTS. ....	26
FIGURE 16 $SNR$ VERSUS RANGE FOR BASELINE AND QUANTUM ENTANGLED PHOTON SOURCES... 27	27
FIGURE 17 NUMBER OF SPATIAL COHERENCE CELLS VERSUS RATIO OF SPOT DIAMETER TO DIFFRACTION-LIMITED RESOLUTION OF RECEIVER OPTICS. $M_{CIRC}$ IS GIVEN BY EQ. (25), WHEREAS $M_3$ IS AN APPROXIMATION, AS DISCUSSED IN THE TEXT.....	29
FIGURE 18 NUMBER OF SPATIAL DEGREES OF FREEDOM VERSUS RANGE FOR A CIRCULAR SOURCE EMANATING FROM A ROUGH TARGET IN THE CASE THAT THE BEAM SIZE IS LARGER THAN THE TARGET. ....	30
FIGURE 19 $SNR$ VERSUS RANGE FOR COINCIDENCE COUNTING.....	32
FIGURE 20 SETUP FOR GENERATING THE SPDC PUMP BEAM. ....	33
FIGURE 21 SETUP FOR (DEGENERATE) SPDC GENERATION.....	33
FIGURE 22 ELECTRICAL LAYOUT FOR THE COINCIDENCE MEASUREMENTS WITH NONDEGENERATE SPDC. ....	35
FIGURE 23 MODIFIED SETUP FOR PUMPING THE SPDC TO REDUCE LASER LEAKAGE AT 1064 NM.. 36	36
FIGURE 24 GAUSSIAN FIT TO TEMPORAL PROFILE OF INGAAS APD OUTPUT (RIGHT), AND PUMP POWER DEPENDENCE OF OFFSET TERM (RIGHT).....	37
FIGURE 25 DARK COUNT PROFILE AT VARIOUS DETECTION PROBABILITIES. ....	37
FIGURE 26 CORRELATION PROFILE: (A) DATA AND (B) CARTOON EXPLANATION.....	39
FIGURE 27 MEASURED COINCIDENCES WITH THE SYSTEM CONFIGURED FOR GHOST IMAGING.....	40
FIGURE 28 EXPERIMENTAL SETUP WITH DISTANCE RELATIONSHIP. ....	41
FIGURE 29 OBJECT WITH TWO WHITE STRIPS. ....	42
FIGURE 30 SECOND ORDER CORRELATION PEAK AT VARIOUS VALUES FOR $X_{st}$ .....	43
FIGURE 31 GHOST IMAGE OF THE OBJECT. THE OBJECT PROFILE (SUITABLY MAGNIFIED PER CALCULATIONS FOR THE NONDEGENERATE CASE IN TABLE 11 IS OVERLAID). ....	44
FIGURE 32 SCHEMATIC OF QPM GRATING TO GENERATE THREE ENTANGLED PHOTONS (LEFT) AND POWER SPECTRAL DENSITY OF THE GRATING (RIGHT). ....	46

FIGURE 33 ENERGY TRANSITIONS USING TWO PHOTONS WITH AN INTERMEDIATE ENERGY EIGENSTATE. ....	47
FIGURE 34 TWO-PHOTON ABSORPTIONS IN CS ATOMS USING VIRTUAL STATES AS THE INTERMEDIATE STATE IN THE TRANSITION. ....	48
FIGURE 35 A SINGLE QUANTUM-WELL LAYER STRUCTURE WITH GAAS WELL MATERIAL WITHIN ALGAAS BARRIER MATERIAL. ....	49
FIGURE 36 A SINGLE QUANTUM WELLS WHERE THE WELL DEPTH IS SET TO CREATE: A) ONE BOUND STATE, B) TWO BOUND STATES, AND C) THREE BOUND STATES WITHIN THE WELL. THE DASHED LINES REPRESENT THE BOUND STATE ENERGIES FOR THE WELL WITH THE CORRESPONDING WAVE FUNCTIONS PLOTTED IN THE SAME COLOR. ....	50
FIGURE 37 A PAIR OF ASYMMETRIC QUANTUM WELLS WITH A DEGENERATE STATE, WHERE THE SEPARATION OF THE WELLS IS: A) 4A, B) 2A, AND C) A, WHERE A IS THE THICKNESS OF EACH WELL. ....	50
FIGURE 38 A PAIR OF ASYMMETRIC QUANTUM WELLS WHERE THE SEPARATION OF THE WELLS IS A, AND THE WELL DEPTHS ARE CHOSEN SO NONE OF THE STATES ARE DEGENERATE. ....	51
FIGURE 39 TRANSITIONS FOR THE FINITE QUANTUM-WELL SYSTEM CALCULATED USING ELECTRIC-DIPOLE INTERACTIONS. ....	51
FIGURE 40 ELECTRON SPONTANEOUS LIFETIME FOR THE FIRST EXCITED STATE IN A 1-EV DEEP QUANTUM WELL. ....	52
FIGURE 41 SPONTANEOUS LIFETIME FOR THE FIRST EXCITED STATE IN A 4-NM WIDE QUANTUM WELL. ....	52
FIGURE 42 CONDUCTION-BAND ENERGY STRUCTURES AND FOR ASYMMETRIC COUPLED QUANTUM-WELL SYSTEM. ....	53
FIGURE 43 TWO-PHOTON TRANSITION RATE WHERE THE INTERMEDIATE LEVEL IS TUNED INTO AND OUT OF RESONANCE WITH THE PHOTON ENERGIES. ....	53
FIGURE 44 TWO-PHOTON ABSORPTION TRANSITION RATE FOR VARYING BARRIER THICKNESS, WHERE THE TRANSITION ENERGIES ARE SLIGHTLY OFF RESONANCE WITH THE PHOTON ENERGIES. ....	53
FIGURE 45 (A) ASYMMETRIC COUPLED QUANTUM WELL STRUCTURE THAT MIMICS (B) TWO-PHOTON ABSORPTION ORGANIC CRYSTAL MATERIAL (FROM LEE AND GOODSON REF.[55]).	54
FIGURE 46 LINEAR ETPA RATE AND QUADRATIC RANDOM TPA FOR PORPHYRIN DENDRIMER AT DIFFERENT ENTANGLEMENT TIMES (FROM LEE AND GOODSON REF. [55]). ....	55
FIGURE 47 GAAS/ALGAAS PROPOSED TEST STRUCTURE. ....	55
FIGURE 48 SCHEMATIC OF QUANTUM IMAGING WITH ENTANGLED PHOTONS IN STATE (A) AND (B). THE DISTANCE FROM THE CRYSTAL OUTPUT SURFACE TO THE OBJECT IS $z_0$ , IS THE DISTANCE FROM THE OBJECT TO THE TWO-PHOTON DETECTOR $z_1$ , IS THE DISTANCE FROM THE CRYSTAL OUTPUT SURFACE TO THE IMAGING LENS WITH FOCAL LENGTH $f$ . $z_1$ IS THE LENGTH FROM THE IMAGING LENS TO THE SINGLE-PHOTON DETECTOR $D_2$ , WHICH SCANS THE COMING SIGNAL ON ITS TRANSVERSE PLANE. "C.C." REPRESENTS THE JOINT-DETECTION MEASUREMENT. ....	60
FIGURE 49 (A) THE DOMAIN STRUCTURE OF A HEXAGONALLY POLED LITHIUM TANTALATE (HEXPLT) AFTER A SLIGHT ETCH IN ACID. (B) THE CORRESPONDING RECIPROCAL-VECTOR SPACE WHICH HAS THE SIX-FOLD SYMMETRY PROPERTY BUT WITH ROTATION BY $90^\circ$ . ....	65
FIGURE 50 A NUMERICAL SIMULATION OF THE THIRD-ORDER CORRELATION FUNCTION, $G^{(3)}(\tilde{t}_{31}, \tilde{t}_{32})$ . ....	68
FIGURE 51 SCHEMATIC EXPERIMENTAL SETUP FOR THREE-BEAM TEMPORAL CORRELATION MEASUREMENT. ....	69
FIGURE 52 A TYPICAL $G^{(3)}(\tilde{t}_{31}, \tilde{t}_{32})$ MEASUREMENT. ....	70
FIGURE 53 (A) PROJECTION OF $G^{(3)}(\tilde{t}_{31}, \tilde{t}_{32})$ ONTO AXIS $T_{32}$ . (B) OVERLOOK AT $G^{(3)}(\tilde{t}_{31}, \tilde{t}_{32})$ ....	70
FIGURE 54 SCHEMATIC EXPERIMENTAL SETUP OF THREE-BEAM GHOST IMAGING. THE OBSERVED GHOST INTERFERENCE PATTERN INDICATES THAT THE GHOST IMAGE HAS TWICE SPATIAL RESOLUTION COMPARING WITH A CLASSICAL IMAGE OF THE TARGET (DOUBLE-SLIT). ....	71



FIGURE 55 SCHEMATIC OF GHOST IMAGING SYSTEM FOR MODELING OF SCATTERING EFFECTS ON ENTANGLED PHOTONS. ....	78
FIGURE 56 (UPPER) SCHEMATIC OF GHOST IMAGING SYSTEM ANALYZED HERE, (LOWER) SCHEMATIC OF ORIGINAL GHOST IMAGING SYSTEM. ....	84
FIGURE 57 KLYSHKO PICTURE OF A GHOST IMAGING SYSTEM. ....	90
FIGURE 58 CORRELATED BEAMS OF SIGNALS, S, AND IDLERS, I, ARE PRODUCED BY DOWN-CONVERSION. THE IDLERS FROM THE LOWER BEAM ARE FREQUENCY SHIFTED. THE CRYSTAL XU IS CHOSEN SO THERE IS PHASE MATCHING THAT ALLOWS AN IDLER FROM EACH BEAM TO BE UP-CONVERTED TO A PHOTON. ....	104
FIGURE 59 THE PLUS SIGN ON THE $I_2$ PHOTON LINE IS A FREQUENCY SHIFTER. FOR $ \chi_2\rangle$ WE ONLY SHOW ONE DIAGRAM, THERE IS A DIAGRAM WHERE S IS DETECTED AT B AND TWO MORE DIAGRAMS WITH $S_1$ DETECTED RATHER THAN $S_2$ . ....	106

## LIST OF TABLES

TABLE 1 QSP PROGRAM OBJECTIVES FROM THE BAA.....	1
TABLE 2 STATES EXAMINED BY NGC/UMBC FOR QSP GO/NO-GO CRITERIA. ....	2
TABLE 3 QSP PROGRAM OBJECTIVES FROM THE BAA.....	5
TABLE 4 KEY PARAMETERS OF BASELINE FOR ESTIMATING DIFFRACTION LIMITED MTF. ....	8
TABLE 5 KEY PARAMETERS FOR ESTIMATING TURBULENCE INDUCED MTF. THE MULTIPLE VALUES CORRESPOND TO DIFFERENT LEVELS OF TURBULENCE, AS EXEMPLIFIED BY THE YELLOW AND MAGENTA CURVES OF FIGURE 1. ....	8
TABLE 6 QUALITATIVE COMPARISON OF QUANTUM VERSUS CLASSICAL SYSTEMS. ....	16
TABLE 7 VALUES OF RELEVANT PARAMETERS FOR SNR/CAR CALCULATIONS OF FIGURE 9. ....	20
TABLE 8 SPDC EFFICIENCY.....	34
TABLE 9 COMPARISON OF SPDC EFFICIENCY BETWEEN DEGENERATE AND NON-DEGENERATE CASES. ....	34
TABLE 10 VALUES FOR THE DISTANCES IN FIGURE 28. ....	41
TABLE 11 CALCULATION OF $R_{\text{IMG}}$ AND $M_{\text{IMG}}$ . ....	42
TABLE 12 TEST STRUCTURE MATERIALS AND THICKNESSES. ....	56
TABLE 13 QUANTUM-WELL ENERGIES FOR PROPOSED TEST STRUCTURE. ....	56
TABLE 14 QSP PROGRAM OBJECTIVES FROM THE BAA.....	58

## ACKNOWLEDGMENTS

The team gratefully acknowledges the support of the Strategic Technology Office at DARPA (and, in particular, Dr. Peter Haaland and Dr. Esko Jaska) for its support, under Contract Number FA8750-07-C-0201, of the work reported here.

The technical contributors to the work reported herein at Northrop Grumman Corporation and The University of Maryland at Baltimore County are as follows.

### *Northrop Grumman Corporation*

- Dr. Gary Kanner
- Dr. Charles Kim
- Dr. Donald Miller
- Dr. Doyle Nichols
- Dr. Michael Fitelson

### *The University of Maryland at Baltimore County*

- Professor Morton Rubin
- Professor Yanhua Shih
- Professor Terrance Worchesky
- Dr. Jianming Wen
- Mr. Hui Chen
- Mr. Sanjit Karmakar
- Mr. Jianbin Jiu
- Mr. Zhenda Xie
- Mr. Yu Zhou

# 1 Summary

The QSP Program goals are shown in tabular form in Table 1. The central question being addressed by the NGC QSP team was whether entangled states could offer an enhancement in performance in a standoff imaging sensor. In particular, NGC examined ghost imaging where photons scattered from a target to a non-resolving detector can be used in conjunction with a spatially resolved image of the source to form an image of the target. During the course of our work, we examined several classes of entangled states (GHZ states, W-states and entangled beams) and different configurations in terms of the numbers of photons that are retained at the sensor as opposed to being propagated to the target.

A summary of the findings with respect to the first four elements of Table 1 and the various configurations cited above is shown in Table 2. Essentially, it was found that elements 1 and 3 of Table 1 were generally satisfied for entangled states of various types and configurations cited above. With regard to elements 2 and 4, it was generally found that the various configurations examined satisfied either one or the other of these, but that no configuration satisfied both at the same time, which is, of course, the *real* metric of success for a proposed sensor configuration under QSP. Thus, it cannot be said that, during the course of this work, a combination of states and conditions was uncovered that would satisfy the go/no-go milestones for the program. An important subtlety of a sensor utilizing entangled states is that, since it is based on correlations between entangled photons, uncorrelated photons (i.e. noise sources) will register detections with a frequency that is far smaller than would be the case with a conventional system (that does not rely on correlated detections.) This has two important implications. The first is that background sources (such as daylight, for example) are less debilitating than what one might expect conventionally. Secondly, large losses tend to increase the time required to form an image but do not, in and of themselves, prevent the formation of the image. However, in a tactical imaging system, the time required to form an image can be very important, depending on the details of the mission. Therefore, image acquisition time is shown as a figure of merit in Table 2, even though it is not a program go/no-go milestone, per se, and one can see that it goes “hand in hand” with the requirement on sensitivity/resolution loss. As we worked through QSP, it quickly became clear

**Table 1 QSP Program Objectives From the BAA.**

The photon's interaction with the target doesn't cause the non-classical state to be entirely lost.
The quantum sensor can resolve two targets at a closer spacing than is possible with a classical sensor.
The energy that travels between the quantum sensor and the target propagates at the single photon wavelength
<p>The quantum sensor suffers a loss of sensitivity and resolution that is no worse than the loss suffered by a classical sensor under the following conditions:</p> <ul style="list-style-type: none"> <li>➤ The transmission medium between the sensor and the target absorbs or diffusely scatters photons.</li> <li>➤ The target is in a daylight environment.</li> <li>➤ The target scatters incident photons non-uniformly over <math>4\pi</math> steradians</li> </ul>
Make a specific calculation of the resolution improvement achieved with a 3 dB loss in the transmission medium and a resulting 26 dB signal to noise ratio.
An experiment whose goal is to provide additional validation of some results demonstrated analytically under the Base effort, particularly if the relevant theoretical base is underdeveloped. The goal of a proposed experiment may be to determine results beyond the scope of the Base effort.

**Table 2 States examined by NGC/UMBC for QSP Go/No-Go criteria.**

Ghost Imaging Configurations	Target interaction does not destroy quantum state	Quantum sensor resolution better than classical	Propagating wavelength same as that of single photon	Sensitivity/Resolution loss not worse due to channel scattering/absorption, daylight Lambertian target	Image acquisition time not worse than classical
Non-degenerate bi-photons	✓	X	✓	✓	✓
N+1 -photon GHZ state → retain N ( $N \geq 2$ )	✓	X	✓	✓	✓
N+1-photon GHZ state → propagate N ( $N \geq 2$ )	✓	✓	✓	X	X
N+1-photon W-state ( $N \geq 2$ )	✓	✓	✓	X	X
N+1 entangled beams ( $N \geq 2$ )	✓	✓	✓	X	X

that resolution may not be readily separated from the signal to noise ratio, even though the calculation of the Rayleigh limit (for example) for an aperture is independent of the *SNR*. The Rayleigh limit represents the separation between the maximum of the point spread function and its first zero. Depending on the *SNR* and signal processing bandwidth available, one may either be able to do better or not quite as well as this limit. Additionally, quantitative determination of the signal to noise ratio is dependent on details of the system that are not well determined at this time, owing to the fact that the behavior of key system elements, such as the source and detectors that are as yet undeveloped, are unknown. Still, we were able to carry out analysis on the program that permitted comparison between the proposed ghost imaging sensor and a baseline sensor utilizing a pseudo-thermal source. This work is summarized in the following paragraph.

Using classical decision theory NGC established a relationship between imaging resolution with respect to the Rayleigh diffraction limit and *SNR*. It was found that, with roughly the same *SNR*, the quantum system proposed could provide the required resolution enhancement relative to a classical baseline. A variety of ways to describe *SNR* for ghost imaging (using only two entangled beams) were utilized to compare the quantum and classical cases to each other. The intensity interferometer approach seemed to be the most appropriate description, especially given the fact that the baseline system also consists of a ghost imaging sensor (a ghost imaging system based on pseudo-thermal light was adopted in the latter stages of the program, replacing the originally contemplated conventional targeting pod). Within this framework it was found that for the same propagating wavelength and source output power that the quantum sensor could provide significantly greater *SNR* due to greater visibility and much tighter beam divergence than would be expected utilizing a pseudo-thermal source. There are several caveats here, however. One involves the assumption of similar optical power for the quantum and classical systems even though the former generally relies on a nonlinear optical process with extraordinarily low conversion efficiency. Second, boosting the optical power output of the source necessarily sacrifices visibility as a result of accidental coincidences in the detection circuit. Additionally, *N*-photon absorption detectors (at least beyond  $N = 2$ ) do not exist, and, when they do exist, the efficiency is expected to be extremely small. Lastly, the calculations ignore the degradation, and possible annihilation of the quantum entanglement upon the extremely high losses inherent to

remote sensing with a diffuse target. Nevertheless, since source and detector development were not areas of emphasis for QSP Phase I, we suspended detailed treatment of these issues, and simply dealt with them as system trades in the early portion of the analysis.

As a result of its experimental work, NGC was able to measure second order correlation with its coincidence detection setup. This is, to our knowledge the first time such correlation has been observed for a nondegenerate pulsed source. This has enabled us to qualitatively see the expected drop in visibility with increased power of the entangled beams, which highlights one of the critical trades that must be considered in developing a concept of a quantum sensor. Using this source, we have observed (just after the completion of the QSP program, on IR&D funding) what we believe to be the first ghost image realized with a pulsed nondegenerate source of entangled photons. This is reported here since, clearly, it was enabled by the work on the QSP program. Incorporating a three-entangled beam source, such as the one conceived by NGC, would allow us to demonstrate the resolution enhancement that has been the focus of the theoretical work in this program. Experimental work to the end of demonstrating imaging with tri-photons has also been carried out at UMBC. UMBC utilized hexagonally poled LiTaO<sub>3</sub> crystals to realize two sets of quasi-phase matching conditions simultaneously. UMBC was able to show temporal correlations (i.e. a measurement of  $G^{(3)}(\tilde{t}_{31}, \tilde{t}_{32})$ ) for tri-photons from this source since the width of the correlation pulse ( $\sim 1ns$ ) was significantly smaller than the width of the pump pulse or other subsystems ( $\sim 15ns$ ), but did not succeed, as of the end of the QSP program, in forming a ghost image with the tri-photons.

Based on our examination of the asymmetric coupled quantum well system, we believe that two-photon absorption can be obtained with temporal characteristics required for correlated photon measurements. The correlation times can be controlled through the barrier strength of the region separating the core quantum well and the coupled quantum well. A structure has been suggested for epitaxial growth and subsequent study as a means to verify our calculations. The main unresolved question with regard to multi-photon absorption in coupled quantum wells, however, revolves around the absorption strength, which will need to be increased by orders of magnitude ultimately to make detectors that are reasonably efficient. This can be addressed to some degree simply by growing large superlattices. However, the realizable improvement here is limited to about a factor of 100, which, while helpful, does not completely solve the problem.

## 2 Introduction

This report describes work carried out under Contract Number FA8750-07-C-0201 on an effort entitled “Quantum Enhanced Imaging by Entangled States,” a part of DARPA STO’s Quantum Sensors Program (QSP). Northrop Grumman’s work on QSP was carried out in collaboration with the University of Maryland at Baltimore County. Our work on the program has centered around the use of entangled photons in a prospective standoff sensor based on the phenomenon of ghost imaging.

Entanglement is a consequence of quantum mechanics and was first discussed in the seminal paper by Einstein, Podolsky and Rosen in 1935.<sup>1</sup> It is known that groups of entangled photons act as a system and that (for example) when sets of two entangled photons of a given wavelength pass through an aperture a diffraction pattern is produced (with the appropriate detection of the system of entangled photons) as though the wavelength was half that of the individual photons. In ghost imaging with entangled states, entangled photons are scattered from an object onto a non-resolving “bucket” detector while photons directly from the source are incident on a resolving detector (i.e. a focal plane array [FPA] or scanning single element detector) and an image is formed via correlation of the detection events on the resolving and non-resolving detectors. This phenomenon has been demonstrated under laboratory conditions, but far less is known about ghost imaging under tactically relevant conditions. The central questions taken up in our work on the program, then, were fourfold. First, how can the improved resolution inherent to entangled states cited above be merged with the concept of ghost imaging. As a corollary, can we achieve the resolution inherent to short optical wavelengths while reaping the propagation advantages of long optical wavelengths? Secondly, how is ghost imaging affected by various transmission impairments encountered in standoff imaging systems, such as loss and scattering. Thirdly, how does the signal to noise ratio required to achieve a given level of resolution in our quantum sensor compare to that which would be required in a classical baseline system? Finally, can an experiment be fashioned to demonstrate the feasibility of our quantum sensor concept?

In the following sections, we will see that the key question with respect to the viability of the proposed sensor concept in a tactical environment came down to developing a combination of entangled states and sensor configuration that allowed one to realize enhanced resolution while showing robustness to the optical losses arising both from path loss and Lambertian scattering by the target that characterize standoff sensor systems. While we found configurations that accomplished each of these goals individually, no combination we have uncovered to date satisfied these criteria simultaneously, which is *really* the goal of the QSP program. We also found that, subject to certain conditions that will be discussed below, one could expect an advantage in terms of the signal to noise ratio required to achieve a given level of resolution for a ghost imaging system utilizing entangled states as opposed to a similar sensor utilizing (for example) a pseudo-thermal source of photons. Based on our examination of the asymmetric coupled quantum well system, we believe that two-photon absorption can be obtained with temporal characteristics required for correlated photon measurements. The correlation times can be controlled through the barrier strength of the region separating the core quantum well and the coupled quantum well. A structure has been suggested for epitaxial growth and subsequent study as a means to verify our calculations. The main unresolved question with regard to multi-photon absorption in coupled quantum wells,

however, revolves around the absorption strength, which will need to be increased by orders of magnitude ultimately to make detectors that are reasonably efficient. This can be addressed to some degree simply by growing large superlattices. However, the realizable improvement here is limited to about a factor of 100, which, while helpful, does not completely solve the problem. We also formulated a design for a source of beams of tri-photons based upon aperiodic gratings. Since source development was not viewed as central to Phase I objectives, this was not fabricated, though it may be a candidate for source work going forward. As a result of its experimental work, NGC was able to measure second order correlation with its coincidence detection setup. This is, to our knowledge, the first time such correlation has been observed for a nondegenerate pulsed source. This observation has enabled us to qualitatively see the expected drop in visibility with increased power of the entangled beams, which highlights one of the critical trades that must be considered in developing a concept of a quantum sensor.

The experimental setup was then configured for ghost imaging but, owing to the much smaller collection efficiency in the imaging setup (as opposed to the correlation measurement setup) the measured signal to noise ratio was not sufficient to re-produce the characteristics of the target before the end of the program. However, we will see below that the work toward producing a ghost image on the QSP setup was continued after the end of the program (on NGC IR&D funds). As a result, we were able to obtain what we believe to be the first ghost image obtained with a pulsed nondegenerate source of entangled photons. Clearly, even if the actual image was not obtained during the course of the program, the result was, in large measure enabled by QSP and so is reported here. UMBC (per correlation measurements) was able to generate a source of tri-photons using hexagonally poled lithium tantalate. However, as of the program end date, UMBC had not succeeded in forming a ghost image with these tri-photons. The generation of ghost images with high flux beams of entangled photons as well as the realization of ghost imaging with tri-photons (and resultant expected enhanced resolution) are both areas where further study is warranted.

This report is organized as follows. The program goals are shown, for reference, in Table 3 and the first four elements were addressed based on fundamental theoretical considerations by the team at UMBC. These results are discussed in Section VI. The fifth element in Table 3 (along with systems related considerations) was addressed by NGC's team at Rolling Meadows and these results are discussed in Section II.

**Table 3 QSP Program Objectives From the BAA.**

The photon's interaction with the target doesn't cause the non-classical state to be entirely lost.
The quantum sensor can resolve two targets at a closer spacing than is possible with a classical sensor.
The energy that travels between the quantum sensor and the target propagates at the single photon wavelength
<p>The quantum sensor suffers a loss of sensitivity and resolution that is no worse than the loss suffered by a classical sensor under the following conditions:</p> <ul style="list-style-type: none"> <li>➤ The transmission medium between the sensor and the target absorbs or diffusely scatters photons.</li> <li>➤ The target is in a daylight environment.</li> <li>➤ The target scatters incident photons non-uniformly over <math>4\pi</math> steradians</li> </ul>
Make a specific calculation of the resolution improvement achieved with a 3 dB loss in the transmission medium and a resulting 26 dB signal to noise ratio.
An experiment whose goal is to provide additional validation of some results demonstrated analytically under the Base effort, particularly if the relevant theoretical base is underdeveloped. The goal of a proposed experiment may be to determine results beyond the scope of the Base effort.



Experimental work was carried out at both NGC (in Rolling Meadows) and at UMBC. Efforts from these endeavors are described in Sections III and VII, respectively. It is perhaps worth noting that, in spite of the fact that the results are reported in separate sections, there was considerable collaboration between the experimentalists at UMBC and NGC. Though source and detector development were not primary thrusts on the program, they were included in the statement of work and efforts aimed at addressing source considerations and multiple photon detection in coupled semiconductor quantum well systems are recounted in Sections IV and V, respectively. Finally, we summarize our results in Section VIII and provide suggestions for future study in Section IX.

### 3 System Analysis

This portion of the final report for the NGC-UMBC QSP team describes the resolution and Signal to Noise Ratio ( $SNR$ ) analyses that were conducted in order to assess the potential advantage of a quantum ghost imaging sensor relative to a classical baseline system. While UMBC showed that it is possible to obtain a resolution enhancement of a factor of  $N$  relative to the Rayleigh diffraction limit using an  $|N,1\rangle$  source, we still need to determine what the  $SNR$  requirement is for that resolution. We also need to see whether the needed  $SNR$  for a quantum source is greater than that of a classical baseline. Consequently, we can establish a relationship between resolution and  $SNR$ , and then define  $SNR$  for ghost imaging sensors. We will see that a quantum sensor can provide both resolution and  $SNR$  advantages with respect to a classical baseline, but the calculated benefits involve assumptions that may not be entirely plausible in a realistic system.

#### 3.1 Resolution

A goal of QSP is to develop a remote imaging sensor that offers a tenfold increase in spatial resolution for a given  $SNR$  compared to a classical system. We discuss below first considerations of resolution for classical sensors, and then relate the possible resolution to  $SNR$  for the classical and quantum cases. We first note that, as mentioned in the proposal and discussed at the kickoff, NGC had identified a baseline product that could potentially benefit from QSP technology. Our first investigations of  $SNR$  and resolution therefore assumed parameters that were relevant to that baseline. In addition, the quantum system has always employed a ghost imaging scheme with different wavelengths in the two arms of the interferometer. Because the spatial resolution enhancement depends on momentum correlation among all of the photons in the quantum state an important question is whether this correlation is preserved upon spectral separation of the photons emanating from the source. NGC has found precedence in the literature for preservation of quantum entanglement between signal and idler photons following spectral separation of beams from nondegenerate parametric down converters.<sup>2</sup> Essentially, because the spectral splitting does not constitute a measurement of transverse position of the photons in either beam, it should not disturb the spatial entanglement in the plane perpendicular to the propagation direction. Furthermore, under QSP, as we show in a later section, we experimentally prove that the photons remain entangled by detecting the correlation between photons that are spectrally separated after exiting a nondegenerate spontaneous parametric down converter (SPDC).

##### 3.1.1 Modulation Transfer Function

The NGC team first began a quantitative analysis of the resolution of the baseline classical sensor, and then folded this into a modulation transfer function ( $MTF$ ). This quantity is used to characterize the resolution and performance of imaging systems, and describes their ability to transfer contrast from object to image as a function of angular spatial frequency  $f$ . In fact, imaging system performance of an airborne sensor is often cast directly in terms of  $MTF$  through the use of bar target patterns on the ground. The  $MTF$  of the sensor can be degraded by aberrations, obscurations, or defocusing in the optics or by turbulence in the channel between the object and imaging plane. There are a variety of specific  $MT$  functions associated with the components of the system. In each

case, the quality of the component is measured by how much the actual *MTF* falls below the ideal curve. Generally, it is only at the lowest spatial frequencies, corresponding to large features, at which maximum contrast can be achieved, which is consistent with the MTF results shown below.

We considered two dominant effects: diffraction-limit and turbulence. The diffraction-limited MTF for an aberration-free system with a perfectly circular aperture is defined by<sup>3</sup>

$$H_{diff}(x) = \frac{2}{\pi} \left[ \arccos(x) - x\sqrt{1-x^2} \right] \quad (1)$$

where  $x$  is the normalized spatial frequency,  $x = \frac{f}{f_c}$  and  $f_c$  is the cutoff angular frequency given by

$$f_c = \frac{D}{\lambda}, \quad (2)$$

**Table 4 Key parameters of baseline for estimating diffraction limited MTF.**

Parameter	Unit	Value
System aperture	inch	6
Pixel size	$\mu\text{m}$	12
Focal length	mm	1700
Wavelength	$\mu\text{m}$	1.57

where  $D$  is system aperture diameter and  $\lambda$  is the wavelength. Table 4 shows the key parameters of the baseline system that have been used to determine the MTF. From Equation (2), one then finds that that contrast falls to zero at an angular spatial frequency of  $f_c = 95$  cycles/mrad. In an actual experiment, a square-wave target is often used, consisting of a pattern of alternating dark and light bars of equal width. The cutoff frequency then describes, for a given aperture and wavelength, the maximum density of bars below which imaging contrast is possible.

In addition to diffraction, the atmospheric induced MTF is defined by<sup>4</sup>

**Table 5 Key parameters for estimating turbulence induced MTF. The multiple values correspond to different levels of turbulence, as exemplified by the yellow and magenta curves of Figure 1.**

Parameter	Unit	Values
$C_n^2$	$\text{m}^{-2/3}$	$5 \times 10^{-16}$ $5 \times 10^{-15}$
Range to target	kft	20 20
Transverse coherence length	cm	29 7.4

$$H_{atmosphere}(f) = \exp \left[ -3.44 * \left( \frac{\lambda}{r_o} f \right)^{5/3} \right], \quad (3)$$

where  $r_o$  is the transverse coherence length (also known as the Fried, or seeing parameter – see the section below on atmospheric considerations for a link model) that depends on the range and  $C_n^2$ .  $C_n^2$  varied from  $10^{-14} \text{m}^{-2/3}$  to  $10^{-17} \text{m}^{-2/3}$  as a function of altitude as shown in a previous report. For easy comparison, we assumed that  $C_n^2$  is constant over the range where the sensor would be used. Table 5 shows the key parameters that were used in calculating the turbulence-induced MTF.

Figure 1 shows both diffraction limited MTF (blue curve) and turbulence induced MTF for  $C_n^2 = 5 \times 10^{-16} \text{m}^{-2/3}$  and  $C_n^2 = 5 \times 10^{-15} \text{m}^{-2/3}$  (yellow

and magenta curves, respectively). The abscissa is angular spatial frequency, which varies from 0 to 100 *cycles/mrad*. The ordinate is *MTF*, which runs from 0 to 1. In the absence of atmosphere and with infinite aperture the *MTF* would equal 1 at all frequencies. In this example, however, the contrast decreases with angular spatial frequency due to the finite aperture in the diffraction-limited case, and due to the seeing parameter for the case of turbulence.

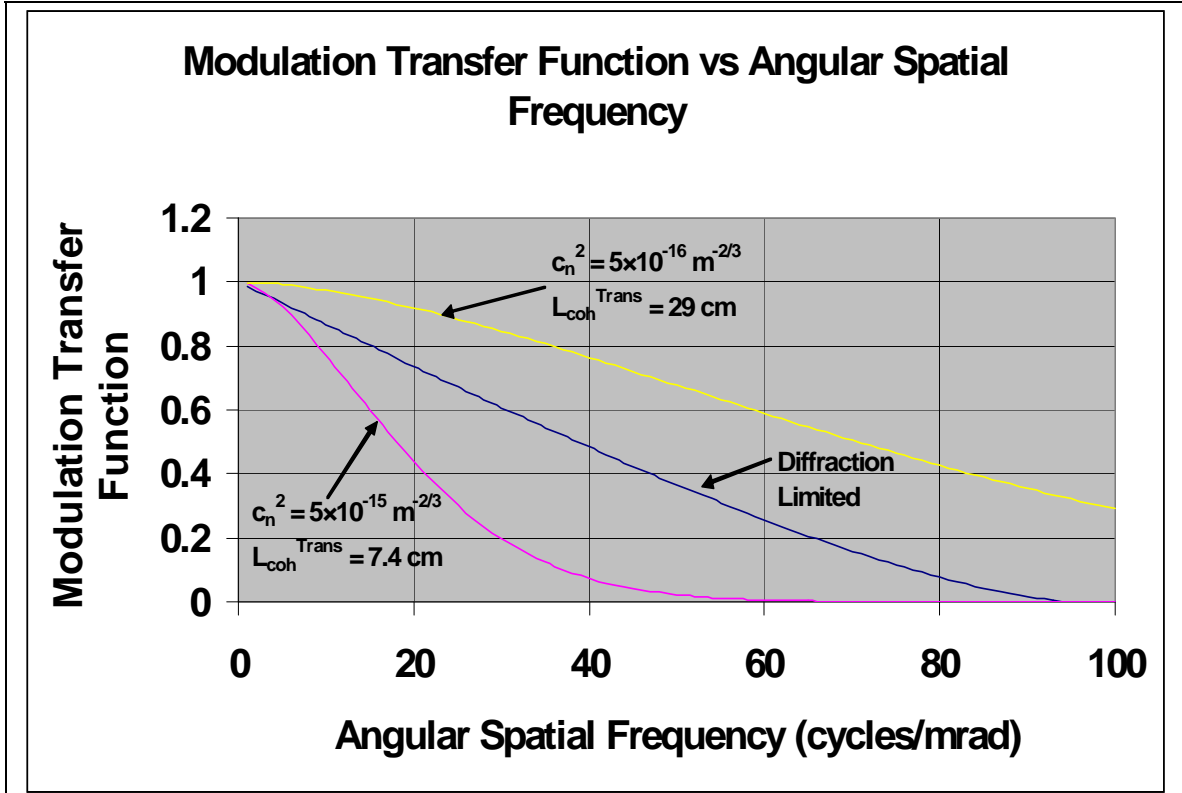


**Figure 1** Diffraction limited MTF (blue curve) and turbulence-induced MTF for  $C_n^2 = 5 \times 10^{-16} \text{ m}^{-2/3}$  and  $C_n^2 = 5 \times 10^{-15} \text{ m}^{-2/3}$  (yellow and magenta curves, respectively). The range to target was 20 *kft*.

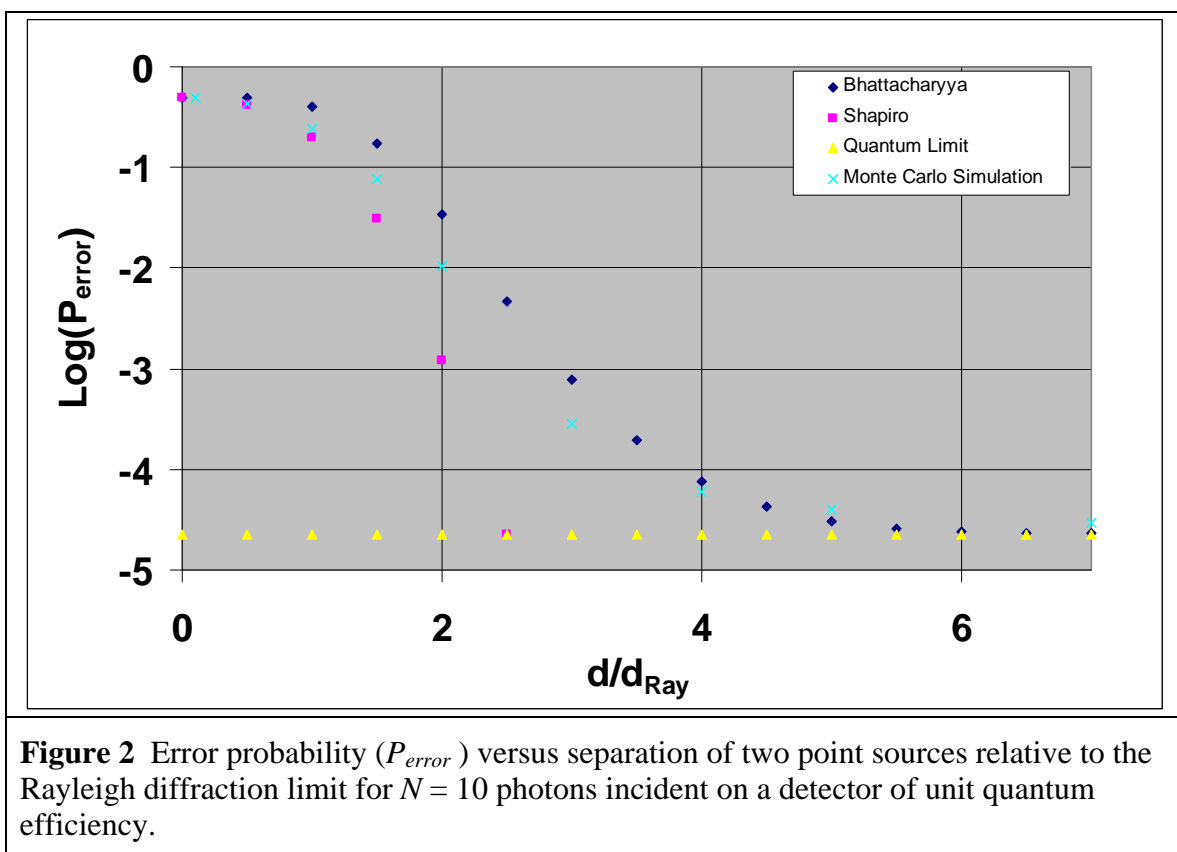
With respect to diffraction, the resolution is degraded more or less by this phenomenon than by turbulence depending on the value of  $C_n^2$ . We expect, for the diffraction-limited case, that the resolution is given by  $\Delta\theta_{\text{diff}} \cong \lambda/D = 10 \text{ } \mu\text{rad}$ , whereas for turbulence, with an infinitely large aperture, the resolution is governed by the seeing parameter according to  $\Delta\theta_{\text{urb}} \cong \lambda/r_0 = 5.4 \text{ } \mu\text{rad}$  and  $21 \text{ } \mu\text{rad}$ , respectively for  $r_0 = 29$  and  $7.4 \text{ cm}$ . These estimates explain the degradation in contrast seen in Figure 1. The performance of the sensor can therefore depend dramatically on atmospheric conditions near the ground, which can vary with time of day.

### 3.1.2 Real Space Description of Resolution: Rayleigh Diffraction Limit

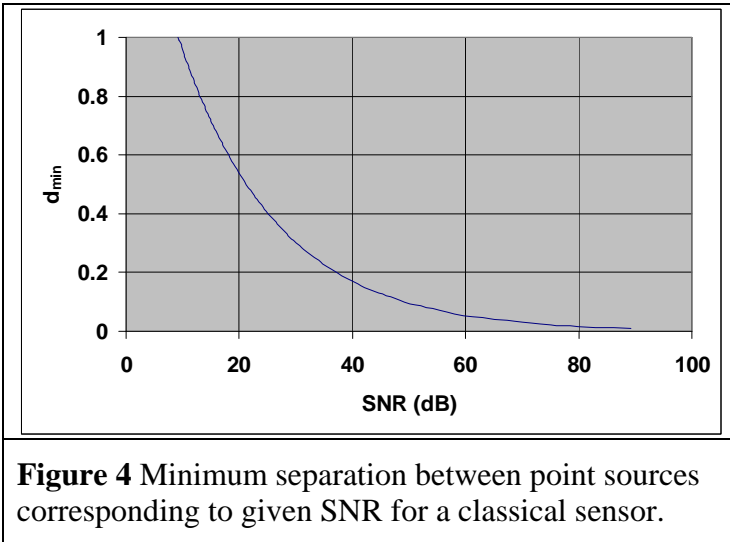
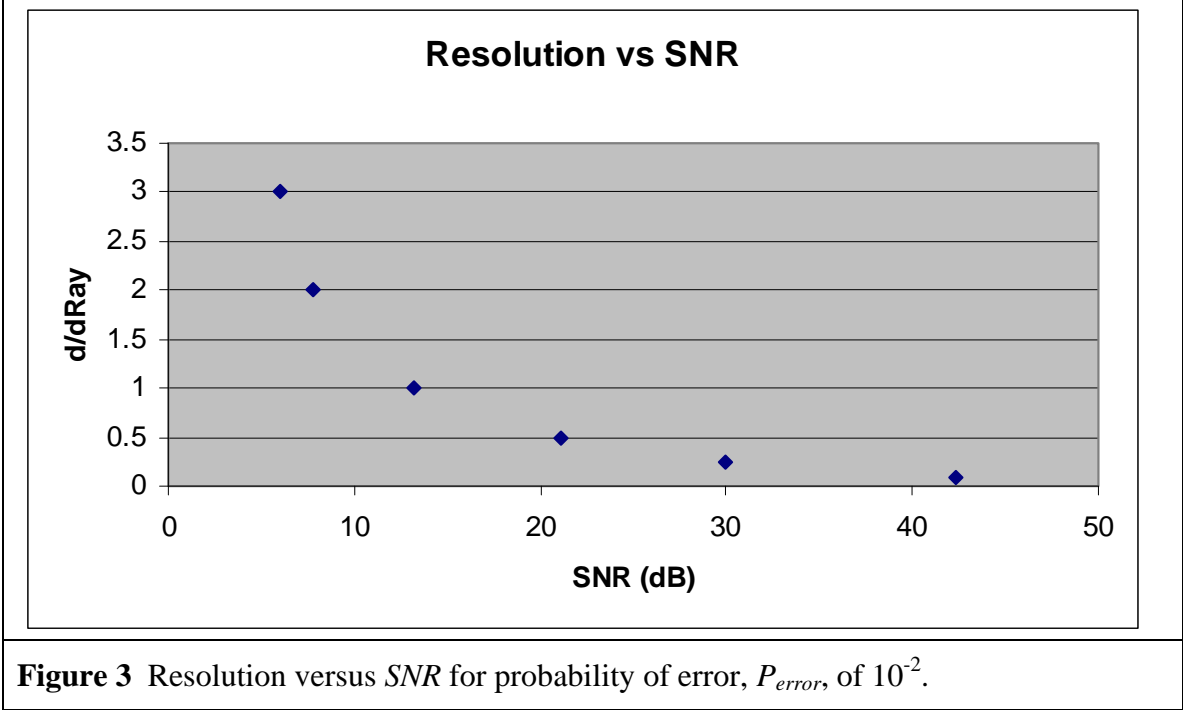
Although *MTF* versus spatial frequency is a standard measure of sensor performance at range using bar targets, one can also utilize a description of resolution in real space relating to the Rayleigh diffraction limit. We therefore began conducting a resolution analysis along the lines reported by BBN Technologies at the March 2008 Workshop. In

this work, the resolution problem is posed in terms of statistics as described by Carl Helstrom in 1964:<sup>5</sup> two targets are Helstrom-resolvable if the maximum *a priori* (MAP) probability of error is below some small number.

A Monte Carlo simulation was coded for direct detection, with the expected irradiance distribution subject to Poisson noise. A hard circular aperture was assumed, and the separation between sources was normalized to the angular Rayleigh resolution. The simulation results were consistent with those reported by BBN at the workshop in Utah. Figure 2 shows the results for  $N = 10$  photons incident on a detector of unity quantum efficiency. The simulation is compared to the upper bound predicted by Bhattacharyya,<sup>6</sup> a lower bound estimate formulated by Shapiro,<sup>7</sup> as well as the quantum limit of detection.<sup>8</sup> We have also calculated the error probability as a function of the SNR (equal to the mean photon number for Poisson statistics), and *SNR* versus target separation.



The decision theory analysis was also used to calculate resolution versus *SNR* assuming Poisson-distributed noise for a separation of two point sources of 0.1 to 3 times the Rayleigh criterion. Figure 3 shows the results of a Monte Carlo simulation in which we assumed an error probability of  $10^{-2}$  based on the parameters of probability of detection  $P_D = 0.9$  and false alarm  $P_{FA} = 10^{-6}$  respectively, as outlined in the DARPA metrics in the BAA. The result is that obtaining Rayleigh resolution requires about 13 *dB* *SNR*.



A slightly different decision theory approach led to a similar result. In this case, the classical baseline system was analyzed in terms of a generalized likelihood ratio test<sup>9</sup> with Gaussian noise statistics and binary hypotheses  $H_0$  and  $H_1$  corresponding to presence of either one or two point sources, and a  $jinc^2$  point spread function.  $SNR$  was calculated analytically as a function of separation between two point sources up to the

Rayleigh distance using the model of Shahram.<sup>10</sup> Figure 4 predicts that in order to achieve Rayleigh resolution, we need to have  $SNR = 11$  dB per pixel. This is then the level of  $SNR$  that the quantum system would have to achieve in forming images with a pixel size that is smaller by a factor of ten.

### 3.1.3 Resolution of Quantum versus Classical Ghost Imaging

We extend the above results to a quantum ghost imaging sensor by incorporating a point spread function ( $PSF$ ), derived<sup>11</sup> for the  $|N,1\rangle$  state, into the Monte Carlo simulation of resolution versus  $SNR$ . We assume that there are  $N$  photons propagating to the target and

that in the sensor have wavelengths  $\lambda_1$  and  $\lambda_2$ , respectively. For two point sources on the object plane symmetrically located about the origin at radius  $a/2$ , we have

$$PSF_{entangled} = \frac{1}{2} \left\{ \text{somb} \left( \frac{\pi D_R}{\lambda_2 L_2} \left( \bar{\rho}_2 - \frac{\bar{a}}{2} \right) \right)^2 + \text{somb} \left( \frac{\pi D_R}{\lambda_2 L_2} \left( \bar{\rho}_2 + \frac{\bar{a}}{2} \right) \right)^2 \right\}, \quad (4)$$

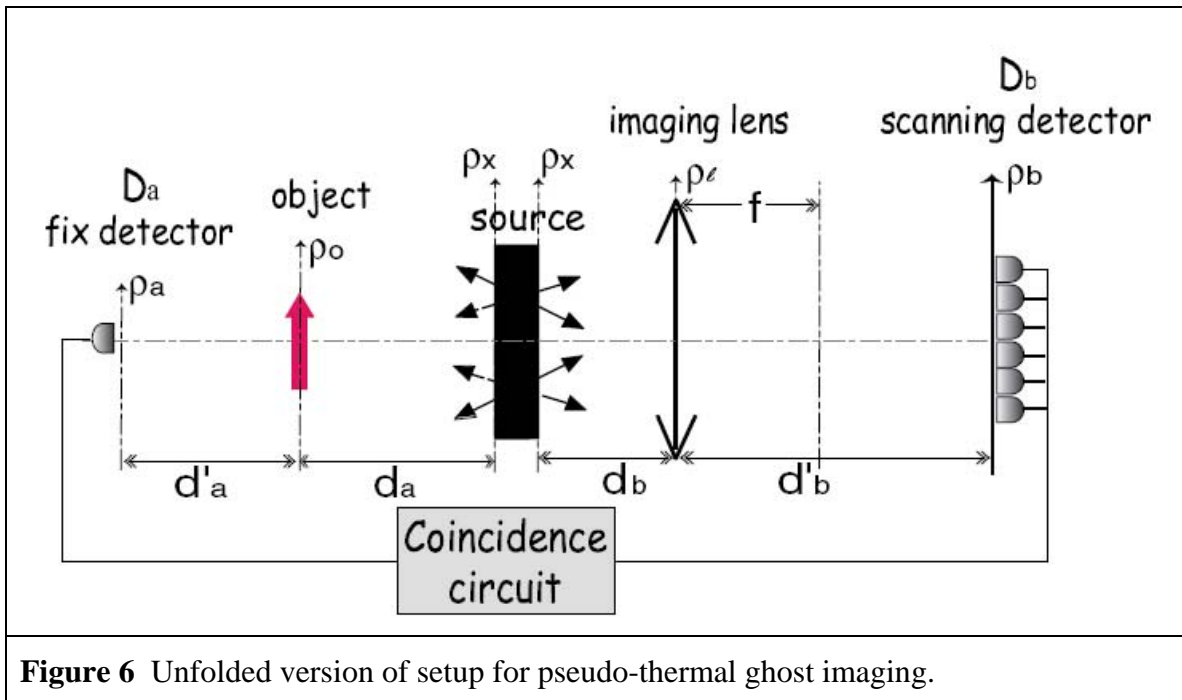
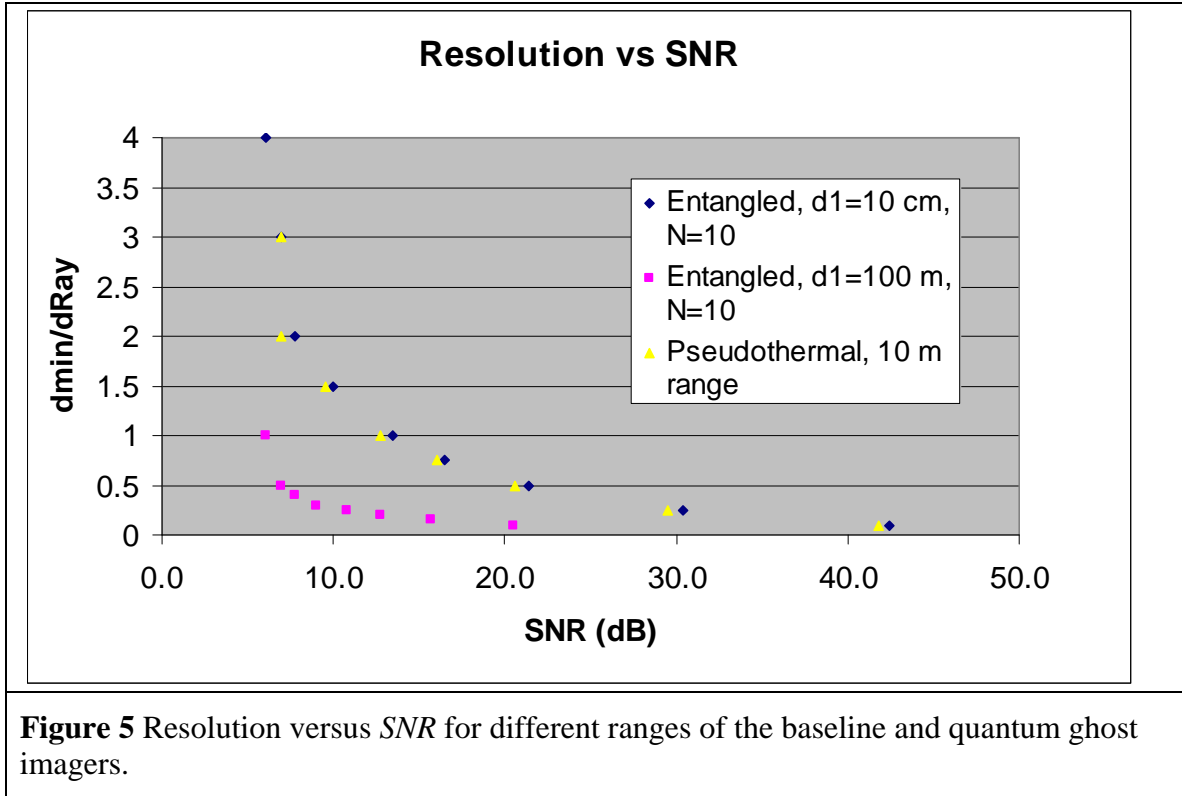
where  $\bar{\rho}_2$  is position on the image plane,  $L_2$  is the distance from the imaging lens to the array sensor, and  $d_{eff}$  is the effective distance between the lens and the object plane, defined as<sup>12</sup>

$$d_{eff} = d_2 + d_1 \left( \frac{\lambda_1}{N \lambda_2} \right), \quad (5)$$

where  $d_1$  is the distance between the source and the object and  $d_2$  is that between the source and the imaging lens of focal length  $F$ . The relation to  $L_2$  and  $F$  is given by the Gaussian thin lens equation as

$$L_2 = \frac{1}{\frac{1}{F} - \frac{1}{d_{eff}}}. \quad (6)$$

As discussed above, we set the error probability for distinguishing between one and two point sources to  $P_{err} = 0.01$ . In the case of the new baseline sensor,  $\lambda_1 = \lambda_2$ , and  $N=1$ , we obtain the same result as for the original classical imager, leading to  $d_{min}/d_{Ray} = 1$  at  $SNR = 13 \text{ dB}$ . For the quantum case, Wen et al.<sup>11</sup> showed that the resolution is a function of the relative values of  $d_1$  and  $d_2$ . For  $N = 10$ ,  $\lambda_1 = 1550 \text{ nm}$ ,  $\lambda_2 = 800 \text{ nm}$ ,  $F = 5 \text{ cm}$ ,  $D = 2.5 \text{ cm}$ , and  $d_2 = 10 \text{ cm}$ , the best resolution requires values of  $d_1 > 10 \text{ m}$ . Figure 5 shows the results for  $d_1 = 100 \text{ m}$ ; greater distances do not increase resolution. We also see that the resolution is not increased by a factor of ten for a given  $SNR$ . This may be a consequence of loosely defining the number of counts per pixel to be equal to  $C_{pixel} = SNR \times PSF$ . In ideal photodetection of Poisson-distributed photons with average number  $\langle n \rangle$  incident on a single detector of quantum efficiency  $\eta_{det}$ ,  $SNR = \eta_{det} \langle n \rangle$ . For real detectors, and in particular, for the photons arriving at the bucket detector of the quantum ghost imager, the  $SNR$  is more complicated (see the section below on  $SNR$  in coincidence counting) and can be enhanced if the photons obey sub-Poisson statistics, or by signal averaging, or it can be depressed as the number of background photons increases. With respect to coincidence counting, our definition of  $C_{pixel}$  is strictly valid in the case of equal counts on both detectors, a visibility  $V = 1$ , and multiplication by an additional factor corresponding to the square root of the number of counting intervals.<sup>13</sup> The main point of Figure 5, however, is to schematically compare the resolution offered by the quantum case to that of the baseline ghost imager for the same  $SNR$ .



The calculation of the resolution for the pseudo-thermal ghost imaging baseline assumes the paths shown in the setup of Figure 6. The associated *PSF* is



$$PSF_{thermal} = \frac{1}{2} \left\{ \text{somb} \left( \frac{\pi D_R}{\lambda d'_b} \left( \bar{\rho}_2 - \frac{\frac{\bar{a}}{2}}{d_a - d_b} \right) \right)^2 + \text{somb} \left( \frac{\pi D_R}{\lambda_2 d'_b} \left( \bar{\rho}_2 + \frac{\frac{\bar{a}}{2}}{d_a - d_b} \right) \right)^2 \right\}, \quad (7)$$

where  $s_o = d_a - d_b$  and  $s_i = d'_b$  are the effective object and image distances, respectively, according to the Gaussian thin lens equation for this system.<sup>14</sup> This equation is derived from the terms in the second order correlation function proportional to the product of Green's functions for the two different paths. Note that the lens here forms a secondary image since the thermal source already produces a lensless image at  $d_b = d_a$ . As noted above, the lens is therefore necessary in remote sensing in order to allow for a much longer distance in the path to the target. The yellow markers in Figure 5 show that for sufficiently long range the resolution is the same as in the bi-photon system. This is because the resolution of the secondary ghost image is governed by the aperture of the lens, which is assumed to have the same diameter as that in the quantum setup.

Overall, the above resolution analysis indicates that for the same  $SNR$  (11-13  $dB$ ) the quantum system increases spatial resolution with respect to the Rayleigh diffraction limit by a factor close to the number of entangled photons interacting with the target.

In the above analysis, we have used classical decision theory analysis. In a strictly quantum hypothesis test we would need to form the density operators for the quantum state. In the case of pure states for the two hypotheses, Helstrom has shown that the probability of error is given by<sup>15</sup>

$$P_e = \frac{1}{2} \left[ 1 - \sqrt{1 - |\langle \psi_1 | \psi_0 \rangle|^2} \right], \quad (8)$$

where  $|\psi_0\rangle$  and  $|\psi_1\rangle$  are the states corresponding to  $H_0$  and  $H_1$  respectively. Specifically, for the entangled  $N+1$  state that we consider for our quantum imaging system, the two hypothesis states would differ by electric field operators acting on the crystal output; in one case the Green's function for the field would contain an aperture function for a single point source, whereas the other's aperture function contains two delta functions for the two separated sources. In order to use the above expression, however, the states must be properly normalized, which has not yet been done. Additionally, we do not have an analytically expression for the case of  $N > 2$  entangled beams (versus photons).

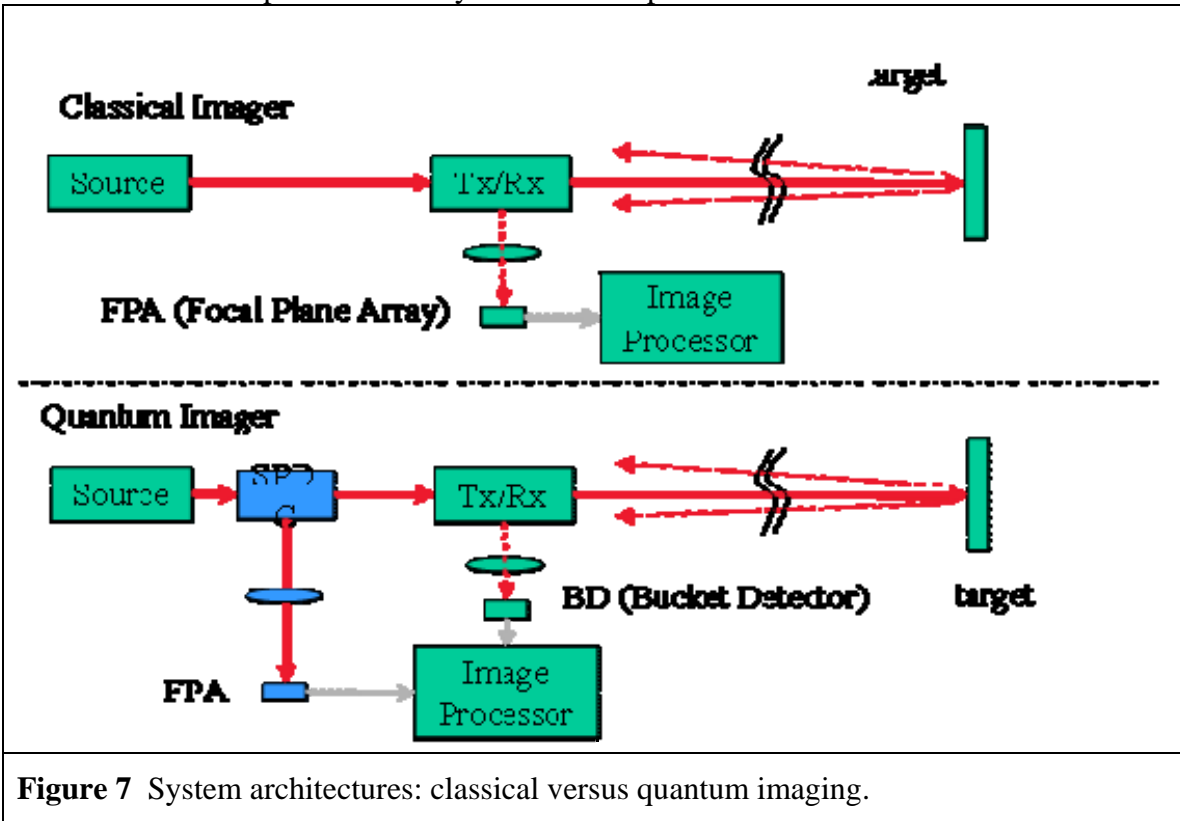
## 3.2 SNR Analysis

### 3.2.1 General Quantum versus Classical Considerations

We first discovered a direct comparison between  $SNR$  for quantum-correlated versus classical photons in the work by Jackson et al.<sup>16</sup> The entangled photons were considered to be captured by a single detector with multi-photon efficiency  $\eta_{n-ph}$ , similar to what NGC had envisioned for its QSP sensor, and the dominant noise term was assumed to be shot noise due to photons entering the detector. According to this analysis the ratio of the  $SNRs$  ( $R$ ) in the correlated and classical cases is given by

$$\frac{SNR_{correlated}}{SNR_{classical}} \sim \sqrt{\frac{P_t' \eta_{SPDC} \eta_{n-ph}(n\omega_0)}{P_t \eta_{det}}}, \quad (9)$$

where  $P_t$  and  $P_t'$  are the transmitted laser power to the target in the classical case, and the nonlinear optical crystal pump power in the case of the quantum sensor,  $\eta_{NLO}$  is the efficiency of the nonlinear optical (NLO) process for generating entangled photons, and  $\eta_{det}$  is the classical detector efficiency. One also assumes here that shot noise is dominated by signal as opposed to background photons. If one further assumes that laser and pump powers are equal to each other, then  $R < 1$  due to the inefficiency of the NLO process. However, if the pump power is much greater than that of the laser one can have  $R > 1$  as long one does not enter into a “stimulated emission” regime for which the downconverted output is diluted by uncorrelated photons.



When the background photons (i.e., solar) dominate the shot noise  $R$  was shown to be governed by

$$\frac{SNR_{correlated}}{SNR_{classical}} \sim \frac{P_t \eta_{SPDC} \eta_{n-ph}(n\omega_0)}{\sqrt{P_t \eta_{det} \eta_{1-ph}(n\omega_0)}}, \quad (10)$$

where  $\eta_{1-ph}$  is the single-photon detection efficiency of the multi-photon detector,  $n = 2$ , and the pump power is no longer required to exceed the laser power if the detector is designed such that  $\eta_{n-ph} \gg \eta_{1-ph}$ . Of course, for  $n > 2$ , we will have to consider the

possibilities of many other multi-photon (i.e., 3, 4, ...,  $n-1$ ) absorption processes that compete with the  $n$ -photon absorption of interest.

The above treatment is not adequate for describing the case of ghost imaging because one must consider joint detection between a bucket detector after the free space idler path, and an array detector in the local signal beam. The classical versus quantum imaging scenarios are depicted in Figure 7. One of the main benefits of ghost imaging is the ability to capture the idler photons with a point detector rather than array, giving a gain in signal proportional to the number of pixels. However, the system setup is more complicated because of the need to perform joint detection. These system trades are summarized in Table 6.

**Table 6 Qualitative comparison of quantum versus classical systems.**

	Classical Imager	Quantum Imager	Comments
<b>Source</b>	Laser	Laser with SPDC	Efficiency to create entangled photons is critical for quantum imager
<b>Atmospheric Effect</b>	Two Ways (round trip)	One Way (from system to target)	Under severe turbulence and attenuation, quantum imager is better
<b>Optics</b>	System aperture limits resolution (diffraction limit per given wavelength)	Diffraction limit can be overcome by multi-wavelengths (or multi-photons)	Implementation will require more work on source and configuration
<b>Detector</b>	Array detector for imaging target	Bucket detector for imaging target.	Quantum imager has a gain by the number of pixels over classical imager.

### 3.2.2 SNR and CAR of Classical and Quantum Systems

In our first system analysis of ghost imaging we described the detection process by a quantity – the coincidence to accidental ratio (*CAR*) - unique to joint detection. We then analyzed the classical baseline (which at that time was not a ghost imaging sensor), according to the *SNR* per pixel as a function of range to the target as shown in Figure 8. The power *SNR* is then defined as

$$SNR = \frac{(GN_{sig})^2}{(Noise)^2}, \quad (11)$$

where  $G$  is a gain factor for the imaging sensor,  $N_{sig}$  is the number of signal photoelectrons, and noise is the total shot noise due to the number of dark electrons  $N_{dark}$ , solar photoelectrons  $N_{solar}$ , and  $N_{sig}$ . This noise was calculated as

$$Noise = \sqrt{F^2 G^2 (N_{dark} + N_{solar} + N_{sig})}, \quad (12)$$

where  $F$  is the noise factor. We see in Figure 8 that the slope changes, as expected, from a  $1/R^2$  to a  $1/R^4$  dependence as the optical beam size exceeds the area of the target.

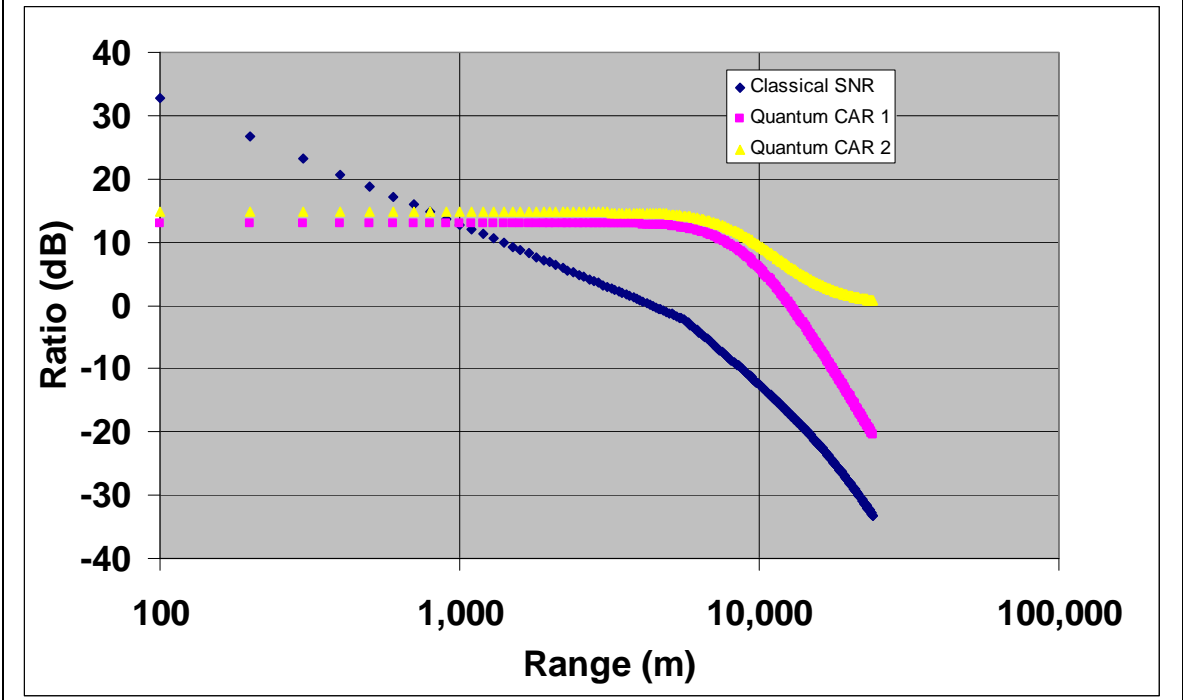


**Figure 8** Comparison of *CAR* of quantum sensor to *SNR* of classical one.

For the quantum case we assumed the existence of an  $N+1$ -entangled photon source employed in a ghost imaging geometry. The source emits photons in short pulses at a repetition frequency  $\nu_{rep}$  limited by the dead times of the sensors. We denote as the “idler” the  $N$  photons emitted in a spectral range favorable for atmospheric transmission for propagation to the target and back. We choose the  $1.55 \mu m$  wavelength because of the maturity of InGaAs avalanche photodiodes (APDs) in Geiger mode operation, and advanced components at that wavelength developed for telecommunications. Ultimately, however, we may choose a photon wavelength in the long-wave infrared for mitigating losses due to atmospheric turbulence, and requiring Mercury Cadmium Telluride (MCT) detection.

The “signal” photon (entangled with the  $N$  idler photons cited above) is retained for coincidence detection with the idler photons when they return from the target. Initially, we considered the case of  $N = 2$  (i.e., one signal, one idler) to simplify the analysis. An SPDC source pumped at  $532 nm$  would generate a  $0.81 \mu m$  wavelength signal photon correlated with the above idler. This wavelength lends itself to the lower noise, higher speed Si and emerging array detection.

In recent studies of quantum correlated photons, it was shown that the ratio of coincidence counts per integration interval  $R_{coinc}$  to accidental counts  $R_{acc}$  peaks at detected entangled pair levels per pulse of  $< 10^{-2}$ .<sup>17</sup> We therefore considered that the flux incident on the idler detector or on each pixel of the signal detector array per gate interval was kept at or well below single-photon level to preclude saturation, and for achieving optimal *SNR*. We noted that one of the key objectives of the UMBC work on QSP was to investigate means by which the counting rates could be raised while maintaining workable levels of *SNR* using methodologies such as entangled beams and current correlation. Next, one could imagine a scheme in which the flux per array pixel is scaled

as a function of range and target cross-section either by adjusting the source flux or by attenuation of the photons at the detector. As a practical matter, one must be careful, however, because the source output cannot be arbitrarily increased without running into a “stimulated emission” regime in which the degree of entanglement is diluted. This occurs in SPDC sources, for instance when the single-pass gain crosses over from a low to a high gain region, where it goes from being quadratic in field magnitude (linear in pump power) to exponential.<sup>18</sup> Still, for the purposes of our analysis, we sought to develop some required levels of output flux from a prospective source, which would serve as a development challenge for a subsequent phase of the QSP program.

For the quantum ghost imager, we calculated the ratio  $CAR$ .<sup>19</sup> This is not exactly the same quantity as  $SNR$  because it is a ratio of signal to background, rather than of signal to shot noise fluctuations, but we used it as a starting point for comparison with the classical system. We surmised that a fraction  $f_c$  of the photons emitted from the source were quantum-correlated with each other. Assuming that the correlated pair production rate is  $\mu_{pair}$ , the roundtrip loss for the idler photons is  $\eta_{2-way}$ , the optical loss for the signal is  $\eta_{local}$  and the quantum efficiencies of the signal and idler photodetectors are  $\eta_s$  and  $\eta_i$ , respectively, we have, for the number of coincidence counts,

$$N_{coinc} = f_c \mu_{pair} \eta_{2-way} \eta_{local} \eta_s \eta_i. \quad (13)$$

The total number of signal counts  $\mu_s$  is a sum of contributions from twin photons, uncorrelated (background) photons  $\mu_b^s$ , and dark electrons that are detected at a rate  $d_s$ . If the coincidence peak has a temporal width of  $T_c$ , determined by detector jitter, then we find

$$\mu_s = (\mu_{pair} + \mu_b^s) \eta_{local} \eta_s + d_s T_c. \quad (14)$$

The number of idler counts has an additional term due to the number  $\mu_{solar}$  of solar photons hitting the target. Considering that these have a one-way loss of  $\eta_{1-way}$ , and that the idler detector dark count rate is  $d_i$ , the total number of idler counts is

$$\mu_i = ((\mu_{pair} + \mu_b^i) \eta_{2-way} + \mu_{solar} \eta_{1-way}) \eta_i + d_i T_c. \quad (15)$$

The coincidence peak is superimposed on a background of counts due to all of the above sources, including members of twin photon pairs that arrive at the same time as members of other pairs to which they are not correlated. We referred to this background as accidental counts, given by

$$N_{acc} = \mu_s \mu_i. \quad (16)$$

We defined the power ratio of coincidence to accidental counts as

$$CAR1 = \frac{N_{coinc}^2}{N_{acc}}. \quad (17)$$

However, since accidental counts are measured within the coincidence time, it is more appropriate to add them to the coincidence counts before normalizing to the background, leading to

$$CAR2 = \frac{(N_{coinc} + N_{acc})^2}{(N_{acc})^2}. \quad (18)$$

We used this quantity to compare with the *SNR* of the classical system, given that the following parameters in the quantum case were the same as in the classical one, in accordance with the QSP guidelines: wavelength of photons propagating to the target and back, average optical power out of the sensor, aperture size, geometric losses, background and target cross-sections. Both sensors were assumed to emit light in the form of a train of pulses. For photon coincidence counting statistics, however, it is advantageous to have a high pulse repetition rate (i.e.,  $\geq 100 \text{ kHz}$ ), whereas as for the classical system it is better to flood the target with a very high energy pulse, concomitant with lower repetition rate lasers.

Given an array format of the classical system we assumed that the quantum sensor array had a resolution cell smaller by a factor of ten to conform to QSP's goals. An advantage of ghost imaging, however, is that the array can be placed in the signal path, for which optical loss is very low, and the weak idler return goes into a bucket detector. The main challenge is therefore to make the source flux high enough for adequate return of the idler from the target, while reducing the signal flux to single photon level required for the coincidence measurement. The signal flux can be reduced by using a telescope to magnify the beam on the array, and/or a series of beam splitters to direct the light to multiple arrays that would be engaged in joint coincidence. We assume for this analysis that only one array would suffice.

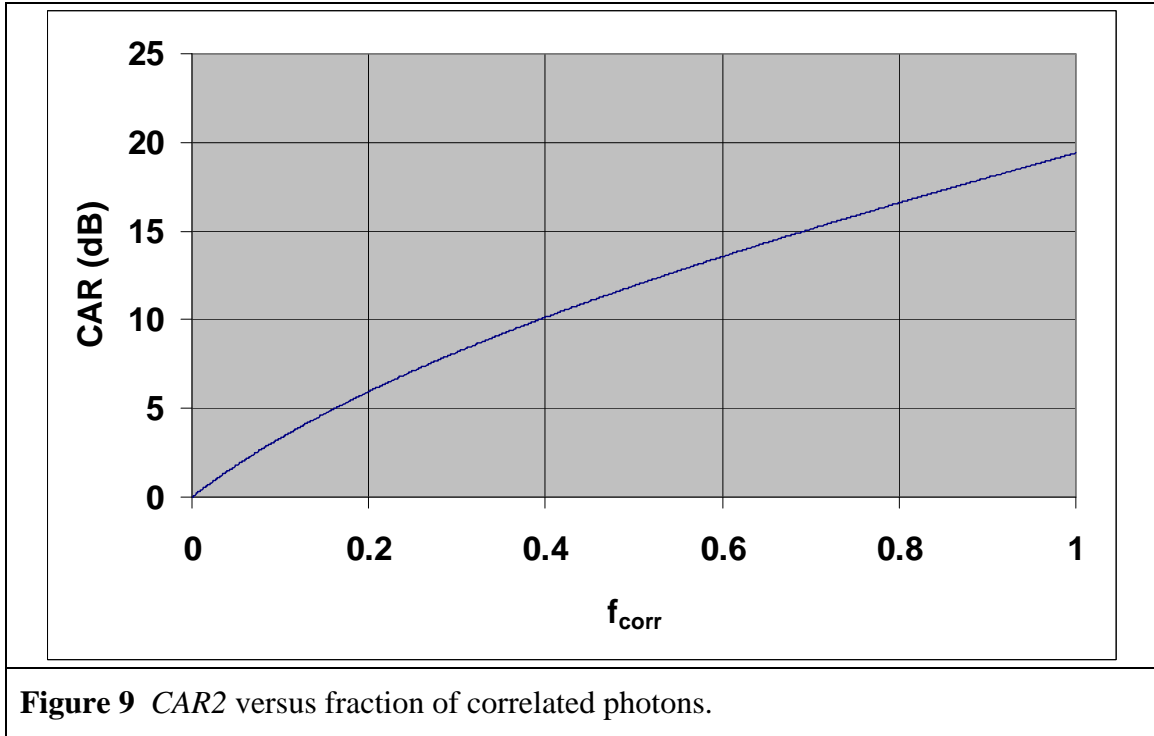


**Table 7** Values of relevant parameters for SNR/CAR calculations of Figure 9.

Parameter	Value
Laser Pulse Width	5 ns
Pulse Repetition Rate	20 kHz
Beam Divergence	0.2 mrad
Signal Wavelength	0.81 $\mu\text{m}$
Idler Wavelength	1.55 $\mu\text{m}$
Receiver Optics Transmission	0.5
Signal Detector Efficiency	0.5
Signal Coupling Efficiency	0.8
Signal Array Time Jitter	200 ps
Signal Array Dark Count Rate	1 kHz
Idler Detector Efficiency	0.1
Idler Coupling Efficiency	0.1
Idler Detector Time Jitter	800 ps
Idler Detector dark Count Rate	200 kHz
Coincidence Detection Gate Width	10 ns
Target Physical Area	18 $\text{m}^2$
Target Reflectivity	0.3
Aperture Diameter	10 cm
Solar Spectral Flux	267 $\text{W}/\text{m}^2 \cdot \mu\text{m}$
Atmospheric Attenuation	2 dB/km

becomes a small number, and  $CAR_2$  approaches 1, but exceeds the classical  $SNR$  for all  $R > 1 \text{ km}$ .

For a fixed range ( $R \cong 2 \text{ km}$ ) Figure 9 shows how  $CAR_2$  increases with degree of

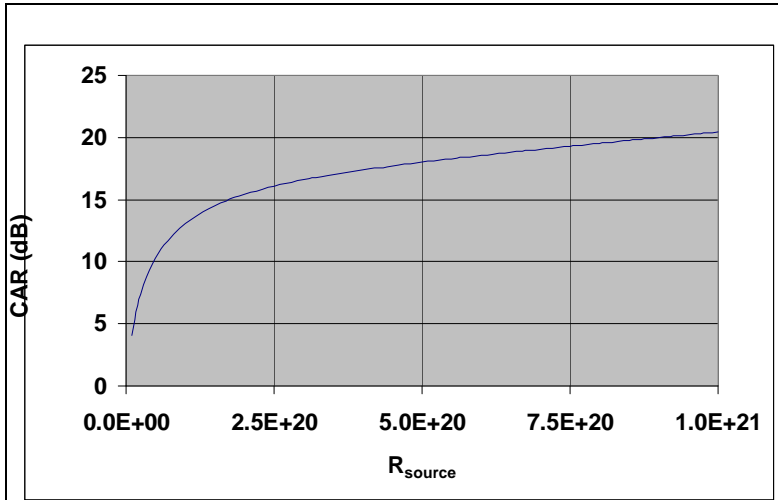


**Figure 10**  $CAR_2$  versus source flux (photons per second).

quantum correlation, and Figure 10 shows its dependence on the source rate of photons per second. Obviously, this rate is extraordinarily high, and would probably be difficult to achieve without significantly reducing visibility. Furthermore, such fluxes may not allow the use of single photon counting. Instead, we may need to view the output of the quantum sensor in this

regime in terms of entangled beams, rather than entangled pairs. For detection, current-current correlation techniques may need to be employed. These have been investigated

by UMBC for several years in the case of pseudo-thermal photons,<sup>20</sup> but have only recently been explored with entangled photon sources.

### 3.2.3 Atmospheric Effects

One of the main goals of the experimental work was to eventually determine the effect of scintillation on quantum entanglement. Consequently, NGC modeled beam propagation for a remote sensing scenario commensurate with the initial baseline.

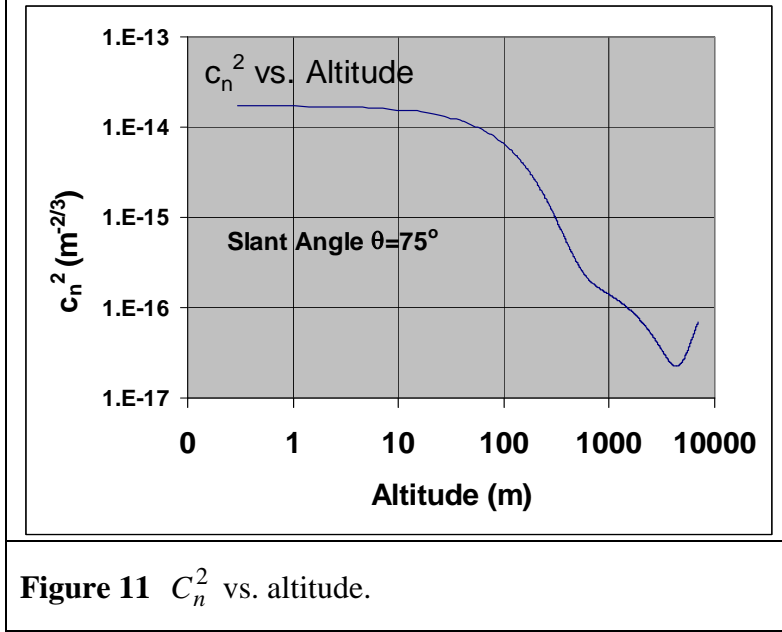


**Figure 11**  $C_n^2$  vs. altitude.

effects we considered the sensor to be located at an altitude of 20 *kft* with a range of 24 *km* and moving at 200 *m/s*. Using the Hufnagel-Valley model for the refractive index structure constant,  $C_n^{2,21}$  assuming a wind speed at the ground of 20 *mph*, and a logarithmic dependence of wind speed with altitude  $h$ ,<sup>22</sup> we determined the height dependence of  $C_n^2$  to be as shown in Figure 11. The Fried parameter was then calculated for sections of the propagation path both for the downlink and uplink, varying between about 10 and 300 *cm*. Gaussian beam propagation was modeled using GLAD software in which we iteratively performed diffractive propagation with phase aberration steps associated with each section of the path. Figure 12 (a) – (c) shows spatial profiles of the beam at the starting point, at the ground (target), and back to the sensor, where it is diffracted by the 15 *cm* aperture. Scintillation with these seeing parameters is clearly sufficient to break apart the beam into numerous spikes. However, the effect on the spatial frequency distribution does not appear to be as drastic. As seen in the FFTs of these irradiance distributions (Figure 12(d) – (e)) the initial peak is greatly sharpened due to the broadening of the beam (toward a plane wave) with distance, but higher spatial frequencies are introduced due to aperture diffraction (rings) and turbulence (lobes). We conjectured that this spatial frequency redistribution disturbed the anti-correlation of transverse wave vectors between the free space propagating idler photon beam and the local signal beam, which does not propagate in atmosphere. In fact, UMBC has shown that scattering of the returning idler has no effect on this anti-correlation as long as the photon is picked up by the bucket detector. However, this may not true of the outgoing beam.

In order to include in our *SNR* model losses, both classical and quantum mechanical, associated with atmospheric turbulence, NGC modeled the propagation of beams from the airborne baseline sensor to a target on the ground and back. To begin with, we study the effect of atmosphere on the spatial profile and spatial frequencies of the beam as modeled with physical optics code. To account for atmospheric



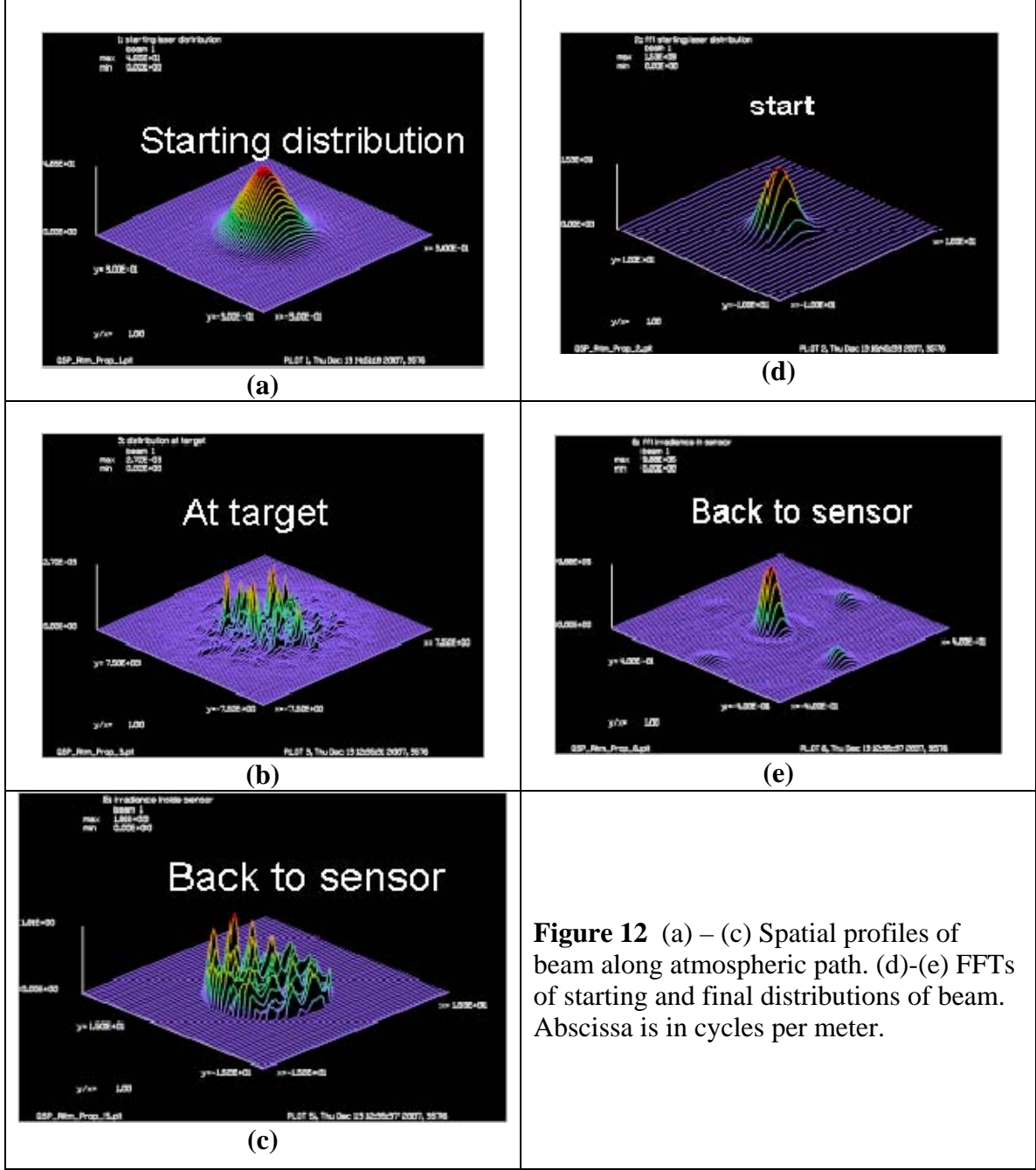


**Figure 12** (a) – (c) Spatial profiles of beam along atmospheric path. (d)-(e) FFTs of starting and final distributions of beam. Abscissa is in cycles per meter.

An additional loss factor of potential importance in our quantum enhanced system is also associated with the atmosphere and is due to fluctuations in idler photon arrival times. A loss is incurred if the fluctuations cause the photons to arrive outside of the entangled pair coincidence window. According to Young et al.,<sup>23</sup> the time-of-arrival variance for a Gaussian pulse of initial half-width  $T_0$  propagating a distance  $z$  in a turbulent medium with outer-scale size turbulence  $L_0$  and index of refraction structure constant  $C_n^2$  is given by

$$\sigma_a^2 = \frac{T_0^2}{4} + 2\alpha, \quad (19)$$

where  $\alpha = 0.3908 \cdot C_n^2 \cdot L_0^{5/8} / c^2$ ,  $c$  is the speed of light, and  $L_0$  is the outer-scale parameter. If we consider  $T_0$  to be the initial coincidence width, and take conservative values of  $L_0 = 10 \text{ m}$ , and  $C_n^2 = 10^{-12} \text{ m}^{-2/3}$  we estimate the square-root of the variance, as shown in

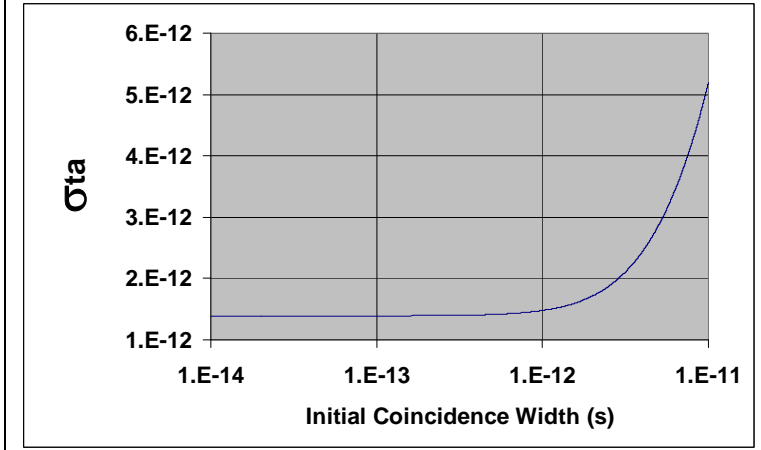


**Figure 13** Variance in arrival time as a function of initial coincidence width after propagation through 40 km in atmosphere.

Figure 13. The amount of broadening is seen to be negligible for widths greater than 1 to 10 ps. In reality, the measured coincidence peak width will be broadened primarily by the much greater 100 to 1000 ps overall jitter of the detectors. Experimentally, fine adjustments to the idler sensor gate duration are used for coincidence count optimization. The gate width is much wider than the coincidence width, especially for optical pulses  $> 1 \text{ ns}$ .

#### 3.2.4 Ghost Imaging SNR Model

We eventually developed a signal-to-noise ratio (SNR) model for quantum imagers that superseded our initial description of joint detection in terms of CAR. The model incorporated the effect of photon states peculiar to the quantum imager and the effects of solar background that are significant for systems operating outdoors. The model also took into account the effect of joint detection that is unique to quantum imagers. This work is summarized in a paper presented at the SPIE Conference entitled “Quantum Communications and Quantum Imaging VI” (San Diego, Aug. 10-14, 2008).<sup>24</sup>

Briefly, the model assumed an avalanche photodiode (APD) running in Geiger mode for both classical and quantum imagers. The unified model defines noise equivalent count (NEC) by

$$NEC = 2 \sqrt{\frac{[\eta_q (F-1) M_{sig}] + M_{sig} + \chi_{joint} (M_{back} + M_{dark})}{T_c}}. \quad (20)$$

The first term in the square root comes from the beam splitter relation for photons incident on an inefficient photodetector in the quantum model of direct detection.<sup>25</sup> Here,  $\eta_q$  is quantum efficiency,  $F$  is the Fano factor,  $T_c$  the total counting period, and  $\chi_{joint} = T_w M_{local}$  is a scale factor for joint detection, with  $T_w$  being the coincidence counting window duration, and  $M_{local}$  the count rate per pixel in the local detector.  $M_{sig}$ ,  $M_{back}$ , and  $M_{dark}$  are the count rates for return signal from target, background, and dark count, respectively.  $F$  describes the degree of entanglement of the quantum state: In a perfectly

entangled number state  $F = 0$ , whereas  $F = 1$  for classical photons.  $\chi_{joint} = 1$  for the classical imager and can be reduced far below 1 for the quantum sensor by adjusting the photon count rate in the local path and temporal window.  $SNR$  is then given by

$$SNR = \frac{M_{sig}}{NEC}. \quad (21)$$

Using this expression we performed a trade study of parameters for a quantum ghost imager. The model assumed an entangled photon source that transmits  $N$  degenerate photons at  $1.55 \mu m$  to a Lambertian target  $1 km$  away while keeping a photon of different wavelength for local coincidence detection. This configuration was based on modeling by UMBC that showed  $N$ -fold increase in spatial resolution for an  $N+1$ -photon state if  $N$  photons were sent to the object to be imaged and one was held locally. The photons returned from the target were assumed to be detected simultaneously (i.e., by an  $N$ -photon absorber). Because such a source and sensor do not exist, and we were not doing development of these components in this phase, we were limited to treating their efficiencies as variables.

For the assumed value of  $C_n^2$  of the atmosphere we required  $10 dB$  of fade margin for the  $SNR$ . This was based on a time series of the irradiance  $I$  generated by creating a normal random distribution of the log-amplitude parameter  $\chi$ , and then calculating (with low-pass filtering for atmospheric time constant) the cumulative probability distribution of  $I$ , such that 99% of the time,  $I$  is greater than 5% of the mean (normalized to 1). This percentage is then translated to a required margin for fading of  $10 dB$ . Consequently, the overall  $SNR$  needed for the sensor is this margin plus the level required to achieve the Rayleigh diffraction limit, i.e.,  $10 dB + 11 dB = 21 dB$ .

Before proceeding with the quantum case, we modeled a classical system in which the source output power was adjusted to a level commensurate with  $SNR = 21 dB$ . The same average power was then assumed for the quantum system, as well as the same aperture size. However, the quantum sensor beam waist was maximized, while avoiding clipping by the aperture, in order to minimize divergence, and therefore the size of the illuminated spot on the object. This was necessary to attempt to satisfy the requirement of UMBC's model that the  $N$  photons hit the same point on the target and return together to the sensor.<sup>26</sup> We also assumed that the source output was an entangled beam that consisted of a large number of sets of  $N$ -photons, in each pulse, and, that perhaps multiple pulses would have to be transmitted to increase the probability that one of the sets of photons would return to the source unscathed; otherwise the entanglement is completely lost.

Figure 14 shows the dependence of  $SNR$  versus detector efficiency for  $F = 0.9$  assuming unity detector quantum efficiency, and  $SNR$  versus  $F$  for both source and detector efficiencies equal to 1. In these calculations we assumed that the output current of the  $N$ -photon was linear in incident photon flux, in accordance with theory of multi-photon absorption of entangled states.<sup>27</sup> This dependence holds if the entangled flux is very low, which is likely in the case of a return from a remote diffuse object.

At the March '08 QSP Workshop there was a question regarding the relevance in the beam splitter relation of the Fano factor  $F$ , which was shown to be only slightly less than 1 by Rarity et al. in the case of post-selection following an SPDC.<sup>28</sup> For the GHZ state

we have been considering,  $F = 0$  by definition since the state has zero variance in photon number as long as the quantum state remains intact. For W states the photon number may change while still retaining entanglement among the remaining photons, so  $0 < F < 1$ . Entangled beams, on the other hand are generated at high gain with intense pump excitation. Because of a concomitant increased probability of accidental coincidences this tends to degrade visibility,<sup>29</sup> with an expected corresponding reduction in  $F$ . As a result of all of these considerations we retain this factor in our modeling since we can always set it to 1 in the limit of classical photons.

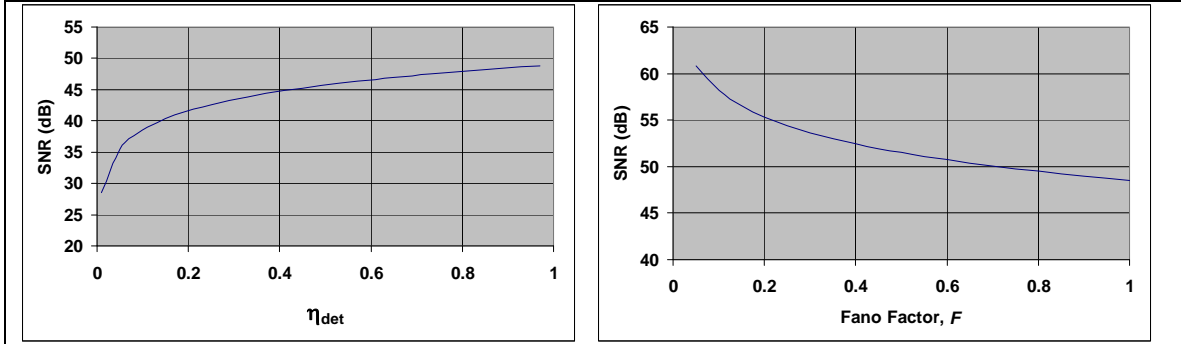


**Figure 14** SNR versus detector efficiency for  $F = 0.9$  and unity bucket detector efficiency (left), and SNR versus  $F$  for unity source and detector efficiencies (right).

While the actual values produced from this analysis are not yet meaningful, the results point out the issues that must be addressed in developing a quantum sensor for a real system. One is the trade just discussed involving high photon flux versus visibility loss. Another involves the requirement that the  $N$  photons travel in a tight beam together throughout the round trip. Even if it were possible, this means that the image acquisition time is substantially increased over the classical case due to the need to now scan across the target.

### 3.2.5 Ghost Imaging SNR: Intensity Interferometer Approach

Late in the program, pursuant to DARPA's suggestion, we decided that the baseline system should also be a ghost imager for the most direct comparison between quantum and classical sensors. From an historical standpoint, ghost imaging is rooted in the famous intensity correlation experiments of Hanbury-Brown and Twiss, which were used to measure the angular diameters of stars.<sup>30</sup> It therefore makes sense to describe SNR of the ghost imaging systems under consideration in terms of intensity interferometry.<sup>31</sup> Essentially, the signal is determined by the correlation between fluctuations in the detected photocurrents. The noise has contributions from shot noise ( $N_{ss}$ ), wave noise ( $N_{ii}$ ) due to fluctuations in the intensity of light incident on the photodetectors, and a cross-term ( $N_{si}$ ) associated with correlation between wave and shot noise. In stellar interferometry, shot noise is the dominant contribution.<sup>32</sup> However, for pseudo-thermal light the wave noise term can be the greatest source of photocurrent fluctuations. We therefore retain all of these noise terms for comparison.

#### 3.2.5.1 Photocurrent correlation

As a first step we assume detection parameters similar to those of recent ghost imaging current correlation measurements.<sup>33</sup> In order to determine the fraction of photons hitting the target we need to know the divergence of the beams in the object path. The

pseudo-thermal source generates light emitting in a hemisphere, but a portion of it can be collimated with a lens. We consider an initial source size  $d_0 = 1 \text{ mm}$ ,  $D = 10 \text{ cm}$  lens with  $f = 20 \text{ cm}$  focal length for both the baseline and entangled photon sources. For the entangled case, the nonlinear optical crystal bandwidth is given by  $\Delta k_z L = \pi$ , where  $\Delta k_z$  is the deviation from perfect phase matching ( $z = \text{beam propagation direction}$ ), and  $L$  is the crystal length. Using momentum conservation, the small angle approximation, and Snell's law for the beams exiting the crystal, the divergence of the target (idler) beam can be calculated for bi-photons from

$$\theta_i = \sqrt{\frac{2\pi}{L} \frac{k_s}{k_i k_p}}, \quad (22)$$

where  $k_p$ ,  $k_s$ , and  $k_i$  are the wave vectors of pump, signal, and idler, respectively. For pump, signal, and idler wavelengths of 532, 810, and 1550 nm, respectively, this gives, for an  $L = 5 \text{ cm}$  long PPLN crystal, a divergence  $\theta_i = 13 \text{ mrad}$  before the collimating lens. Assuming average CW output power of 100 W, 1550 nm wavelength, a  $25 \text{ m}^2$  area diffuse target of reflectivity 0.3, but ignoring light reflected from clutter, we calculate the expected rate of photons captured by the sensor aperture as a function of range for both baseline and quantum sources, and compare to the rate of solar photons scattered off the target into the sensor, using an irradiance on Earth of  $267 \text{ W}/\mu\text{m}\cdot\text{m}^2$ ,<sup>34</sup> and to the dark current, calculated from the noise equivalent power of the photodiode of  $1.5 \text{ pW}/\text{Hz}^{1/2}$  and an electronic bandwidth of 100 kHz. Figure 15 shows that the solar photons yield a negligible contribution compared to the dark current, and that the photocurrents in the baseline and entangled photon systems fall below the dark currents at 1 km and 10 km, respectively. One also sees that the baseline signal begins to decrease as  $R^4$  (due to laser spot size exceeding target area) at around 100 m, whereas this does not happen until

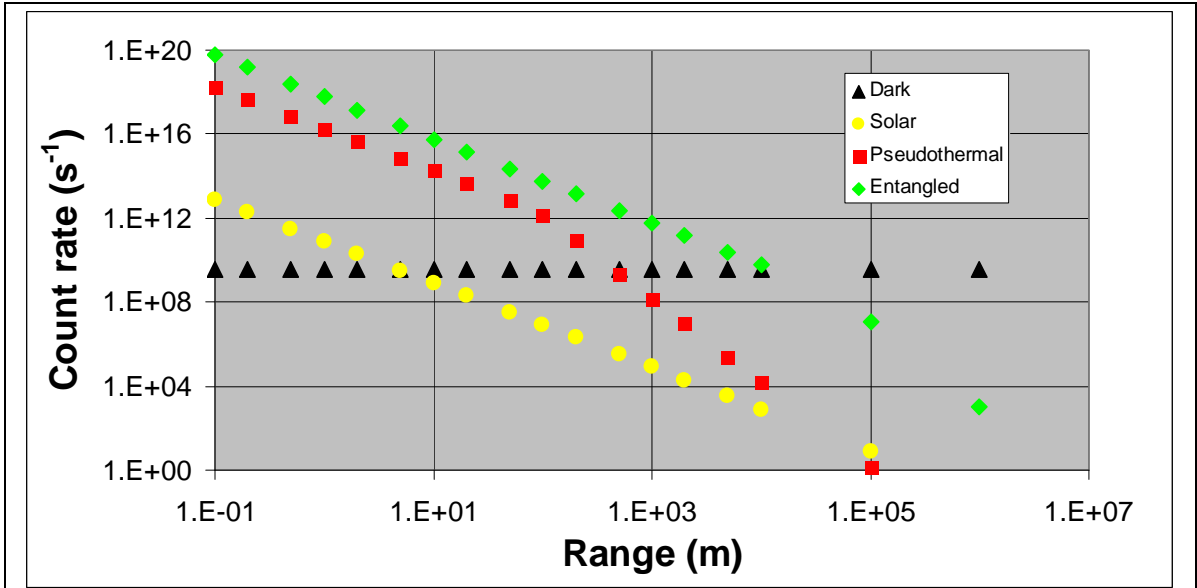


**Figure 15** Comparison of rate of photons incident on detector for baseline and entangled photon sources against that due to solar photons and dark counts.

ranges greater than 10 *km* for the entangled photon case. This single detection comparison is somewhat misleading, however, because what ultimately matters is the correlation between currents in two detectors, and this is what is calculated in the *SNR* below.

We calculate the *SNR* versus range using the formalism derived by Gamo,<sup>35</sup> for which

$$SNR = \frac{S}{\sqrt{N_{ss}^2 + N_{si}^2 + N_{ii}^2}}, \quad (23)$$

where  $S = \langle \Delta I_1(t) \Delta I_2(t) \rangle$  is the correlation between fluctuations in the photocurrents in the two detectors, and the explicit expressions for the noise terms are given in the referenced paper. Here we ignore the solar and dark current contributions, and we assume that the locally retained photons provide a photocurrent that is maintained at a level equal to one tenth of the detector's saturation level. In the case of an entangled source, the wavelength of these photons is 810 *nm*. Figure 16 shows the *SNR* for the two sensors versus range. The *SNR* is constant for ranges up to 1 *km* for the baseline and up to greater than 100 *km* for entangled photons. This is due to the dominance in this range of intensity noise, which has the same dependence (i.e.  $\propto I_1 I_2$ ) on detector photocurrents as  $S$ , leading to a range-independent *SNR*. A similar saturation of *SNR* has also been recently calculated for photocurrent correlation for both classical and non-classical sources in the limit of high brightness (i.e., short range in our case).<sup>36</sup> For longer range the correlation of shot noise with wave noise (beating term) dominates, leading to a reduction in *SNR* due to a different proportionality ( $\propto I_2 \sqrt{I_1}$  and  $\propto I_1 \sqrt{I_2}$ ) with the photocurrents.

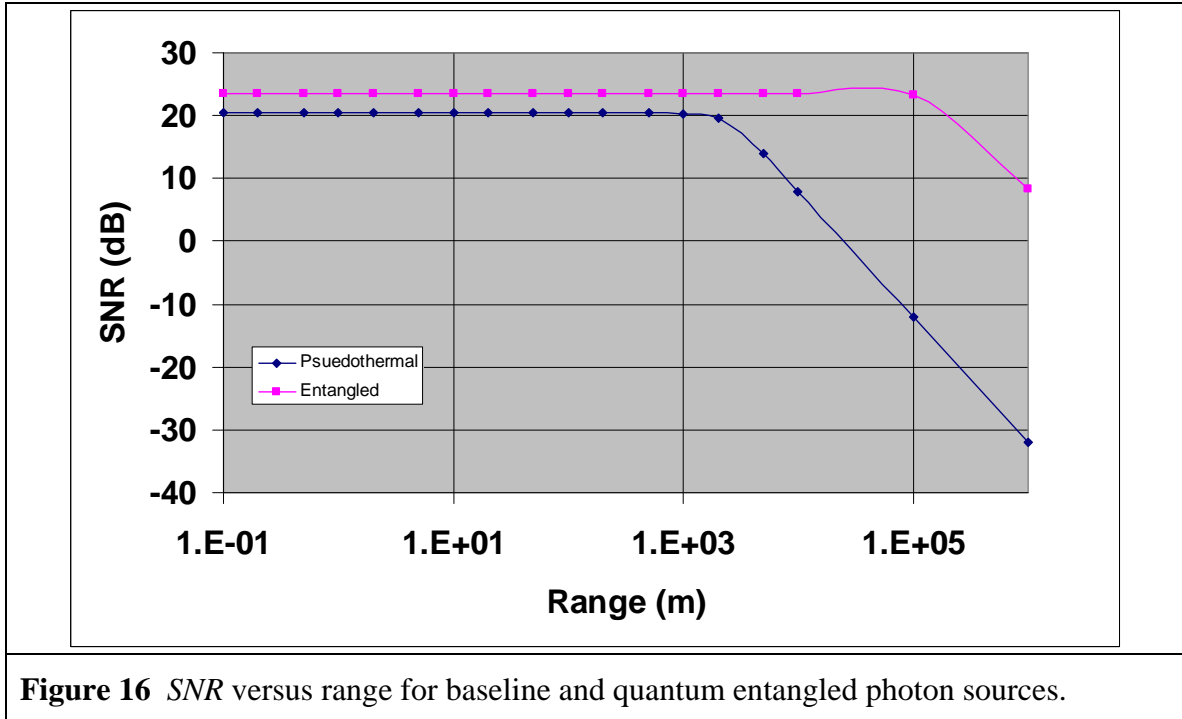


**Figure 16** *SNR* versus range for baseline and quantum entangled photon sources.

The difference between the  $SNR$  for the two sources for short range is due to a higher visibility (100%) assumed for the entangled photon versus pseudo-thermal (33%) source (ideal cases).<sup>37</sup> Of course, the actual visibility of an entangled photon source producing multiple watts optical power may actually be much smaller than the baseline case,<sup>38</sup> which may nullify any advantage afforded by the more collimated beam. In this situation the more sensitive single photon detection would enable weaker source intensities to be used. It is more likely that shot noise will dominate over shorter ranges. The extent to which shot or wave noise dominates is determined by a degeneracy parameter representing the number of degrees of freedom  $M$  (both temporal and spatial) of the intensity incident on the photodetectors within the measurement interval. The role of  $M$  in coincidence counting will be discussed below.

### 3.2.5.2 Coincidence Counting

Above we considered the case of very powerful beams emanating from the source, enabling detection of photocurrent from the photons returning from the diffuse target. Photocurrent detection is the standard mode of correlation measurement for pseudo-thermal ghost imaging. Here we assume lower light intensities, allowing the use single photon detection, which is the usual method employed in ghost imaging with entangled photons.

For coincidence counting over  $N_c$  intervals, the  $SNR$  is expressed as<sup>31</sup>

$$SNR = \frac{\sqrt{N_c} \sqrt{N_1 N_2} |\mu_{12}|^2}{M}, \quad (24)$$

where  $N_1$  and  $N_2$  are the counts in the two detectors, and  $\mu_{12}$  is the complex coherence function. The latter is equal to the visibility when  $N_1 = N_2$ , as is typical in bench top entangled photon ghost imaging experiments. We assume as above ideal cases for which  $\mu_{12} = 1$  and  $1/3$  for the entangled and pseudo-thermal sources, respectively. We note that  $M = M_s M_t$  associated with the number of spatial ( $M_s$ ) and temporal ( $M_t$ ) modes within the detection aperture and integration time  $T$ , respectively.

To estimate the number of temporal modes we take the spectral bandwidth of the SPDC output to be  $10 \text{ nm}$ ,<sup>39</sup> which corresponds to  $\tau_c = 800 \text{ fs}$  coherence time for the  $\lambda = 1.55 \text{ }\mu\text{m}$  wavelength photons. Given a detector integration time  $T$  greater than the coherence time  $\tau_c$ , we have  $M_t \approx T/\tau_c$ . The time resolution is dominated by the jitter in the InGaAs detector, which is on the order of  $T = 1 \text{ ns}$ . Consequently,  $M_t = 1250$  modes. For a pseudo-thermal source the coherence time can be many orders of magnitude longer. In Scarcelli's work,<sup>40</sup> for example,  $\tau_c = 1 \text{ }\mu\text{s}$ , much greater than the APD rise time so that  $M_t = 1$ .

The value of  $M_s$  depends on the size and shape of the receiving aperture and optical beam, as well as roughness of the target.<sup>41</sup> In the case of transmitting and receiving optics that share the same circular aperture, and a beam that is smaller than a diffuse target,  $M_s$  is exactly equal to 3.77. For a beam that is only partially intercepted by the target,  $M_s$  varies according to

$$M_s = \left[ \frac{16}{\pi} \int_0^1 \xi \left( \arccos \xi - \xi \sqrt{1 - \xi^2} \left( 2 \frac{J_1(\pi \beta \xi)}{\pi \beta \xi} \right)^2 \right) d\xi \right]^{-1}, \quad (25)$$

Where  $\beta = D_{lens} D_{spot} / \lambda R$ . In this equation it is assumed that the illumination spot  $D_{spot}$  on the target is a fixed size, independent of range, which can be accomplished through an adjustable telescope in the transmitter. In general,  $M_s \approx A_{det} / A_c$  when the active area of the photodetector  $A_{det}$  encompasses a large number of coherence cells each of area  $A_c$ . For an incoherent source that is uniformly bright across its surface we have<sup>13</sup>

$A_c = \frac{\lambda^2 R^2}{A_{spot}}$ , where  $A_{spot} = \pi \left( \frac{D_{spot}}{2} \right)^2$ .<sup>42</sup> For our ghost imaging configuration the number of coherence cells captured is determined by the receiver aperture, which then directs all of the received photons onto the bucket detector, so that for  $A_{lens} \gg A_c$ , which is the case for very short range ( $\beta \gg 1$ ), we have  $M_{s, \beta \gg 1} = \frac{A_{lens}}{A_c} = \left( \frac{\pi \beta}{4} \right)^2$ .

Figure 17 shows, assuming  $\lambda_i = 1.55 \mu m$ , 10 cm aperture, and target of 5 m linear dimension, how  $M_s$  varies with  $\beta$ ; for long range, where  $\beta$  becomes very small,  $M_s$  approaches 1. For very short range ( $\beta > 10$ ),  $M_s$  approaches  $A_{det} / A_c$ . In general, we can then write (denoted as  $M_3$  in Figure 17)

$M_s = 1 + \left( \frac{\pi \beta}{4} \right)^2$ . For our calculations, however, we assume that we have a fixed

telescope so that the beam size is given by diffraction spreading. Consequently, the range dependence of the coherence area cancels out, and  $M_s$  depends solely on whether the beam is smaller or larger than the target cross-section. Thus, for fixed beam divergence - no zoom optics to keep the spot size constant on the target -  $M_s$  is constant

until the range is great enough so that the beam grows larger than the target cross-section. This occurs at a distance for which

$$R_{threshold} = \frac{2}{\Delta \theta} \sqrt{\frac{A_{target}}{\pi}}$$

is the range at which the beam of full width divergence  $\Delta \theta$  of the outgoing beam begins to exceed the effective radius of the target. Beyond this distance we take the spot size to be equal to the effective diameter of the target,

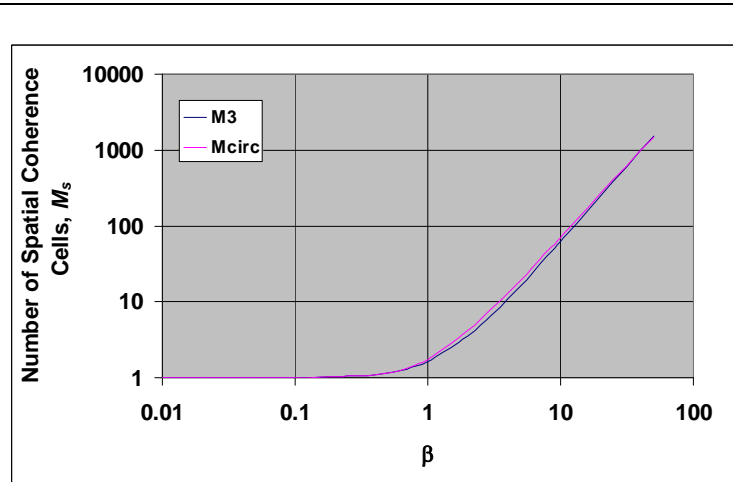


**Figure 17** Number of spatial coherence cells versus ratio of spot diameter to diffraction-limited resolution of receiver optics.  $M_{circ}$  is given by Eq. (25), whereas  $M_3$  is an approximation, as discussed in the text.



ignoring any clutter surrounding it.

The range dependence of  $M_s$  is shown in Figure 18 for both the

baseline and entangled beams. As expected, in the limit of very long range, the beam acquires a spatial coherence tending toward  $M_s = 1$ . When the beam is totally intercepted by the target,  $M_s$  depends on the

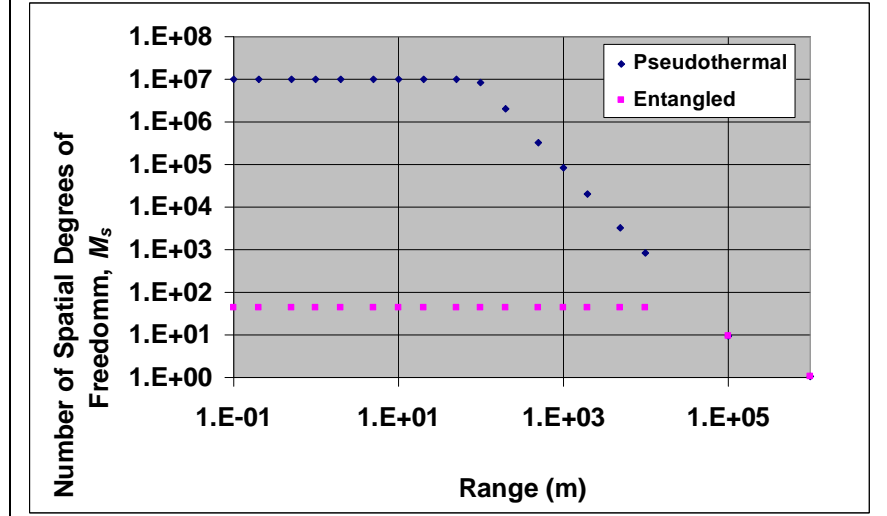


**Figure 18** Number of spatial degrees of freedom versus range for a circular source emanating from a rough target in the case that the beam size is larger than the target.

relative sizes of the transmitting and receiving apertures. For the baseline, these two are equal to each other, whereas for the entangled case, the transmitted beam is much smaller than the receiver lens. Note that because of the huge divergence of the pseudo-thermal beam,  $R_{threshold}$  is quite small ( $\approx 90$  m), whereas this figure of merit is over 40 km of propagation distance for the significantly tighter entangled beam size to exceed the effective target diameter. However, for greater range the spot size is the same for both cases giving equal values of coherence area and therefore  $M_s$ .

The theory of intensity interferometry was developed primarily for measurements of the angular diameters of stars, and in such cases the values of  $M$  in the two arms of the interferometer should be very similar, if not identical to each other. In ghost imaging, however, the number of spatial coherence cells can be vastly different for the two detectors in the coincidence setup.

A rough measure of the transverse coherence cell area associated with the bi-photon can be estimated from the phase space cell size based on the uncertainty principle. Following Gatti et al.,<sup>43</sup> given the transverse momentum  $\Delta p_y$  of the idler photon at the output plane of an SPDC crystal of length  $L$ , the uncertainty in position of the signal photon is

$$r_c = \sqrt{\frac{\lambda_i L}{2\pi n_i}}, \quad (26)$$

for a refractive index  $n_i$ , so that the coherence area  $A_c = (\lambda_i L)/2n_i$ . For  $L = 5$  cm,  $n_i = 2.14$  (PPLN crystal), we have  $A_c = 5.6 \times 10^{-9}$  m<sup>2</sup> at the SPDC output plane and then magnification by  $\approx 3$  ( $= F\theta/d_0$ ) at the collimating lens. We expect that no further magnification occurs through the ghost imaging lens (which would be true for long range targets and  $d_2 = F$  in Equation (5)). In ghost imaging experiments the detector in the reference arm is either a fixed array or a single element detector that is scanned in the transverse plane. We assume that the detector is a 512×512 array and that the optical

power directed to this arm is divided equally among the  $(512)^2$  pixels, each of  $10 \mu m$  size. Assuming a photosensitive area of the detector of  $10 \mu m$  linear dimension (i.e.,  $1 \times 10^{-10} m^2$  area), the detector intercepts only a portion of the coherent area so that for the bi-photon signal (reference) arm we have  $M_{s,ref} = 1$ . In the case of the pseudo-thermal source the speckle size at the collimating lens is  $D_{speckle} = (\lambda f)/d_0 = 31 \mu m$ , which is also larger than the pixel size, again giving  $M_{s,ref} = 1$ . We then make the assumption that  $M_s = \sqrt{M_{s,ref} M_{s,obj}}$ , where  $M_{s,obj}$  is the number of degrees of freedom for the object arm calculated in Figure 18.

So far in our consideration of  $SNR$  in coincidence counting we have ignored the effect of background counts due to uncorrelated photons from the source, solar photons, and dark counts. Following Hanbury-Brown,<sup>32</sup> we introduce a factor  $(1+a)$  to account for background (although we continue to neglect uncorrelated photons from the source since these depend on the details of entangled photon generation) such that

$$SNR = \frac{\sqrt{N_c} \sqrt{N_1 N_2} |\mu_{12}|^2}{M(1+a)} . \quad (27)$$

Here  $(1+a)$  is the ratio of the total number of counts from all sources to the counts originating solely from the source photons. For a pseudo-thermal source the value of  $a$  is negligible at short range ( $< 100 m$ ), but at greater distances it grows larger than 1 as the source photon rate in the bucket detector begins to compete with the solar and dark counts. For the entangled source the background is negligible over the entire range.

Although the relative significance of this type of background makes sense for these two sources, the particular dependence on range depends on what source output power is chosen. We arbitrarily chose a value of  $0.1 W$  in order to keep the entangled photon rate of return from the target much greater than that from dark counts at ranges up to  $10 km$ . Despite this power being three orders of magnitude smaller than that assumed for the photocurrent correlation case above, it is still many orders of magnitude greater than the bi-photon limit of SPDC output, for which we can expect the visibility ( $\approx \mu_{12}$ ) to be equal to one. Consequently, if one accounts for a drop in visibility due to accidental coincidences from uncorrelated photons, the  $SNR$  will probably much smaller than predicted in Figure 19. Another assumption made in the calculation was that the output of both sources was split equally between the two arms of the interferometer. This was within a range of splitting ratios that optimized the  $SNR$  for the entangled beam case, particularly at  $10 km$  range.

Overall we see again see that when we assume the ideal values of visibility (1, and  $1/3$ ) for the entangled beam and pseudo-thermal sources, the former gives rise to a superior  $SNR$  over all values of range to the target. This is primarily a result of the significantly smaller beam divergence of the entangled beam. When one properly accounts for uncorrelated photons from the sources, this  $SNR$  advantage may be minimized or even reversed. However, the degree of visibility reduction depends critically on the output power assumed, and may also depend on details of the source, which we do yet know for the hypothetical case of  $N \geq 3$  entangled beams.

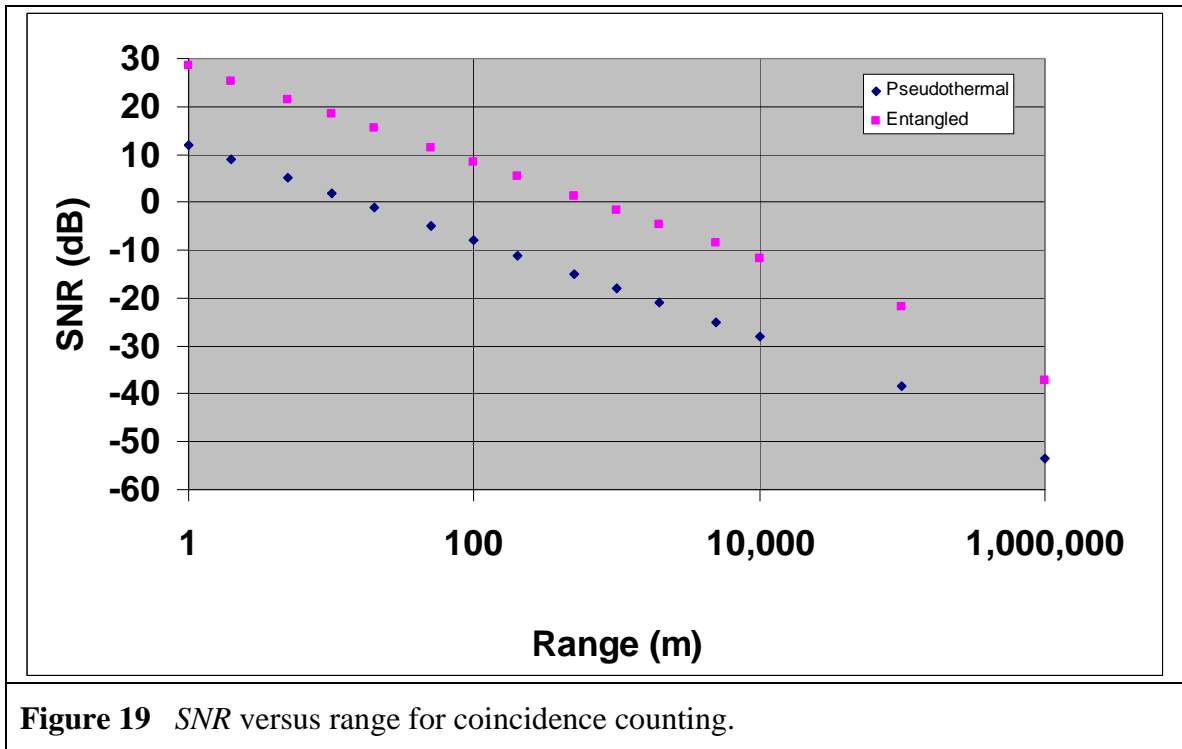


**Figure 19** *SNR* versus range for coincidence counting.

## 4 Quantum Imaging Experiments

Since the goal of QSP is to determine whether quantum effects can be used to some advantage in a remote sensor in a militarily relevant environment, NGC set up a ghost imaging apparatus with the intention of eventually testing interaction of the entangled photons with an outdoor target. The main idea was to study the degradation of imaging resolution due to atmospheric effects. The first task involved acquiring the necessary SPDC source crystals, single photon detectors, and correlation electronics, and then setting up correlation measurements on a lab bench. The sections below describe the progress that NGC made in this undertaking.

### 4.1 SHG System Setup and Diagnostics

#### 4.1.1 Nonlinear Optics

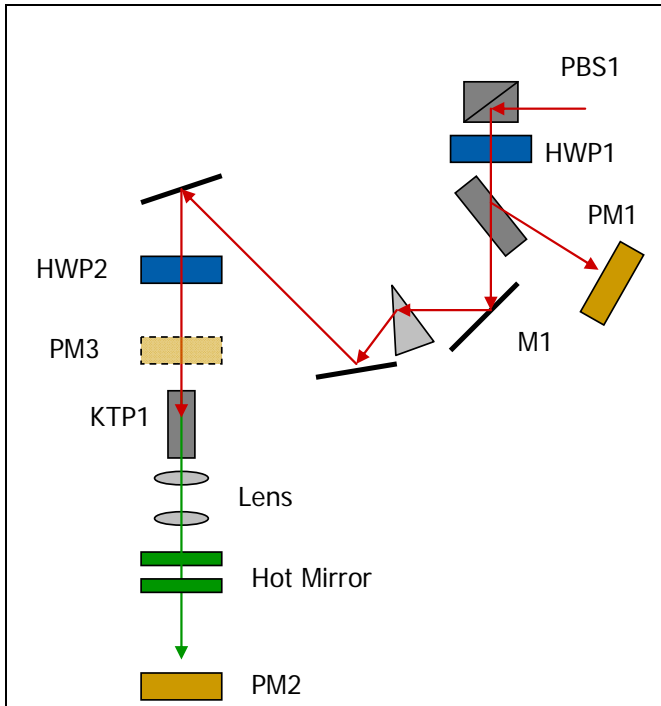


**Figure 20** Setup for generating the SPDC pump beam.

We used a frequency-doubled (Figure 20) 1064 nm Q-switched laser (Spectra Physics, H10-106QW) for pumping SPDC sources to generate entangled photons (bi-photons) at pulse repetition rates up to 100 kHz. Initial coincidence/imaging experiments at NGC employed degenerate spontaneous parametric down conversion (SPDC) producing entangled photons at 1064 nm. This required (see Figure 20) generating a pump beam at 532 nm for which we used the above Nd:YAG pump laser, and a nonlinear crystal (SuperOptronics, KTP type II - designated as KTP1, and AR-coated for input and output wavelengths) to double its frequency. The crystal was 3 mm×3 mm×20 mm, with second order nonlinear optical susceptibility given by  $d_{eff} = 3.55 \text{ pm/V}$  and cut for

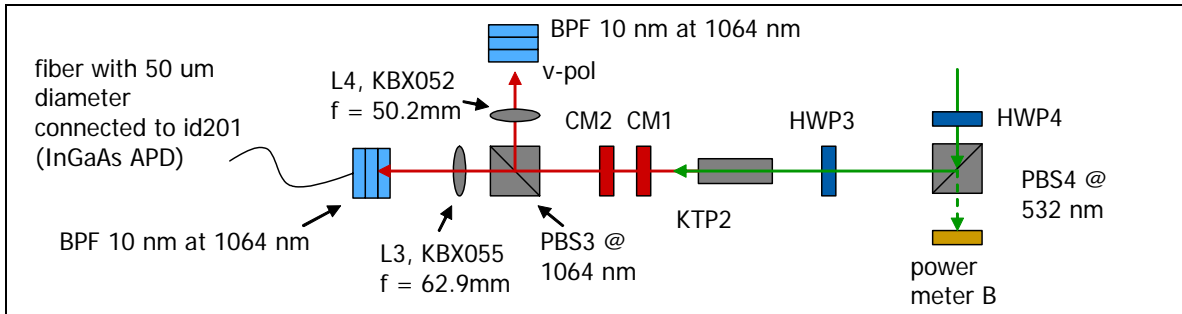


**Figure 21** Setup for (degenerate) SPDC generation.

noncritical phase matching. The crystal was housed in an oven (SuperOptronics, crystal oven controller) set at  $80^{\circ}\text{C}$  to avoid cumulative damage due to gray-tracking at high optical intensity.

Figure 21 shows the setup for generating entangled photons via another nonlinear crystal - KTP2, which is nominally identical to that of KTP1, and is also AR-coated. The output beam from KTP1 is vertically polarized with respect to the optical bench, which becomes the pump beam for KTP2. After the two hot mirrors (Figure 20), two colored glasses were added to further reduce any residual pump beam for KTP1 at  $1064\text{ nm}$ . HWP3 at  $532\text{ nm}$  controls the polarization direction of the pump beam for KTP2. The optical axis for KTP2 is horizontal to the optical bench - the same configuration as KTP1. KTP2 is also in an oven with temperature set at  $80^{\circ}\text{C}$ . Two cold mirrors (CM) were set up to block residual light at  $532\text{ nm}$ . A lens with a focal length of  $50\text{ mm}$  was used to

**Table 8 SPDC efficiency.**

Parameter	Symbol	Unit	RM	UMBC
Average Input Power	$P_{\text{avg}}$	mW	100	300
Pulse Repetition Frequency	$F_{\text{pulse}}$	kHz	50	8
Pulse Energy	$E_{\text{pulse}}$	mJ	2	37.5
Number of Photons	$N_{\text{photon}}$	Photons/pulse	$5.36 \times 10^{12}$	$1.00 \times 10^{14}$
Number of Photon Pairs	$M_{\text{photon}}$	Pairs/pulse	1045	5000
SPDC Efficiency	$\eta_{\text{SPDC}}$		$1.95 \times 10^{-10}$	$4.98 \times 10^{-11}$

focus entangled photons into a smaller area for better detection. Table 8 compares the efficiencies of the SPDC setups at NGC to that at UMBC. Both show how weak -  $\sim 10^{-10}$  - the conversion is for optical parametric generation at these pump pulse energies. This shows that the assumption in the *SNR* calculations regarding similar outputs for the quantum versus baseline systems may be completely unrealistic given the amount of electrical power that would be required, for instance to generate a  $100\text{ W}$  idler beam in an airborne platform. The efficiency is seen to be even weaker for the case of nondegenerate SPDC in Table 9.

**Table 9 Comparison of SPDC efficiency between degenerate and non-degenerate cases.**

Parameter	Symbol	Unit	Degenerate	Non-Degenerate
Average Input Power	$P_{\text{avg}}$	mW	100	200
Pulse Repetition Frequency	$F_{\text{pulse}}$	kHz	50	50
Pulse Energy	$E_{\text{pulse}}$	mJ	2	4
Number of Photons	$N_{\text{photon}}$	Photons/pulse	$5.36 \times 10^{12}$	$1.07 \times 10^{13}$
Number of Photon Pairs	$M_{\text{photon}}$	Pairs/pulse	1045	732
SPDC Efficiency	$\eta_{\text{SPDC}}$		$1.95 \times 10^{-10}$	$6.83 \times 10^{-11}$

#### 4.1.2 Coincidence Detectors and Electronics

NGC obtained from idQuantique four avalanche photodiodes (APDs) – two Si (id100-MMF50-ULN), and two InGaAs (id201-MMF-ULN) in order to enable degenerate ghost imaging experiments at  $1\ \mu\text{m}$ , nondegenerate at  $810\ \text{nm}$  and  $1550\ \text{nm}$ , as well as tri-photon experiments in which either two Si detectors and one InGaAs or one Si and two InGaAs detectors would be used. These were always operated in Geiger (as opposed to linear) mode in order to perform single photon detection. The Si APD operated continuously, whereas the InGaAs APD was gated with a trigger input. The dark count rate  $R_{\text{dark}}$  for the Si APD was extraordinarily low - less than  $20\ \text{Hz}$  – in agreement with the vendor’s specifications. The InGaAs APD had many operational parameters such as trigger rate, detector gate width, dead time, photon detection probability. The gate width could be varied from  $2.5\ \text{ns}$  to  $100\ \text{ns}$ . Generally, the trigger rate, as determined by the pulse repetition rate of the Nd:YAG laser, was  $50\ \text{kHz}$  to  $100\ \text{kHz}$ . The latter was

practically the highest rate that

could be employed as a result of detector dead time constraints. With the single photon detection probability (SPDP) set at 25 % we measured the dark count rates at  $10\ \text{kHz}$  and  $100\ \text{kHz}$ . When everything else was fixed except trigger rate, the dark count probability was lowest at  $10\ \text{kHz}$  among the available internal rates. The data showed a dark count rate of  $300\ \text{kHz}$  at a trigger rate of  $100\ \text{kHz}$ ; we assumed a conservative value of  $800\ \text{kHz}$  dark count rate in our SNR model above.

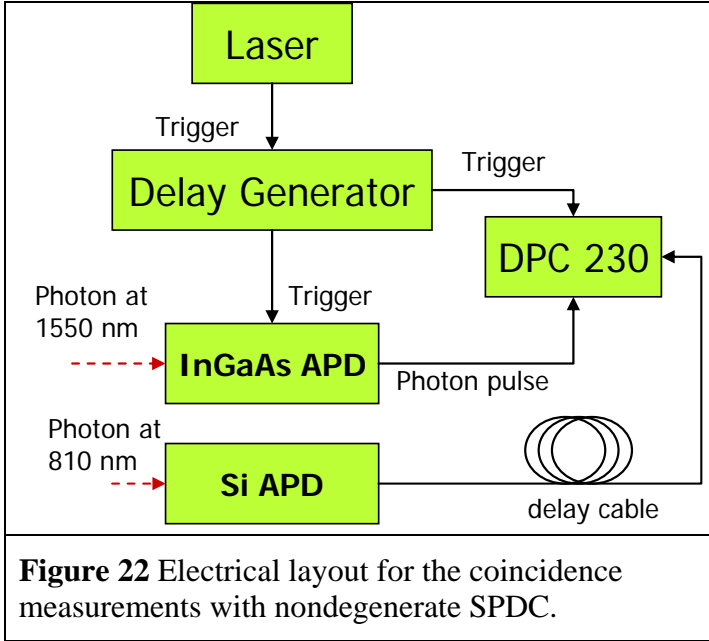


**Figure 22** Electrical layout for the coincidence measurements with nondegenerate SPDC.

shown in Figure 22 for the case of nondegenerate SPDC. The InGaAs APD required an electrical trigger since it operated in gated mode. The output of this detector was correlated with that from the Si APD using a time-correlated single photon counter (Becker & Hickl, DPC230). The master laser Q-switch provided a delay generator (SRS, DG535) with the trigger source. The delay generator compensated for the time ( $\sim 350\ \text{ns}$ ) between the optical pulse and the electrical trigger output. Since the InGaAs APD could detect an incoming photon only during the gate width, timing was critical. The Si APD was able to accept incoming photons at any time. However, a long cable was introduced between the Si APD and the DPC230 so that the photon pulse at  $810\ \text{nm}$  could be further delayed with respect to that of  $1550\ \text{nm}$ , and both positive and negative sides of temporal correlation could be captured. We therefore measured coincidences by treating the photon pulse of  $1550\ \text{nm}$  as “start” and that of  $810\ \text{nm}$  as “stop” inputs to the correlator board.

## 4.2 Experimental Issues

### 4.2.1 Background light

The first experimental issue we faced was that of a large amount of background generated by scattered light from the Nd:YAG laser. Since the SPDC pump beam (the KTP SHG beam) was generated externally to the laser this light had the opportunity to scatter everywhere around the optical table, and eventually find its way to the APDs. We minimized the scattered light effect by enclosing the receiver region with baffles. In addition to the scattered light were photons from the SHG pump that were collinear with the SPDC output, and therefore could leak through the hot mirrors, colored glass filters, and HR  $1.064 \mu\text{m}$  mirrors directly into the detectors. All of these uncorrelated photons contributed to a background that reduced the visibility in correlation measurements. We mitigated this contribution to background by adding crystal dichroic mirrors before the SPDC to highly reflect the  $532 \text{ nm}$  light while highly transmitting the desired  $1064 \text{ nm}$  light, as well as a Pellin Broca prism for further spatial discrimination against the laser leakage (see Figure 23).

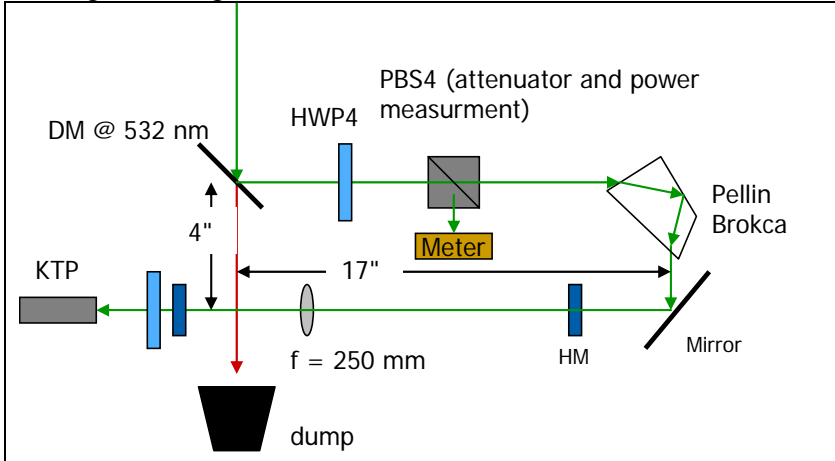


**Figure 23** Modified setup for pumping the SPDC to reduce laser leakage at  $1064 \text{ nm}$ .

An additional way to circumvent the background problem was to replace the KTP crystal with one that was phase matched to produce two entangled beams that are nondegenerate at  $810 \text{ nm}$  and  $1550 \text{ nm}$ . It also created an opportunity to explore the viability and benefit of a nondegenerate source for ghost imaging for

the first time. Our aim was to test the recent UMBC predictions for resolution of such a configuration.<sup>44</sup> For example, atmospherically transmissive photons can be used for the target, while the shorter wavelength ones would be retained locally by the more sensitive detector.

### 4.2.2 Spurious Effects of InGaAs APD

Another contribution to background counts came from the InGaAs APD that was used to detect photons at  $1550 \text{ nm}$ . This included the effect of high bias voltage in the detector, and an increase in the background count in proportion to input photon flux. As an example, Figure 24 shows the temporal profile of an entangled beam at  $1550 \text{ nm}$  captured by an InGaAs APD. The pulse (fit by a Gaussian) sits on top of an offset that is linear in pump power (see the right side of Figure 24); this was not observed in the Si APD, however. Those spurious counts were therefore deemed to be unique to the InGaAs device and not to input photons.

The InGaAs APD had several parameters that could be adjusted for optimization: time delay, dead time, photon detection probability and gate width. The device offers four options: 10 %, 15%, 20% and 25%. Figure 25 shows the temporal profile of dark counts at all of those values. As we show in the figure, the huge spike at the start of detector gate was due to the high value of detection probability. The data were collected for 100 s with respect to the master trigger from the laser while its beam was off, and with the detector sealed off from any external photons. Although the starting times of each temporal profile were the same, they are shifted from each in the plots by 10 ns consecutively for easy comparison. The spike at the start of the gate disappeared at 10 % and 15 %. The inset on the right side illustrates it more clearly. The graph on the right side shows the total dark count, which is exponential in detection probability, not linear. The operational parameter is related to detector bias voltage. Although the higher value increases sensitivity, a user has to take into account its side effect as shown in this temporal profile. Such spurious pulses created at random time will affect coincidence measurements in such a way that it washes away the correlation peak when it is used as a start. After discovering the relation between the spike and offset with the higher photon detection probabilities, we kept the latter at the low value of 15%.

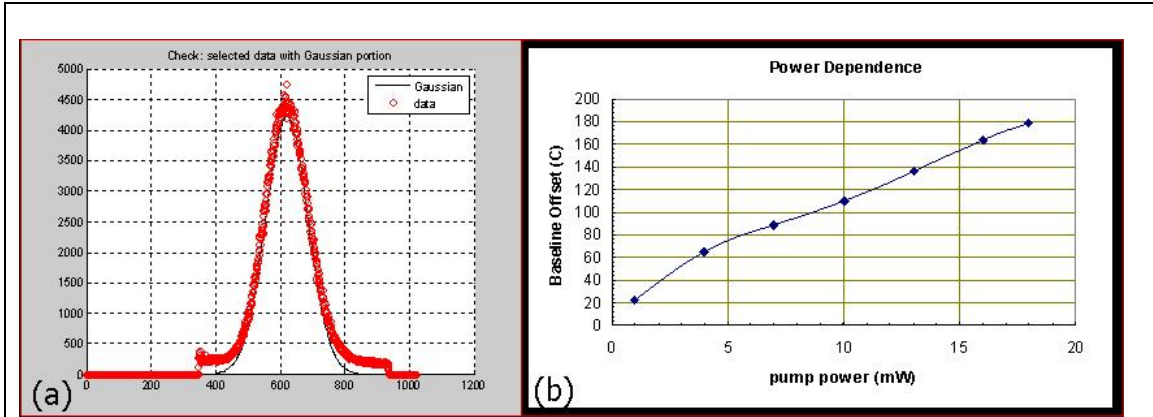


**Figure 24** Gaussian fit to temporal profile of InGaAs APD output (right), and pump power dependence of offset term (right).

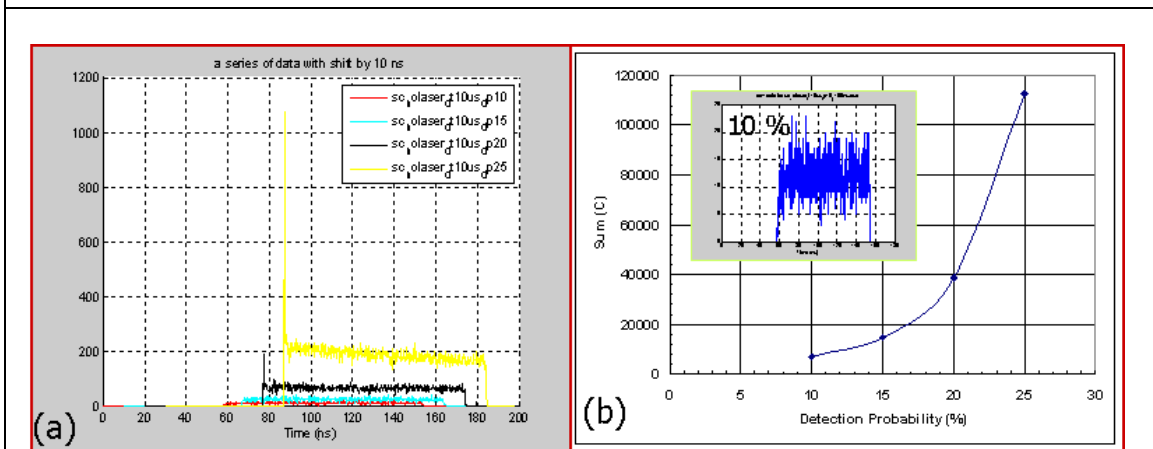


**Figure 25** Dark count profile at various detection probabilities.



#### 4.2.3 Spatial overlap of correlated photons

In obtaining the correlation peak, we learned the critical importance of the spatial overlap of the correlated photons. Each of the bi-photons in the entangled beam observes the relation (i.e. the phase matching condition)

$$\vec{k}_p = \vec{k}_i + \vec{k}_s, \quad (28)$$

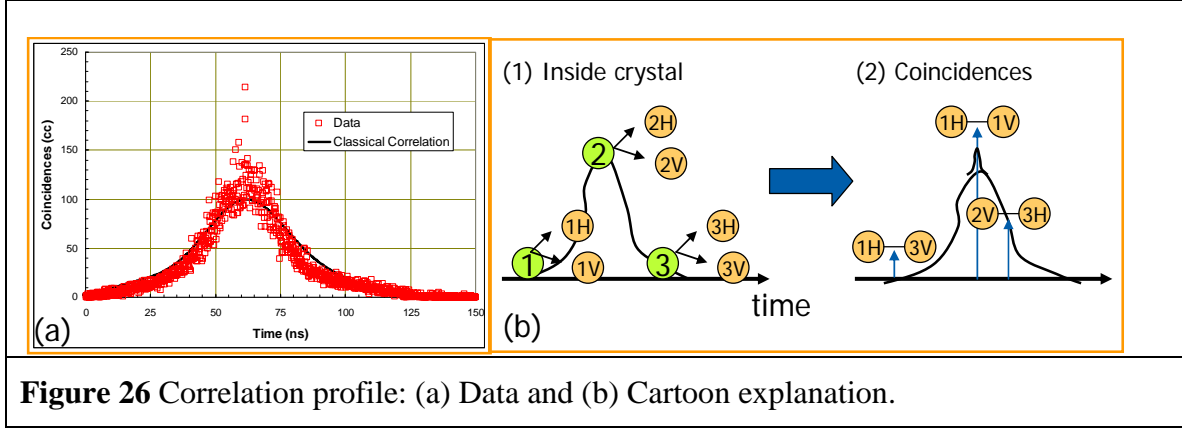
where  $\vec{k}_p$ ,  $\vec{k}_i$  and  $\vec{k}_s$  are the wave vector of the pump, idler, and signal, respectively. While  $\vec{k}_p$  is the same for every bi-photon,  $\vec{k}_s$  is not the same all the time. Rather, it spreads over a space like a cone and its cross section is a circle. In order to capture all of the photons regardless of the value of  $\vec{k}_s$ , a bucket detector in one arm is set up at the focus of a lens with a large aperture. The detector should be larger than the size of beam spot at the focus. When it is done properly, the other detector can be located anywhere in the given space to produce the correlation peak. Otherwise, the correlation peak depends on the location of the detector. For example, when we connected an optical patch cable with a fiber core diameter of  $62.5 \mu m$  to the end of the fiber collimator we could not observe the correlation peak. But when we replaced the patch cord with one that had a core diameter of  $400 \mu m$ , the peak was detected. This was direct evidence for the importance of maximizing the capture efficiency of the bucket detector in order to guarantee detection of photons with wave vectors correlated with those of the signal photons entering the other detector.

In our setup at NGES, we used optical patch cables with core diameter  $50 \mu m$ . This was because our detector diameter was  $50 \mu m$  and there seemed to be nothing to gain by increasing the core diameter of optical patch. On the other hand, the beam diameter was on the order of  $200 \mu m$  as determined with the InGaAs camera. It was at this point that we realized that our two detectors were not configured properly from the spatial perspective so that we might not efficiently (or indeed, *ever*) observe correlated pairs of photons. The observation of correlation peak required a very fine and reproducible 3D stage and optical patch cables with larger core diameters than what we normally used in our lab. The latter might not increase the single count rate, but it will surely increase the probability for spatially overlapping correlated photons. Therefore, we henceforth employed multimode optical patches with 200 and  $400 \mu m$  core diameters.

### 4.3 Observation of a Correlation Peak

After working closely with UMBC on their pulsed correlation setup with our InGaAs detectors we identified the technical obstacles to detecting correlation peaks, including those outlined above as well as others not reported here. And after taking measures to minimize detector artifacts and classically correlated counts, and incorporating fiber pigtailed large enough to capture the spatially correlated photons, we were able to detect true bi-photon coincidences, as shown in Figure 26(a). The square marks in this figure show the correlation profile with an average pump power of  $2 mW$ . It consists of two parts: a very narrow peak at the center and a large hump. The former is the correlation peak  $g^{(2)}(0)$ , the FWHM of which is less than  $1 ns$ . The large hump has  $50 ns$  FWHM and is unique to the correlation profile of a pulsed beam, since it is not shown in the correlation profile by a CW pump (as observed at UMBC). The solid curve in Figure

26(a) was generated by correlating the temporal profile of the 1550 nm beam to that at 810 nm. It was scaled and shifted to be compared to the data, which mimics the hump of the data. In light of this, the hump represents the classical correlation of the two temporal profiles.



The two entangled photon beams each contain a huge number of bi-photons per pulse. However, each APD detects only one photon per pulse since its dead time is much longer than the pulse duration. Thus, each detector has a finite probability of observing photons created at different times within the pulse duration. Figure 26(b) illustrates the underlying mechanism for the classical correlation. We suppose, for instance, that three bi-photons are created via SPDC while the pulsed pump passes through the crystal. Note that each of the three can be generated at different times within the pulse duration. As a result, coincidences show a combination of different pairs (right part of Figure 26(b)), giving rise to the classical correlation. Of course, the greater the number of pairs produced, the greater the probability of measuring coincidences among “wrong” pairs. This is therefore the fundamental tradeoff in terms of attempting to generate a large flux of entangled photons for a remote sensor: the greater this flux, the smaller the contribution of true coincidences to the second order correlation  $g^{(2)}(0)$ . In the December 2008 monthly we specifically compared the performance of pulsed versus CW sources with the same average power, and showed that, because of a much greater number of photons per mode, the pulsed system is expected to have a  $g^{(2)}(0)$  that is several orders of magnitude smaller. Consequently, we assume a CW source in our modeling in Section II above.

#### 4.4 Performance Comparison Between Correlation Peak and Ghost Imaging

During the final days of QSP, NGC attempted to obtain a ghost image of a transmissive target. The setup for obtaining ghosting imaging was similar to that for obtaining a correlation peak, except one notable difference: the detector on the reference arm was at the image plane of the imaging lens. For clarity, the lens on the reference arm was called a “collimating” lens in the configuration for finding correlation peak and an “imaging” lens in the configuration for ghost imaging. The location of imaging lens and detector was determined by Gaussian Thin Lens Equation (GTLE)

$$\frac{1}{f} = \frac{1}{a} + \frac{1}{b}, \quad (29)$$

where  $f$  is the focal length of imaging lens,  $a$  is the distance from the object plane to the imaging lens and  $b$  is the distance from the imaging lens to the imaging plane. Since the detector was not located at the smallest spot size of the entangled beam, the configuration for ghost imaging collected fewer photons during this acquisition than in that for the correlation peak. In fact, the reference detector is collecting only a small fraction of the light in the image plane in order to spatially resolve it, whereas in the correlation measurements virtually all of the photons in each arm are collected by the detectors.

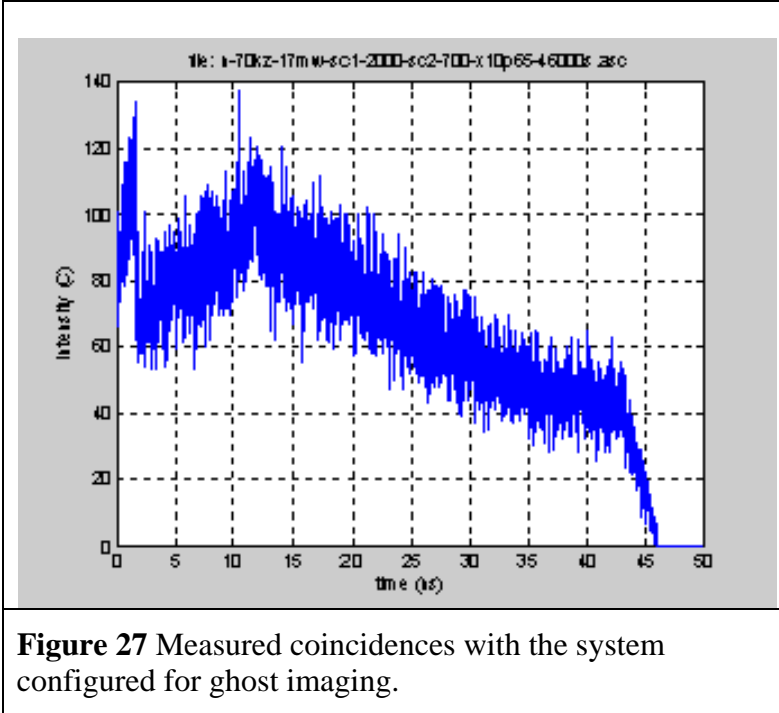


**Figure 27** Measured coincidences with the system configured for ghost imaging.

Figure 27 shows one of the results with the system configured for ghost imaging. For easy comparison, no targets were set on the target arm meaning 100 % transmittance. The imaging lens had focal length of 100 mm. The data were acquired at one “point” in the image plane for 46000 s, nearly 13 hours. The average pump power was 17 mW. One can compare this result with that shown in Figure 26(a). It is easy to conclude that the SNR is significantly reduced in the case of ghost imaging.

Upon further examination of the setup it was determined that the detector deviated a bit from the calculated image plane. Furthermore, because of the small focal length used, any small deviation could have a significant effect, leading to a large amount of blur in the image. We were therefore not able to accurately reproduce the object features in our first ghost imaging trial.

#### 4.5 Ghost Imaging with a Diffusive Target

Under the program, we sought to determine whether there is a degradation in entanglement (or the status of quantum source) due to the presence of a diffusive target. UMBC concluded theoretically that a diffusive target would not change the entanglement of the source. Recently UMBC published a joint paper with ARL on the ghost imaging with a pseudo-thermal source and a diffusive target that indirectly corroborates this assertion.<sup>45</sup>

Earlier UMBC reported ghost imaging with a degenerate source at 900 nm. The pump beam was CW at a wavelength of 450 nm, and the nonlinear crystal was BBO. The target was a mask with double slit. NGC visited UMBC and worked closely with one of the

researchers there in order to (1) reproduce the result together and (2) apply the system to a diffusive target. NGC confirmed the initial result with the mask target in transmittal mode. When the mask target was replaced by a diffusive target, we could not obtain a correlation peak, much less a ghost image. There were two possible explanations for this fact. First, the diffusive target did not preserve entanglement and ruined the correlation peak in the coincident measurement. Secondly, the pump power was too weak to overcome the loss due to diffusive scattering. At the time of the experiment, the pump source was an Ar ion laser that had a plasma tube that was not operating at its maximum output power. Its maximum power was only 100 mW. In light of the efficiency of generating entangled photons we estimated the required pump power to be at least 1 W to overcome the loss in the diffusive target. Given these limitations, we could not reach a meaningful conclusion on this study, but given the resources necessary to repair the laser, it is hoped that UMBC can eventually repeat this experiment when its pump source is restored to its full capacity.

#### 4.6 Ghost Imaging with Nondegenerate Source → Post QSP Activity Following Immediately from QSP Efforts

As detailed immediately above, at the end of the QSP program, NGC had not succeeded in forming a ghost image with its pulsed non-degenerate source of entangled photons. However, immediately after the end of the program, some IR&D funding was applied to

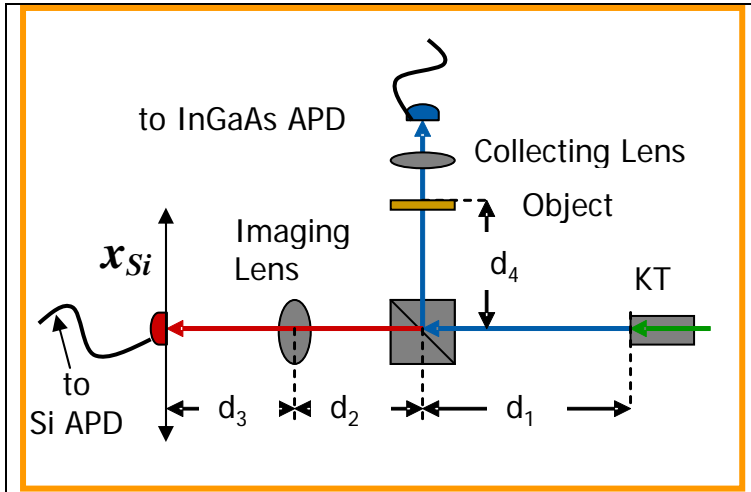


**Figure 28** Experimental setup with distance relationship.

continue with the work directed at obtaining a ghost image with the setup developed on the QSP program. As a result we have measured what is, to our knowledge, the first ghost image realized with a pulsed nondegenerate entangled source. This work is described in the following paragraphs.

We had previously modified the existing setup for making coincidence measurements in order to obtain a ghost image, as

**Table 10** Values for the distances in Figure 28.

Parameters	$d_1$	$d_2$	$d_4$	$f_{img}$
Values (mm)	304.8	50.8	44.4	62.9

UMBC has published a paper on ghost imaging with a nondegenerate source.<sup>46</sup> In accordance with the theoretical development in this work, we calculated the distance

$R_{img}$  from the imaging lens to an image plane along the reference arm and the corresponding magnification  $M_{img}$ . For comparison, we calculated the same for the degenerate case. Table 11 summarizes the results where  $\lambda_{obj}$  and  $\lambda_{ref}$  are the central wavelengths along the object arm and reference arm, respectively.

**Table 11 Calculation of  $R_{img}$  and  $M_{img}$ .**

Parameter	Unit	Nondegenerate Source	Degenerate Source
$\lambda_{obj}$	nm	1550	1064
$\lambda_{ref}$	nm	810	1064
$R_{img}$	mm	67.0	69.1
$M_{img}$		0.065	0.098

results as follows. We printed out an object on transparent film (3M, PP2500) as shown in Figure 29. It was prepared so that it could be mounted directly on a lens holder. The circle represents the inner diameter (1 inch) of the holder, which was used for alignment. The two white strips had a width of 1.4 mm and the width of the black strip at the center was 1.2 mm.

We moved the tip of the optical patch cord for the Si APD toward the imaging lens. We set it 5 mm off the calculated value for  $R_{img}$ , since the single count rate was decreasing and eventually became comparable to the background count rate as we approached the calculated 67 mm imaging distance from Table 11. The 5 mm offset does not represent a particularly optimum value, but we will see below that we were able to obtain a ghost image in this way. We obtained correlation peaks as we scanned the fiber across the plane (in the direction of  $x_{Si}$  in Figure 28) in steps of 0.5 mil. Each correlation profile took 1 hour with the average pump power fixed at 10 mW.

Figure 30 shows several correlation profiles taken at various location  $x_{Si}$  of the fiber tip for the Si APD. Each channel in the abscissa on the graph in Figure 30 corresponds to a time shift of 164 ps. The as-measured correlation profiles lay one on top of the other. However, in order to aid with visualization, each profile is shifted to in proportion to the change in  $x_{Si}$  for each profile (a conversion of about 260 ps per  $\mu m$  of  $x_{Si}$  proved to be convenient for display purposes). The legend in Figure 30 shows the actual value for  $x_{Si}$  with for the particular trace. Two of the measured correlation profiles show strong peaks that are related to the clear strips at the center of the object. Other profiles do not have the same peak. These are related to opaque part of the object.

In an earlier report, we defined three useful parameters from each correlation profile:  $C_{max}$ ,  $C_{min}$  and  $\Delta C$ . We plotted  $C_{max}$  and  $C_{min}$  as a function of  $x_{Si}$ . (shown as “Position” in the graph) and Figure 31 is the result. The error bar in  $C_{min}$  reflects the standard deviation  $\Delta C$ . The black line in this figure represents the pattern in the object (multiplied by the magnification for the nondegenerate case.) The maximum and minimum values in the line are chosen to follow the highest value for  $C_{max}$  and the average value for  $C_{min}$ , respectively. Although it appears blurred, it can be seen that we have observed a ghost

The magnification by the nondegenerate source configuration is about 65% of that obtained with the degenerate source, so the two cases may be easily distinguished. We validated the theory through our experimental

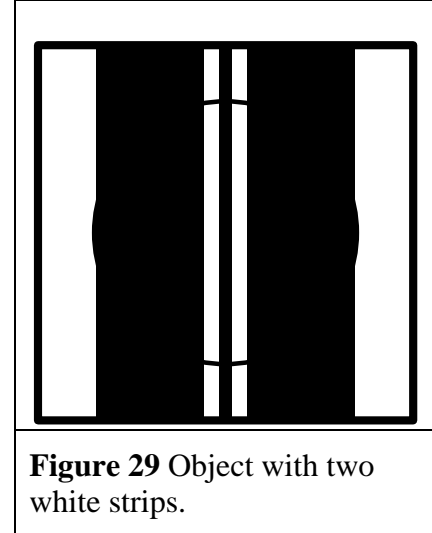
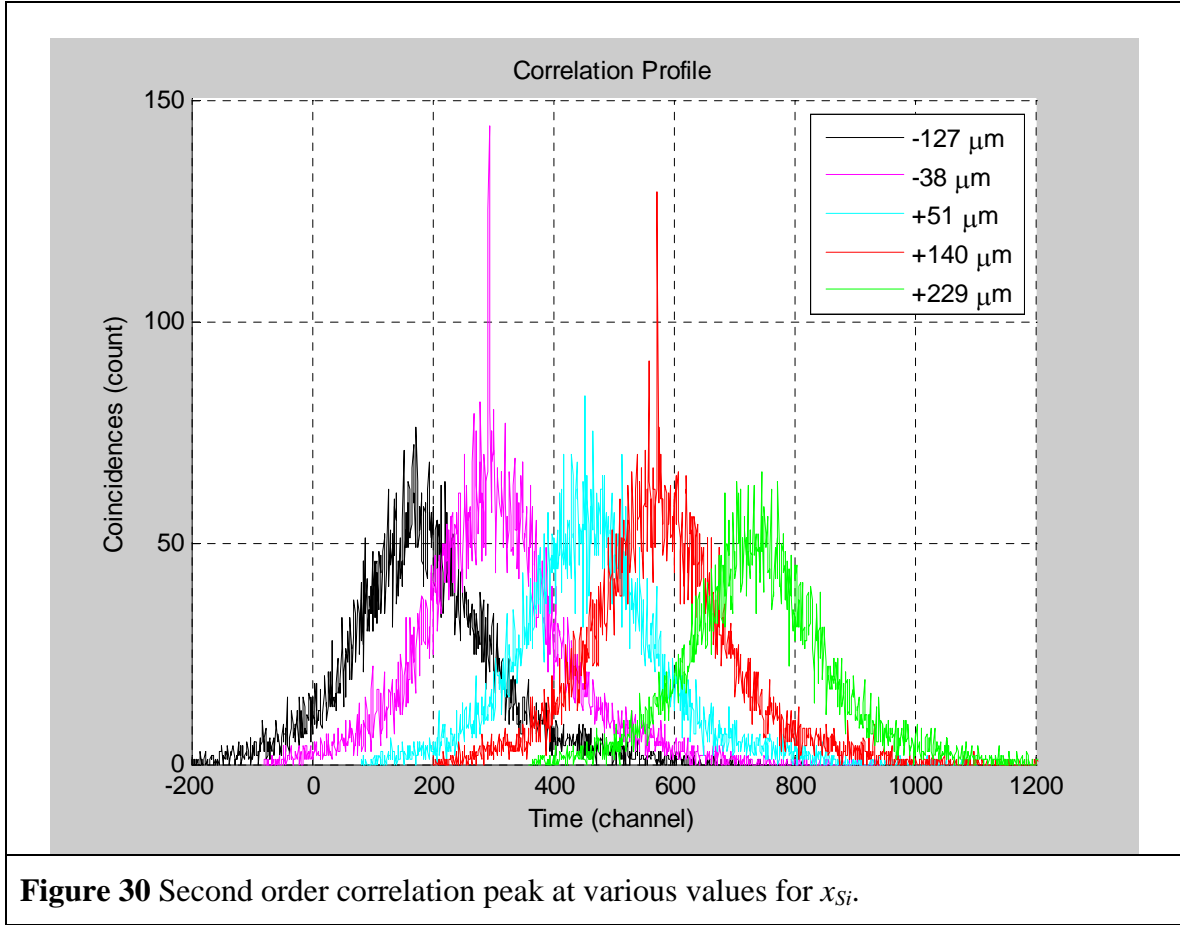


image of the two white strips in our object/target. The image is certainly not as sharp as the original pattern, but it can be improved by adjusting some of the parameters in the

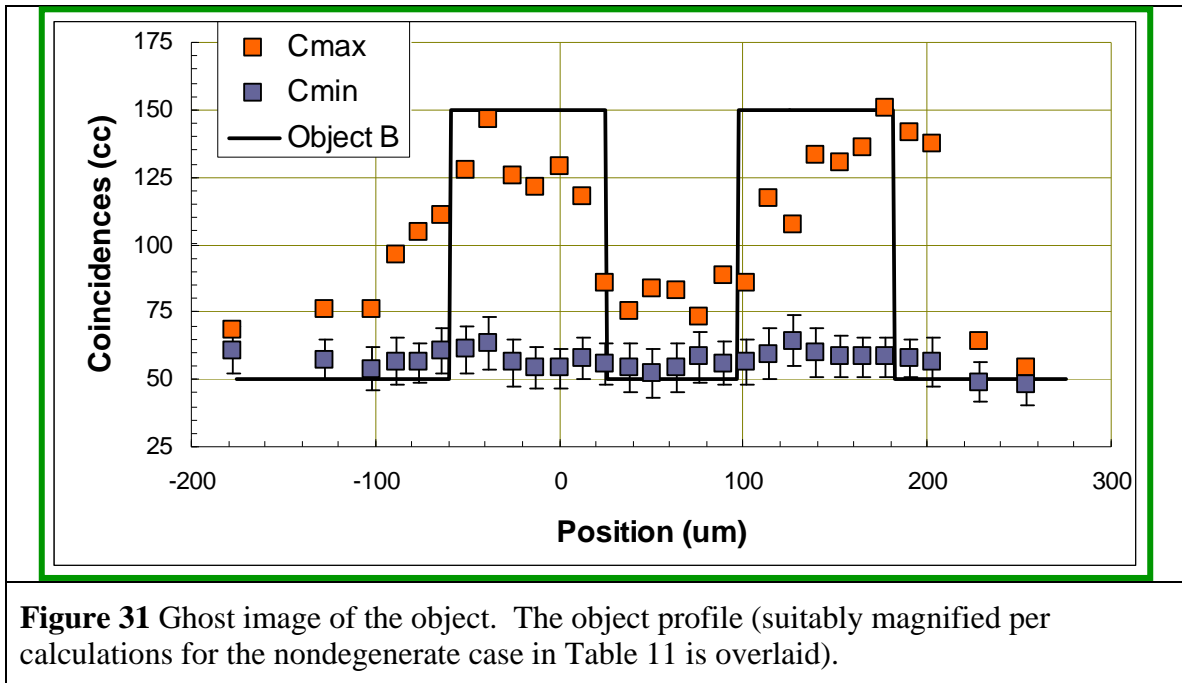


setup. The agreement between the measured ghost image and the magnified image of the object serves to confirm that the theory developed in [46] describes the experimental results obtained here. Note also that in Figure 31, we see a total of 30 correlation profiles each of which was approximately one hour in duration. Thus, the total time to collect this image was of order 30 hours. Finally, we note that, defining the visibility as

$$V = \frac{C_{\max} - C_{\min}}{C_{\max} + C_{\min}}, \quad (30)$$

we can deduce an approximate value for the visibility in our measured ghost image that is of order

$$V = \frac{130 - 60}{130 + 60} = \frac{70}{190} = 0.37. \quad (31)$$



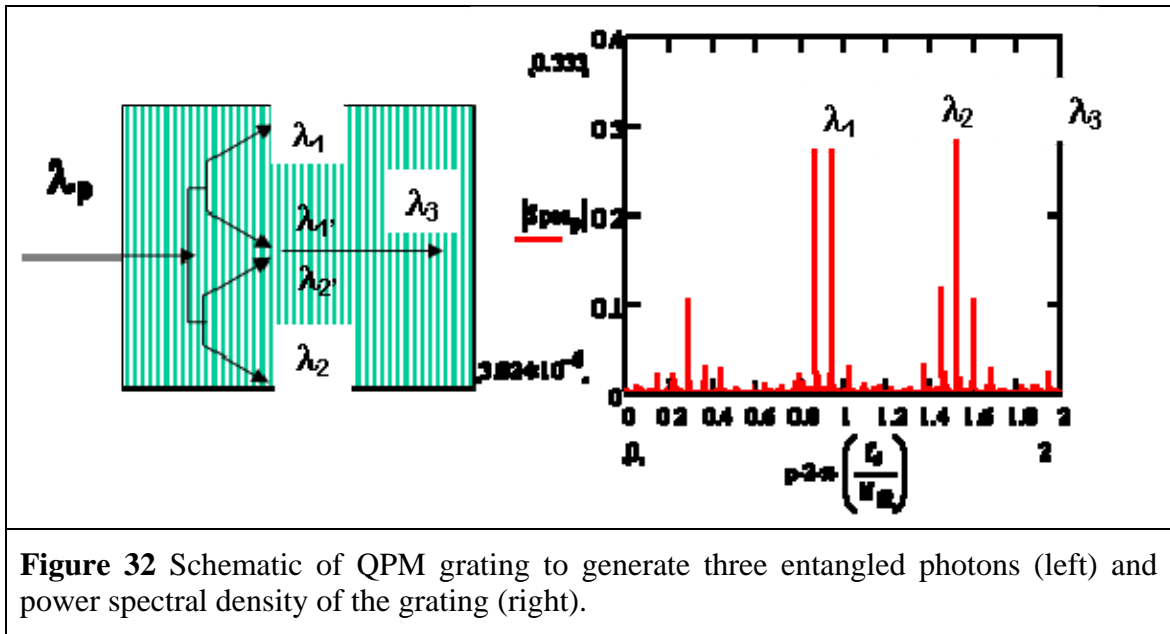
## 5 Triphoton Source Development

Although source development was not a major thrust of the program, the task was nonetheless defined in the SOW, and such development would appear to be necessary from the standpoint of eventually demonstrating resolution enhancement in quantum ghost imaging. Consequently, NGC spent a minimal amount of time modeling aperiodic gratings for producing tri-photon ( $N = 3$ ) beams using the numerical procedure outlined by Kartoglu et al.<sup>47</sup> Specifically, we considered two simultaneous optical parametric generators (OPGs) followed by a sum frequency generator (SFG) to generate one idler around 1550 nm and two photons in the visible and near IR (810 nm) that will stay local and be detected with Si APDs we have purchased. Recently, UMBC has reported generation and coincidence detection of a ( $N=3$ ) triphoton in which the state was created using a hexagonally poled photonic crystal. This takes advantage of two down conversion processes, and one up conversion process that are simultaneously quasi-phase matched (QPM). Such a crystal is not commercially available. However, we can design aperiodic gratings for the 1-D case, and have the nonlinear optical crystal poled in a ferroelectric medium, or epitaxially grown in a non-oxide semiconductor.

Because the photons that illuminate the target will propagate outdoors one must choose a wavelength for which there is low loss due to atmospheric attenuation and turbulence, and that is eye safe as well. Photons in the infrared can satisfy these requirements. The photon retained locally in the laboratory (or in a sensor on an airborne platform) can be chosen to have wavelengths compatible with a Si avalanche photodiode to take advantage of their low noise. Figure 32 (left), for example, shows a schematic diagram of a crystal pumped by visible photons. By setting appropriate phase matching conditions, the first two (SPDC) interactions can be made to have equal amplitude. Two of the products then mix to form a third photon, in the visible ( $\lambda_3$ ), which is entangled with two others - one visible ( $\lambda_2$ ) and one infrared ( $\lambda_1$ , for atmospheric propagation) - formed from the first two SPDCs. In Figure 32 (right) we plot the power spectral density of the QPM spatial grating, showing that the overwhelming energy is channeled into the interactions yielding these three photons. The other features in the spectrum can be minimized through an iterative process in the algorithm for the grating design widths. The relative amplitudes of the photon fluxes can also be adjusted, for example, to maximize the output power in the beam that propagates to the target.

Subsequent to UMBC's theoretical finding that at least two photons must interact with the target, the design for the  $N = 3$  state was changed to allow for the these two photons to have wavelengths compatible with the atmosphere, and to locally hold a near-infrared photon that could be detected by a Si APD with high efficiency. In order to accomplish this we again had two simultaneous OPG interactions, but then mixed  $s_2$  and  $i_1$  in difference frequency interaction to form  $\lambda_{dfg} = 1.55 \mu m$ . We also lengthened the crystal in the design to 5.5 cm to create an extremely high flux beam. A custom mask design was submitted to Deltronic, but we were subsequently told it could not currently be fabricated due to constraints in their poling technology. We therefore ordered only a uniform grating of 5.5 cm length to achieve extremely high flux for outdoor experiments; a different vendor or approach would have to be pursued for the aperiodic idea.



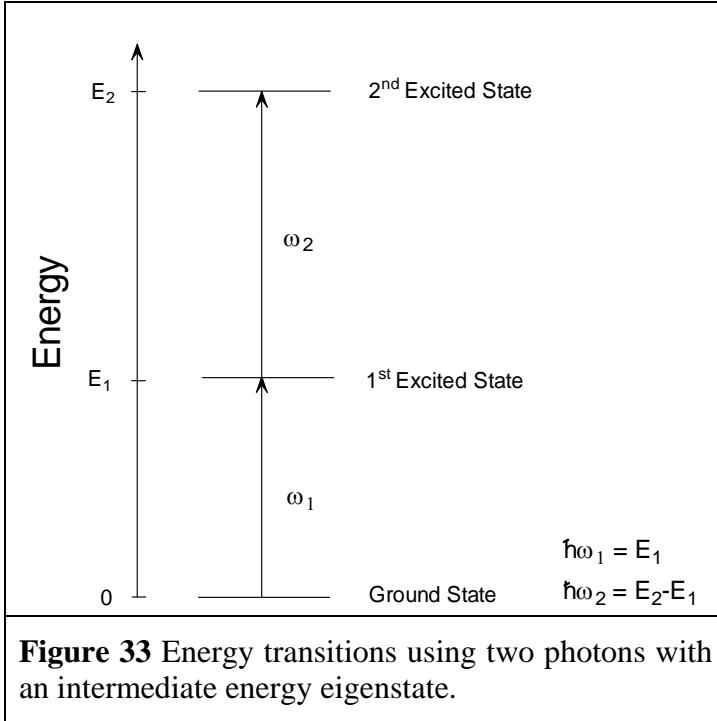


## 6 Quantum Well Multiple Photon Absorbers

### 6.1 Introduction

The use of entangled state systems for high-resolution imaging depends on the simultaneous detection of the entangled photon pairs used in the imaging. Present experiments employ two separate photodetectors and contain electronics that count simultaneous detections events in the two photodetectors. Besides inherent inefficiencies of this technique, this method is viable only with single-element detectors; and imaging detector arrays cannot be used. To create a high-resolution imaging system with entangled-state photons, true two-photon detection in a single detector element is required.

In multi-photon detection, the key characteristics of the absorption are the wavelengths of the photons detected, the delay time allowed between the absorption of the individual photons of the photon pair, and the absorption cross-section for the two-photon absorption. The goal of this work was to examine each of these characteristics in the context of an absorption region created by a coupled quantum-well semiconductor layer structure. By varying the semiconductor material and layer parameters in a coupled quantum-well system, the positions of the discrete energies in the quantum wells can be controlled. The energy alignment of these levels determines the wavelengths of the photon absorptions. In addition, the barriers between the wells can be used to control the transition rates among the energy states. This controls the simultaneity required between the times of the absorption of the two photons. Finally, the number of quantum-well layers coupled to the virtual state will determine the relative two-photon absorption coefficient of the system.

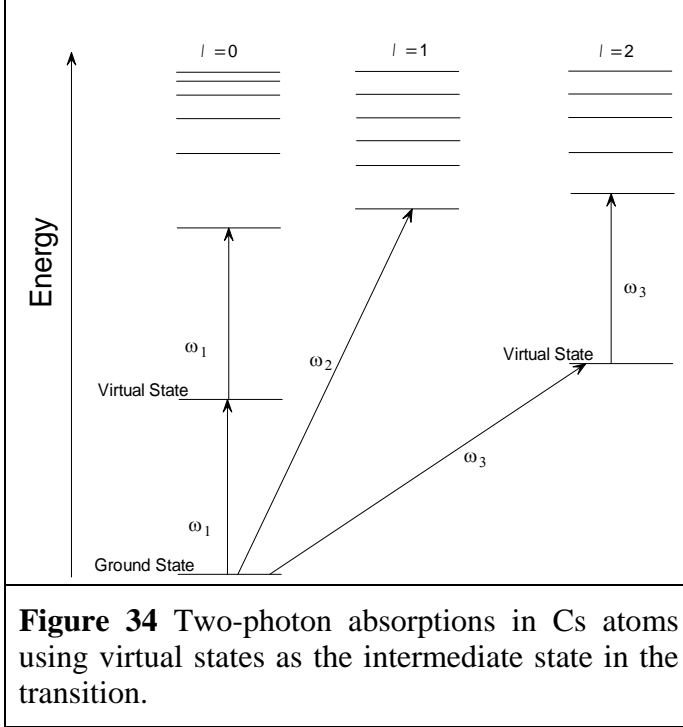


A two-photon device must make use of a virtual energy state in the absorbing material to ensure that the photons are absorbed simultaneously, or nearly simultaneously. In a material with a standard absorption of multiple photons as illustrated in Figure 33, the system first absorbs a photon that matches the energy for a transition from one energy eigenstate of the system to a second energy eigenstate. Subsequently, a second photon of the correct energy is absorbed by the material and the system makes the transition from the second to a third energy eigenstate. In this energy structure, the system will remain

in the intermediate excited state for some period of time. Thus, uncorrelated photons that are not part of an entangled pair can be accidentally detected if their arrival is within

some finite time window. In a detection system that is used for imaging, these false counts will be a background noise that may overwhelm the true signal.

Since any energy eigenstate that is used in the absorption process will have a relatively large relaxation time, it is difficult for a two-photon detector to use such an arrangement; and for this reason, a two-photon process is preferable. For a two-photon process, the system cannot use an intermediate energy eigenstate, but it must use a virtual energy state. Such a system occurs in Cs-vapor atoms where two-photon absorptions



have been examined<sup>48</sup>. As is shown in Figure 34, a transition from the ground electronic state of the atom to one of the first excited states can occur by one of two means. For a transition from the ground state with  $l = 0$  to the first excited state with  $l = 1$ , a single photon of the proper energy  $\Delta E = \hbar\omega_1$  can supply the required energy. In the same system, the transition from the ground state with  $l = 0$  to the first electronic excited state with  $l = 0$  or  $l = 2$  is first-order forbidden. However, for an intense beam of photons with energy that is half the energy separation between the ground state and the  $l = 0$  first excited state two photons can be absorbed simultaneously. This pair of

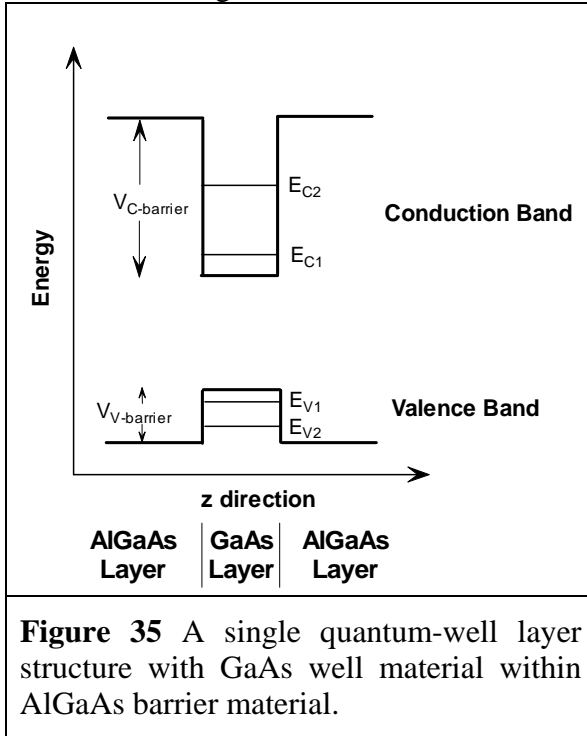
photons supplies the required energy for the electron transition to the excited energy eigenstate. The pair of photons interacts with the material to form a virtual energy state allowing the absorption of these photons to occur. Since the two photons must arrive simultaneously, the virtual state has a zero lifetime. Thus, the probability that two identical energy photons will arrive at the atom simultaneously is vanishingly small. Therefore, background photons cannot activate the two-photon absorption process and will not produce noise in the detection system.

The two-photon absorption process is inefficient even if the energy and time constraints on the photon pair are fulfilled. This process can be increased, if the total system has a nearby energy state that enhances the virtual state absorption process. The most well known application of this method is in resonance Raman scattering<sup>49</sup>, where the nearby energy state is an energy eigenstate of the atom. We have examined enhancement of the two-photon process using asymmetric semiconductor quantum wells that create the necessary energy states to resonantly enhance the two-photon process.

## 6.2 Asymmetric Coupled Quantum Well Absorption Structure

A semiconductor quantum well consists of a single layer of material  $A$  embedded between two thick layers of material  $B$ , where  $B$  has an energy band gap larger than  $A$  and where the valence and conduction band discontinuities are such that carriers are

confined in the A material. This is the situation for a variety of pairs of semiconductor materials GaAs/AlGaAs, GaInAs/AlInAs, GaSb/AlSb, GaInAsP/InP, etc. In this work, we focused on the well-analyzed GaAs/AlGaAs semiconductor layer system that can be easily obtained. The energy level scheme in the conduction and valence bands of the semiconductor-layered structure is well described by simple carrier confinement in a quantum-well potential, shown in Figure 35. Two discrete bound states in the conduction band of the quantum well, with a continuum of states available above the barrier energy, and two discrete bound states in the valence band of the quantum well, with a continuum of states below the barrier energy are shown in the figure. Electronic transitions can occur between the bound quantum-well states through the absorption or emission of photons. These transitions are the same as the single-photon transitions that were illustrated in Figure 33.



To determine the absorption spectra of these structures properly, the energy gaps between the valence and conduction bands of the well and barrier materials are required. In our analysis, the energy levels of the conduction band electrons are calculated in the envelope wave function approximation using a Kane model;<sup>50</sup> and the hole bands are described using the Luttenger Hamiltonian<sup>51</sup>. The offsets for the valence and conduction bands are taken from Watanabe, et al.<sup>52</sup> It is assumed that the initial detector structures will operate at cryogenic temperatures to reduce phonon-scattering effects; thus, temperature-dependent effects on the band energies were included. Semi-empirical models by Varshni<sup>53</sup> and Pässler<sup>54</sup> for the thermal effects on band gaps were used to determine the energy gaps used in the quantum-well layers. These calculations

allow the determination of the material structures needed to produce the quantum well and barrier characteristics for the two-photon absorption region.

To analyze the coupled quantum-well structures to determine the transition rate characteristics, we used a transfer matrix model and employed Mathematica code to calculate the bound-state wavefunctions and energies. Initially, simple layer systems were examined and the results were compared to analytic results. As an example, the bound-state conduction-band energies and eigenfunctions of a single quantum well with one, two, and three bound states, are shown in Figure 36.

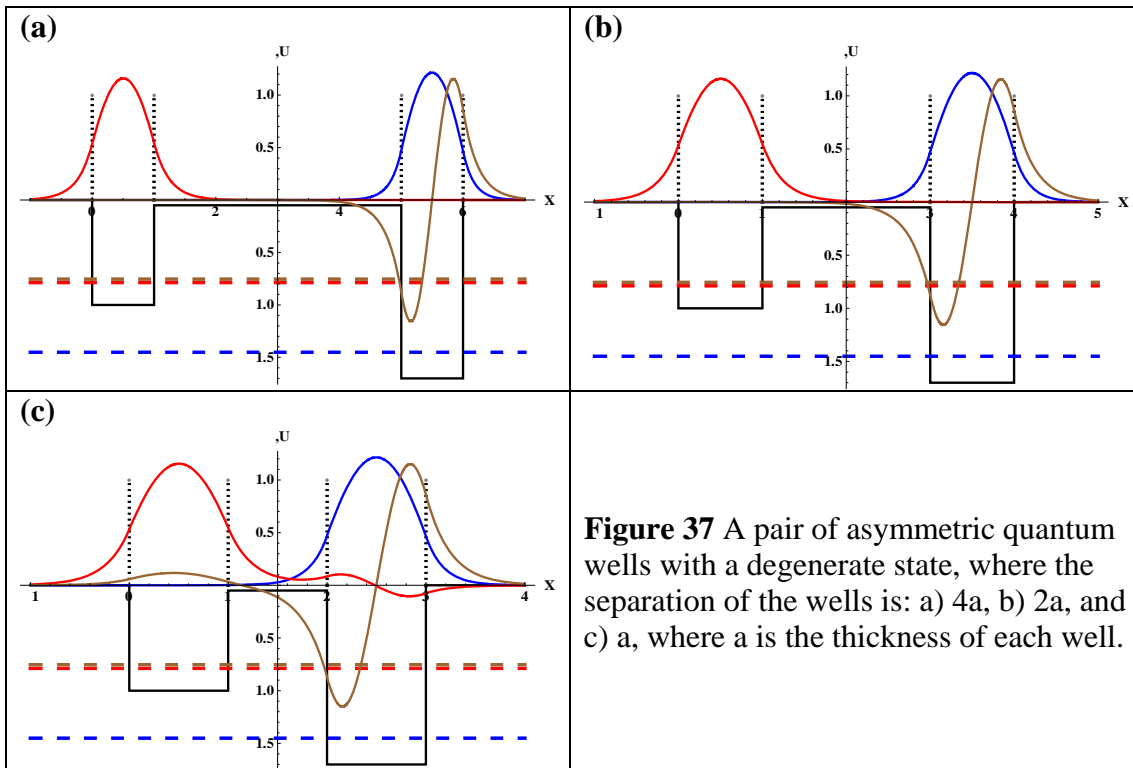
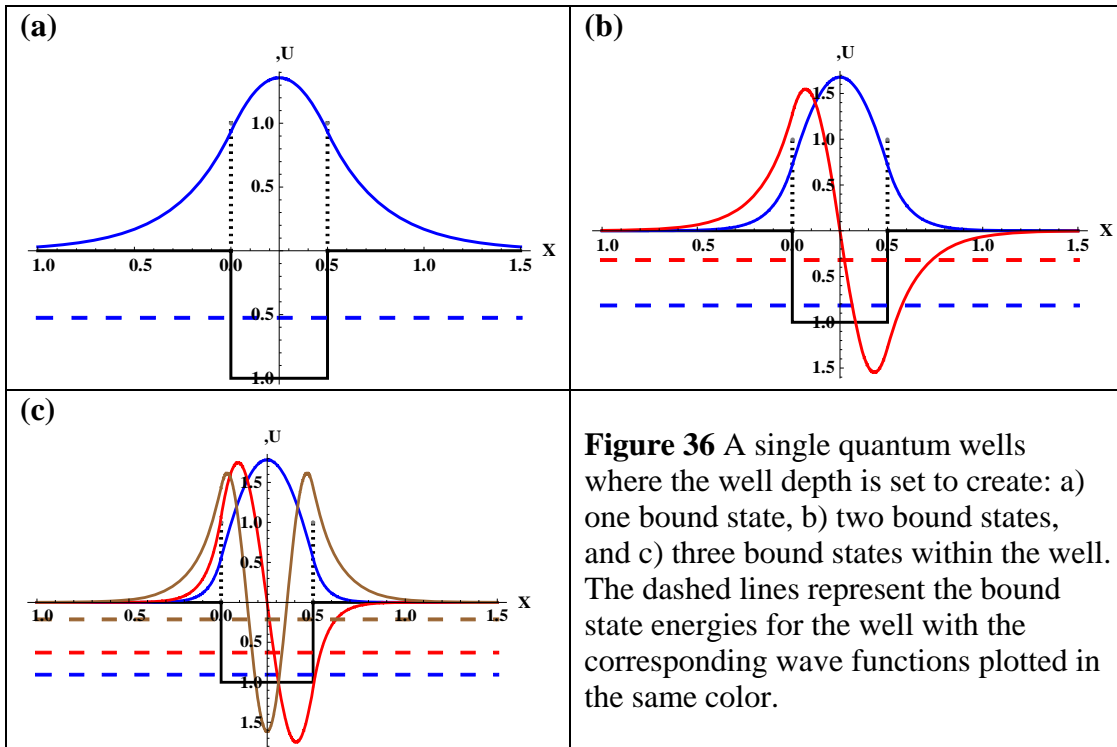
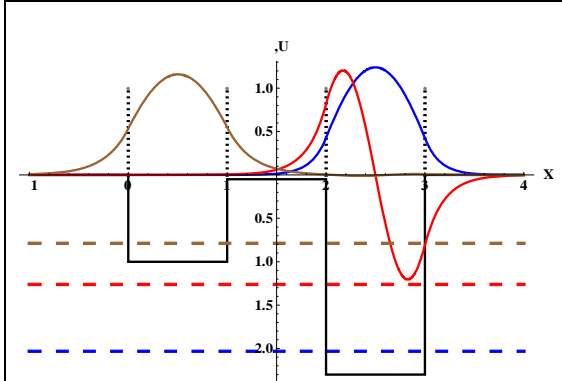


Figure 37 illustrates two asymmetric quantum wells that are separated by successively smaller barriers. In this pair of quantum wells, the well widths and depths are chosen so that the second bound state of the deep quantum well has the same energy

as the lone bound state in the shallow well. As expected, there is very little interaction between the wells with a large barrier separating them and a large interaction between the wells with small barriers.



**Figure 38** A pair of asymmetric quantum wells where the separation of the wells is  $a$ , and the well depths are chosen so none of the states are degenerate.

spontaneous lifetimes for energy eigenstates in various quantum-well structures. These calculations are based on standard first-order electric-dipole transitions between the

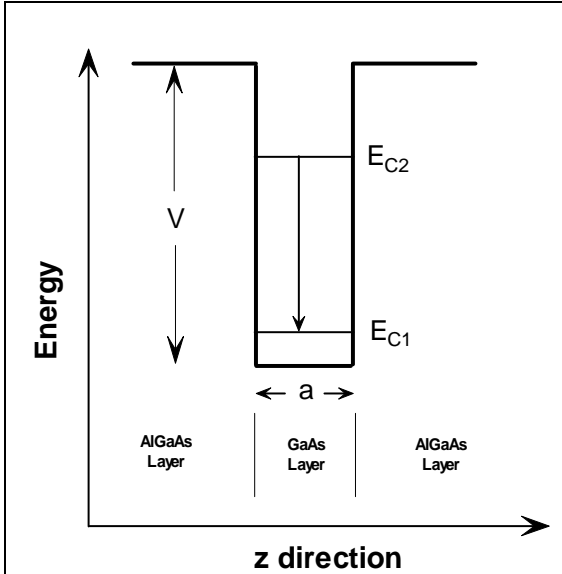


**Figure 39** Transitions for the finite quantum-well system calculated using electric-dipole interactions.

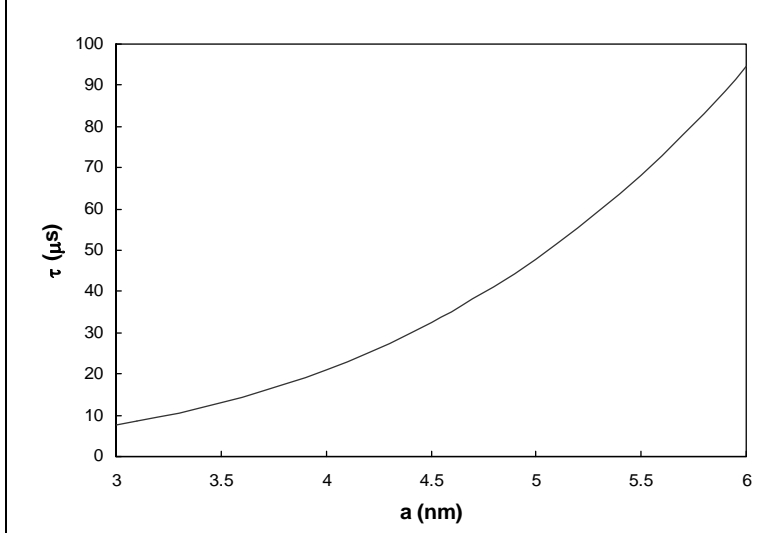
well state than the well *width* has on this lifetime. The lifetime of a 4-nm wide, infinite quantum well was found to be 14  $\mu\text{s}$ , a small shift from the lifetimes for wells a few eV deep. Finally, we calculated the lifetime

Figure 38 shows a pair of wells where the levels are not degenerate. Although the separation of the wells is equivalent to that in Figure 37(c), the wave function from the first quantum well state that is present in the second quantum well is much smaller than that shown in Figure 37(a).

These energy-level and energy-eigen function calculations are used to guide the structure design. The energy-level differences yield the absorption wavelengths and the energy-eigen functions determine transitions rates and transition times between the bound states in the quantum-well system. Using our transfer matrix calculations, we can examine the spontaneous lifetimes for energy eigenstates in various quantum-well structures. In the first set of calculations, simple single quantum wells were examined, as shown in the following figures.

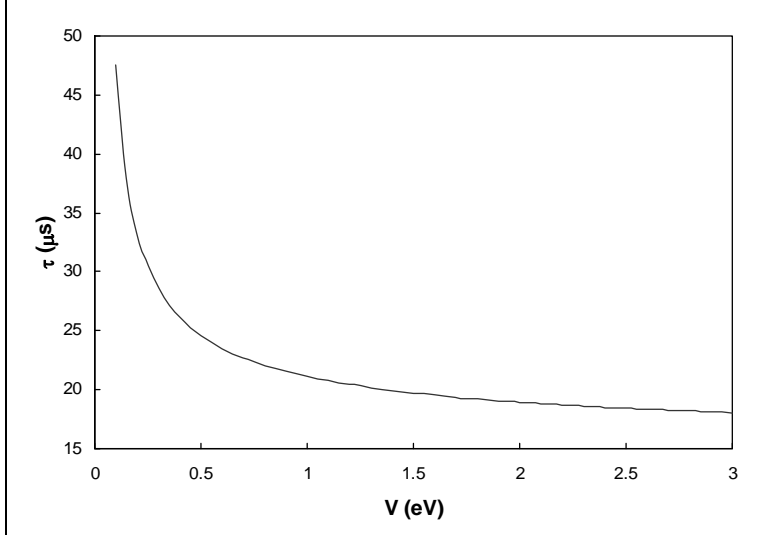
Figure 40 illustrates the effect of increasing the width of the quantum well from  $a = 3$  to  $a = 6$  nanometers (tens of atomic layers) for a  $V = 1$  eV energy well. These parameters are within the range of values for standard semiconductor quantum-well structures grown for a variety of applications. As expected, the lifetimes found are on the order of tens of microseconds for these well parameters.

Figure 41 shows the effect of varying the well depth for a fixed well size of 4 nm. Again, as expected the spontaneous lifetime for the quantum-well states increases with well depth. These simulations show that the well *depth* has a much smaller effect on the spontaneous lifetime of the excited quantum



**Figure 40** Electron spontaneous lifetime for the first excited state in a 1-eV deep quantum well.

transition probabilities and lifetimes for single and two-photon absorption in our asymmetric coupled quantum-well systems. In this system, a pair of quantum wells with different well widths is coupled through a thin barrier. This system is illustrated in Figure 42. Two states are present in the first well; these states are labeled  $E_{C1}$  and  $E_{C3}$ . The second well is the same well width as the first well; however, it is not as deep as the first well.



**Figure 41** Spontaneous lifetime for the first excited state in a 4-nm wide quantum well.

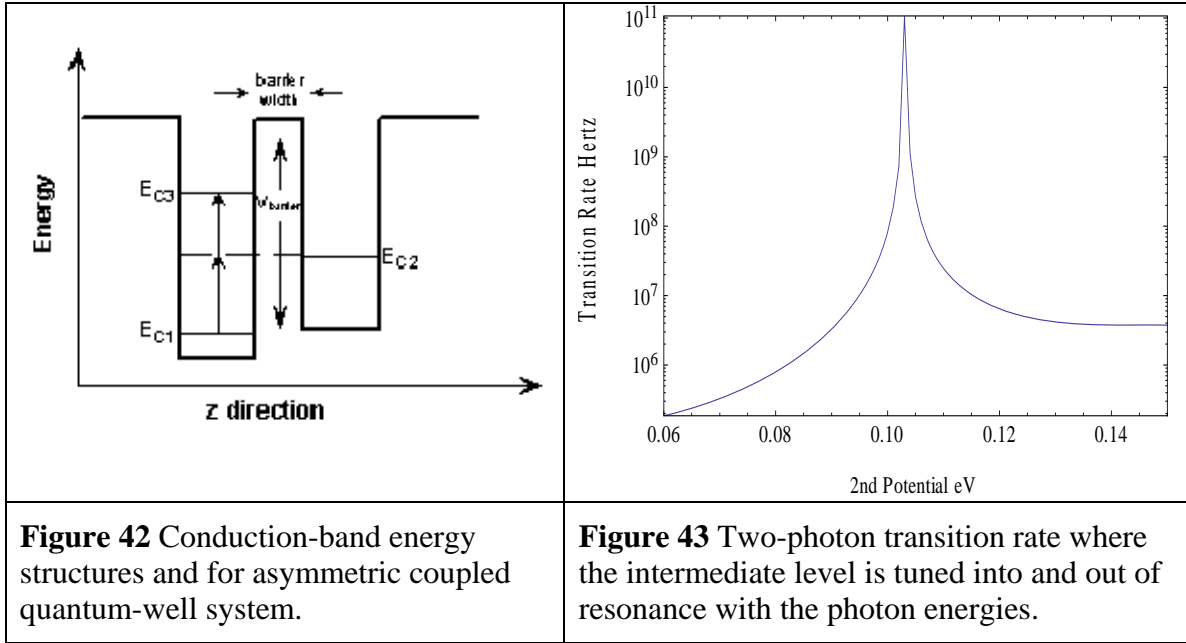
strength (barrier height and barrier thickness).

Figure 43 is a plot of the two-photon absorption rate that occurs when the second well depth is varied. In this simulation, the barrier width is 0.5 nm, one-half the well widths used. The transition rate increases by more than  $10^5$  when the first photon energy matches the  $E_{C1}$  to  $E_{C2}$  transition energy and the second photon energy matches the  $E_{C2}$  to

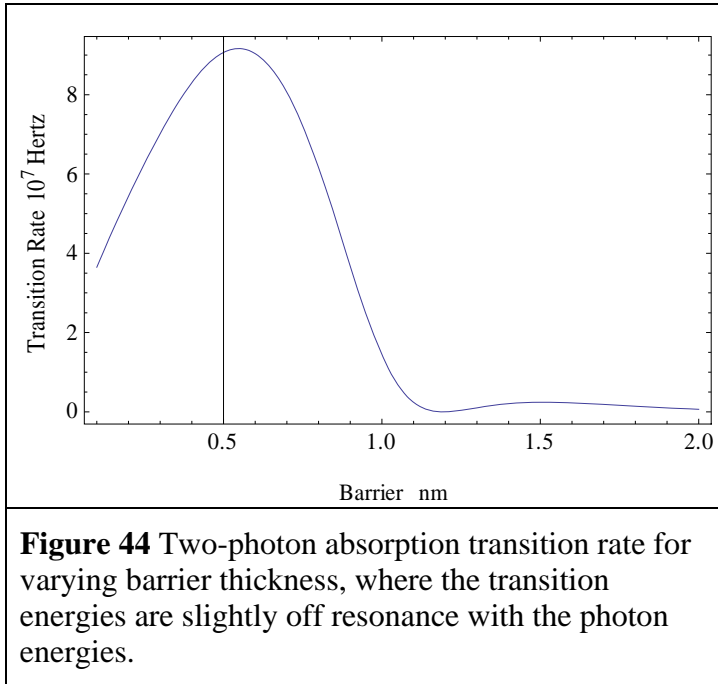
for a 0.2-nm square well that has a well depth of 17.6 eV. This is approximately the size of a hydrogen atom, and the energy separation of the states in the well is 13.6 eV, the same as the  $2p$  to  $1s$  transition in the hydrogen atom. The calculated lifetime of  $6 \times 10^{-10}$  s is comparable to the hydrogen atom lifetime of  $2 \times 10^{-10}$  s, when one takes into account the degeneracy of the  $2p$  state of the hydrogen atom.

Next, we examined the bound-state conduction-band energy ( $E_{C2}$ ) in the second well is larger than the lowest bound state in the first well. Because the wells are separated by a thin barrier, the second-well energy state couples through the barrier, and a virtual well state is found at energy  $E_{C2}$  in the first quantum well. The coupling strength, and thus transition rates for single and two-photon absorptions can be controlled through the choice of the barrier

$E_{C3}$  transition energy. Thus, by including the coupled well state, a virtual two-photon absorption system can be created in the semiconductor structure.



In Figure 44, we show the variation in the two-photon absorption transition rate as the barrier width is changed. From this figure we can see that as the barrier strength is increased, the intermediate transition is less coupled to the core quantum well, and the two-photon absorption strength decreases. This is true for both resonant and non-resonant cases.



intermediate, and excited states in the accompanying Figure 45(a). In the organic crystal material, the additional states that form the virtual intermediate states are supplied by the energy states of the surrounding organic crystal structure. Again, as in the organic

The quantum-well structure that we have analyzed is analogous to organic crystal materials that have demonstrated high two-photon absorption enhancement.<sup>55</sup> The basis for the design of the organic crystals was discussed with Dr. Goodson at the DARPA QSP workshop, and it is similar to our asymmetric coupled quantum well design. In the organic crystals, three eigenstates of the underlying structure that binds the carrier are present. In our structure, these are supplied by the core quantum-well system, and they are designated as the ground,



crystals, a set of states that are not part of the bound-state structure are formed with energies near resonance with the intermediate state of the bound system. These are supplied by the asymmetric coupled quantum wells, and in Figure 45 they are designated as the extended states of the system. The extended states are not eigenstates of the underlying core and are the basis for a virtual state that is nearly resonant with a true eigenstate. The near-resonance enhances the transition probability for the virtual state, and the extended states form a basis for a larger optical absorption cross section. Superlattices (the asymmetric coupled quantum wells in our design) with many periods have been used in various electronic and optical quantum-well devices and these structures can be fabricated to examine the absorption cross section of the designs. The additional feature shown in Figure 45(a) is the use of a non-square well in the core well layer. This non-square well allows additional tuning of the absorption energy from the intermediate to the upper state of the core quantum well.

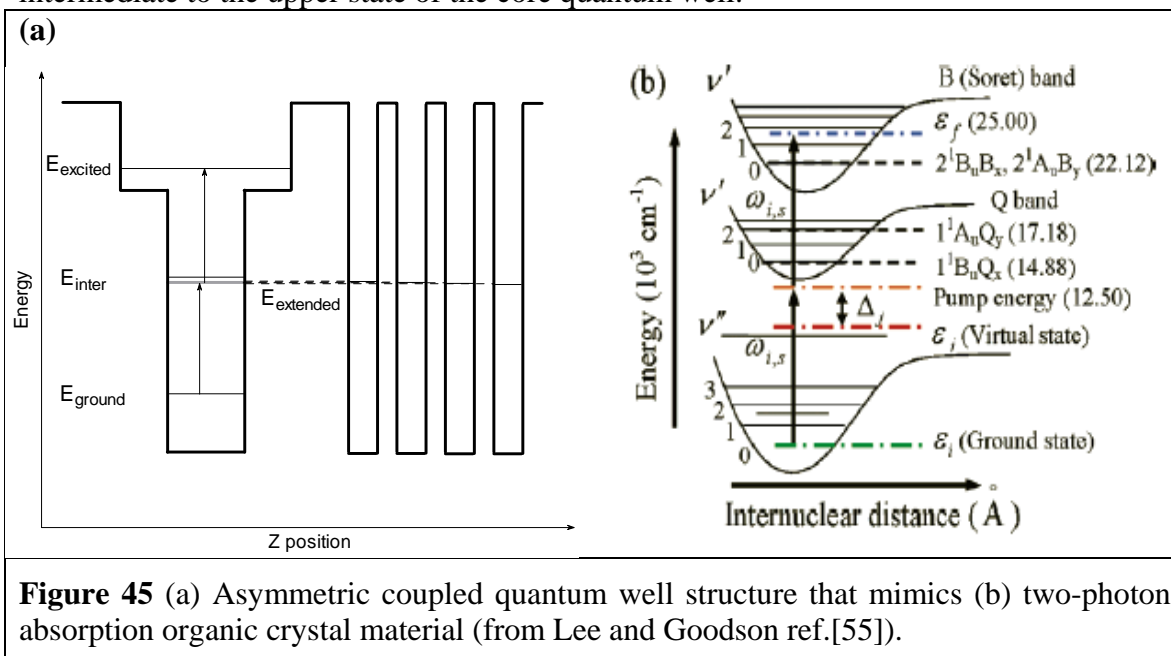


**Figure 45** (a) Asymmetric coupled quantum well structure that mimics (b) two-photon absorption organic crystal material (from Lee and Goodson ref.[55]).

The use of these virtual intermediate states has two effects. The first is an increase in the overall two-photon absorption cross section. This increase is related to the geometric size of the absorbing region for the second incident photon of the two-photon pair. In the case of the organic crystal, this goes from the initial absorbing atom, to the size of the crystal molecule. In the case of the semiconductor quantum-well structure, this changes from the size of the core quantum well to the size of the core plus the size of the coupled well structure. Superlattices (multiple quantum well structures) of a hundred periods that exhibit coherent (band structure) characteristics have been grown using molecular beam epitaxy techniques. With this structure the two-photon absorption cross section can be increased by several orders of magnitude using this structure.

A second benefit of using the virtual photon technique is the non-classical absorption properties of entangled two-photon absorption (ETPA) compared to the classical two-photon absorption (TPA). The theoretical modeling of virtual state absorption ETPA predicts that for low photon number the absorption is linear with intensity, compared to the quadratic absorption of non-entangled photon pairs.<sup>56</sup> Using the enhanced absorption in their organic crystals, Lee and Goodson were able to demonstrate this linear ETPA

rate compared to the quadratic nonlinear TPA rate (as shown in Figure 46). This linear effect increases the ETPA absorption rate slightly over the TPA absorption rate for extremely low photon flux rates.

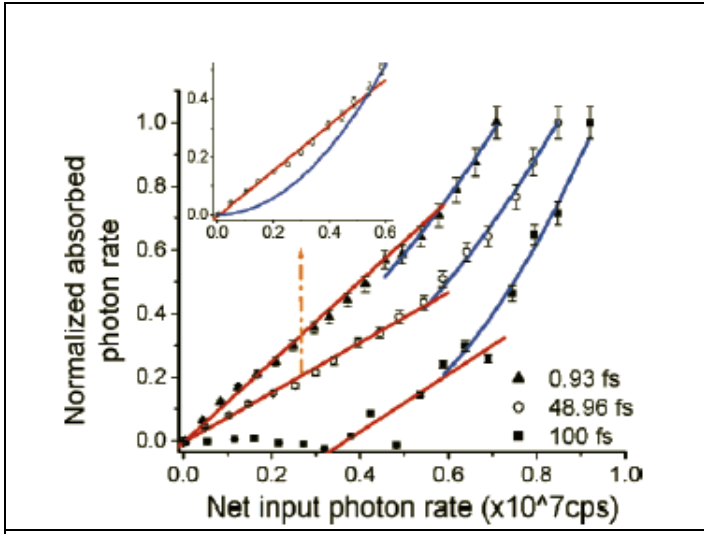


**Figure 46** Linear ETPA rate and quadratic random TPA for porphyrin dendrimer at different entanglement times (from Lee and Goodson ref. [55]).

### 6.3 Proposed Semiconductor Quantum-Well Test Structure

Based on our examination of the asymmetric coupled quantum-well system we propose the following test structure design to corroborate the modeling done under this project. The test design is a modification of the analysis, allowing special measurement capabilities to be used. We have chosen the GaAs/AlGaAs material system for the test structure. This semiconductor system is the best understood III-V semiconductor layer system and one that can be grown in the most controlled

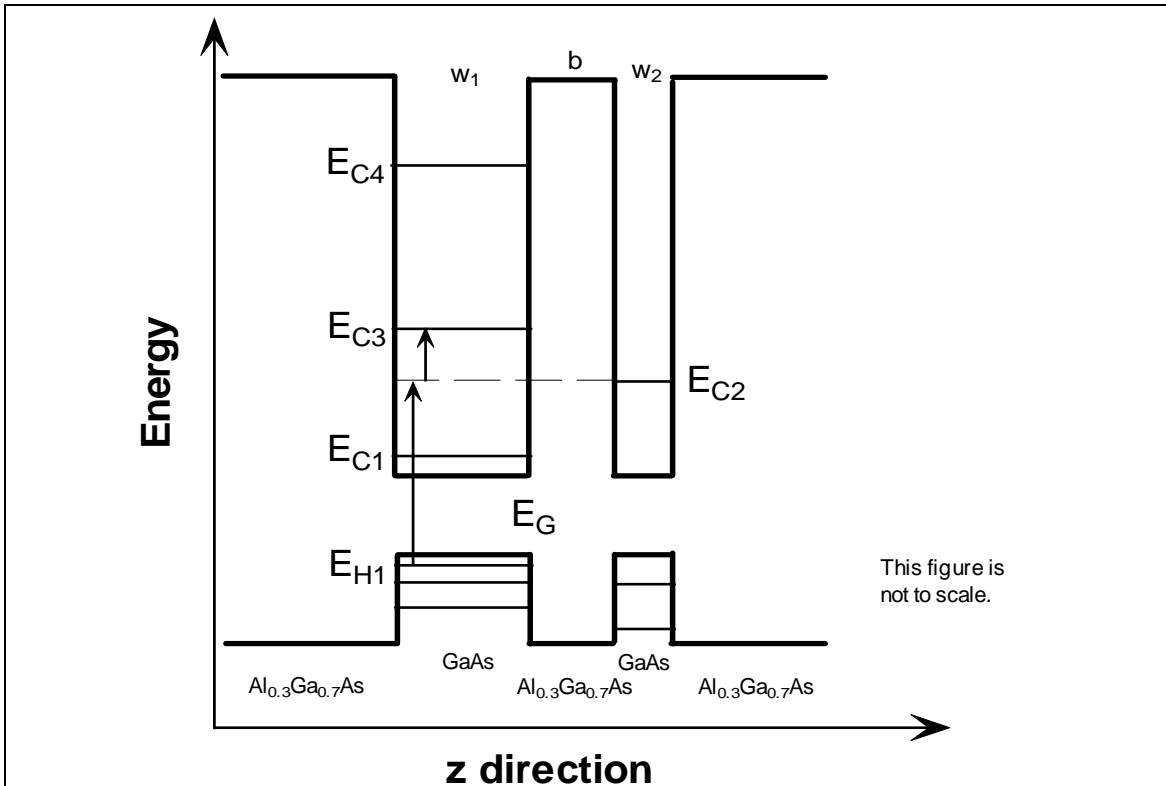


**Figure 47** GaAs/AlGaAs proposed test structure.

fashion with the lowest number of crystal defects. Molecular beam epitaxial (MBE) is routinely used for growing these materials and this growth technique has atomic monolayer precision that is needed to realize these structures. Figure 47 illustrates the first test structure, used to measure the two-photon absorption rate and various relaxation rates in the system. Table 12 lists the layer characteristics of the test structure. The quantum well materials are GaAs with a bandgap at 60K of 1.514 eV, and the outer and barrier materials are  $\text{Al}_{0.3}\text{Ga}_{0.7}\text{As}$ . This material is virtually lattice matched to the GaAs layer, thus minimizing any crystal defects due to lattice mismatch between the layers. The barrier width of 2 nm was chosen to allow strong coupling of the quantum well states, as shown in the calculations.

The test structure system is grown on a GaAs substrate and a series of GaAs/AlGaAs superlattices that lattice stabilize the substrate surface, pinning any possible substrate defects. To increase the absorption in the sample, the test structure should be repeated 10 times, with approximately 50 nm of  $\text{Al}_{0.3}\text{Ga}_{0.7}\text{As}$  between the test structures to isolate them from each other. Finally, a 50-nm GaAs layer should be deposited on the top of the test structures to cap the AlGaAs layer preventing oxidation. A second test structure with a slightly larger barrier (3 nm) can also be created to examine the change in the transition times as predicted by the model. A third test structure that incorporates multiple coupled quantum wells (as shown in Figure 45) can be examined to address the increase in two-photon absorption cross section due to the extended states in the coupled quantum well region. In this test structure the GaAs coupled well (4 nm) and the  $\text{Al}_{0.3}\text{Ga}_{0.7}\text{As}$  barrier (2 nm) would be repeated (10 $\times$ ) before the outer barrier layer of  $\text{Al}_{0.3}\text{Ga}_{0.7}\text{As}$ .

**Table 12 Test structure materials and thicknesses.**

Material	Description	Width (nm)
$\text{Al}_{0.3}\text{Ga}_{0.7}\text{As}$	Outer Barrier	---
GaAs	Core Well ( $W_1$ )	10
$\text{Al}_{0.3}\text{Ga}_{0.7}\text{As}$	Inner Barrier (B)	2
GaAs	Coupled Well ( $W_2$ )	4
$\text{Al}_{0.3}\text{Ga}_{0.7}\text{As}$	Outer Barrier	---

absorption. Based on the calculated quantum-well energies, the first photon of the two-photon absorption is at an energy of 1.610 eV, or a wavelength of 770 nm. The second photon of the two-photon absorption is at an energy of 0.019 eV, a wavelength of 65  $\mu\text{m}$ , or a frequency of 4.6 THz. These wavelengths match well with the optical-pump / THz-probe spectroscopic system used at UMBC. The titanium-sapphire optical-probe laser has a range 750 to 800 nm and the THz-probe source has a range of 1 to 10 THz covering the absorption features of the asymmetric coupled quantum-well system. The

Table 13 lists the quantum-well eigenstates and their energies with respect to the top of the valence band and the bottom of the conduction band. The use of the conduction band hole state as the ground state of the two-photon absorption was chosen to allow the use of standard tunable sources for the characterization of the two-photon

**Table 13 Quantum-well energies for proposed test structure.**

Designation	Description	Energy measured from band edge (eV)
EH1	First Heavy-Hole Energy in Core Well	-0.008
EC1	First Electron Energy in Core Well	0.027
EC2	First Electron Energy in Coupled Well	0.088
EC3	Second Electron Energy in Core Well	0.107
EC4	Third Electron Energy in Core Well	0.226

pump-probe system has a temporal resolution on the order of 100 fs and allows the examination of the various absorption and relaxation times in this system. With this information, the possible two-photon correlation times can be determined.

#### **6.4 Conclusions → Quantum Well Multiple Photon Absorbers**

Based on our examination of the asymmetric coupled quantum well system, we believe that two-photon absorption can be obtained with temporal characteristics required for correlated photon measurements. The correlation times can be controlled through the barrier strength of the region separating the core quantum well and the coupled quantum well. The wavelengths for the two-photon absorption can be determined by the proper choice of the semiconductor barrier and well materials and the quantum well thicknesses. The test structures and optical characterization proposed will demonstrate that the asymmetric coupled quantum wells perform as a two-photon absorption system in TPA and ETPA experiments similar to the organic crystal structures of Lee and Goodson. The optical characterization using femtosecond pump-probe spectroscopy will confirm that the correlation time can be controlled using the barrier width, as predicted by the model.

The major issue that has not been resolved is the large two-photon absorption strength that is needed for low-photon-flux detection. In our design the absorption cross section can be enhanced by the use of multiple coupled quantum wells; however this is limited to a factor of  $\sim 10^2$  due to technical difficulties in maintaining a fixed superlattice period (well-barrier thicknesses) for superlattices above a hundred periods.

## 7 Theoretical Analysis of Imaging with Entangled States

The objectives of the QSP program as outlined in the BAA are shown again (for convenience) in Table 14. The first four objectives involved the use of analysis to certify that our approach to imaging satisfies the first four criteria shown in Table 14. Additionally, we sought to devise and carry out an experiment that serves as a “proof of concept” for the phenomenology we intended to exploit in our sensor concept. The results of these endeavors have been recounted in previous sections. We have also made comparisons of the resolution and signal to noise ratio (*SNR*) that are available from our proposed quantum sensor as opposed to a classically based analog. These results are also presented above. In the present section, we discuss the analysis that has been carried out to establish compliance (or non-compliance, as the case may be) of our proposed imaging sensor scheme.

### 7.1 Interaction with the Target

The fact that non-classical states do not become completely classical upon interaction with a target has been verified both theoretically and experimentally in many calculations and experiments carried out at UMBC and other institutions. This point has thus been well established. It is also shown in the calculations performed under this contract that are shown in Appendix A. In the simplest case non-classical states are preserved if the interaction with the target is lossless. In the case of loss, especially large loss, the complete state that scatters from the target may, in fact, be classical; however, by post-selection, i.e. by judicious choice of detection, a non-classical state may be detected. The post-selected state can produce the same results as the non-classical state in the lossless case, but at a reduced detection rate.

### 7.2 Resolution and Energy Propagation

The program undertaken was to study ghost imaging with entangled photons. A number of theoretical and experimental studies of two-photon ghost imaging had been done at UMBC. These studies had focused on studying imaging and interferometry in various configurations to test and expand the underlying theory descriptive of various situations in a laboratory setting. They concentrated on improving visibility and counting rates. The questions of whether ghost imaging could be used in sensor technology over long

**Table 14 QSP Program Objectives From the BAA.**

The photon's interaction with the target doesn't cause the non-classical state to be entirely lost.
The quantum sensor can resolve two targets at a closer spacing than is possible with a classical sensor.
The energy that travels between the quantum sensor and the target propagates at the single photon wavelength
<p>The quantum sensor suffers a loss of sensitivity and resolution that is no worse than the loss suffered by a classical sensor under the following conditions:</p> <ul style="list-style-type: none"> <li>➤ The transmission medium between the sensor and the target absorbs or diffusely scatters photons.</li> <li>➤ The target is in a daylight environment.</li> <li>➤ The target scatters incident photons non-uniformly over <math>4\pi</math> steradians</li> </ul>
Make a specific calculation of the resolution improvement achieved with a 3 dB loss in the transmission medium and a resulting 26 dB signal to noise ratio.
An experiment whose goal is to provide additional validation of some results demonstrated analytically under the Base effort, particularly if the relevant theoretical base is underdeveloped. The goal of a proposed experiment may be to determine results beyond the scope of the Base effort.

distances and with large losses had not been explored prior to the advent of the QSP program.

On the QSP program, we began our study by looking at the resolution using the Rayleigh criterion. This criterion is simple and useful since it was assumed that the targets were of approximately equal brightness. Furthermore, we examined cases of imaging beyond simply distinguishing two targets. We examined the resolution of non-degenerate spontaneous parametric down-conversion.<sup>57</sup> This was stimulated by the question of whether the use of a long wavelength photon to illuminate the target while retaining a short wavelength photon as a reference would yield imaging as though the target was illuminated by the short wavelength photon. It was shown that for sensors this was not the case. It was shown that the resolution was determined by the wavelength of the light that illuminated the target. This analysis is presented in detail in Appendix B.

The question posed by the third objective listed in Table 14 was interpreted as asking whether entangled photons behaved as single photons. It was well-known that the propagation of each photon was determined by Maxwell's equations. However, entangled states are more strongly correlated than classical states and can provide effects that are not possible with classically correlated states. For two-photon ghost imaging entangled states have visibility much greater than can be obtained with classical states.

We were led to examine states with more entangled photons. Starting from our previous work on ghost imaging with three photons,<sup>58</sup> we have examined resolution issues for ideal cases. This work will be summarized here and is shown in greater detail in Appendix C. One case we examined was that in which one photon is sent to the target while two photons are retained in the laboratory. Scattered photons are collected and three photon coincidences are measured. The detection measurements are single photon detections. We have found that for the case in which all three photons have different wavelengths there is no improvement in the imaging. When the two retained photons are degenerate (and measured jointly by a two-photon absorption material), that is, they have the same wavelength, and the Airy disk has a radius half of what it would have with a single photon of the same wavelength as each of the retained photons. In this case no improvement in resolution was found, however.

In the case in which two photons illuminated the target and one was retained in the laboratory, more promising results appeared with respect to achievable resolution. These were generalized to the multi-photon case.<sup>59</sup> We analyzed the spatial resolution improvement using three-photon imaging process beyond the Rayleigh diffraction limit. Our analysis showed that with the entangled state  $|2,1\rangle$ , where one photon is non-degenerate ( $\lambda_2$ ) while the other two photons are degenerate ( $\lambda_1$ ), the ability to resolve two point sources in the object plane can be improved by a factor of two by sending two degenerate photons to the target while keeping the non-degenerate and imaging lens in the lab. Referring Figure 48 below, we showed that an image was formed if the Gaussian thin lens formula

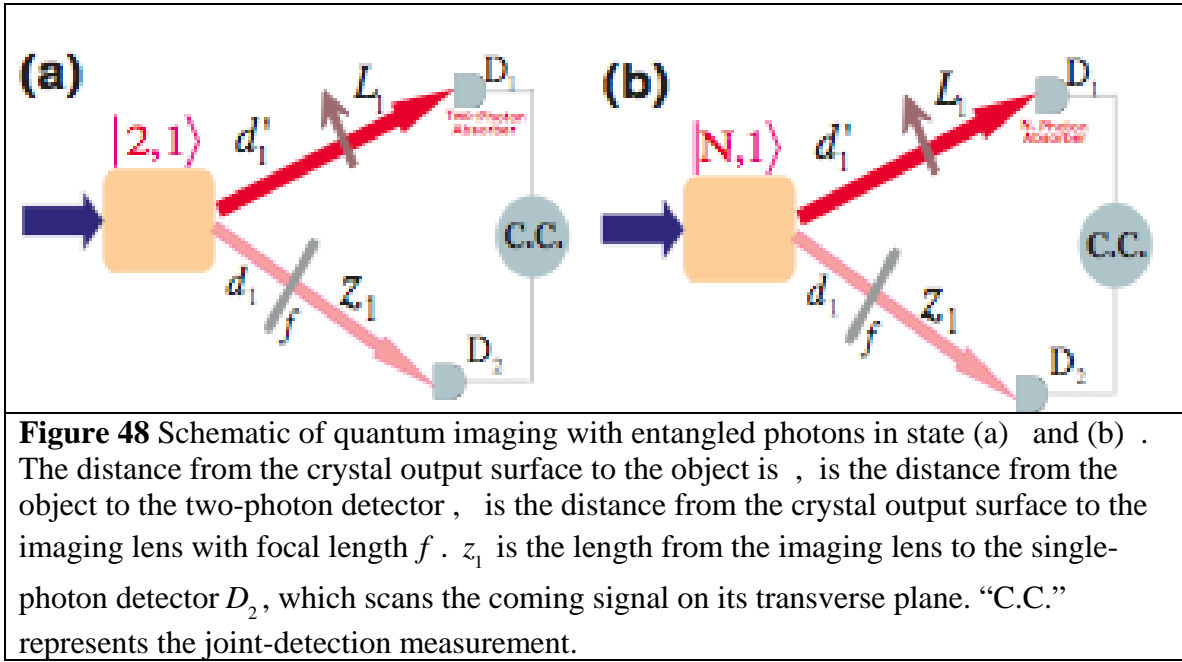
$$\frac{1}{f} = \frac{1}{z_1} + \frac{1}{d_1 + d'_1(\lambda_1 / 2\lambda_2)} \quad (32)$$

held. The minimum distance was found to be

$$a_{\min} = 1.22 \frac{\lambda_2}{2R} \left( d_1 + \frac{\lambda_1}{2\lambda_2} d'_1 \right) \approx 1.21 \frac{(\lambda_1/2)d'_1}{2R} \quad (33)$$

where  $d'_1 \gg d_1$ .

The scanning detector  $D_2$  may be replaced by a CCD detector and the detector  $D_1$  is a two-photon bucket detector. A central assumption of this calculation was that the degenerate photons illuminate the same area of the object. This would not be a problem if we only wish to distinguish two large objects, but does present a problem for imaging. The illuminated area must be small on the scale over which the target reflectivity changes appreciably.<sup>59</sup>



We generalized this scheme to the entangled state  $|N,1\rangle$  and showed that a factor of  $N$  can be achieved for the spatial resolution enhancement which cannot be obtained in classical optics. This conclusion is borne out in the following expressions.

$$\frac{1}{f} = \frac{1}{z_1} + \frac{1}{d_1 + d'_1(\lambda_1 / N\lambda_2)} \quad (34)$$

$$a_{\min} = 1.22 \frac{\lambda_2}{2R} \left( d_1 + \frac{\lambda_1}{N\lambda_2} d'_1 \right) \approx 1.22 \frac{(\lambda_1 / N)d'_1}{2R}$$

Note that this expression is qualitatively similar to what one would expect for the Rayleigh criteria, however, the wavelength  $\lambda_1$  is divided by  $N$ , leading to proportionately improved resolution.

We concluded that to realize such an imaging system with an  $N$ -photon bucket detector, a number of conditions should be satisfied. First of all, the  $N$  degenerate

photons should be delivered to the same point on the target. Secondly, the use of the bucket detector requires that all  $N$  degenerate photons scattered be detected in a single temporal counting window. We also pointed out that the system is very sensitive to the levels of optical path loss that will typically be present in a standoff imaging system. Although the loss of the vast preponderance of degenerate photons would not affect the quality of the image, it does have an effect on the counting rate, or equivalently, the exposure time. While not an explicit figure of merit in the go/no-go criteria for the program, the time required to form an image is important for a tactical imaging system and can certainly spell the difference between the viability and non-viability of such a system.

To overcome the issue of loss mentioned above, we were motivated to study the optical properties of other three-photon states entangled in time-energy and space. It is well known that for  $N$ -photon states with  $N \geq 3$ , there are many different classes of entangled states. In tripartite systems two classes of genuine tripartite entanglement have been discovered, namely, the Greenberger-Horne-Zeilinger (GHZ) class and the W class. The GHZ-like entangled state  $|1,1,1\rangle$  and the W-like state  $|2,1\rangle$  were studied during the course of the QSP Program.<sup>60</sup> As expected the GHZ-like state becomes a randomly mixed state if one photon is lost while the W-like state retains some two-photon entanglement if one of the degenerate photons is lost.

### 7.3 Impact of Transmission Impairments

Broadly speaking the transmission impairments cited in Table 14 above fall into two categories, noise processes and losses. The noise processes would include such things as background counts from external sources such as the sun and dark counts in one or more of the detectors. These processes produce counts in the detectors occurring at random times with respect to the counts produced by the entangled photons themselves. Our prospective imaging system produces counts by measuring correlations between entangled photons produced at the source and incident on detectors that are spatially separated from one another. The arrival times of the entangled photons on the detectors will have a well-defined temporal relationship that will enable them to be distinguished from detector responses arising from noise processes which do not have such a precise relationship. Therefore, one may say that, not only is it expected that the performance of an imaging system based on entangled states is not degraded with respect to a classical imaging system; the resiliency of the system in the face of noise is expected to improve with respect to that which can be expected from a more conventional imaging system. The trade one must make as the frequency of noise counts becomes higher and higher compared to the frequency of signal counts is that the timing that defines correlation must become more and more precise, which adds complexity to the system. Unfortunately, resiliency in the face of large optical path losses appears to be rather less encouraging.

Large photon losses appear, in fact, to be fatal to the use of entangled states at the photon level. While the correlation measurements are effective in eliminating noise and the losses do not affect the results of the imaging, they do affect the counting rate in such away as to make the required time to obtain an image unacceptably long. To see this, consider the fact that in the case of GHZ states discussed previously, we know that one must propagate  $N$  photons to a target, and, ultimately, to a detector in order to recognize an  $N$ -fold gain in resolution. Whatever the various sources of loss may be, we can expect that, in a standoff imaging system, the probability of detection  $P_{det}$ , of any one photon



given its launch from the source will be of order  $10^{-10}$ . Furthermore, the fact that the entangled photons, once launched, propagate independently to the target and detector suggests that the probability that all  $N$  of them will reach the detector is  $P_{\text{det}}^N = 10^{-10 \cdot N}$ . Now, if  $N = 2$  (that is a twofold resolution increase...a total of three entangled photons are created of which two are propagated to the target and one is retained locally), we need to launch  $10^{20}$  entangled photon “triplets” per second in order to collect one “triplet” at the detectors per second. At  $f = 200\text{THz}$  ( $E_{\text{photon}}^{200\text{THz}} = 133 \times 10^{-21} \text{J}$ ) this amounts to a total source power of approximately 40 W, if entangled triplets are generated with unit efficiency. Of course the efficiency will be ***much much*** less than unity in practice. For  $N = 3$  we would need about 530 GW of power so we can see that the scaling with loss is prohibitive for expected values of sensor standoff loss and values of  $N$  going up from  $N = 2$  which are of interest to the QSP program.

As mentioned above, whereas a loss of a single photon from a GHZ states means a loss of entanglement so that no signal may be realized from the detection of the remaining photons, some entanglement is maintained with W-states. However, we have concluded that, despite their increased tolerance to loss compared to their GHZ counterparts, W-states nonetheless suffer from the difficulty that the total probability for detection of a group of photons scales exponentially with the number of photons in that group. In the case where we detect only a subset ( $N$  photons) of our original group ( $M$  photons), we can also derive some advantage from the fact that any combination of our original  $M$  photons taken  $N$  at a time will generate a correlation. However, as long as  $M$  and  $N$  are relatively small, this gain will pale in comparison to the substantial losses added with each additional required photon in a practical standoff sensor system as shown above.

One possible way around this problem was to examine the case in which the target was illuminated by intense beams that were entangled with a single reference photon that acted as a trigger for the correlation measurement. In this case, the single photon would be retained near the source and so would not be subject to loss. There were two questions to be answered here. First, as discussed above, if we send out a very large number ( $M$ ) of photons and may detect correlations between *any* small combination ( $N$  in number) of them, we would expect our detection rate to go up. Secondly, and perhaps more obviously, the notion of an entangled beam implies that we will be able to generate more photons per unit time than would be the case with GHZ or W-states. The question is how *much* greater? We presented a preliminary work modeling so-called entangled beams in a previous report and a more complete version of this analysis is attached (in Appendix D) to this final report. With respect to the second question, we examined the model of one particular scheme for generating entangled beams in detail for its temporal correlations. We estimate that under ideal conditions, we can only get a generation frequency of about  $5 \times 10^9 / \text{s} \cdot \text{cm}^2$ . Consequently, in the high loss environment envisioned for the quantum sensor this scheme will not work. Currently, there is experimental work being carried out at UMBC on schemes in which much higher fluxes of up-converted photons may be generated. However, because of the intensity of the up-converted beam, a different detection scheme is required. With respect to the first question, we have determined that the nature of the entanglement in beams is rather similar to that in the GHZ states, for example, so that entangled states are generated (and must be detected) in groups of  $N$ . This means that it is not possible to drive up the

“combinatoric” gain to very high levels via the use of entangled beams (that is, by detecting *any* combination of  $N$  photons from a *very large* number  $M$  of launched photons). However, it is the case that one can generate these groups of entangled photons at significantly greater rates. That said, the scaling of the power requirements with  $N$  quickly derived above indicates that one will not reach the required flux level as  $N$  approaches 10 by increasing power since the launched power must increase by a factor of  $1/P_{\text{det}}$  (a *big* number in standoff detection systems) each time a photon is added to the size of the entangled group in order to maintain a given rate of detection.

Therefore we have concluded that while we have shown states and conditions for which the sought after ten-fold increase in resolution appears to be possible in principle, these states and conditions give performance that is significantly degraded with respect to a conventional imaging system with path loss that will be typical of a standoff imaging system. Conversely, while we found that loss could be tolerated for GHZ states where one photon was propagated to the target and  $N$  were kept back, it was determined that no advantage in resolution could be gained under this condition. Finally, while W-states offer an advantage insofar as the entanglement of the group is not completely lost with the loss of one entangled photon, ultimately the power requirements and loss tolerance for a given level of  $N$  is nearly identical to that of GHZ states. So, while states and conditions have been found that satisfy each of the requirements at various times and under various conditions, no one set of states and conditions satisfies the requirements *simultaneously*, which is of course the *real* requirement of the program.

## 8 Experimental Study on Entangled Triphoton Beams

Entangled multi-particle states of  $n \geq 3$  have attracted a great deal of interest because of their roles in probing the foundations of quantum theory<sup>1,61,62</sup> and their potential applications in quantum information processing.<sup>63,64</sup> In the past decades, experimental efforts in the realization of GHZ<sup>65</sup> and other multi-photon states<sup>66</sup> have led the study of multi-particle ( $n \geq 3$ ) entanglement to a new stage.

Beyond the multi-photon state at low light levels, the research presently reported studies entangled multi-photon beams. The entanglement is no longer restricted to single-photons but is achievable between high intensity beams. The objective of this part of our QSP research (undertaken in parallel with theoretical efforts at UMBC) is aimed at the generation of entangled multi-photon beams and the study of their temporal and spatial correlation for possible quantum sensor applications.

An experimental realizable true triphoton EPR state was proposed by Keller, *et al.*<sup>67</sup> Keller, *et al.*, calculated a three-photon state via optical nonlinear interaction. In an optical medium, which has significant second-order nonlinear susceptibility,  $\chi^{(2)}$ , a laser beam, namely the pump, produces two pairs of signal-idler photons in the process of spontaneous parametric down-conversion (SPDC).<sup>68</sup> By up-converting the two idlers from two individual signal-idler pairs, the up-converted photon along with the remaining two signal photons form an entangled tri-photon EPR state. To achieve both SPDC and up-conversion, two sets of phase matching conditions must be satisfied in the nonlinear interaction simultaneously:

$$\begin{aligned}\vec{k}_1 + \vec{k}_{1'} &= \vec{k}_p \\ \vec{k}_2 + \vec{k}_{2'} &= \vec{k}_p \\ \vec{k}_{1'} + \vec{k}_{2'} &= \vec{k}_3\end{aligned}\tag{35}$$

where the subscript  $p$  stands for the pump, 1 (signal) and 1' (idler), 2 (signal) and 2' (idler) denote the signal-idler pairs of 1 and 2, and 3 denotes the up-converted photon. Achieving the three phase-matching conditions simultaneously within a nonlinear material has been a major challenge in crafting an experimental realization. It is the use of a hexagonally poled 2-D photonic crystal of quasi-phase-matching<sup>69</sup> that has made it possible to achieve both SPDC and up-conversion and to generate the reported triphoton EPR state.

To analyze the triphoton state, we start with the Hamiltonian of the time dependent interaction

$$H_I = \frac{\varepsilon_0}{2} \int_V d\vec{r} \chi^{(2)}(\vec{r}) \left[ E_p^{(+)} E_1^{(-)} E_{1'}^{(-)} + E_p^{(+)} E_2^{(-)} E_{2'}^{(-)} + E_3^{(-)} E_{1'}^{(+)} E_{2'}^{(+)} \right] + H.C., \tag{36}$$

where  $V$  is the interaction volume and  $\chi^{(2)}(\vec{r})$  characterizes the spatial modulation of the second-order nonlinear susceptibility. The entangled triphoton state can be calculated from the third-order perturbation theory,

$$|\psi\rangle = \Psi_0 \sum_{\vec{k}_1, \vec{k}_2, \vec{k}_3} \delta(2\omega_p - \omega_1 - \omega_2 - \omega_3) \delta(2\vec{k}_p - \vec{G} - \vec{k}_1 - \vec{k}_2 - \vec{k}_3) \hat{a}_{\vec{k}_1}^+ \hat{a}_{\vec{k}_2}^+ \hat{a}_{\vec{k}_3}^+ |0\rangle, \quad (37)$$

where we have approximated the pump field as CW, classical, and non-depleted, while treating the signal, idler and up-converted fields quantum mechanically with multiple modes. The constant vector,  $\vec{G}$ , arising from the 2-D periodically modulated  $\chi^{(2)}(\vec{r})$ , makes the quasi-phase-matching possible.<sup>69</sup> The wave vector  $\delta$ -function in Eq. (37) includes two sets of idealized quasi phase-matching:

$$\begin{aligned} \vec{k}_p - \vec{k}_1 - \vec{k}_{1'} - \vec{G}_{1,0} &= 0 \\ \vec{k}_p - \vec{k}_2 - \vec{k}_{2'} - \vec{G}_{1,0} &= 0 \\ \vec{k}_3 - \vec{k}_{1'} - \vec{k}_{2'} - \vec{G}_{0,1} &= 0 \end{aligned} \quad (38)$$

where  $\vec{G}_{1,0}$  and  $\vec{G}_{0,1}$  are the reciprocal-vectors of the 2-D hexagonally poled photonic crystal as shown in Figure VII.1(b). The frequency  $\delta$ -function,  $\delta(2\omega_p - \omega_1 - \omega_2 - \omega_3)$  is the result of the time integral in the perturbation which has been taken from  $-\infty$ . Examining Eq. (37), the non-factorizable spectral function of the state ties photons 1, 2, and 3 together as a typical EPR state. In Eq. (37), the energy and momentum of neither photon is determined. But, if one of them is measured with a certain value, the sum of the other two is completely determined, and vice versa.

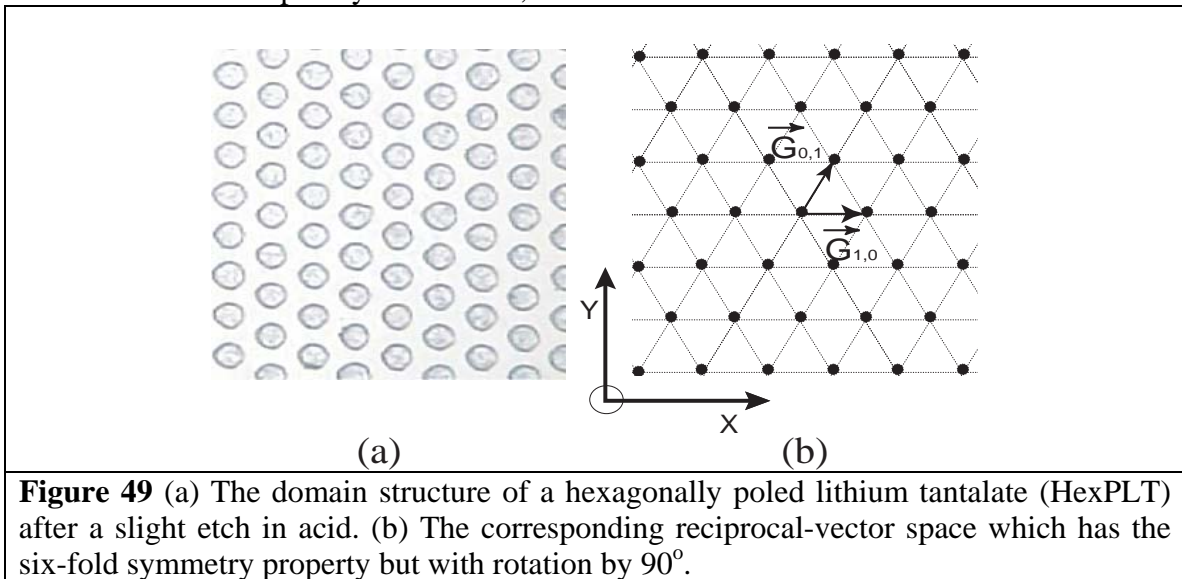


**Figure 49** (a) The domain structure of a hexagonally poled lithium tantalate (HexPLT) after a slight etch in acid. (b) The corresponding reciprocal-vector space which has the six-fold symmetry property but with rotation by  $90^\circ$ .

The 2-D  $\chi^{(2)}$  photonic crystal used in the experiment is a hexagonally poled LiTaO<sub>3</sub> (HexPLT wafer of  $15\text{mm} \times 15\text{mm} \times 0.5\text{mm}$ ).<sup>70</sup> Figure 49(a) shows a schematic picture of its domain structure. The nearly circularly inverted domain (with  $-\chi^{(2)}$ ) distributes in a  $+\chi^{(2)}$  background periodically with  $a = 0.95\mu\text{m}$ . This specific design realizes the two sets of quasi-phase-matching in Eq. (35) simultaneously. The phase-matching  $\vec{k}_p - \vec{k}_{1,2} - \vec{k}_{1',2'} - \vec{G}_{1,0} = 0$  for SPDC is in the  $\vec{G}_{1,0}$  direction. The other phase-matching  $\vec{k}_3 - \vec{k}_1 - \vec{k}_2 - \vec{G}_{0,1} = 0$  for up-conversion is in the  $\vec{G}_{0,1}$  direction. Reciprocal vectors  $\vec{G}_{1,0}$  and  $\vec{G}_{0,1}$  arise from the hexagonal modulation of the second-order susceptibility. Fig. 49(b) illustrates schematically the reciprocal-vectors of the hexagonally poled photonic crystal. Due to the six-fold symmetry in the reciprocal vector space, the depicted  $\vec{G}_{1,0}$  and  $\vec{G}_{0,1}$  have the same vector magnitude and the same Fourier component coefficients. Besides achieving phase matching, another big advantage for using a HexPLT crystal is the ability of utilizing  $d_{33}$ , the largest component of the  $\chi^{(2)}$  tensor for LiTaO<sub>3</sub>. This makes the quasi-phase-matched nonlinear interaction occur with very high efficiency. For example, by using a few hundred milliwatts of pump power, gains may be achieved in the range from 14 to 16 and the spontaneous process can enter the stimulated regime. Due to the use of  $d_{33}$ , the signal-idler pair as well as the up-converted fields and the pump are all polarized along the optical axis of the crystal.

Achieving the energy-momentum  $\delta$ -functions in Eq.(37) is only half of the story for the study of quantum entanglement. To complete the story, we must examine the space-time EPR correction function.<sup>71</sup> Experimentally, we have successfully measured the third-order temporal correlation function of the three-photon system and observed a typical EPR correlation in time. The third-order correlation function is given by

$$\begin{aligned} G^{(3)}(\tau_1, \tau_2, \tau_3) &= \langle \psi | E_1^{(-)} E_2^{(-)} E_3^{(-)} E_3^{(+)} E_2^{(+)} E_1^{(+)} | \psi \rangle \\ &= \left| \langle 0 | E^{(+)}(t_3, z_3) E^{(+)}(t_2, z_2) E^{(+)}(t_1, z_1) | \psi \rangle \right|^2 \\ &= |\Psi(\tau_1, \tau_2, \tau_3)|^2 \end{aligned} \quad (39)$$

Here,  $\Psi(\tau_1, \tau_2, \tau_3)$ , the probability amplitude of annihilating photon 1, photon 2, and photon 3, respectively, at  $(t_1, z_1)$ ,  $(t_2, z_2)$  and  $(t_3, z_3)$ , is named as the effective three-photon wave function, or triphoton. In Eq. (39)  $\tau_j = t_j - z_j/c$ ,  $j = 1, 2, 3$ , with  $t_j$  as the registration time of the  $j^{\text{th}}$  photo detector and  $z_j$  as the longitudinal coordinate of the  $j^{\text{th}}$  photo-detector along the  $j^{\text{th}}$  optical path. The calculation of  $\Psi(\tau_1, \tau_2, \tau_3)$  is straightforward, namely

$$\begin{aligned} \Psi(\tau_1, \tau_2, \tau_3) &= \langle 0 | E_3^{(+)} E_2^{(+)} E_1^{(+)} | \psi \rangle \\ &= \Psi_0 \int d\omega_1 d\omega_2 d\omega_3 \delta(2\omega_p - \omega_1 - \omega_2 - \omega_3) f(k_1, k_2, k_3) \exp(i\omega_1 \tau_1) \exp(i\omega_2 \tau_2) \exp(i\omega_3 \tau_3) \end{aligned} \quad (40)$$

where  $f(k_1, k_2, k_3)$  formally denotes the realistic longitudinal phase-matching function in SPDC and up-conversion. To complete the integral, we take frequency de-tunings  $\nu_m$  as variables, where  $\omega_m = \omega_0 + \nu_m$  ( $m=1,2,3$ ) and  $\omega_m^0$  is the corresponding central frequency of  $\omega_m$ , based on first-order dispersion; and use the frequency  $\delta$ -function, i.e.,  $\nu_3 = -(\nu_2 + \nu_1)$ , to reduce the integral from 3-D to 2-D. The triphoton is then simplified as

$$\begin{aligned} \Psi(\tau_{31}, \tau_{32}) &= \Psi_0 \exp[-i(\omega_1^0 \tau_{31} + \omega_2^0 \tau_{32})] \\ &\times \int d\nu_1 d\nu_2 \exp[-i(\nu_1 \tau_{31} + i\nu_2 \tau_{32})] \text{sinc}\left(\frac{\nu_1 D_{31'l} + \nu_1 D_{32'l}}{2}\right) \text{sinc}\left(\frac{\nu_1 D_{11'l}}{2}\right) \text{sinc}\left(\frac{\nu_2 D_{22'l}}{2}\right) \end{aligned} \quad (41)$$

where  $\tau_{jk} = \tau_j - \tau_k$  and  $D_{mn} = 1/u_m - 1/u_n$  with  $u_m$  ( $u_n$ ) the group-velocity of the  $m^{\text{th}}$  ( $n^{\text{th}}$ ) field.

Now, we introduce variables  $\nu_+$  and  $\nu_-$  with  $\nu_+ = (\nu_1 + \nu_2)/2$ ,  $\nu_- = (\nu_1 - \nu_2)$  and apply  $D_{31'l} = D_{32'l}$ . Eq. (41) can then be further simplified as

$$\Psi(\tau_{31}, \tau_{32}) \propto \int_{-\Delta\nu_+/2}^{+\Delta\nu_+/2} d\nu_+ \text{sinc}(\nu_+ D_{31'l}) \exp\left[\frac{-i\nu_+(\tau_{31} + \tau_{32})}{2}\right] \int_{-\Delta\nu_-/2}^{+\Delta\nu_-/2} d\nu_- \exp[-i\nu_-(\tau_{31} - \tau_{32})] \quad (42)$$

where functions  $\text{sinc}(\nu_1 D_{11'l}/2)$  and  $\text{sinc}(\nu_2 D_{22'l}/2)$  have been used to determine the upper and the lower limits of the integral. Taking into account realistic experimental parameters, Eq. (42) can be easily integrated numerically. In the extreme case, when we take the integral limits of  $\nu_+$  and  $\nu_-$  infinite, the integral in Eq. (42) yields

$$\Psi(\tau_{31}, \tau_{32}) \propto \Pi(T_{31} + T_{32}, -D_{31'l}) \delta(T_{31} - T_{32}) \quad (43)$$

where  $\Pi(x, a) = 1$  for  $0 \leq x \leq a$  and vanishes otherwise. Comparing the width  $D_{31'l}$  of the  $\Pi$  function along  $\tau_{31} + \tau_{32}$  and the  $\delta$ -function in  $\tau_{31} - \tau_{32}$ , we would expect a nonsymmetrical tri-photon wave function.

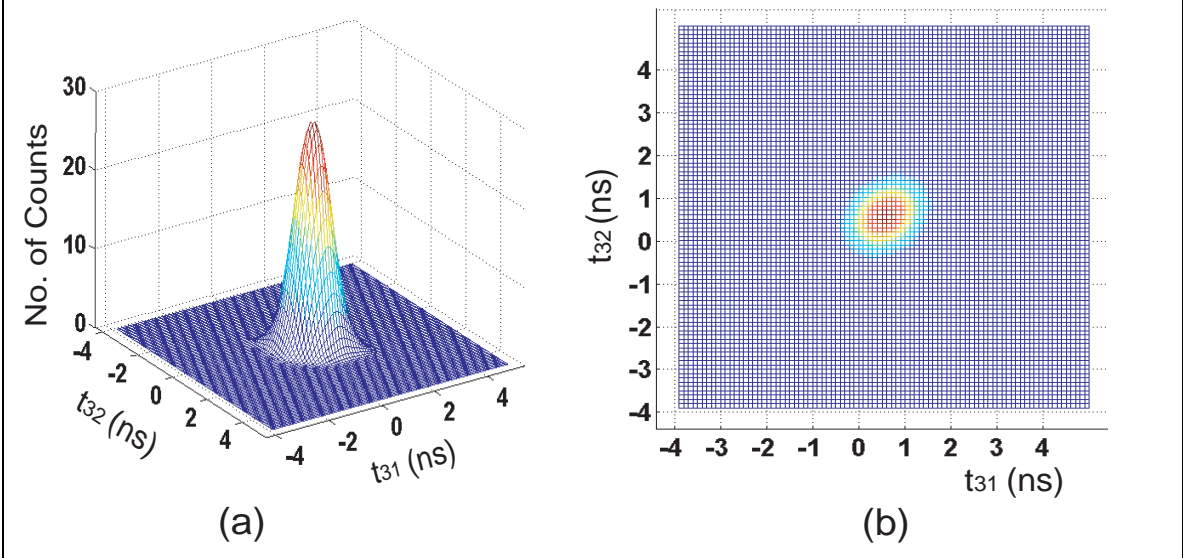


**Figure 50** A numerical simulation of the third-order correlation function,  $G^{(3)}(\tilde{t}_{31}, \tilde{t}_{32})$ .

Taking into consideration the limited response time of the photon counting detectors and their associated electronics, the measured  $G^{(3)}(\tilde{t}_{31}, \tilde{t}_{32})$ , for fixed  $z_1$ ,  $z_2$  and  $z_3$ , is thus determined by

$$G^{(3)}(\tilde{t}_{31}, \tilde{t}_{32}) = \int_{t_c} dt_{31} dt_{32} |\Psi(\tau_{31}, \tau_{32})|^2 \quad (44)$$

where  $\tilde{t}_{31}$  and  $\tilde{t}_{32}$  are the average times within  $\tilde{t}_{31} \pm t_c$  and  $\tilde{t}_{32} \pm t_c$ . We have assumed all three photo-detectors and their associated electronics have the same limited response time, or uncertainty,  $t_c$ . The sub-index  $t_c$  of the integral denotes a time average in the neighborhood of  $\tilde{t}_{31} \pm t_c$  and  $\tilde{t}_{32} \pm t_c$ . A numerical simulation of  $G^{(3)}(\tilde{t}_{31}, \tilde{t}_{32})$  is provided in Figure 50. The simulation is based on Eq. (42) and Eq. (44) with true experimental parameters.

The experimental setup is illustrated in Figure 51. The pump is a ~15 nanosecond pulsed Q-switched Nd:YAG laser with tunable repetition rate from a few  $kHz$  to 200  $kHz$ . A lens with focal length  $f = 15cm$  focuses the pump beam into the thin LiTaO<sub>3</sub> crystal ( $15mm \times 15mm \times 0.5mm$ ). When the  $e$ -polarized pump beam of  $\lambda = 532nm$  is incident along the  $\vec{G}_{1,0}$  direction and the temperature of the HexPLT crystal is set at 178°C, the signal, which is centered at  $\lambda = 873nm$ , and the idler at  $\lambda = 1362nm$  are collinearly generated along with the pump; while the up-converted beam, which is centered at  $\lambda = 681nm$ , emits 5° aside from the pump, is governed by the quasi-phase-matching conditions of Equation (38). To block the remaining pump beam, mirrors ( $HR532$ ) and band blocking glass filters ( $GF$ ) were applied. A 50/50 beam splitter ( $BS$ ) was used to split the collinearly propagated two signals while the two idlers were up-converted to  $\lambda = 681nm$ .

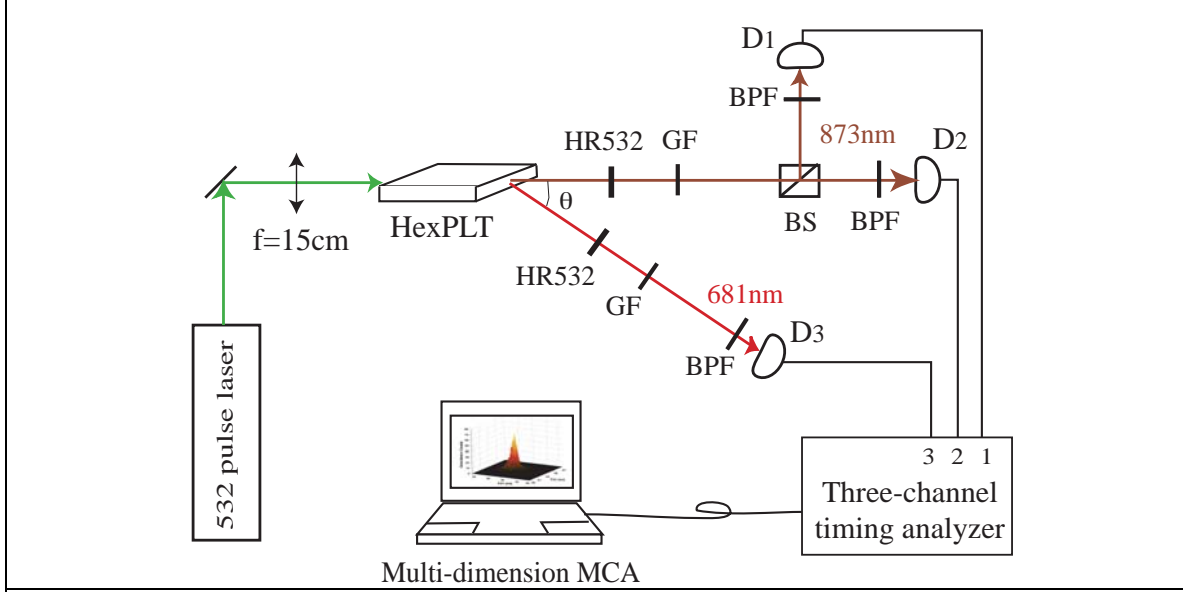


**Figure 51** Schematic experimental setup for three-beam temporal correlation measurement.

The separated two signals ( $\lambda = 873\text{nm}$ ) were then detected by photon counting detectors  $D_1$  and  $D_2$ , respectively, while the up-converted photon ( $\lambda = 681\text{nm}$ ) triggers photon counting detector  $D_3$ . Bandpass spectral filters (BPF) are used for passing the expected wavelengths to the photo-detectors. The registration time differences of  $t_{31} = t_3 - t_1$  and  $t_{32} = t_3 - t_2$  for each three-fold joint photo-detection event are recorded. The data is analyzed and reported as a 3-D histogram: the number of three-fold joint photo-detection events against  $t_{31}$  and  $t_{32}$ , which corresponds to  $G^{(3)}(\tilde{t}_{31}, \tilde{t}_{32})$  with fixed values of  $z_1$ ,  $z_2$  and  $z_3$ .

The experiment was implemented in the high-gain stimulated regime. The three entangled beams are observable easily by the human eye, which indicates a Fock state with occupation number  $n \gg 1$ . The correlation function  $G^{(3)}$  was measured in the photon counting regime and neutral density filters were used to attenuate each generated beam down to single photon level. Although the use of neutral density filters may destroy EPR correlation of a multi-photon source in the spontaneous regime, we have found that in the stimulated regime, the  $\delta$ -function-like spectrum of the state, which gives rise to the EPR correlation, remains unchanged. The physics is rather simple. In the spontaneous regime, each generated tri-photon may be characterized with a different initial phase, i.e., randomly distributed in phase space, which corresponds to random creation times of the triphoton. If one selects subsystems from different tri-photons for a joint detection event, the time correlation will be lost. In the stimulated regime, however, the modes are coherently excited. Roughly speaking, all generated tri-photons are in the same state, i.e., condensed into one point in phase space. There is no chance to pick up "wrong" subsystems for a joint detection event. The theory has been experimentally verified recently in our laboratory.<sup>72</sup> The experimental observation, as well as the theory, will be published separately.



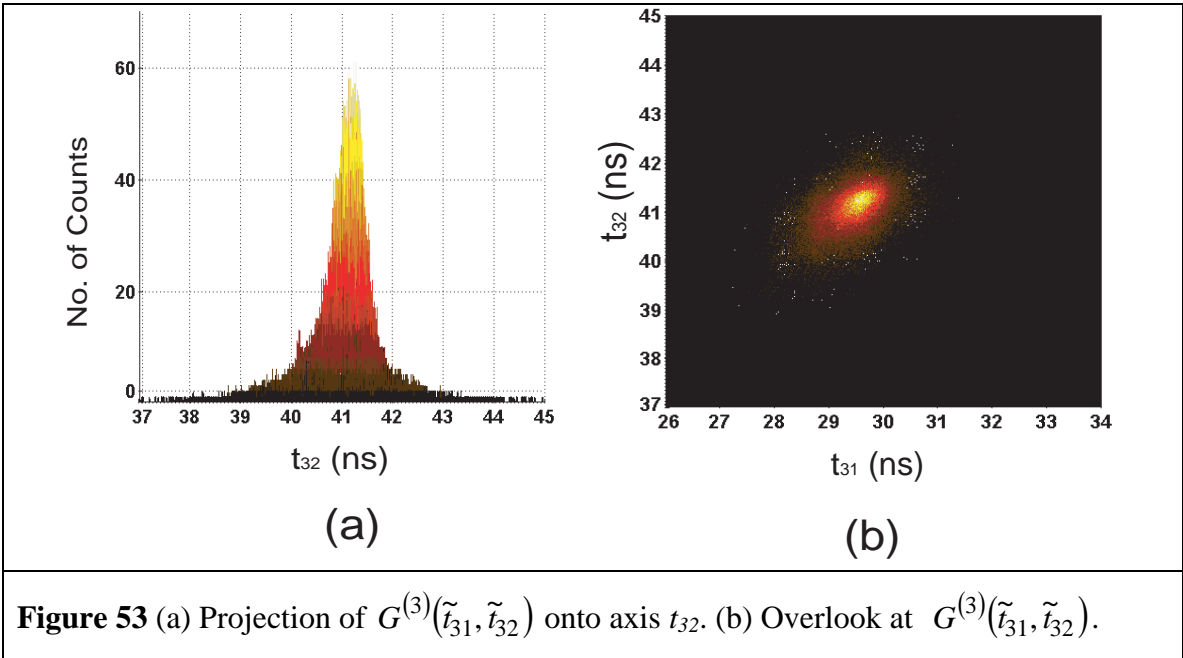
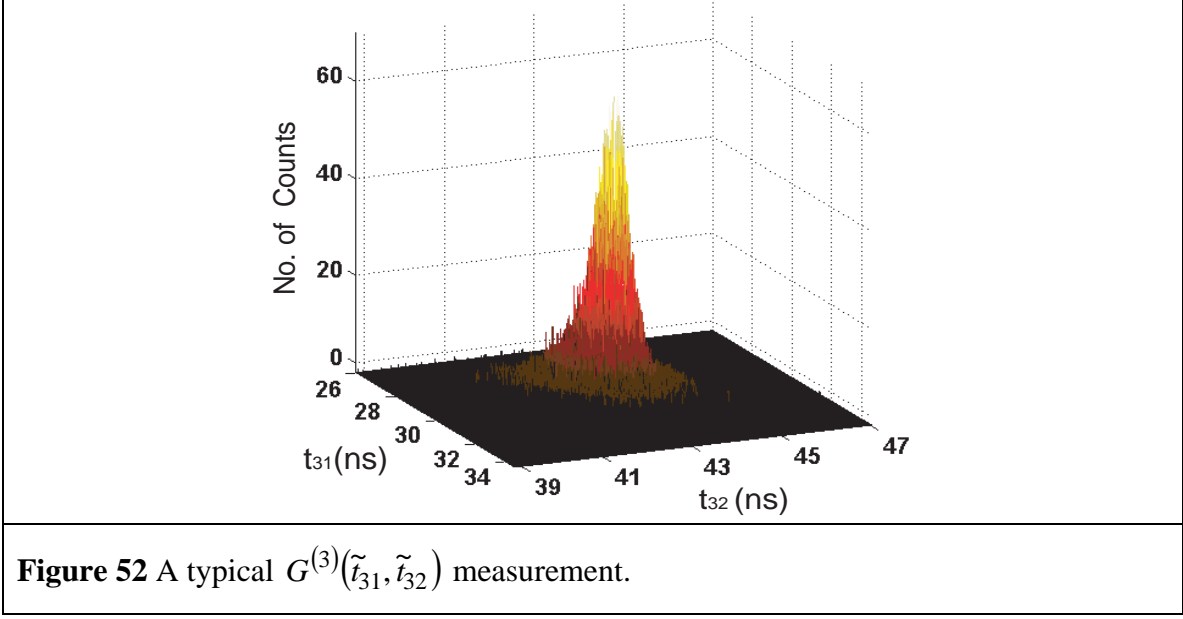
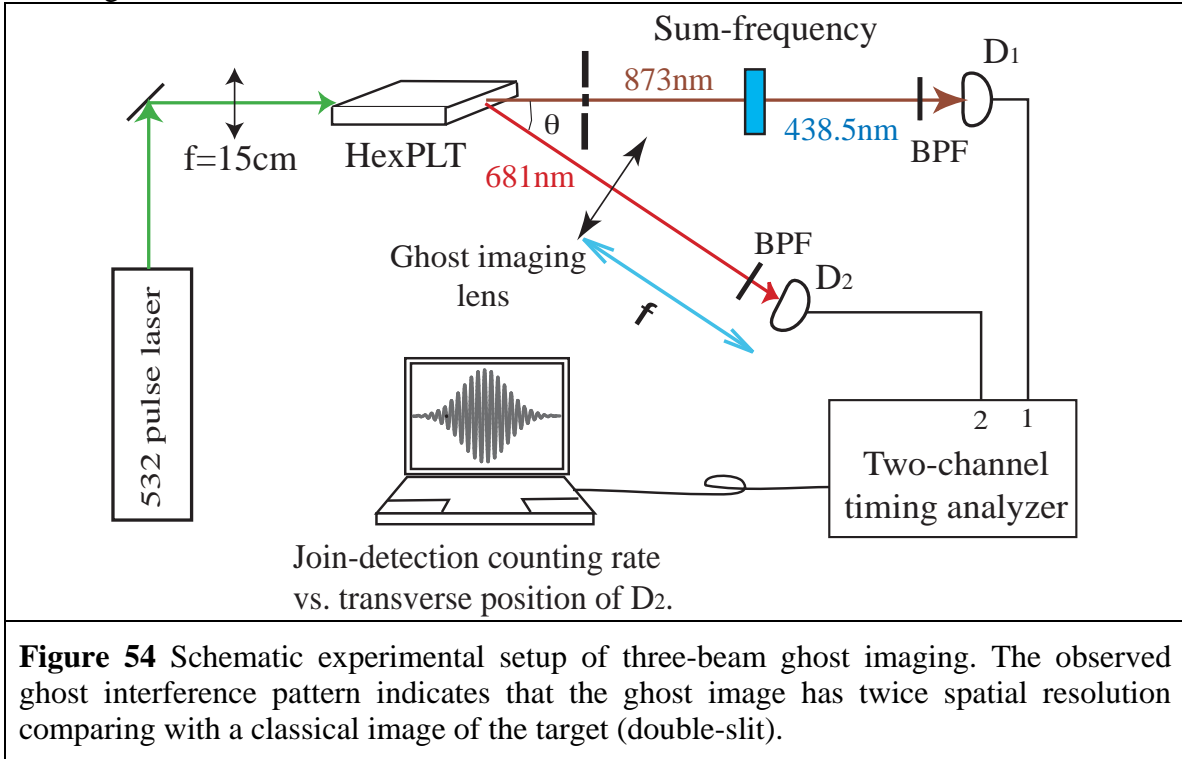


Figure 52 shows a typical measured temporal correlation function of  $G^{(3)}(\tilde{t}_{31}, \tilde{t}_{32})$ . The tri-photon is located within a very narrow time window as shown. To ensure that each measurement of the field occurs at the single-photon level, we adjusted the  $ND$  filters until the single photon counting rates reach  $\sim 30$  counts per second ( $30/13,000 \approx 2.3 \times 10^{-3}$  per pulse). Figure 53(a) shows the projection of  $G^{(3)}(\tilde{t}_{31}, \tilde{t}_{32})$  onto axis  $t_{32}$  (or  $t_{31}$ ). The width of the projection gives  $\sim 1ns$ , which is less than that of the measured width of the subsystems as well as the pump pulse ( $\sim 15ns$ ). The most interesting observation of the experiment is illustrated in Figure 53(b). The striking

feature of this measurement is the time-squeezing along  $(t_{31} - t_{32})$ , which is in good agreement with our numerical simulation of Figure 50, a convincing observation of the tri-photon wave packet.

The experimental setup for the spatial correlation measurement looks similar to that of the temporal correlation, however, the measurement is directly related to the spatial resolution of three-beam ghost imaging. Figure 54 is a schematic of one of the experimental setups. In fact, this setup is a ghost imaging experiment. As a result, we refer to this scheme as “ghost imaging of 2 +1 beams.” A double-slit, which plays the role of the object-target, is inserted in the entangled beams 1 and 2 with degenerate wavelengths  $\lambda = 873\text{nm}$ . The point photo detector  $D_2$  is may be scanned transversely, as indicated by the double arrowed line. The measurement of  $D_2$  is in the far-field Fourier transverse plane. A sum-frequency (second harmonic for degenerate wavelength) device is applied to up-convert the wavelength to  $\lambda = 436.5\text{nm}$ . The use of a nonlinear sum-frequency serves for the purpose of ensuring that the entangled two beams of  $\lambda = 873\text{nm}$  come from the same point of the target. A photo-detection event of  $D_1$  at  $\lambda = 436.5\text{nm}$  indicates the simultaneous measurement of two  $\lambda = 873\text{nm}$  beams. A coincidence measurement between  $D_1$  and  $D_2$  effectively achieves a three-beam joint detection. Our theoretical study has indicated that the spatial resolution of the ghost imaging will be enhanced by a factor of two, beyond the classical limit (see Section VI of this report). Corresponding to the theoretical prediction, in this measurement we expect to observe a far-field double-slit interference-diffraction pattern with half pattern width and twice interference modulation. According to Fourier optics, this result means an enhanced twice spatial resolution on the ghost imaging plane. Unfortunately, we have not been able to obtain publishable measurement data before the submission of this report. The experimental study will continue until achieving the goal of this investigation.



## 9 Suggestions for Further Work

In principle, the resolution analysis discussed above should be extended to a quantum treatment of hypothesis testing.<sup>15</sup> This could be performed for the case of an  $N = 11$  photon state, for instance, given proper normalization of the spatial part of the wave function, but in the case of entangled beams, the problem may be intractable. However, it would be important to at least compare error probability versus separation between point targets relative to the Rayleigh limit, and resolution versus  $SNR$  using Helmstrom's quantum formalism to our treatment in which we incorporated the quantum mechanically derived point spread functions into the classical model for the binary hypothesis test. This would test the validity of our results in terms of the comparison of  $SNR$  required for a given resolution between the entangled photon and baseline sources.

There are several aspects of the  $SNR$  calculations that need further study. One is the validity of a Fano factor to represent sub-Poissonian statistics in the case of entangled photons or beams. We used this factor in our initial studies of the  $SNR$  comparison to our original baseline, but abandoned it upon establishing the new baseline and employing the intensity interferometer approach to  $SNR$ . If this factor is valid, then it could establish an additional advantage to entangled photon ghost imaging, assuming that such a source yields an approximate number state.

Another area warranting further study is incorporating a factor in the  $SNR$  calculation to represent the degradation in visibility as a function of the output beam brightness. This would allow us to determine an upper limit to the useful power one could use for a remote ghost imaging sensor.

Perhaps the most critical need for further work remains in the experimental area. Now that NGC has established its quantum imaging setup with the detection of second order correlation, it should (in collaboration with UMBC) continue to embark on ghost imaging experiments. These first should be performed with two entangled beams, and the predictions<sup>12</sup> for the location of the image plane, as given by the thin lens equation, and the resolution in terms of the ratio of the output wavelengths, should be tested. Subsequently, once a suitable source is identified, the experiments should be extended to three entangled beams. This would enable us to demonstrate the ability to obtain resolution enhancement in ghost imaging. The most important test would be a measurement of resolution for a diffusely reflecting object. If resolution enhancement is still observed it would show that the use of entangled beams offers some degree of immunity to the loss of a portion of the entangled photons. Once such measurements are performed on a lab bench we would return to the original notion of using our atmospheric optical path to perform ghost imaging with a remote target in free space, subject to a large degree of turbulence. This would provide the most convincing preliminary evidence that quantum states could provide an advantage for an imaging sensor in a militarily relevant environment. The generation of ghost images with high flux beams of entangled photons as well as the realization of ghost imaging with tri-photons (and resultant expected enhanced resolution) are both areas where further study is warranted.

Finally, the development of sources (whether based on hexagonally poled lithium tantalate as developed at UMBC or upon aperiodic gratings as conceived at NGC or on some other technology) will clearly be central to progress in the development of sensors based on entangled states. UMBC has also provided a prospective coupled quantum well

structure whose multi-photon absorption dynamics may be further studied experimentally.

## References

- <sup>1</sup> A. Einstein, B. Podolsky and N. Rosen, *Phys. Rev.*, **47**, 777 (1935).
- <sup>2</sup> M. Pelton et al., *Opt. Express* **12**, 3573 (2004) ; H. Guillet de Chatellus, A.V. Sergienko, B.E.A. Saleh, and M.C. Teich, *Opt. Express*, **14**, 10060 (2006) ; G. Ribordy et al, *Phys. Rev. A* **63**, 012309-1 (2001).
- <sup>3</sup> The Infrared Handbook (ed. By W.L. Wolfe and G.J. Zissis, The Information Analysis Center, Environmental Research Institute of Michigan, 1993), p. 8-32.
- <sup>4</sup> L.C. Andrews and R.L. Phillips, Laser Beam Propagation Through Random Media (SPIE, Bellingham, WA, 1998), p. 143.
- <sup>5</sup> C.W. Helstrom, *IEEE Trans. Info. Thy*, **IT-10**, 275 (1964).
- <sup>6</sup> A. Bhattacharyya, *Bull. Calcutta Math. Soc.*, **35**, 99 (1943).
- <sup>7</sup> J.H. Shapiro, *J. Opt. Soc. Am. A*, **16**, 53 (1999).
- <sup>8</sup> C.W. Helstrom, *IEEE Trans. Info. Thy*, **IT-19**, 389 (1973).
- <sup>9</sup> S.M. Kay, Fundamentals of Statistical Signal Processing: Detection Theory (Prentice Hall, NJ, 1998).
- <sup>10</sup> M. Shahram and P. Milanfar, *IEEE Trans. Info. Theory*, **52**, 3411 (2006)
- <sup>11</sup> J. Wen, M.H. Rubin, and Y. Shih, submitted to *Phys. Rev. A*.
- <sup>12</sup> M.H. Rubin and Y. Shih, *Phys. Rev. A*, **78**, 033836 (2008).
- <sup>13</sup> J.W. Goodman, Statistical Optics (J. Wiley & Sons, Inc, New York, 1985).
- <sup>14</sup> A. Valencia, G. Scarcelli, M. D'Angelo, and Y. Shih, *Phys. Rev. Lett.*, **94**, 063601 (2005).
- <sup>15</sup> C.W. Helstrom, Quantum Detection and Estimation Theory (Academic Press, NY, 1976).
- <sup>16</sup> D. Jackson et al., *J. Modern Opt.*, **49**, 2383 (2002).
- <sup>17</sup> C. Liang et al., *Opt. Express*, **15**, 1322 (2007); Q. Zhang et al., *Opt. Express* **15**, 10288 (2007).
- <sup>18</sup> R.L. Beyer and R.L. Herbst in Nonlinear Infrared Generation (Topics in Applied Physics, vol. 16, ed. by Y.-R. Shen, Springer-Verlag, Berlin), p.97 (1977).
- <sup>19</sup> Q. Zhang et al., *Opt. Express*, **15**, 10288 (2007).
- <sup>20</sup> G. Scarcelli, PhD thesis, UMBC (2006).
- <sup>21</sup> L.C. Andrews and R.L. Phillips, Laser Beam Propagation Through Random Media (SPIE, Bellingham, WA, 1998), p. 225.
- <sup>22</sup> H.A. Panofsky and J.A. Dutton, Atmospheric Turbulence, (Wiley, New York) p.122.
- <sup>23</sup> C.Y. Young, L.C. Anderson, and A. Ishimaru, *Appl. Opt.*, **37**, 7655 (1998).
- <sup>24</sup> C. Kim and G. Kanner, *Proc. SPIE*, **7092**, 709218 (2008).
- <sup>25</sup> R. Loudon, The Quantum Theory of Light (Oxford University Press, Inc, New York, 2000).
- <sup>26</sup> J. Wen, M.H. Rubin, and Y. Shih, submitted to *Phys. Rev. A*.
- <sup>27</sup> J.A. Perina, B.E.A. Saleh, and M.C. Teich, *Phys. Rev. A*, **57**, 3972 (1998).
- <sup>28</sup> J.G. Rarity, P.R. Tapster, and E. Jakeman, *Opt. Commun.*, **62**, 201 (1987).
- <sup>29</sup> S. Thanvantri and M.H. Rubin, *Phys. Rev. A*, **70**, 063811 (2004).
- <sup>30</sup> R. Hanbury Brown and R.Q. Twiss, *Proc. R. Soc. A*, **242**, 300 (1957).
- <sup>31</sup> J.W. Goodman, Statistical Optics (J. Wiley & Sons, Inc, New York, 1985).
- <sup>32</sup> R. Hanbury Brown, The Intensity Interferometer (Taylor & Francis, Ltd, London, 1974).
- <sup>33</sup> G. Scarcelli, PhD thesis, UMBC (2006).
- <sup>34</sup> M.P. Thekakara, *Optical Spectra*, **6**, 32 (1972).
- <sup>35</sup> H. Gamo, *J. Opt. Soc. Am.*, **56**, 441 (1966).
- <sup>36</sup> B.I. Erkmen and J.H. Shapiro, arXiv: 0809.4167v2.
- <sup>37</sup> M. D'Angelo et al., *Phys. Rev. A*, **72**, 013810 (2005).
- <sup>38</sup> S. Thanvanthri and M.H. Rubin, *Phys. Rev. A*, **70**, 063811 (2004).
- <sup>39</sup> O.A. Ivanova et al., *Quantum Electr.*, **36**, 951 (2006).
- <sup>40</sup> G. Scarcelli, PhD thesis, UMBC (2006).
- <sup>41</sup> J.W. Goodman, Speckle Phenomena in Optics: Theory and Applications (Roberts and Company, Greenwood Village, CO, 2007).
- <sup>42</sup> In these calculations we ignore scintillation, which causes optical beams to break up into coherent cells (see the referenced books by Goodman and by Andrews and Phillips).
- <sup>43</sup> A. Gatti, E. Brambilla and L.A. Lugiato, *Proc. SPIE*, **5161**, 192 (2004).
- <sup>44</sup> M.H. Rubin and Y. Shih, *Phys. Rev. A*, **78**, 033836 (2008).
- <sup>45</sup> R. Meyers, K.S. Deacon, and Y. Shih, *Phys. Rev. A*, **77**, 041801 (2008).
- <sup>46</sup> M. H. Rubin and Y. Shih, *Phys. Rev. A*, **78**, 033836 (2008).

- 
- <sup>47</sup> T. Kartoglu et al., *J. Opt. Soc. Am. B*, **20**, 343 (2003).
- <sup>48</sup> Okuda, T., Kishi, K., Sawada, K., *Applied Physics Letters*, **15**, 181-3 (1969).
- <sup>49</sup> Mortensen, O. S., *Molecular Physics*, **22**, 179-82 (1971).
- <sup>50</sup> G. Bastard, Wave Mechanics Applied to Semiconductor Heterostructures, New York: Wiley and Sons (1991).
- <sup>51</sup> B. Shanabrook, O. Glembocki, and D. Broido, *Phys. Rev. B*, **39**, 3411 (1989).
- <sup>52</sup> M. Watanabe, J. Yoshida, M. Mashita, T. Nakanishi, A. Hojo, *J. Appl. Phys.*, **57**, 5340 (1985).
- <sup>53</sup> Y. Varshni, *Physics (Utrecht)*, **34**, 149 (1967).
- <sup>54</sup> R. Pässler and G. Oelgart, *J. Appl. Phys.*, **82**, 2611 (1997).
- <sup>55</sup> Lee and Goodson, *Jour. Phys. Chem.*, **110**, 25582 (2006).
- <sup>56</sup> H. Fei, b. Jost, S. Popescu, B. Saleh, M. Teich, *Phys. Rev. Lett.*, **78**, 1679 (1997).
- <sup>57</sup> Morton H. Rubin and Yanhua Shih, *Phys. Rev. A*, **78**, 033836 (2008).
- <sup>58</sup> Jianming Wen, P. Xu, Morton H. Rubin, Yanhua Shih, *Phys. Rev. A*, **76**, 023828 (2007).
- <sup>59</sup> Jianming Wen, Morton H. Rubin, and Yanhua Shih, submitted to *Phys. Rev. A*, and arXiv:0812.2032v2 [quant-ph].
- <sup>60</sup> Jianming Wen and Morton H. Rubin, *Phys. Rev. A*, **79**, 025802 (2009).
- <sup>61</sup> E. Schrodinger, *Naturwissenschaften* **23**, 807 (1935); **23**, 823 (1935); **23**, 844 (1935).
- <sup>62</sup> D. M. Greenberger, M. Horne and A. Zeilinger, in Bell's Theorem, Quantum Theory, and Concepts of the Universe, ed. M. Kafatos (Kluwer, Dordrecht 1989).
- <sup>63</sup> M. A. Nielsen and I. L. Chuang, Quantum Computation and Quantum Information, (Cambridge University Press, Cambridge, 2000).
- <sup>64</sup> A. K. Ekert, *Phys. Rev. Lett.*, **67**, 661 (1994); N. Gisin, G. Ribordy, W. Tittel and H. Zbinden, *Rev. Mod. Phys.*, **74**, 145 (2002).
- <sup>65</sup> D. Bouwmeester, J. W. Pan, M. Daniell, H. Weinfurter, and A. Zeilinger, *Phys. Rev. Lett.* **82**, 1345 (1999); Z. Zhao, T. Yang, Y.-A. Chen, A.-N. Zhang, M. Zukowski, and J.-W. Pan, *Phys. Rev. Lett.*, **91**, 180401 (2003); K. J. Resch, P. Walther, and A. Zeilinger, *Phys. Rev. Lett.*, **94**, 070402 (2005); Z. Zhao, Y.-A. Chen, A.-N. Zhang, T. Yang, H. J. Briegel and J.-W. Pan, *Nature*, **430**, 54 (2004).
- <sup>66</sup> M. Eibl, N. Kiesel, M. Bourennane, C. Kurtsiefer, and H. Weinfurter, *Phys. Rev. Lett.*, **92**, 077901 (2004); H. Weinfurter and M. Zukowski, *Phys. Rev. A*, **64**, 010102 (2001); H. Mikami, Y. Li, and T. Kobayashi, *Phys. Rev. A*, **70**, 052308 (2004).
- <sup>67</sup> T.E. Keller, M.H. Rubin, Y.H. Shih and L.A. Wu, *Phys. Rev. A*, **57** 2076 (1998).
- <sup>68</sup> D. N. Klyshko, Photons and Nonlinear Optics, (Gordon and Breach, New York, 1988); Y.H. Shih, *Rep. Prog. Phys.*, **66**, 1009 (2003); L. Mandel, *Rev. Mod. Phys.*, **71**, S274 (1999).
- <sup>69</sup> J. Armstrong, et al., *Phys. Rev.*, **127**, 1918 (1962); P. A. Franken and J. F. Ward, *Rev. Mod. Phys.*, **35**, 23 (1963).
- <sup>70</sup> N. G. R. Broderick, et al., *Phys. Rev. Lett.*, **84**, 4345 (2000); P. Xu, S. H. Ji, S. N. Zhu, et al., *Phys. Rev. Lett.*, **93**, 133904 (2004).
- <sup>71</sup> M. Dangelo, Y.-H. Kim, S. P. Kulik, and Y.H. Shih, *Phys. Rev. Lett.*, **92**, 233601 (2004).
- <sup>72</sup> Y. Zhou, P. Xu, et al., (in preparation).

## List of Acronyms

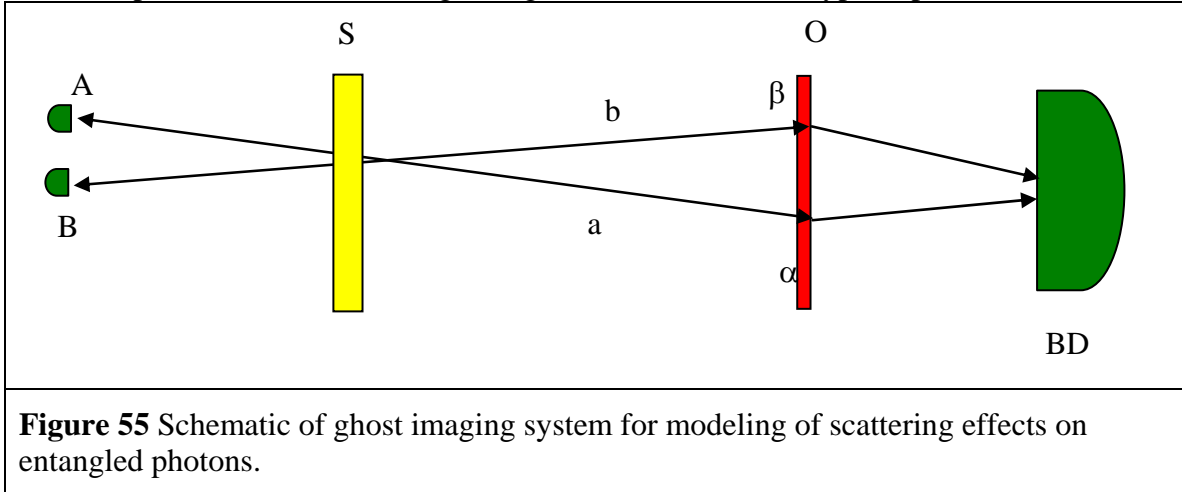
AlInAs: Aluminum Indium Arsenide (a III-V compound semiconductor)  
 AlSb: Aluminum Antimonide (a III-V compound semiconductor)  
 APD: Avalanche Photo Diode  
 AR: Anti-Reflection  
 ARL: Army Research Laboratory  
 BAA: Broad Agency Announcement  
 BD: Bucket Detector  
 BPF: Band Pass Filter  
 CAR: Coincidence to Accidental Ratio  
 CM: Cold Mirror  
 CW: Continuous Wave (as opposed to pulsed)  
 DARPA: Defense Advanced Research Projects Agency  
 EPR: Einstein, Podolsky and Rosen  
 ETPA: Entangled Two-Photon Absorption  
 FFT: Fast Fourier Transform  
 FPA: Focal Plane Array (an optical detector)  
 GaAlAs: Gallium Aluminum Arsenide (a III-V compound semiconductor)  
 GaAs: Gallium Arsenide (a III-V compound semiconductor)  
 GaInAs: Gallium Indium Arsenide (a III-V compound semiconductor)  
 GaInAsP: Gallium Indium Arsenide Phosphide (a III-V compound semiconductor)  
 GHZ: Greenberger-Horne-Zeilinger (a class of entangled states)  
 GLAD: General Laser Analysis and Design (software package)  
 GTLE: Gaussian Thin Lens Equation  
 HexPLT: Hexagonally Poled Lithium Tantalate ( $\text{LiTaO}_3$ ...a non-linear crystal)  
 InP: Indium Phosphide (a III-V compound semiconductor)  
 IR&D: Internal Research and Development  
 KTP: Potassium Titanyl Phosphate (a non-linear crystal)  
 MAP: Maximum *a priori* Probability  
 MBE: Molecular Beam Epitaxy  
 MCT: Mercury Cadmium Telluride ( $\text{HgCdTe}$ , an infrared detector material)  
 MTF: Modulation Transfer Function  
 ND: Neutral Density (describes an element whose loss is invariant with wavelength)  
 NEC: Noise Equivalent Counts  
 NGC: Northrop Grumman Corporation  
 NGES: Northrop Grumman Electronic Systems (a sector of NGC)  
 Nd:YAG: Neodymium doped Yttrium Aluminum Garnet Crystal (a laser gain medium)  
 NLO: Non-Linear Optical  
 NOON: A class of entangled states ( $|N,0\rangle\langle 0,N|$ )  
 ONB: Ortho-Normal Basis  
 OPG: Optical Parametric Generation  
 POVM: Positive Operator Valued Measures  
 PPLN: Periodically Poled Lithium Niobate ( $\text{LiNbO}_3$ )  
 PSF: Point Spread Function  
 QPM: Quasi-Phase Matched

QSP: Quantum Sensors Program  
SFG: Sum Frequency Generation  
SHG: Second Harmonic Generation  
Si: Silicon  
SNR: Signal to Noise Ratio  
SPDC: Spontaneous Parametric Down-Conversion  
SPIE: Society of Photo-Optical Instrumentation Engineers  
STO: Strategic Technology Office  
THz: Terahertz ( $10^{12}$  cycles per second)  
TPA: Two-Photon Absorption  
UMBC: University of Maryland, Baltimore County



## Appendix A Effect of Scattering on Ghost Imaging

We briefly discuss ghost imaging to provide a concrete model of our general discussion. In Figure 55 we illustrate the essential features of ghost imaging. The source  $S$  emits pairs of entangled photons, one photon is detected in a focal plane array (FPA) and its twin is detected by the bucket detector BD after it scatters off the object  $O$ . In Figure 55, we have shown two pairs: for the first pair, one photon is detected at  $A$  and its twin  $a$  scatters at  $\alpha$ , for the second pair, one photon is detected at  $B$  and its twin  $b$  scatters at  $\beta$ . The detection in the FPA determines the transverse wave vector of the photon within the limits set by diffraction. If there is a coincidence with the firing of  $BD$  and  $A$ , we know that the twin has scattered from  $\alpha$ . Recall that timing discrimination is such that only one pair at a time can be detected. If the twin is not detected there is no coincidence. Similarly for  $B$  and  $b$ . Now suppose that a pair  $A$ - $a$  is emitted and that between  $S$  and  $O$  the photon  $a$  is scattered, for example by fluctuations in the index of refraction, so that it scatters off of  $\beta$  and is detected in  $BD$ . In this case when  $A$  fires we get an error although the entanglement has not necessarily been destroyed. Note that if there is scattering between  $O$  and  $BD$  no error is introduced because the detector  $BD$  does not discriminate between pairs. We now want to give a general model for this type of process.



A pure state of a bipartite system, a system composed of two subsystems, can always be written in the form

$$|\Psi\rangle = \sum_j c_j |\phi_j\rangle |\chi_j\rangle \quad (45)$$

where  $\{|\phi_j\rangle, j=1, \dots\}$  and  $\{|\chi_j\rangle, j=1, \dots\}$  are orthonormal bases of states (ONB), and  $\sum_j |c_j|^2 = 1$ . The state is *separable* if only one  $c_j$  is non-vanishing, otherwise, the state is *entangled*. The summation is symbolic and may be an integral. For example, the wave function for a bi-photon produced by a monochromatic pump of angular frequency  $\omega_p$  may be written as

$$|\Psi\rangle = \int d\varpi \int d^2\kappa c(\varpi, \vec{\kappa}) |\varpi, \vec{\kappa}\rangle |\varpi_p - \varpi, -\vec{\kappa}\rangle \quad (46)$$

where  $\{|\varpi, \vec{\kappa}\rangle, \varpi > 0\}$  is a set of one photon states with angular frequency  $\omega$ , wave

number,  $\vec{k} = \hat{e}_z \sqrt{\frac{\omega^2}{c^2} - \kappa^2} + \vec{\kappa}$  and normalization

$$\langle \varpi, \vec{\kappa} | \varpi', \vec{\kappa}' \rangle = (2\pi)^3 \delta(\varpi - \varpi') \delta(\vec{\kappa} - \vec{\kappa}').$$

### Simple Model of Measurement

Now suppose that the subsystems are transformed separately so

$$\begin{aligned} |\Psi\rangle &\rightarrow |\Psi'\rangle = \sum_j c_j |\phi'_j\rangle |\chi'_j\rangle \\ |\phi'_j\rangle &= U |\phi_j\rangle \quad |\chi'_j\rangle = V |\chi_j\rangle \end{aligned} \quad (47)$$

where  $U$  and  $V$  are unitary transformations, then  $|\Psi'\rangle$  is entangled and has the same degree of entanglement as  $|\Psi\rangle$ . This follows from the fact that unitary transformations map ONB onto ONB. Suppose we want to obtain information about the set  $\{|\chi'_j\rangle, c_j \neq 0\}$  (in ghost imaging, the second subsystem contains information of interest about the object). To do this we make projective measurements of correlations between the two subsystems. The set of projections is given by

$$\{P_{\alpha\beta} = |\alpha\rangle\langle\alpha| \otimes |\beta\rangle\langle\beta|\} \quad (48)$$

where  $\{|\alpha\rangle\}$  and  $\{|\beta\rangle\}$  are ONB for subsystem 1 and 2, respectively. If we make a measurement then the probability of the outcome being  $(\alpha, \beta)$  is

$$p_{\alpha\beta} = \langle \Psi' | P_{\alpha\beta} | \Psi' \rangle = \sum_j |c_j|^2 |\langle \alpha | \phi'_j \rangle|^2 |\langle \beta | \chi'_j \rangle|^2. \quad (49)$$

If the set  $\{|\alpha\rangle = |\phi'_\alpha\rangle\}$  we get

$$p_{\alpha\beta} = |c_\alpha|^2 |\langle \beta | \chi'_\alpha \rangle|^2 = |c_\alpha|^2 |\langle \beta | V | \chi_\alpha \rangle|^2; \quad (49a)$$

therefore, we can obtain information about the scattering from the second system.

More generally, suppose that

$$|\alpha\rangle = \sqrt{b_\alpha} |\phi'_\alpha\rangle + |\zeta_\alpha\rangle \quad (50)$$

where  $\langle \phi'_\alpha | \zeta_\alpha \rangle = 0$ , then a measurement with the outcome  $(\alpha, \beta)$  has probability

$$p'_{\alpha\beta} = b_{\alpha} p_{\alpha\beta} + n_{\alpha\beta} \quad (51)$$

where the first term is the signal with  $p_{\alpha\beta}$  given by Eq. (49a) and the noise term is

$$n_{\alpha\beta} = \sum_{j \neq \alpha} |c_j|^2 \left| \langle \zeta_{\alpha} | \phi_j' \rangle \right|^2 \left| \langle \beta | \chi_j' \rangle \right|^2. \quad (52)$$

In summary, we can obtain information about the scattering of the second subsystem by making a correlation measurement with the first subsystem. If we assume that we know the state of the first subsystem perfectly, then we can project the scattered subsystem onto a set of known states and determine the probability distributions  $p_{\alpha\beta}$ . In the ghost imaging case this corresponds to measuring the intensity distribution of the light scattered from the object, and the non-ideal case modeled by Eq. (50) corresponds to the case that detection in the state  $|\zeta_{\alpha}\rangle$  occurs because the twin photon has been scattered by atmospheric variation of the index of refraction. The formulation just given in terms of projective measurements is not the most general formulation of the problem. It is useful to give the more general picture.

### General Model of Measurement

The simple picture does not illustrate what really happens in laboratories in a clear way. We need to take into account the fact that we are not interested in the entire wave function. For example, in order to form an image using a light beam, we only detect part of the light coming from the source because it is necessary that the object being imaged absorb or scatter some of the incident light. From the point of view of the detection, there is loss. Loss due to absorption simply reduces the counting rate since if one of the subsystems is not detected there is no correlation measurement. The source of noise we consider here occurs when scattering generates false correlations such as illustrated in Eq. (50).

To model the measurement process more exactly we consider the most general form of measurement based on positive operator valued measures (POVM). In the simplest case, a POVM is a set of positive operators  $S = \{E_{\alpha} = M_{\alpha}^{\dagger} M_{\alpha}, \alpha = 0, 1, \dots, N\}$  that satisfy the condition

$$\sum_{\alpha=0}^N E_{\alpha} = I \quad (53)$$

where  $I$  is the identity operator on the Hilbert space,  $H$ , of interest. We have used the fact that any positive operator,  $E_{\alpha}$ , can be written as the product of another operator,  $M_{\alpha}$ , and its Hermitian adjoint,  $M_{\alpha}^{\dagger}$ . For simplicity we label the measurements with discrete indices. The standard projective measurements are a special case of this; however, the more general case allows us to model experiments in which, for example, one photon of a two photon state is absorbed. If the state of a system in  $H$  is described by a density matrix  $\rho$  is measured using the POVM (B.9), the probability of getting the result  $\alpha$  is

$$p_{\alpha} = \text{tr}[E_{\alpha} \rho]. \quad (54)$$

Because  $E_\alpha$  is a positive operator,  $p_\alpha > 0$  (note that if  $p_\alpha = 0$  then we never get the outcome  $\alpha$ ), and Eq. (48) ensures that the set  $\{p_\alpha\}$  is a probability distribution. After the measurement the state of the system is given by

$$\rho \rightarrow \rho_\alpha = \frac{M_\alpha \rho M_\alpha^\dagger}{p_\alpha}, \quad (55)$$

A projective measurement corresponds to the case where the set  $S$  is composed of orthogonal projections, *i.e.*  $E_\alpha \rightarrow P_\alpha$  where  $P_\alpha P_\beta = \delta_{\alpha\beta} P_\alpha$ . For a POVM, the operators  $E_\alpha$  need not be orthogonal.

We will be interested in the case

$$E_\alpha = A_\alpha \otimes B_\alpha \quad (56)$$

where  $\{A_\alpha\}$  and  $\{B_\alpha\}$  are POVM that operate on subsystem one and two, respectively. Now consider the system to be in the state Eq. (45) and a measurement using the POVM  $S$  that gives the outcome  $\alpha$ . Then

$$p_\alpha = \langle \Psi | E_\alpha | \Psi \rangle = \sum_{jk} c_j^* c_k \langle \phi_j | A_\alpha | \phi_k \rangle \langle \chi_j | B_\alpha | \chi_k \rangle. \quad (57)$$

We have absorbed the propagation from the source to the detector into the measurement operators. Eq. (56) is too general for most purposes so we will now specialize it keeping in mind the application to ghost imaging. To this end, we shall assume that the measurement outcome  $\alpha$  projects onto a state such that

$$\langle \phi_j | A_\alpha | \phi_k \rangle = \delta_{jk} a_{j\alpha}. \quad (58)$$

In the ghost imaging case this corresponds to a measurement in which when one pixel in the focal plane array (FPA) is excited with a transverse momentum vector that is determined within a small uncertainty. If we assign an operator

$$A_\alpha = \sum_j a_{j\alpha} |\phi_j\rangle \langle \phi_j|, \quad 0 < a_{j\alpha} \leq 1 \quad (59)$$

for  $\alpha = 1, \dots, N$ , then  $A_0 = I - \sum_{\alpha=1}^N A_\alpha$  corresponds to no pixel being excited. The summation over  $j$  in (59) allows for the fact that there may be some uncertainty in which state excites the pixel, in the ideal case there will only be one term. In an experiment the overlap in the transverse momenta corresponding different  $\alpha$  is small. With assumption (58), Eq. (57) becomes

$$p_\alpha = \sum_j |c_j|^2 a_{j\alpha} \langle \chi_j | B_\alpha | \chi_j \rangle. \quad (60)$$

Now let us assume that

$$\begin{aligned} B_\alpha &= \sum_j t |\chi_j\rangle \langle \chi_j| t^\dagger = B, \alpha = 1, \dots, N \\ B_0 &= I_2 - \sum_{\alpha=1}^N B_\alpha = I_2 - NB \end{aligned} \quad (61)$$

where  $I_2$  is the identity operator on the Hilbert space of the second subsystem. To understand the meaning of this last assumption, suppose we only measure subsystem two and ignore subsystem one. Then for  $\alpha = 1, \dots, N$ , we get

$$\langle \Psi | I_1 \otimes B | \Psi \rangle = \sum_j |c_j|^2 \left| \langle \chi_j | t | \chi_j \rangle \right|^2. \quad (62)$$

Comparing this to (A.16)

$$p_\alpha = \sum_j |c_j|^2 a_{j\alpha} \left| \langle \chi_j | t | \chi_j \rangle \right|^2 \quad (62a)$$

we see that, because of our assumption about the  $a_{j\alpha}$ , information is lost if we do not make the coincidence measurement. This is particularly clear in the ideal case  $a_{j\alpha} = a_j \delta_{j\alpha}$  where only one term appears in (A.16a). The assumption in Eq. (61) may be thought of as modeling a bucket detector in the ghost imaging. Recall that the bucket detector only tells us if light scattered from an object is detected but gives no details of the image.

Finally, let us see how noise can occur in this picture. We now assume that subsystem two undergoes the transformation in which  $|\chi_j\rangle$  scatters into the correctly correlated state with probability  $b_j$ , into an incorrectly correlated state with probability  $q_r$ , and a state that is not detected  $|\zeta_{jr}\rangle$ ,

$$|\chi_j\rangle \rightarrow \sqrt{b_j} t |\chi_j\rangle + \delta t_r |\chi_j\rangle + |\zeta_{jr}\rangle, \quad (63)$$

(in general  $b_j$  may also depend on  $r$ ).

In this case we can write

$$B_\alpha = \sum_j b_j t |\chi_j\rangle \langle \chi_j| t^\dagger + \sum_{r,j} q_r \delta t_r |\chi_j\rangle \langle \chi_j| \delta t_r^\dagger, \quad \alpha = 1, \dots, N. \quad (64)$$

In the ghost imaging case the second term in (A.19) may be thought of as scattering due to index of refraction fluctuations in the path between the source-object-detector. Now a measurement with outcome  $\alpha$  occurs with probability

$$\begin{aligned}
p'_\alpha &= s_\alpha + n_\alpha, \quad \alpha = 1, K, N \\
s_\alpha &= \sum_j b_j |c_j|^2 a_{j\alpha} \left| \langle \chi_j | t | \chi_j \rangle \right|^2 . \\
n_\alpha &= \sum_{j,r} q_r |c_j|^2 a_{j\alpha} \left| \langle \chi_j | \delta t_r | \chi_j \rangle \right|^2
\end{aligned} \tag{65}$$

In conclusion, we see that the correlation due to the entanglement appears as the signal and will be detectable provided the noise is not too great. In this discussion, we have only included noise generated due to scattering effects that may not necessarily degrade the entanglement of the pairs detected. We also wish to emphasize that losses, characterized by  $B_0$ , only affect the counting rate not the signal to noise ratio.

## Appendix B Imaging with Non-Degenerate Bi-Photons

We consider the ghost imaging systems shown in Figure 56. Figure 56 (Upper) is the one of interest to us here. Figure 56 (Lower) is the original ghost imaging configuration. In both cases a pump from a laser is incident on a crystal that produces entangled photon pairs (bi-photons). One of the photons, called the signal photon, scatters from the object and is detected by detector A. A point detector B located in the image plane detects the second photon, called the idler photon. The signals from the two detectors go to a coincidence counter. The point detector scans the image plane or can be an array of point detectors. Detector A is called a bucket detector and collects all scattered light incident on it. For the system of interest, the distances  $D_s$  and  $L_s$  will in general be of order 1-10 km. The arm in which the imaging lens is placed differs in the two systems. In Figure 56 (Upper), a beam expander is used to produce a collimated beam that is aimed at the

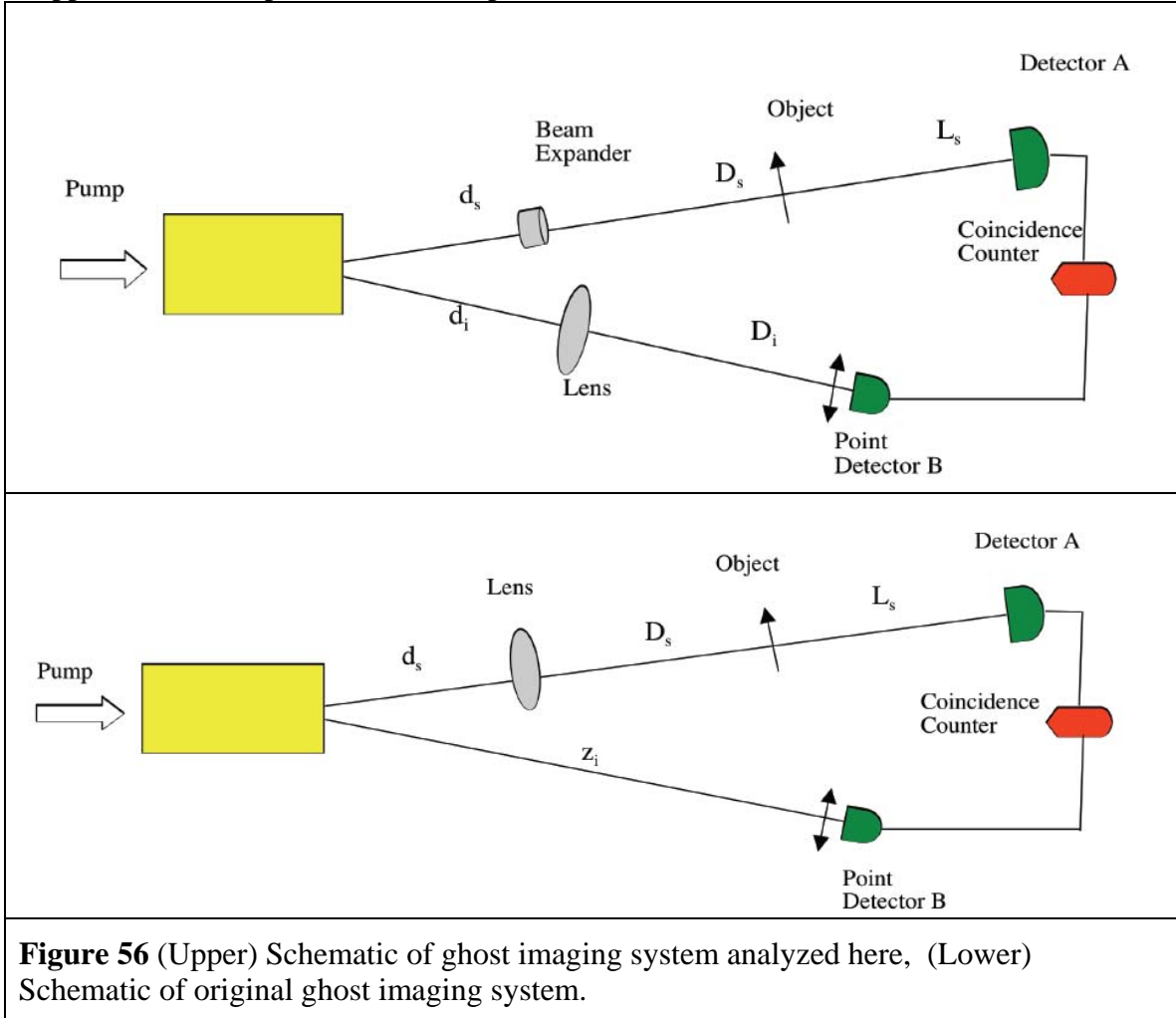


**Figure 56** (Upper) Schematic of ghost imaging system analyzed here, (Lower) Schematic of original ghost imaging system.

object. The bi-photon source, detectors, lens, beam expander, and coincident counter will be located in the laboratory. The image plane is determined by a Gaussian lens formula, Equation (83) (below) and the Airy disk depends on the idler wavelength, Equation (89). However, the resolution of two points on the object depends on the signal

wavelength, Equation (90); consequently, the system discussed here does not lead to improved resolution over the classical case.

This Appendix is organized as follows: first we formulate the coincident counting rate in terms of the fields at the detectors, then we compute these fields, finally we compute the minimum transverse distance on the target that can be resolved. We shall discuss the system shown in Fig. 56 (Upper).

The coincident counting rate may be written as

$$C = \frac{1}{T} \iint dt_A dt_B S(t_B, t_A) \int_{\alpha_A} d^2 \rho_A \alpha_B G_{AB} \quad (66)$$

where  $S$  is the coincident time window that vanishes unless  $0 \leq t_B - t_A < T$ ,  $\alpha_A$  is the area of the bucket detector,  $\alpha_B$  is the area of the point detector,

$$G_{AB} = \text{tr} [E_A^{(-)} E_B^{(-)} E_B^{(+)} E_A^{(+)} \rho], \quad (67)$$

$\rho$  is the quantum mechanical state of the electromagnetic field on the output face of the crystal and, for  $j=A$  or  $B$ ,  $E_A^{(+)}(\vec{r}_j, t_j)$  is the positive frequency part of the electric field at the point  $\vec{r}_j$  evaluated at time  $t_j$  and  $E_j^{(-)} = (E_j^{(+)})^H$ , where the superscript  $H$  denotes the Hermitian adjoint. It is convenient to use electric fields with dimensions so that  $E^H E$  is a photon number flux. We will ignore the polarization of the photons but adding it in is not difficult. The detailed expression for the fields at the detectors will be given below.

For the case in which the output of the crystal is a sequence of non-overlapping biphotons, we can write  $G_{AB} = |\aleph_{AB}|^2$  in terms of the bi-photon amplitude

$$\aleph_{AB} = \langle 0 | E_B^{(+)} E_A^{(+)} | \Psi \rangle, \quad (68)$$

Where  $|0\rangle$  is the vacuum state and  $|\Psi\rangle$  is the bi-photon state vector.

We begin by computing the field at detector  $B$ ,

$$E_B^{(+)} = \sqrt{\frac{c}{2V_Q}} \sum_{\vec{k}} a_B(\vec{k}) e^{-i\omega t_B}, \quad (69)$$

where  $c$  is the speed of light in the atmosphere,  $V_Q$  is the quantization volume, and the operator  $a_B(\vec{k})$  destroys a photon with a wave vector  $\vec{k}$  at point  $B$ , and  $\omega = kc$ . We shall omit the factor  $\sqrt{c/2V_Q}$  in what follows. It is easy to restore it at the end of the calculation. In order to compute the bi-photon amplitude defined in Equation (68), it is necessary to express the field in terms of the destruction operator at the surface of the crystal. We write



$$E_B^{(+)} = \sum_{\vec{k}} g(\vec{k}, \omega, \vec{\rho}_B, z_i) a_i(\vec{k}) e^{-i\omega t_B}, \quad (70)$$

where  $a_i(\vec{k})$  is the destruction operator for an idler photon of wave number  $\vec{k}$  at the output surface of the crystal,  $g$  is the optical transfer function that can be computed using classical optics, and

$$[a_n(\vec{k}), a_m^H(\vec{k}')] = \delta_{\vec{k}, \vec{k}'} \delta_{mn}. \quad (71)$$

In writing out the transfer function, it is convenient to introduce coordinates  $\vec{r} = z\hat{e}_z + \vec{\rho}$ , where the unit vector  $\hat{e}_z$  points along the path through the center of the optical system and  $\vec{\rho}$  is a two dimensional vector perpendicular to the path. Using the thin lens formula, one can show that

$$E_B^{(+)} = \sum_{\vec{k}} \psi\left(\vec{\rho}_B, \frac{k}{D_i}\right) \left[ \int d^2 \rho_L \psi\left(\rho_L, k\left(\frac{1}{D_i} - \frac{1}{f}\right)\right) \exp\left(i\left(\vec{k} - k\frac{\vec{\rho}_B}{D_i}\right) \cdot \vec{\rho}_L\right) P_L(\vec{\rho}_L) \right] \times \frac{1}{i\lambda D_i} \exp[i(kz_i - \omega t_B)] \psi\left(\kappa, -\frac{d_i}{k}\right) a_i(\vec{k}), \quad (72)$$

where  $z_i = d_i + D_i$ . The physics of Equation (72) may be understood by noting that the term in square brackets expresses the scattering of a plane wave with wave number  $\vec{k} = \sqrt{k^2 - \kappa^2} \hat{e}_z + \vec{\kappa} \approx k\hat{e}_z + \vec{\kappa}$  incident on a thin lens into a wave with transverse wave number  $k\vec{\rho}_B/D_i$ . The output wave then propagates to the detector. The remaining terms in Equation (72) arise from the propagation of the plane wave created at the crystal surface to the input face of the lens. Using a similar analysis, with the object described by a transparency function,  $t(\vec{\rho})$ , it can be shown that

$$E_A^{(+)} = \sum_{\vec{k}} \psi\left(\rho_A, \frac{k}{L_s}\right) \left[ \int d\rho_a \psi\left(\rho_a, \frac{k}{L_s}\right) t(\vec{\rho}_a) \exp\left(-i\left(k\frac{\vec{\rho}_A}{L_s} + \vec{\kappa} \frac{f_1}{f_2}\right) \cdot \vec{\rho}_a\right) \right] \times \frac{1}{i\lambda L_s} \frac{f_1}{f_2} \exp[i(kz_s - \omega t_A)] \psi\left(\kappa, \frac{P - d_s}{k}\right) a_s(\vec{k}), \quad (73)$$

where  $P = \frac{f_1^2}{f_2^2} \left(-D_s + f_2 + \frac{f_2^2}{f_1}\right)$ , and  $f_1$  and  $f_2$  are the focal lengths of the input and output lenses of the beam expander. We assume that the lens aperture  $P_L$  is the limiting aperture function for the entire system.

### Bi-photon Imaging

We are now in a position to compute the bi-photon amplitude. For the case of interest, the system is constructed so that we may take

$$E_j^{(+)} = e^{i(K_j z_j - \Omega_j t_j)} e_j^{(+)}(\vec{\rho}_j, t_j), \text{ for } j=A, B. \quad (74)$$

Where  $e_j^{(+)}$  is slowly varying on the length and time scales,  $1/K_j$  and  $1/\Omega_j$ . This allows us to make the several simplifying approximations. For the signal field in arm A of the system, we take

$$\begin{aligned} \varpi &= \Omega_s + \nu_s \\ \vec{k} &= \vec{\kappa}_s + \sqrt{\frac{(\Omega_s + \nu_s)^2}{c^2} + \kappa_s^2} \hat{e}_z = \vec{\kappa}_s + \left( K_s + \frac{\nu_s}{c} + \Delta k_z \right) \hat{e}_z \\ K_s &= \frac{\Omega_s}{c} \\ \Delta k_z &= \frac{\nu_s}{c} \frac{\nu_s}{\Omega_s} + \frac{\kappa_s^2}{2K_s} + \dots \end{aligned} \quad (75)$$

where we can drop the term  $\Delta k_z$ . Frequency filtering ensures that  $\nu_s/\Omega_s$  is sufficiently small so that terms containing it can be ignored. Similarly, spatial filtering ensures that  $\kappa_s/K_s$  is also sufficiently small to be ignored. In arm B, we make the same approximations where the subscript becomes  $i$  for idler. We can now write

$$\begin{aligned} \aleph_{AB} &= -\frac{K_s K_i}{(2\pi)^2 D_i L_s} \exp[i(K_s z_s + K_i z_i - \Omega_s t_A - \Omega_i t_B)] \aleph' \\ \aleph' &= \sum_{\vec{k}_s, \vec{k}_i} g_A(\vec{\rho}_A, \nu_s, \vec{\kappa}_s) g_B(\vec{\rho}_B, \nu_i, \vec{\kappa}_i) \langle 0 | a_s(\vec{k}_s) a_i(\vec{k}_i) | \Psi \rangle \end{aligned} \quad (76)$$

where  $g_A$  and  $g_B$  are slowly varying functions determined from Equations (72) and (73). Note that we must keep the  $\nu$ 's in the time factor of the exponential expressions. It is convenient to replace the summations by integrals in the standard fashion.

$$\begin{aligned} \sum_{\vec{k}_s} &\rightarrow \frac{V_Q}{(2\pi)^3} \int d^3 k_s \rightarrow \frac{V_Q}{(2\pi)^3} \int d^2 \kappa_s \int d\nu_s \frac{dk_{sz}}{d\omega_s} \rightarrow \frac{V_Q}{(2\pi)^3 c} \int d^2 \kappa_s \int d\nu_s \\ \frac{dk_{sz}}{d\omega} &= \frac{\omega_s}{k_{sz}} \cong \frac{\Omega_s}{K_s} = \frac{1}{c} \end{aligned} \quad (77)$$

and similarly for the idler. In a similar fashion, going from discrete indices to continuous indices, we have

$$\begin{aligned} \sqrt{\frac{V_0}{c}} a_s(\vec{k}_s) &\rightarrow a_s(\vec{k}_s, v_s) \\ [a_s(\vec{k}_s, v_s), a_s^H(\vec{k}'_s, v'_s)] &= (2\pi)^3 \delta(\vec{k}_s - \vec{k}'_s) \delta(v_s - v'_s) \end{aligned} \quad (78)$$

The idler terms are treated similarly.

We take the simplest model for the bi-photon. A plane wave pump of angular frequency  $\omega_p$  and wave vector  $k_p \hat{e}_z$  propagates in crystal of length  $L$ , then it can be shown that

$$\begin{aligned} \langle 0 | a_s(\vec{k}_s, v_s) a_i(\vec{k}_i, v_i) | \Psi \rangle &= -i(2\pi)^3 \gamma \delta(\omega_p - \Omega_s - \Omega_i - v_s - v_i) \delta(\vec{k}_s + \vec{k}_i) \sin c\left(\frac{\Delta k_z L}{2}\right) \\ &= -i(2\pi)^3 \gamma \delta(v_s + v_i) \delta(\vec{k}_s + \vec{k}_i) \sin c\left(\frac{v_s d_{si} L}{2}\right) \end{aligned} \quad (79)$$

where  $\gamma$  is a dimensionless constant,  $D_{si} = \frac{1}{u_s} - \frac{1}{u_i}$  and  $u_s$  ( $u_i$ ) is the group velocity of the signal (idler) photon inside the crystal. The filters are chosen so that  $\Omega_s + \Omega_i = \omega_p$  and  $\Omega_s n_s(\Omega_s) + \Omega_i n_i(\Omega_i) = ck_p$ , where  $n_j$  is the index of refraction for  $j=s$  and  $i$ . In this case the temporal and the transverse terms factor and we have

$$\aleph' = \left[ -i\gamma \int dv_s e^{iv_s \tau_{AB}} \sin c(v_s D_{si} L/2) \right] V(\vec{\rho}_A, \vec{\rho}_B). \quad (80)$$

To compute  $V$ , we first do the integrals over the  $\vec{k}$ 's. Evaluating the integral over  $\vec{k}_i$  using Equations (72) and (73) gives  $\vec{k}_i = -\vec{k}_s$  so that we may obtain

$$\begin{aligned} \int d^2 \kappa_s \psi\left(\kappa_s, \frac{P-d_s}{K_s} - \frac{d_i}{K_i}\right) \exp\left[-i\left(\vec{k}_s \bullet \left(\vec{\rho}_L + \vec{\rho}_a \frac{f_1}{f_2}\right)\right)\right] &= \frac{1}{i\lambda_s R_s} \psi\left(\left|\vec{\rho}_L + \vec{\rho}_a \frac{f_1}{f_2}\right|, \frac{K_s}{R_s}\right) \\ R_s = (d_s - P) + \frac{\lambda_i}{\lambda_s} d_i &= -\frac{f_1^2}{f_2} \left(1 + \frac{f_2^2}{f_1^2}\right) + \left(\frac{f_1^2}{f_2^2} D_s + d_s\right) + \frac{\lambda_i}{\lambda_s} d_i \end{aligned} \quad (81)$$

where  $R_s$  is the optical path length from the lens to the object in the sense that  $k_s R_s$  is the phase change that a plane wave would acquire in traveling from the lens to the object. If the beam expander is not present,  $R_s = D_s + d_s + \frac{\lambda_i}{\lambda_s} d_i$ . Now, substituting Equation (81)

into the equation for  $V$  gives

$$V(\vec{\rho}_A, \vec{\rho}_B) = \frac{1}{i\lambda_s R_s} \psi\left(\rho_A, \frac{K_s}{L_s}\right) \psi\left(\rho_B, \frac{K_i}{D_i}\right) \int d^2 \rho_a t(\vec{\rho}_a) \psi\left(\rho_a, K_s \left(\frac{1}{L_s} + \frac{f_1}{f_2} \frac{1}{R_s}\right)\right) e^{-iK_s \vec{\rho}_A \bullet \vec{\rho}_a / L_s} \times$$

$$\int d^2 \rho_L \psi\left(\rho_L, \frac{K_s}{R_s} + K_i \left(\frac{1}{D_i} - \frac{1}{f}\right)\right) \exp\left[iK_s \left(\frac{\vec{\rho}_a}{R_s} \frac{f_1}{f_2} - \frac{\vec{\rho}_B}{D_i} \frac{\lambda_s}{\lambda_i}\right) \bullet \vec{\rho}_L\right] P_L(\vec{\rho}_L) \quad (82)$$

Using the imaging condition

$$\frac{\lambda_i}{\lambda_s} \frac{1}{R_s} + \frac{1}{D_i} = \frac{1}{f} \quad (83)$$

gives

$$V(\vec{\rho}_A, \vec{\rho}_B) = \frac{1}{i\lambda_s R_s} \psi\left(\rho_A, \frac{K_s}{L_s}\right) \psi\left(\rho_B, \frac{K_i}{D_i}\right) \times$$

$$\int d^2 \rho_a \tilde{P}_L\left(K_s \left(\frac{\vec{\rho}_a}{R_s} \frac{f_1}{f_2} - \frac{\vec{\rho}_B}{D_i} \frac{\lambda_s}{\lambda_i}\right)\right) t(\vec{\rho}_a) \psi\left(\rho_a, K_s \left(\frac{1}{L_s} + \frac{f_1}{f_2} \frac{1}{R_s}\right)\right) e^{-iK_s \vec{\rho}_A \bullet \vec{\rho}_a / L_s} \quad (84)$$

Where  $\tilde{P}_L(\vec{\kappa})$  is the Fourier transform of  $P_L(\vec{\rho})$ . If the lens aperture is infinite then  $\tilde{P}_L(\vec{\kappa}) \approx \delta(\vec{\kappa})$  and  $V \approx t\left(\vec{\rho}_B \frac{R_s}{D_i} \frac{f_2}{f_1} \frac{\lambda_s}{\lambda_i}\right) = t\left(\frac{\vec{\rho}_B}{m}\right)$  so the magnification,  $m$ , depends on the ratio of the wavelengths.

In order to give some more insight into these results, we consider an unfolded version of Figure 56 (Upper), which was developed by David Klyshko. In the Klyshko picture (shown in Figure 57), the source is shown to emphasize that the ideal phase matching condition corresponds to transverse wave number conservation which can be represented as a ray passing through the system. The object distance has been weighted with an effective index of refraction and we omit the beam expander. It is now a simple matter to use geometrical optics to obtain Equation (83) and the magnification

$$m = \frac{s_i}{s_o} = \frac{D_i}{\lambda_s R_s / \lambda_i}.$$

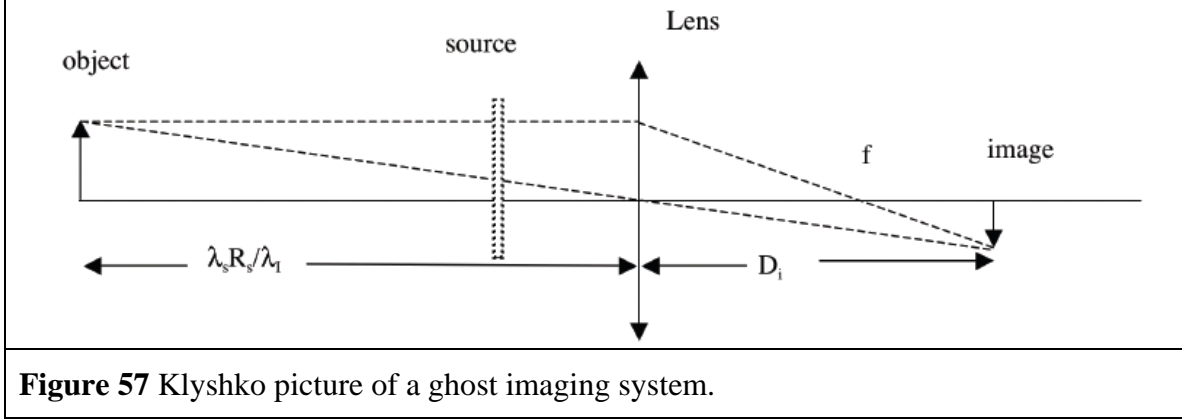
To compute the counting rate, we need to sum over the surface of the bucket detector assuming that each point of the surface detects the intensity of the light incident on it

$$\int d^2 \rho_a |V(\vec{\rho}_A, \vec{\rho}_B)|^2 = \frac{L_s^2}{R_s^2} \int d^2 \rho_a \left| \tilde{P}_L\left(K_s \left(\frac{\vec{\rho}_a}{R_s} \frac{f_1}{f_2} - \frac{\vec{\rho}_B}{D_i} \frac{\lambda_s}{\lambda_i}\right)\right) t(\vec{\rho}_a) \right|^2. \quad (85)$$

Therefore, the coincident counting rate is

$$C = \frac{1}{T} \iint dt_A dt_B S(t_A, t_B) \left| \int dv_s \exp[iv_s \tau_{AB}] \sin c(v_s D_{si} L/2) \right|^2 \times$$

$$\alpha_B \frac{\gamma^2}{\lambda_s^2 \lambda_i^2} \frac{1}{R_s^2 D_i^2} \int d^2 \rho_a \left| \tilde{P}_L \left( K_s \left( \frac{\vec{\rho}_a}{R_s} \frac{f_1}{f_2} - \frac{\vec{\rho}_B}{D_i} \frac{\lambda_s}{\lambda_i} \right) \right) t(\vec{\rho}_A) \right|^2. \quad (86)$$



### Resolution

To discuss the resolution we consider a target made up of two point scatterers, one located at the origin and the other at the point  $\vec{a}$  in the target plane,

$$t(\vec{\rho}_a) = t_0 \delta(\vec{\rho}_a) + t_1 \delta(\vec{\rho}_a - \vec{a}). \quad (87)$$

From Equation (84), we have

$$V(\vec{\rho}_A, \vec{\rho}_B) = \frac{1}{i \lambda_s R_s} \psi \left( \rho_A, \frac{K_s}{L_s} \right) \psi \left( \rho_B, \frac{K_i}{D_i} \right) \times \left[ t_0 \tilde{P}_L \left( -\frac{\vec{\rho}_B}{D_i} \frac{2\pi}{\lambda_i} \right) + t_1 \tilde{P}_L \left( K_s \left( \frac{\vec{a}}{R_s} \frac{f_1}{f_2} - \frac{\vec{\rho}_B}{D_i} \frac{\lambda_s}{\lambda_i} \right) \right) \psi \left( a, K_s \left( \frac{1}{L_s} + \frac{f_1}{f_2} \frac{1}{R_s} \right) \right) e^{-i K_s \vec{\rho}_A \cdot \vec{a} / L_s} \right] \quad (88)$$

From the first term in the square brackets of Equation (88), we see that the point spread function is determined by the Fourier transform of the lens aperture function. For a circular aperture, the radius of the Airy disk is given by

$$\alpha_B = x \frac{\lambda_i D_i}{R_L} \quad (89)$$

where  $R_L$  is the radius of the aperture and  $\tilde{P}_L(\vec{\kappa}_L)$  is negligible provided  $\kappa_L \geq 2\pi x / R_L$ ,  $x=1.22$ . Note that the radius of the Airy disk is proportional to the idler wavelength. This is the standard result, as can be seen by taking  $R_s \gg D_i$  in Equation (83) so that  $D_i \cong f$  and  $\alpha_B = x \lambda_i / NA$  where  $NA = R_L / f$  is the numerical aperture of the lens. Referring to Figure 57, we see that this is the same result we would obtain from classical optics.

We now use the Rayleigh criterion to determine the resolution of two image points. It should be noted that there are different, related, meanings of the Rayleigh criterion. The one used here refers to the ability to resolve two point sources in the object plane. The other is the minimum angle between plane waves falling on an aperture that can be resolved and can be interpreted as resolving two point sources at infinity. The image of the second term in Equation (88) is assumed to lie on the edge of the Airy disk of the first term, so

$$a_{\min} = \frac{\lambda_s \alpha_B f_2}{\lambda_i D_i f_1} R_s = x \frac{\lambda_s}{R_L} \frac{f_2}{f_1} R_s. \quad (90)$$

We see that the resolution depends on the signal wavelength. In the type of system of interest, Equation (81) gives  $R_s \approx \frac{f_1^2}{f_2^2} D_s$ . For typical parameters  $\lambda_s = 1\mu m$ ,  $R_L = 10cm$ ,

$\frac{f_2}{f_1} = 10$ ,  $x = 3$  and  $D_s = 1 - 10 km$ , we get  $a_{\min} = 3 - 30 mm$ . The second meaning of the Rayleigh criterion give the ratio  $a_{\min}/R_s$  as the smallest angle that can be resolved by the lens and it is given by a numerical factor times  $\lambda_s/R_L$ . Finally, let us rewrite Equation (90) as

$$\frac{\alpha_{\min}}{\alpha_B} = \frac{\lambda_s}{\lambda_i} \frac{R_s}{D_i} \frac{f_2}{f_1} = \frac{f}{D_i - f} \frac{f_2}{f_1} \quad (91)$$

where we have used Equation (83) to obtain this last expression.

## **Appendix C   Spatial Resolution Enhancement in Quantum Imaging beyond the Diffraction Limit Using Entangled Photon- Number State**

# Spatial Resolution Enhancement in Quantum Imaging beyond the Diffraction Limit Using Entangled Photon-Number State

Jianming Wen,\* Morton H. Rubin, and Yanhua Shih

*Physics Department, University of Maryland, Baltimore County, Baltimore, Maryland 21250, USA*

(Dated: October 13, 2008)

In this paper we study the resolution of images illuminated by sources composed of  $N + 1$  photons in which one non-degenerate photon is entangled with  $N$  degenerate photons. The  $N$  degenerate photons illuminate an object and are collected by an  $N$  photon detector. The signal from the  $N$  photon detector is measured in coincidence with the non-degenerate photon giving rise to a ghost image. We discuss the case of three photons in various configurations and generalize to  $N + 1$ . Using the Rayleigh criterion, we find that the system may give an improvement in resolution by a factor of  $N$  compared to using a classical source. For the case that the  $N$ -photon number detector is a point detector, a coherent image is obtained. If the  $N$ -photon detector is a bucket detector, the image is incoherent. The visibility of the image in both cases is 1. In the opposite case in which the non-degenerate photon is scattered by the object, then, using an  $N$ -photon point detector may reduce the Airy disk by a factor of  $N$ .

PACS numbers: 42.50.Dv, 42.30.Kq, 42.50.St, 07.07.Df

## I. INTRODUCTION

Diffraction puts a limit on the resolution of optical devices. According to the Rayleigh criterion [1, 2], the ability to resolve two point sources is limited by the wavelength of the light. The Rayleigh or diffraction limit is not an absolute limit and proposals to exceed it have been known for a long time [2]. Recently, new proposals to improve resolution beyond the Rayleigh limit have been made based on the use of entangled sources and new measurement techniques. Improving the resolving power of optical systems beyond the diffraction limit not only is of interest to the fundamental research, but also holds promise applications in remote sensing and quantum sensors.

Classical imaging can be thought of as a single photon process in the sense that the light detected is composed of photons each of which illuminates the object, consequently, the image can be constructed one photon at a time. What we mean by referring to this as classical is that the source of the light may be described by a density matrix with a positive P-function [3, 4]. In this sense the Rayleigh limit may be thought of as a single photon limit. Recall that ideal imaging is a process in which there is a point-to-point mapping of the object to a unique image plane. Diffraction causes each point of the object to be mapped onto a disk, the Airy disk, in the image plane.

One of the new approaches to improving resolution is based on using non-classical light sources. Quantum ghost imaging [5–10] is a process that uses two-photon entanglement. The unique features of this process are that entanglement allows only one photon to illuminate the object while the second photon does not. All the photons that illuminate the object are detected in a single (bucket) detector that does not resolve the image. The point detectors that detect the second photon must lie in a specific plane. This plane is called the image plane although there is no image in that plane; the image is formed in the correlation measurement of entangled photons. The image is constructed one pair at a time. The resolution of this system has recently been discussed [11, 12]. Losses in this system affect the counting rate but not the quality of the image.

A second approach using non-classical source is based on entangled photon-number states [13], e.g., NOON state. When the number of entangled photons exceeds two there are many possible imaging schemes that can be envisioned and so the analysis of these cases is still being carried out. This interferometric approach achieves a sub-wavelength spatial resolution by a factor  $N$  and requires an  $N$ -photon absorption process. Another quantum source used to study imaging is to generate squeezed states [14]. The image can be reconstructed through the homodyne detection [15]. However, both of these techniques are severely limited by the loss of photons.

A second class of approaches to improving resolution uses classical light sources. One method uses classical light with measurements based on correlations similar to ghost imaging and the Hanbury-Brown and Twiss experiment [16, 17]. This method has the advantage of being more robust with respect to losses [18, 19]. Another approach is to build an interferometric lithography with use of classical coherent state [20, 21], which has similar setup to the case using entangled photon-number states.

---

\* Electronic address: jianm1@umbc.edu



In this paper we will consider improving spatial resolution beyond the Rayleigh diffraction limit using quantum imaging with an entangled photon-number state  $|1, N\rangle$ . In our imaging scheme by sending the  $N$  degenerate photons to the object while keeping the non-degenerate photon and imaging lens in the laboratory, a factor of  $N$  improvement can be achieved in spatial resolution enhancement compared to classical optics. The assumptions required for the enhancement by a factor of  $N$  are that the  $N$  photons sent to the object scatter off the same point and are detected by either an  $N$ -photon number detector or a bucket detector. This sub-Rayleigh imaging resolution may have important applications in such as improving sensitivities of classical sensors and remote sensing. We emphasize that it is the quantum nature of the state that offers such sub-wavelength resolving power with high visibility. However, the system is very sensitive to loss. While we give general results, our main concern will be with the case in which the object is far from the source and the detectors and optics are close to the source. A different but related approach to the one discussed here is given in [22].

We organize the paper as follows. We will discuss our imaging scheme with entangled photon-number state  $|1, 2\rangle$  in some detail in Sec. II. In previous work [23, 24] we have shown that imaging occurs in correlation measurement, as in the ghost imaging case. Here we will show that under certain stringent conditions, the resolution can be improved by a factor of 2 compared to classical optics. In Sec. III we generalize the scheme to the  $|1, N\rangle$  case and show that resolution improvement by a factor of  $N$  can be obtained. In Sec. IV some discussions will be addressed on other experimental configurations. Finally we will draw our conclusions in Sec. V. In an appendix we discuss the meaning of the approximation that the  $N$  photons illuminate the same point on the object.

## II. THREE-PHOTON OPTICS

We start with three photons because this is the easiest case to investigate the various configurations. Throughout the paper we shall assume that the source of the three photons is a pure state and that the three-photon counting rate for three point detectors is given by

$$R_{cc} = \frac{1}{T^2} \int_0^T dt_1 \int_0^T dt_2 \int_0^T dt_3 |\Psi(1, 2, 3)|^2, \quad (1)$$

where the three-photon amplitude is determined by matrix element between the vacuum state and the three-photon state  $|\psi\rangle$

$$\Psi(1, 2, 3) = \langle 0 | E_1^{(+)} E_2^{(+)} E_3^{(+)} | \psi \rangle, \quad (2)$$

and

$$E_j^{(+)}(\vec{\rho}_j, z_j, t_j) = \int d\omega_j \int d^2\alpha_j E_j f_j(\omega_j) e^{-i\omega_j t_j} g_j(\vec{\alpha}_j, \omega_j; \vec{\rho}_j, z_j) a(\vec{\alpha}_j, \omega_j), \quad (3)$$

where  $E_j = \sqrt{\hbar\omega_j/2\epsilon_0}$ ,  $\vec{\alpha}_j$  is the transverse wave vector, and  $a(\vec{\alpha}_j, \omega_j)$  is a photon annihilation operator at the output surface of the source,

$$[a(\vec{\alpha}, \omega), a^\dagger(\vec{\alpha}', \omega')] = \delta(\vec{\alpha} - \vec{\alpha}') \delta(\omega - \omega'). \quad (4)$$

The function  $f_j(\omega)$  is a narrow bandwidth filter function which is assumed to be peaked at  $\Omega_j$ . The function  $g_j$  is the Green's function [2, 7] that describes the propagation of each mode from the output surface of the source to the  $j$ th detector at the transverse coordinate  $\vec{\rho}_j$ , at the distance from the output surface of the crystal to the plane of the detector,  $z_j$ .  $\Psi$  is referred to as the *three-photon amplitude* (or three-photon wavefunction).

We start with the case in which the source produces three-photon entangled states with a pair of degenerate photons, that is  $\psi \rightarrow \psi_{1,2}$

$$|\psi_{1,2}\rangle = \int d\omega_1 d\omega_2 \int d^2\alpha_1 d^2\alpha_2 \delta(2\omega_1 + \omega_2 - \Omega) \delta(2\vec{\alpha}_1 + \vec{\alpha}_2) a^\dagger(\vec{\alpha}_2, \omega_2) [a^\dagger(\vec{\alpha}_1, \omega_1)]^2 |0\rangle, \quad (5)$$

where  $\Omega$  is a constant,  $\omega_{1,2}$  and  $\vec{\alpha}_{1,2}$  are the frequencies and transverse wave vectors of the degenerate and non-degenerate photons, respectively. The  $\delta$ -functions indicate that the source is assumed to produce three-photon states with perfect phase matching. We assume the paraxial approximation holds and that the temporal and transverse behavior of the waves factor. The frequency correlation determines the three-photon temporal properties. The transverse momentum correlation determines the spatial properties of entangled photons. It is this wave-vector correlation that we are going to concentrate on. As discussed in [23], several imaging schemes can be implemented

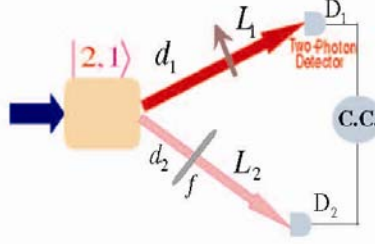


FIG. 1: (color online) Schematic of quantum imaging with a three-photon entangled state  $|1, 2\rangle$ .  $d_1$  is the distance from the output surface of the source to the object.  $L_1$  is the distance from the object to a 2-photon detector,  $D_1$ .  $d_2$  is the distance from the output surface of the source to the imaging lens with focal length  $f$  and  $L_2$  is the length from the imaging lens to a single-photon detector  $D_2$ , which scans coming signal photons in its transverse plane. "C.C." represents the joint-detection measurement.

with this three-photon source. To demonstrate spatial resolution enhancement beyond the Rayleigh diffraction limit, consider the experimental setup shown in Fig. 1. It will be shown that for this configuration the spatial resolving power is improved by a factor of 2, provided the degenerate photons illuminate the same point on the object and are detected by a two photon detector.

As depicted in Fig. 1, two degenerate photons with wavelength  $\lambda_1$  are sent to a two-photon detector ( $D_1$ ) after illuminating an object, and the non-degenerate photon with wavelength  $\lambda_2$  propagates to a single-photon detector ( $D_2$ ) after an imaging lens with focal length  $f$ . The three-photon amplitude (2) for detectors  $D_1$  and  $D_2$ , located at  $(z_1, \vec{\rho}_1)$  and  $(z_2, \vec{\rho}_2)$ , now is

$$\Psi \rightarrow \Psi_{1,2} = \langle 0 | E_2^{(+)}(\vec{\rho}_2, z_2, t_2) [E_1^{(+)}(\vec{\rho}_1, z_1, t_1)]^2 | \psi_{1,2} \rangle, \quad (6)$$

Following the treatments in [2, 7, 23], we evaluate the Green's functions  $g_1(\vec{\alpha}_1, \omega_1; \vec{\rho}_1, z_1)$  and  $g_2(\vec{\alpha}_2, \omega_2; \vec{\rho}_2, z_2)$  for the experimental setup of Fig. 1 assuming that the narrow bandwidth filter allows us to make the assumption that  $\omega_j = \Omega_j + \nu_j$  where  $|\nu_j| \ll \Omega_j$  and  $2\Omega_1 + \Omega_2 = \Omega$ .

In the paraxial approximation it is convenient to write

$$g_j(\vec{\alpha}_j, \omega_j; \vec{\rho}_j, z_j) = \frac{\omega_j e^{i\omega_j z_j/c}}{i2\pi c L_j d_j} \chi_j(\vec{\alpha}_j, \omega_j; \vec{\rho}_j, z_j), \quad (7)$$

then

$$\chi_1(\vec{\alpha}_1, \Omega_1; \vec{\rho}_1, z_1) = e^{-i\frac{d_1}{2} \frac{|\vec{\alpha}_1|^2}{K_1^2}} \int d^2 \rho_o A(\vec{\rho}_o) e^{i\frac{K_1}{2} \frac{|\vec{\rho}_o|^2}{L_1}} e^{-i\frac{K_1}{L_1} \vec{\rho}_1 \cdot \vec{\rho}_o} e^{i\vec{\alpha}_1 \cdot \vec{\rho}_o}, \quad (8)$$

$$\chi_2(\vec{\alpha}_2, \Omega_2; \vec{\rho}_2, z_2) = e^{-i\frac{d_2}{2} \frac{|\vec{\alpha}_2|^2}{K_2^2}} \int d^2 \rho_l e^{i\frac{K_2}{2} \frac{|\vec{\rho}_l|^2}{L_2}} \left(\frac{1}{L_2} - \frac{1}{f}\right) e^{i(\vec{\alpha}_2 - \frac{K_2}{L_2} \vec{\rho}_2) \cdot \vec{\rho}_l}, \quad (9)$$

where we replace  $\omega_j$  by  $\Omega_j$  in  $\chi_j$ ,  $K_j = \Omega_j/c = 2\pi/\lambda_j$ ,  $z_1 = d_1 + L_1$ , and  $z_2 = d_2 + L_2$ , respectively. In Eqs. (8) and (9),  $A(\vec{\rho}_o)$  is the aperture function of the object, and  $\vec{\rho}_o$  and  $\vec{\rho}_l$  are two-dimensional vectors defined, respectively, on the object and the imaging lens planes. With use of Eqs. (3) and (5), the three-photon amplitude (6) becomes

$$\Psi_{1,2} = e^{i(2\Omega_1 \tau_1 + \Omega_2 \tau_2)} \Phi_{1,2}, \quad (10)$$

where  $\tau_j = t_j - z_j/c$  and

$$\Phi_{1,2} = \int d\nu_1 d\nu_2 \delta(2\nu_1 + \nu_2) e^{i(2\nu_1 \tau_1 + \nu_2 \tau_2)} f_1(\Omega_1 + \nu_1)^2 f_2(\Omega_2 + \nu_2) B_{1,2}. \quad (11)$$

where

$$\begin{aligned} B_{1,2} = & B_0 \int d^2 \rho_o A(\vec{\rho}_o) e^{i\frac{K_1}{2} \frac{|\vec{\rho}_o|^2}{L_1}} e^{-i\frac{K_1}{L_1} \vec{\rho}_1 \cdot \vec{\rho}_o} \int d^2 \rho'_o A(\vec{\rho}'_o) e^{i\frac{K_1}{2} \frac{|\vec{\rho}'_o|^2}{L_1}} e^{-i\frac{K_1}{L_1} \vec{\rho}'_1 \cdot \vec{\rho}'_o} \int d^2 \rho_l e^{i\frac{K_2}{2} \frac{|\vec{\rho}_l|^2}{L_2}} \left(\frac{1}{L_2} - \frac{1}{f}\right) e^{-i\frac{K_2}{L_2} \vec{\rho}_2 \cdot \vec{\rho}_l} \\ & \times \int d^2 \alpha_1 e^{-i|\vec{\alpha}_1|^2 \left(\frac{d_1}{K_1^2} + \frac{2d_2}{K_2^2}\right)} e^{-i\vec{\alpha}_1 \cdot (2\vec{\rho}_1 - \vec{\rho}_o - \vec{\rho}'_o)}, \end{aligned} \quad (12)$$

where we collect all the slowly varying quantities into the constant  $B_0$ . To proceed the discussion, in the following we will consider two different detection schemes. One uses a point two-photon detector for two degenerate photons after the object and the other has a two-photon bucket detector.

### A. Point Two-Photon Detector Scheme

In this detection scheme, a point two-photon detector is necessary to retrieve the information of degenerate photons scattered off the same point in the object. We therefore make the key assumption that the detector  $D_1$  is only sensitive to the signals from the same point in the object, i.e.,  $\delta(\vec{\rho}_o - \vec{\rho}_o')$  [The validity of this assumption is addressed in the Appendix]. With this assumption, Eq. (12) becomes

$$B_{1,2} = B_0 \int d^2 \rho_o A^2(\vec{\rho}_o) e^{i \frac{K_1 |\vec{\rho}_o|^2}{L_1}} e^{-i \frac{2K_1 \vec{\rho}_1 \cdot \vec{\rho}_o}{L_1}} \int d^2 \rho_l e^{i \frac{K_2 |\vec{\rho}_l|^2}{L_2}} \left( \frac{1}{L_2} - \frac{1}{f} \right) e^{-i \frac{K_2}{L_2} \vec{\rho}_2 \cdot \vec{\rho}_l} \times \int d^2 \alpha_1 e^{-i |\vec{\alpha}_1|^2 \left( \frac{d_1}{K_1} + \frac{2d_1}{K_2} \right)} e^{-2i \vec{\alpha}_1 \cdot (\vec{\rho}_l - \vec{\rho}_o)}. \quad (13)$$

Completing the integration on the transverse mode  $\vec{\alpha}_1$  in Eq. (13) gives

$$B_{1,2} = B_0 \int d^2 \rho_o A^2(\vec{\rho}_o) e^{i K_1 |\vec{\rho}_o|^2 \left[ \frac{1}{L_1} + \frac{1}{d_1 + (2\lambda_2/\lambda_1)d_2} \right]} e^{-i \frac{2K_1 \vec{\rho}_1 \cdot \vec{\rho}_o}{L_1}} \times \int d^2 \rho_l e^{i \frac{K_2 |\vec{\rho}_l|^2}{L_2}} \left[ \frac{1}{L_2} + \frac{1}{d_2 + (\lambda_1/2\lambda_2)d_1} - \frac{1}{f} \right] e^{-i K_2 \vec{\rho}_l \cdot \left[ \frac{\vec{\rho}_2}{L_2} + \frac{\vec{\rho}_o}{d_2 + (\lambda_1/2\lambda_2)d_1} \right]}. \quad (14)$$

By imposing the Gaussian thin-lens imaging condition in Eq. (14)

$$\frac{1}{f} = \frac{1}{L_2} + \frac{1}{d_2 + (\lambda_1/2\lambda_2)d_1}, \quad (15)$$

the transverse part of the three-photon amplitude reduces to

$$B_{1,2} = B_0 \int d^2 \rho_o A^2(\vec{\rho}_o) e^{i K_1 |\vec{\rho}_o|^2 \left[ \frac{1}{L_1} + \frac{1}{d_1 + (2\lambda_2/\lambda_1)d_2} \right]} e^{-i \frac{2K_1 \vec{\rho}_1 \cdot \vec{\rho}_o}{L_1}} \text{somb} \left( \frac{2\pi R}{\lambda_2 [d_2 + (\lambda_1/2\lambda_2)d_1]} \left| \vec{\rho}_o + \frac{\vec{\rho}_2}{m} \right| \right), \quad (16)$$

where  $R$  is the radius of the imaging lens,  $R/[d_2 + (\lambda_1/2\lambda_2)d_1]$  may be thought of as the numerical aperture of the imaging system, and  $m = L_2/[d_2 + (\lambda_1/2\lambda_2)d_1]$  is the magnification factor. In Eq. (16) the Airy disk is determined, as usual, by  $\text{somb}(x) = 2J_1(x)/x$ , where  $J_1(x)$  is the first-order Bessel function.

Before proceeding with the discussion of resolution, let us look at the physics behind Eqs. (15) and (16). Equation (15) defines the image plane where the ideal the point-to-point mapping of the object plane occurs. The unique point-to-point correlation between the object and the imaging planes is the result of the transverse wavenumber correlation and the fact that we have assumed that the degenerate photons illuminate the same object point. Let us make a comparison with the two-photon and three-photon geometrical optics [7, 11, 23]. In the Gauss thin lens equation the distance between the imaging lens and the object planes,  $d_2 + (\lambda_1/2\lambda_2)d_1$  is similar to the form that appears in the non-degenerate two-photon case except for the factor of 2. This factor 2 comes from the degeneracy of the pair of photons that illuminate the object. As we will show below, this factor of 2 is the source of the improved spatial resolution. Equation (16) implies that a coherent and inverted image magnified by a factor of  $m$  is produced in the plane of  $D_2$ . Of course, there really is no such image and the true image is *nonlocal*. The point-spread function in Eq. (16) is generally determined by both wavelengths of the degenerate and non-degenerate photons.

To examine the resolution using the Rayleigh criterion, we consider an object consisting of two point scatters, one located at the origin and the other at the point  $\vec{a}$  in the object plane,

$$A(\vec{\rho}_o)^2 = A_0^2 \delta(\vec{\rho}_o) + A_a^2 \delta(\vec{\rho}_o - \vec{a}). \quad (17)$$

By substituting Eq. (17) into (16) we obtain

$$B_{1,2} = B_0 \left( A_0^2 \text{somb} \left( \frac{2\pi R}{\lambda_2} \left| \frac{\vec{\rho}_2}{L_2} \right| \right) + e^{i\varphi_2} A_a^2 \text{somb} \left[ \frac{2\pi R}{\lambda_2} \left| \frac{\vec{\rho}_2}{L_2} + \frac{\vec{a}}{d_2 + (\lambda_1/2\lambda_2)d_1} \right| \right] \right), \quad (18)$$

where the phase

$$\varphi_2 = K_1 \left[ |\vec{a}|^2 \left( \frac{1}{L_1} + \frac{1}{d_1 + d_2(2\lambda_2/\lambda_1)} \right) - \frac{\vec{a} \cdot (\vec{\rho}_1 + \vec{\rho}_1')}{L_1} \right] \quad (19)$$

indicates that the image is coherent. For a point 2-photon detector, we require  $\vec{\rho}_1 = \vec{\rho}_1'$  in Eq. (19). As is well-known [2] for coherent imaging the Rayleigh criterion is not the best choice for characterizing the resolution, however, it is

indicative of the resolution that can be attained and it is convenient. For a circular aperture, the radius of the Airy disk,  $\xi$ , is determined by the point-spread function, which is

$$\xi = 0.61 \frac{\lambda_2 L_2}{R}. \quad (20)$$

Note that the radius of the Airy disk is proportional to the wavelength of the non-degenerate photon. This is the standard result as obtained in classical optics. Using the Rayleigh criterion, the image of the second term in Eq. (18) is taken to lie on the edge of the Airy disk of the first term, therefore,

$$a_m = 0.61 \frac{\lambda_2}{R} \left( d_2 + \frac{\lambda_1}{2\lambda_2} d_1 \right). \quad (21)$$

We see from Eq. (21) that the resolution depends on the wavelengths of the degenerate and the non-degenerate photons. In the case that  $d_1 \gg d_2$ , so that  $d_2 + (\lambda_1/2\lambda_2)d_1$ , is approximately  $(\lambda_1/2\lambda_2)d_1$ . In this case Eq. (15) implies that  $L_2 \approx f$  and the radius of the Airy disk approaches to  $1.22\lambda_2 f/R$ , and

$$a_m = 0.61 \frac{\lambda_1 d_1/2}{R}. \quad (22)$$

Equation (22) shows a gain in spatial resolution of a factor of 2 compared to classical optics. Furthermore, there is no background term which is characteristic of the quantum case.

### B. Bucket Detector Scheme

If the two-photon detector is replaced by a bucket detector and the two degenerate photons are collected by two single-photon detection events, located at  $(L_1, \vec{\rho}_1)$  and  $(L_1, \vec{\rho}_1')$ , in the bucket, Eq. (12) becomes

$$\begin{aligned} B_{1,2} = & B_0 \int d^2 \rho_o A(\vec{\rho}_o) e^{i \frac{K_1 |\vec{\rho}_o|^2}{2L_1}} e^{-i \frac{K_1 \vec{\rho}_1 \cdot \vec{\rho}_o}{L_1}} \int d^2 \rho_o' A(\vec{\rho}_o') e^{i \frac{K_1 |\vec{\rho}_o'|^2}{2L_1}} e^{-i \frac{K_1 \vec{\rho}_1' \cdot \vec{\rho}_o'}{L_1}} \int d^2 \rho_l e^{i \frac{K_2 |\vec{\rho}_l|^2}{2}} \left( \frac{1}{L_2} - \frac{1}{f} \right) e^{i \frac{K_2}{L_2} \vec{\rho}_2 \cdot \vec{\rho}_l} \\ & \times \int d^2 \alpha_1 e^{-i |\vec{\alpha}_1|^2 \left( \frac{d_1}{K_1} + \frac{2d_2}{K_2} \right)} e^{-i \vec{\alpha}_1 \cdot (2\vec{\rho}_1 - \vec{\rho}_o - \vec{\rho}_o')}. \end{aligned} \quad (23)$$

Under the assumption that the two degenerate photons are scattered off the same point in the object, Eq. (23) takes the similar form as Eq. (13), except that the second phase term in the first integrand of (13) is replaced by  $\exp[-i \frac{K_1 (\vec{\rho}_1 + \vec{\rho}_1') \cdot \vec{\rho}_o}{L_1}]$ . It is easy to show that the Gaussian thin-lens equation takes the same form as Eq. (15). By performing the same analysis as done in Sec. IIA on the resolving two spatially close point scatters, the three-photon amplitude (18) now is

$$B_{1,2} = B_0 \left( A_0^2 \text{somb} \left( \frac{2\pi R}{\lambda_2} \left| \frac{\vec{\rho}_2}{L_2} \right| \right) + e^{i\varphi_2} A_a^2 \text{somb} \left[ \frac{2\pi R}{\lambda_2} \left| \frac{\vec{\rho}_2}{L_2} + \frac{\vec{a}}{d_2 + (\lambda_1/2\lambda_2)d_1} \right| \right] \right). \quad (24)$$

Since the bucket detector gives no position information, we must square the amplitude and integrating over the bucket detector,

$$I = \int d^2 \rho_1 \int d^2 \rho_1' |B_{1,2}|^2 = s_b^2 |B_0|^2 \left( |A_0|^4 \text{somb}^2 \left( \frac{2\pi R}{\lambda_2} \left| \frac{\vec{\rho}_2}{L_2} \right| \right) + |A_a|^4 \text{somb}^2 \left[ \frac{2\pi R}{\lambda_2} \left| \frac{\vec{\rho}_2}{L_2} + \frac{\vec{a}}{d_2 + (\lambda_1/2\lambda_2)d_1} \right| \right] \right) \quad (25)$$

where  $s_b$  is the area of the bucket detector. It is easy to see that the spatial resolution improvement is the same as in Sec. IIA, the difference is that now we get an incoherent image. The advantage is that a two photon bucket detector should be easier to construct than a point two photon detector.

### III. $N + 1$ PHOTON OPTICS

In Sec. II, we have shown that with the entangled photon-number state  $|1, 2\rangle$ , the ability to resolve two point sources in the object can be improved by a factor of 2 by sending two degenerate photons to the object while keeping the non-degenerate photon and imaging lens in the laboratory. In this section, we are going to generalize the experimental configuration (Fig. 1) with use of the entangled state of  $|1, N\rangle$ , as described in Fig. 2. For simplicity, we first address the

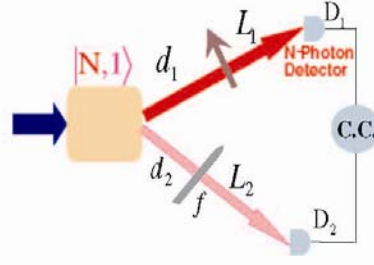


FIG. 2: (color online) Generalization of quantum imaging with  $N + 1$  entangled photons in state  $|1, N\rangle$ . For notations please refer to Fig. 1 except that here  $D_1$  is an  $N$ -photon detector. The image is formed in the coincidence measurement and is not localized at either detector.

case shown in Fig. 2 where the  $N$  degenerate photons traverse to the  $N$ -photon detector,  $D_1$ , after the object and the non-degenerate photon propagates to the single-photon detector,  $D_2$ . The assumption required for the enhancement by a factor of  $N$  are that the  $N$  photons sent to the object scatter off the same point and are detected by the  $N$ -photon detector,  $D_1$ .

The  $N + 1$  photons are assumed to be in a non-normalized pure state

$$|\psi_{1,N}\rangle = \int d\omega_1 d\omega_2 \int d^2\alpha_1 d^2\alpha_2 \delta(N\omega_1 + \omega_2 - \Omega) \delta(N\vec{\alpha}_1 + \vec{\alpha}_2) a_{k_2}^\dagger (a_{k_1}^\dagger)^N |0\rangle. \quad (26)$$

Again the  $\delta$ -functions in Eq. (26) indicate perfect phase matching. The  $N + 1$ -photon coincidence counting rate is defined as

$$R_{cc} = \frac{1}{T} \int_0^T dt_1 \int_0^T dt_2 \cdots \int_0^T dt_{N+1} |\Psi_{1,N}(1, 2, \dots, N+1)|^2, \quad (27)$$

where  $\Psi_{1,N}$  is referred to as the  $N + 1$ -photon amplitude. That is

$$\begin{aligned} \Psi_{1,N}(1, 2, \dots, N+1) &= \langle 0 | E_1^{(+)} E_2^{(+)} \cdots E_{N+1}^{(+)} | \psi_{1,N} \rangle \\ &= \langle 0 | E_2^{(+)}(\vec{\rho}_2, z_2, t_2) [E_1^{(+)}(\vec{\rho}_1, z_1, t_1)]^N | \psi_{1,N} \rangle. \end{aligned} \quad (28)$$

Following the procedure done for the  $|1, 2\rangle$  case, we calculate the transverse part of the  $N + 1$ -photon amplitude  $\Psi_{1,N}$  (28) as

$$\begin{aligned} \Psi_{1,N} &= e^{i(N\Omega_1\tau_1 + \Omega_2\tau_2)} \Phi_{1,N}(\tau_1, \tau_2) B_{1,N} \\ B_{1,N} &= B_0 \underbrace{\int d^2\rho_o A(\vec{\rho}_o) e^{i\frac{K_1|\vec{\rho}_o|^2}{2L_1}} e^{-i\frac{K_1\vec{\rho}_1 \cdot \vec{\rho}_o}{L_1}} \cdots \int d^2\rho'_o A(\vec{\rho}'_o) e^{i\frac{K_1|\vec{\rho}'_o|^2}{2L_1}} e^{-i\frac{K_1\vec{\rho}_1 \cdot \vec{\rho}'_o}{L_1}}}_{N \text{ fold}} \int d^2\rho_l e^{i\frac{K_2|\vec{\rho}_l|^2}{2}(\frac{1}{L_2} - \frac{1}{L_1})} e^{-i\frac{K_2}{L_2}\vec{\rho}_2 \cdot \vec{\rho}_l} \\ &\quad \times \int d^2\alpha_1 e^{-i\frac{N^2|\vec{\alpha}_1|^2}{2}(\frac{d_1}{NK_1} + \frac{d_2}{K_2})} e^{-i\vec{\alpha}_1 \cdot (N\vec{\rho}_1 - \vec{\rho}_o - \cdots - \vec{\rho}'_o)}. \end{aligned} \quad (29)$$

Here  $\Phi_{1,N}(\tau_1, \tau_2)$  describes the temporal behavior of entangled three photons. By applying the same argument that the  $N$ -photon detector  $D_1$  only receives the signals from the same spatial point in the object, Eq. (29) can be further simplified as

$$\begin{aligned} B_{1,N} &= B_0 \int d^2\rho_o A^N(\vec{\rho}_o) e^{i\frac{NK_1|\vec{\rho}_o|^2}{2L_1}} e^{-i\frac{NK_1\vec{\rho}_1 \cdot \vec{\rho}_o}{L_1}} \int d^2\rho_l e^{i\frac{K_2|\vec{\rho}_l|^2}{2}(\frac{1}{L_2} - \frac{1}{L_1})} e^{-i\frac{K_2}{L_2}\vec{\rho}_2 \cdot \vec{\rho}_l} \\ &\quad \times \int d^2\alpha_1 e^{-i\frac{N^2|\vec{\alpha}_1|^2}{2}(\frac{d_1}{NK_1} + \frac{d_2}{K_2})} e^{-N i \vec{\alpha}_1 \cdot (\vec{\rho}_1 - \vec{\rho}_o)}. \end{aligned} \quad (30)$$

Performing the integration on the transverse mode  $\vec{\alpha}_1$  in Eq. (30) gives

$$\begin{aligned} B_{1,N} &= B_0 \int d^2\rho_o A^N(\vec{\rho}_o) e^{i\frac{NK_1|\vec{\rho}_o|^2}{2}[\frac{1}{L_1} + \frac{1}{d_1 + (N\lambda_2/\lambda_1)d_2}]} e^{-i\frac{NK_1\vec{\rho}_1 \cdot \vec{\rho}_o}{L_1}} \\ &\quad \times \int d^2\rho_l e^{i\frac{K_2|\vec{\rho}_l|^2}{2}[\frac{1}{L_2} + \frac{1}{d_2 + (\lambda_1/N\lambda_2)d_1} - \frac{1}{L_1}]} e^{-iK_2\vec{\rho}_l \cdot [\frac{\vec{\rho}_2}{L_2} + \frac{\vec{\rho}_2 + \vec{\rho}_o}{d_2 + (\lambda_1/N\lambda_2)d_1}]}, \end{aligned} \quad (31)$$

where, again, we have assumed multimode generation in the process. Applying the Gaussian thin-lens imaging condition

$$\frac{1}{f} = \frac{1}{L_2} + \frac{1}{d_2 + (\lambda_1/N\lambda_2)d_1}, \quad (32)$$

the transverse part of the  $N + 1$ -photon amplitude (31) between detectors  $D_1$  and  $D_2$  now becomes

$$B_{1,N} = B_0 \int d^2\rho_o A^N(\vec{\rho}_o) e^{i\frac{N K_1 |\vec{\rho}_o|^2}{2} [\frac{1}{L_1} + \frac{1}{d_1 + (N\lambda_2/\lambda_1)d_2}]} e^{-i\frac{N K_1 \vec{\rho}_1 \cdot \vec{\rho}_o}{L_1}} \text{somb} \left[ \frac{2\pi R}{\lambda_2} \left| \frac{\vec{\rho}_2}{L_2} + \frac{\vec{\rho}_o}{d_2 + (\lambda_1/N\lambda_2)d_1} \right| \right]. \quad (33)$$

As expected, Eqs. (32) and (33) have the similar forms as Eqs. (15) and (16) for the  $|1, 2\rangle$  case. The unique point-to-point relationship between the object and the imaging planes is enforced by the Gaussian thin-lens equation (32). The coherent and inverted image is demagnified by a factor of  $L_2/[d_2 + d_1(\lambda_1/N\lambda_2)]$ . The spatial resolution is determined by the width of the point-spread function in Eq. (33). Note that a factor of  $N$  appears in the distance between the imaging lens and the object planes,  $d_2 + d_1(\lambda_1/N\lambda_2)$ . We emphasize again that the image is nonlocal and exists in the coincidence events.

To study the spatial resolution, we again consider the object represented by Eq. (17). Plugging Eq. (17) into (33) yields

$$B_{1,N} = B_0 \left( A_0^N \text{somb} \left( \frac{2\pi R}{\lambda_2} \left| \frac{\vec{\rho}_2}{L_2} \right| \right) + e^{i\varphi_N} A_a^N \text{somb} \left[ \frac{2\pi R}{\lambda_2} \left| \frac{\vec{\rho}_2}{L_2} + \frac{\vec{a}}{d_2 + (\lambda_1/N\lambda_2)d_1} \right| \right] \right). \quad (34)$$

For  $N$  single photon detectors located at  $\vec{\rho}_1^{(1)}, \dots, \vec{\rho}_1^{(N)}$  the phase is given by

$$\varphi_N = K_1 \left[ \frac{N|\vec{a}|^2}{2} \left( \frac{1}{L_1} + \frac{1}{d_1 + d_2(N\lambda_2/\lambda_1)} \right) - \frac{\vec{a} \cdot (\vec{\rho}_1^{(1)} + \vec{\rho}_1^{(2)} + \dots)}{L_1} \right] \quad (35)$$

For a point  $N$ -photon number detector, we require  $\vec{\rho}_1^{(1)} = \vec{\rho}_1^{(2)} = \dots$  and a coherent imaging is achievable in this case. The first term on the right-hand side in Eq. (18) gives the radius of the Airy disk, which is the same as the  $|1, 2\rangle$  case, see Eq. (20). Applying the Rayleigh criterion, the minimum resolvable distance between two points in the transverse plane now is

$$a_m = 0.61 \frac{\lambda_2}{R} \left( d_2 + \frac{\lambda_1}{N\lambda_2} d_1 \right). \quad (36)$$

For the case of  $N = 2$ , Eq. (36) reduces to Eq. (21). In the case that  $d_1 \gg d_2$ , this becomes

$$a_m = 0.61 \frac{\lambda_1 d_1}{NR}. \quad (37)$$

As expected, Eq. (37) shows a gain in sub-Rayleigh resolution by a factor of  $N$  with respect to what one would obtain in classical optics. We therefore conclude that in the proposed imaging protocol, the spatial resolving power can be improved by a factor of  $N$  with use of the entangled photon-number state  $|1, N\rangle$ . Furthermore, because we are using an entangled state with a specific type of detector, the image has high contrast because of the lack of background noise.

By following the analysis in Sec. IIB, we can show that by replacing the  $N$ -photon detector with an  $N$ -photon bucket detector, we get an incoherent image but the sub-Rayleigh imaging process is not changed.

#### IV. DISCUSSIONS AND OTHER CONFIGURATIONS

In the previous two sections, we have analyzed a novel ghost imaging by sending  $N$  degenerate photons to the object while keeping the non-degenerate photon and imaging lens in the lab. We find that if the distance between the object plane and the output surface of the source is much greater than the distance between the imaging lens and the single-photon detector planes, we can gain spatial resolution improvement in the object by a factor of  $N$  compared to classical optics. In the cases that we have discussed in this paper, this enhancement beyond the Rayleigh criterion is due to the quantum nature of the entangled photon-number state. The assumptions required for such an



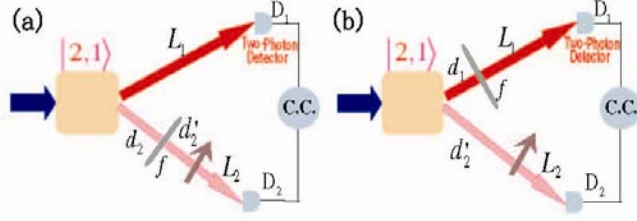


FIG. 3: (color online) Other schematics of quantum ghost imaging with three entangled photons in state  $|1, 2\rangle$ . (a) Both the imaging lens and the object are inserted in the non-degenerate photon channel. (b) The imaging lens is placed in the degenerate photon pathway while the object is in the non-degenerate optical pathway.

enhancement are that the  $N$  degenerate photons sent to the object scatter off the same point and are detected by either an  $N$ -photon number detector or a bucket detector. An  $N$ -photon bucket detector is much easier to realize than an  $N$ -photon point detector. Such a bucket detector could be an array of single photon point detectors which only sent a signal to the coincidence circuit if exactly  $N$  of them fired.

Besides the favorable configuration discussed above, one may wonder what happens if we switch the  $N$  degenerate photons to detector  $D_1$  and the non-degenerate photon to  $D_2$  after an imaging lens and an object? Do we gain any spatial resolution improvement? To answer the questions, let us look at the  $|1, 2\rangle$  case as illustrated in Fig. 3(a). Following the treatments in Sec. IIA, after some algebra we find that the transverse part of the three-photon amplitude (6) is

$$B_{1,2} = B_0 \int d^2 \rho_o A(\vec{\rho}_o) e^{i \frac{K_2 |\vec{\rho}_o|^2}{2} (\frac{1}{L_2} + \frac{1}{d'_2})} e^{-i \frac{K_2 \vec{\rho}_o \cdot \vec{\rho}_o}{L_2}} \times \int d^2 \rho_l e^{i \frac{K_2 |\vec{\rho}_l|^2}{2} [\frac{1}{d'_2} + \frac{1}{d_2 + (\lambda_1/2\lambda_2)L_1} - \frac{1}{f}]} e^{-i K_2 \vec{\rho}_l \cdot [\frac{\vec{\rho}_o}{d'_2} + \frac{\vec{\rho}_l}{d_2 + (\lambda_1/2\lambda_2)L_1}]}. \quad (38)$$

In the derivation of Eq. (38), the Green's functions associated with each beam give

$$\chi_1(\vec{\alpha}_1, \Omega_1; \vec{\rho}_1, L_1) = e^{-i \frac{L_1 |\vec{\alpha}_1|^2}{2K_1}} e^{i \vec{\rho}_1 \cdot \vec{\alpha}_1}, \\ \chi_2(\vec{\alpha}_2, \Omega_2; \vec{\rho}_2, z_2) = e^{-i \frac{d_2 |\vec{\alpha}_2|^2}{2K_2}} \int d^2 \rho_o A(\vec{\rho}_o) e^{i \frac{K_2 |\vec{\rho}_o|^2}{2} (\frac{1}{L_2} + \frac{1}{d'_2})} e^{-i \frac{K_2 \vec{\rho}_o \cdot \vec{\rho}_o}{L_2}} \int d^2 \rho_l e^{i \frac{K_2 |\vec{\rho}_l|^2}{2} (\frac{1}{d'_2} - \frac{1}{f})} e^{i \vec{\rho}_l \cdot (\vec{\alpha}_2 - \frac{K_2 \vec{\rho}_o}{d'_2})}.$$

Applying the Gaussian thin-lens imaging condition

$$\frac{1}{d'_2} + \frac{1}{d_2 + (\lambda_1/2\lambda_2)L_1} = \frac{1}{f}, \quad (39)$$

the transverse spatial part of the three-photon amplitude (38) reduces to

$$B_{1,2} = B_0 \int d^2 \rho_o A(\vec{\rho}_o) e^{i \frac{K_2 |\vec{\rho}_o|^2}{2} (\frac{1}{L_2} + \frac{1}{d'_2})} e^{-i \frac{K_2 \vec{\rho}_o \cdot \vec{\rho}_o}{L_2}} \text{somb} \left( \frac{2\pi R}{\lambda_2} \left| \frac{\vec{\rho}_o}{d'_2} + \frac{\vec{\rho}_1}{d_2 + (\lambda_1/2\lambda_2)L_1} \right| \right). \quad (40)$$

From this we see that the magnification is  $m = [d_2 + (\lambda_1/2\lambda_2)L_1]/d'_2$ . Comparing Eqs. (39) and (40) with Eqs. (15) and (16), we see that the distances between the object and the thin lens and between the thin lens and the imaging plane are interchanged. Since the degenerate photons are measured at the imaging plane in the setup of Fig. 3(a), the requirement of a point  $N$ -photon detector cannot be relaxed.

Computing the spatial resolution as in Sec. II we have

$$B_{1,2} = B_0 \left[ A_0 \text{somb} \left( \frac{2\pi R}{\lambda_2} \left| \frac{\vec{\rho}_1}{d_2 + (\lambda_1/2\lambda_2)L_1} \right| \right) + e^{i\varphi'} A_a \text{somb} \left( \frac{2\pi R}{\lambda_2} \left| \frac{\vec{a}}{d'_2} + \frac{\vec{\rho}_1}{d_2 + (\lambda_1/2\lambda_2)L_1} \right| \right) \right], \quad (41)$$

where  $\varphi' = K_2 [\frac{|\vec{a}|^2}{2} ((\frac{1}{L_2} + \frac{1}{d'_2}) - \frac{\vec{\rho}_2 \cdot \vec{a}}{L_2})]$ . The radius of the Airy disk is

$$\xi = 0.61 \frac{\lambda_2}{R} \left( \frac{\lambda_1}{2\lambda_2} L_1 + d_2 \right). \quad (42)$$

If  $L_1 \gg d_2$ ,  $\xi \rightarrow \frac{0.61L_1}{R}(\frac{\lambda_1}{2})$ , so that the width of the point-spread function shrinks to one half its value compared to the classical cases. Applying the Rayleigh criterion to see the minimum resolvable distance between two point sources in the object. From the second term of Eq. (41) the minimum distance turns out to be

$$a_{\min} = 0.61 \frac{d'_2 \lambda_2}{R}, \quad (43)$$

which only is a function of the wavelength of the non-degenerate photon; therefore, no spatial resolution improvement can be achieved compared to classical optics.

Finally, we consider the configuration shown in Fig. 3(b) which was analyzed in [23] where it was shown that no well-defined images could be obtained.

It is straightforward to generalize the above two configurations with use of the  $|1, N\rangle$  state. By replacing the source state by the state  $|1, N\rangle$  in Fig. 3(a), it can be shown that the radius of the Airy disk becomes

$$\xi = 0.61 \frac{\lambda_2}{R} \left( \frac{\lambda_1}{N\lambda_2} L_1 + d_2 \right). \quad (44)$$

If  $L_1 \gg d_2$ ,  $\xi \rightarrow \frac{0.61L_1}{R}(\frac{\lambda_1}{N})$ , so the Airy disk shrinks to one  $N$ th of its radius compared to classical optics. However, if  $L_1 \ll d_2$ , Eq. (44) gives the same result as in classical optics. Replacing the source with photon state  $|1, N\rangle$  in Fig. 3(b), the above conclusion is still valid. The analysis has been presented in [24] and we will not repeat here.

## V. CONCLUSIONS

In summary, we have proposed a quantum-imaging scheme to improve the spatial resolution in the object beyond the Rayleigh diffraction limit by using an entangled photon-number state  $|1, N\rangle$ . We have shown that by sending the  $N$  degenerate photons to the object, keeping the non-degenerate photon and imaging lens in the lab, and using a resolving  $N$ -photon detector or a bucket detector, a factor of  $N$  can be achieved in spatial resolution enhancement using the Rayleigh criterion. The image is nonlocal and the quantum nature of the state leads to the sub-Rayleigh imaging resolution with high contrast. We have also shown that by sending the  $N$  degenerate photons freely to a point  $N$ -photon detector while propagating the non-degenerate photon through the imaging lens and the object, the Airy disk in the imaging can be shrunk by a factor of  $N$  under certain conditions. However, it may be possible to show that a similar effect can occur using non-entangled sources. In the language of quantum information, the non-degenerate photon may be thought of as an ancilla onto which the information about the object is transferred for measurement. Our imaging protocol may be of importance in many applications such as imaging, sensors, and telescopes.

## VI. ACKNOWLEDGEMENT

This work was supported in part by U.S. ARO MURI Grant W911NF-05-1-0197 and by Northrop Grumman Corporation through the Air Force Research Laboratory under contract FA8750-07-C-0201 as part of DARPA's Quantum Sensors Program.

### Appendix A: Validity of the Assumption Made in Eq. (13)

In going from Eq. (12) to Eq. (13), we have made an assumption that requires the detector  $D_1$  is only sensitive to the scattered photons from the same spatial point in the object. This allowed us to collapse the  $N$  integrations over the object into a single integral. In this Appendix, we give an example of how this assumption may be satisfied for multi-photon scattering off the target. Our example assumes that each point of the object transmits or scatters the light with a random phase which satisfies Gaussian statistics. The result is that the visibility decreases.

We start with the case of  $2 + 1$  photons. From Eq. (12) the integration over the transverse vector  $\vec{\alpha}_1$ , which gives

$$B_{1,2} = B_0 \int d^2 \rho_o A(\vec{\rho}_o) e^{i \frac{K_1 |\vec{\rho}_o|^2}{4} [\frac{2}{L_1} + \frac{1}{d_1 + (\frac{1}{2\lambda_2/\lambda_1}d_2)}]} e^{-i \frac{K_1 \vec{\rho}_1 \cdot \vec{\rho}_o}{L_1}} e^{i \phi(\vec{\rho}_o)} \int d^2 \rho'_o A(\vec{\rho}'_o) e^{i \frac{K_1 |\vec{\rho}'_o|^2}{4} [\frac{2}{L_1} + \frac{1}{d_1 + (\frac{1}{2\lambda_2/\lambda_1}d_2)}]} \\ \times e^{-i \frac{K_1 \vec{\rho}_1 \cdot \vec{\rho}'_o}{L_1}} e^{i \phi(\vec{\rho}'_o)} e^{i \frac{K_1 \vec{\rho}_o \cdot \vec{\rho}'_o}{2[d_1 + (\frac{1}{2\lambda_2/\lambda_1}d_2)]}} \int d^2 \rho_l e^{i \frac{K_2 |\vec{\rho}_l|^2}{2} [\frac{1}{L_2} + \frac{1}{d_2 + (\frac{1}{2\lambda_1/\lambda_2}d_1)} - \frac{1}{f}]} e^{-i K_2 \vec{\rho}_l \cdot [\frac{\vec{\rho}_2}{L_2} + \frac{\vec{\rho}_o + \vec{\rho}'_o}{2d_2 + (\frac{1}{\lambda_1/\lambda_2}d_1)}]}, \quad (A1)$$



where  $\vec{\rho}_{1,j}$  is a point at which a photon is detected on the bucket detector, each point of the amplitude has a random phase associated with its transmission amplitude and, as usual, all the slowly varying terms have been grouped into  $B_0$ . Using the Gaussian thin-lens imaging condition (15) gives

$$B_{1,2} = B_0 \int d^2 \rho_o A(\vec{\rho}_o) e^{i \frac{K_1 |\vec{\rho}_o|^2}{4} \left[ \frac{2}{L_1} + \frac{1}{d_1 + (2\lambda_2/\lambda_1)d_2} \right]} e^{-i \frac{K_1 \vec{\rho}_{1,1} \cdot \vec{\rho}_o}{L_1}} e^{i \phi(\vec{\rho}_o)} \int d^2 \rho'_o A(\vec{\rho}'_o) e^{i \frac{K_1 |\vec{\rho}'_o|^2}{4} \left[ \frac{2}{L_1} + \frac{1}{d_1 + (2\lambda_2/\lambda_1)d_2} \right]} \\ \times e^{-i \frac{K_1 \vec{\rho}_{1,2} \cdot \vec{\rho}'_o}{L_1}} e^{i \phi(\vec{\rho}'_o)} e^{i \frac{K_1 \vec{\rho}_o \cdot \vec{\rho}'_o}{2[d_1 + (2\lambda_2/\lambda_1)d_2]}} \text{somb} \left( \frac{2\pi R}{\lambda_2} \left| \frac{\vec{\rho}_2}{L_2} + \frac{\vec{\rho}_o + \vec{\rho}'_o}{2d_2 + (\lambda_1/\lambda_2)d_1} \right| \right). \quad (\text{A2})$$

Generalizing to the case of  $N + 1$ , using the Gaussian thin-lens equation (32)

$$B_{1,N} = B_0 \int d^2 \rho_{o,1} A(\vec{\rho}_{o,1}) e^{i \frac{K_1 |\vec{\rho}_{o,1}|^2}{2L_1}} e^{-i \frac{K_1 \vec{\rho}_{1,1} \cdot \vec{\rho}_{o,1}}{L_1}} e^{i \phi(\vec{\rho}_{o,1})} \dots \int d^2 \rho_{o,N} A(\vec{\rho}_{o,N}) e^{i \frac{K_1 |\vec{\rho}_{o,N}|^2}{2L_1}} e^{-i \frac{K_1 \vec{\rho}_{1,N} \cdot \vec{\rho}_{o,N}}{L_1}} \\ \times e^{i \phi(\vec{\rho}_{o,N})} e^{i \frac{K_1 |\vec{\rho}_+|^2}{2[d_1 + (\lambda_2/N\lambda_1)d_2]}} \text{somb} \left( \frac{2\pi R}{\lambda_2} \left| \frac{\vec{\rho}_2}{L_2} + \frac{\vec{\rho}_+}{d_2 + (\lambda_1/N\lambda_2)d_1} \right| \right), \quad (\text{A3})$$

where  $\vec{\rho}_+ = \frac{1}{N} \sum_{j=1}^N \vec{\rho}_{o,j}$ .

To compute the counting rate we first calculate the magnitude square of the amplitude averaged over the random phases. Starting with the  $N = 2$  case and assuming that the ensemble average,  $\langle \dots \rangle$ , over those phases satisfies Gaussian statistics so that

$$\langle e^{i[\phi(\vec{\rho}_o) + \phi(\vec{\rho}'_o) - \phi(\vec{\rho}''_o) - \phi(\vec{\rho}'''_o)]} \rangle = \delta(\vec{\rho}_o - \vec{\rho}''_o) \delta(\vec{\rho}'_o - \vec{\rho}'''_o) + \delta(\vec{\rho}_o - \vec{\rho}'''_o) \delta(\vec{\rho}'_o - \vec{\rho}''_o), \quad (\text{A4})$$

we find

$$\langle B_{1,2}^* B_{1,2} \rangle = |B_0|^2 \int d^2 \rho_o \int d^2 \rho'_o |A(\vec{\rho}_o) A(\vec{\rho}'_o)|^2 \text{somb}^2 \left( \frac{2\pi R}{\lambda_2} \left| \frac{\vec{\rho}_2}{L_2} + \frac{\vec{\rho}_o + \vec{\rho}'_o}{2d_2 + (\lambda_1/\lambda_2)d_1} \right| \right) \left[ 1 + e^{-i \frac{K_1 (\vec{\rho}_{1,1} - \vec{\rho}'_{1,1}) \cdot (\vec{\rho}_o - \vec{\rho}'_o)}{L_1}} \right] \quad (\text{A5})$$

When we integrate over the bucket detector, the first term will be a constant while the second term will give us a delta function in  $\vec{\rho}_o$  times the area of the bucket detector,  $s_b$ . Equation (A5) reduces to

$$\int d^2 \rho_{1,1} \int d^2 \rho_{1,2} \langle |B_{1,2}|^2 \rangle = C + |B_0|^2 s_b^2 \left( \frac{L_1 \lambda_1}{2\pi s_b} \right) \int d^2 \rho_o |A(\vec{\rho}_o)|^4 \text{somb}^2 \left( \frac{2\pi R}{\lambda_2} \left| \frac{\vec{\rho}_2}{L_2} + \frac{\vec{\rho}_o}{d_2 + (\lambda_1/2\lambda_2)d_1} \right| \right). \quad (\text{A6})$$

First note that for the second term is similar to Eq. (25), the difference being the term in parenthesis which is the ratio of effect of diffraction to the area of the bucket detector, it is essentially the inverse of the Fresnel number. Computing the constant,  $C$ , is generally difficult and depends in detail on the geometry of the object, we can obtain an upper bound on  $C$  quite easily,

$$|C| \leq s_b^2 |B_0|^2 \left| \int d^2 \rho_o |A(\vec{\rho}_o)|^2 \right|^2, \quad (\text{A7})$$

consequently, the visibility will be much less than for the ideal case discussed above. From Eq. (A6) the second term is proportional to  $L_1 \lambda_1$  which implies that as this product increases the visibility increases, however, recall for the case of sensors  $L_1 \simeq d_1$ , so as this term increases the minimum resolvable distance also increases. The generalization to the case of  $N + 1$  photons is straightforward. The ensemble phase average now becomes

$$\left\langle \exp \left[ i \left( \sum_{j=1}^N \phi(\vec{\rho}_{o,j}) - \sum_{j=1}^N \phi(\vec{\rho}_{o,j}) \right) \right] \right\rangle = \sum_{P_N} \prod_{r=1}^N \delta(\vec{\rho}_{o,r} - \vec{\rho}_{o,P_N(r)}), \quad (\text{A8})$$

where the  $N$  degenerate transmitted or reflected photons acquire random phases  $\phi(\vec{\rho}_{o,j})$  and  $P_N$  is the set of permutations of the numbers  $(1, \dots, N)$ . In Eq. (A8) there are  $N!$  terms. We can show that

$$\langle |B_{1,N}|^2 \rangle = |B_0|^2 \int d^2 \rho_{o,1} \dots \int d^2 \rho_{o,N} |A(\vec{\rho}_{o,1}) \dots A(\vec{\rho}_{o,N})|^2 \text{somb}^2 \left( \frac{2\pi R}{\lambda_2} \left| \frac{\vec{\rho}_2}{L_2} + \frac{\vec{\rho}_+}{N[d_2 + (\lambda_1/N\lambda_2)d_1]} \right| \right) \\ \times \sum_{P_N} e^{-i \frac{K_1}{L_1} \sum_{r=1}^N \vec{\rho}_{1,r} \cdot (\vec{\rho}_{o,r} - \vec{\rho}_{o,P_N(r)})}. \quad (\text{A9})$$

When we integrate over the bucket detector, we get a complicated result. Two terms are simple, the identity permutation gives a constant and the single cycle subgroup give an incoherent image with a resolution that depends on  $\lambda_1/N$ . These are the only terms for  $N = 2$ . The remaining terms will lead to terms which are essentially constant. For  $N = 3$  we get

$$\begin{aligned} \int d^2\rho_{1,1} \int d^2\rho_{1,2} \int d^2\rho_{1,3} \langle |B_{1,3}|^2 \rangle &= C + 3|B_0|^2 s_b^3 \left( \frac{L_1 \lambda_1}{2\pi s_b} \right) \int d^2\rho_+ \int d^2\zeta |A(\vec{\rho}_+ - 2\vec{\zeta})|^2 |A(\vec{\rho}_+ + \vec{\zeta})|^4 \\ &\times \text{somb} \left( \frac{2\pi R}{\lambda_2} \left| \frac{\vec{\rho}_2}{L_2} + \frac{\vec{\rho}_+}{3[d_2 + (\lambda_1/3\lambda_2)d_1]} \right| \right) + |B_0|^2 s_b^3 \left( \frac{L_1 \lambda_1}{2\pi s_b} \right)^2 \int d^2\rho_{o,1} |A(\vec{\rho}_{o,1})|^6 \\ &\times \text{somb}^2 \left( \frac{2\pi R}{\lambda_2} \left| \frac{\vec{\rho}_2}{L_2} + \frac{\vec{\rho}_{o,1}}{d_2 + (\lambda_1/N\lambda_2)d_1} \right| \right). \end{aligned} \quad (\text{A10})$$

From Eq. (A10) the second term shows explicitly how the general terms will lead to a complicated average over the illuminated area of the object. This result shows that the image will have very poor visibility for large  $N$ , it is not certain whether there might be arrangement of detectors for the  $N$  photons which will give better results.

- 
- [1] It should be noted that there are different, related, meanings of the Rayleigh criterion. The one used here refers to the ability to resolve two point sources in the object. The other is the minimum angle between plane waves falling on an aperture that can be resolved and can be interpreted as resolving two point sources at infinity.
- [2] J. W. Goodman, *Introduction to Fourier Optics* (McGraw-Hill Publishing Company, New York, 1968).
- [3] R. J. Glauber, Phys. Rev. **131**, 2766 (1963).
- [4] E. C. G. Sudarshan, Phys. Rev. Lett. **10**, 277 (1963).
- [5] T. B. Pittman, Y.-H. Shih, D. V. Strekalov, and A. V. Sergienko, Phys. Rev. A **52**, R3429 (1995).
- [6] D. V. Strekalov, A. V. Sergienko, D. N. Klyshko, and Y.-H. Shih, Phys. Rev. Lett. **74**, 3600 (1995).
- [7] M. H. Rubin, Phys. Rev. A **54**, 5349 (1996).
- [8] M. D'Angelo and Y.-H. Shih, Laser Phys. Lett. **2**, 567 (2005); Y.-H. Shih, IEEE J. of Selected Topics in Quantum Electronics **9**, 1455 (2003).
- [9] Y.-H. Shih, "The physics of ghost imaging," submitted to Phys. Rev. A (2008); arXiv:0805.1166 [quant-ph].
- [10] M. D'Angelo, M. V. Chekhova, and Y. Shih, Phys. Rev. Lett. **87**, 013602 (2001).
- [11] M. H. Rubin and Y.-H. Shih, Phys. Rev. A **78**, 033836 (2008).
- [12] M. D'Angelo, A. Valencia, M. H. Rubin, and Y.-H. Shih, Phys. Rev. A **72**, 013810 (2005).
- [13] A. N. Boto, P. Kok, D. S. Abrams, S. L. Braunstein, C. P. Williams, and J. P. Dowling, Phys. Rev. Lett. **85**, 2733 (2000).
- [14] H. P. Yuen, Phys. Rev. A **13**, 2226 (1976).
- [15] M. Bache, E. Brambilla, A. Gatti, and L. A. Lugiato, Phys. Rev. A **70**, 023823 (2004); V. Boyer, A. M. Marino, and P. D. Lett, Phys. Rev. Lett. **100**, 143601 (2008).
- [16] R. Hanbury-Brown and R. Q. Twiss, Nature **177**, 27 (1956); **178**, 1046 (1956).
- [17] L. Mandel and E. Wolf, *Optical Coherence and Quantum Optics* (Cambridge University Press, Cambridge, 1995); M. O. Scully, and M. S. Zubairy, *Quantum Optics* (Cambridge University Press, Cambridge, UK, 1997).
- [18] G. Scarcelli, A. Valencia, and Y.-H. Shih, Europhys. Lett. **68**, 618 (2004); A. Valencia, G. Scarcelli, M. D'Angelo, and Y.-H. Shih, Phys. Rev. Lett. **94**, 063601 (2005); G. Scarcelli, V. Berardi, and Y.-H. Shih, *ibid.* **96**, 063602 (2006); R. Meyers, K. S. Deacon, and Y.-H. Shih, Phys. Rev. A **77**, 041801(R) (2008).
- [19] D. Zhang, Y.-H. Zhai, L.-A. Wu, and X.-H. Chen, Opt. Lett. **30**, 2354 (2005); Y. Bai and S. Han, Phys. Rev. A **76**, 043828 (2007); Y. J. Cai and S. Y. Zhu, Phys. Rev. E **71**, 056607 (2005); A. Gatti, E. Brambilla, M. Bache, and L. A. Lugiato, Phys. Rev. A **70**, 013802 (2004); R. S. Bennink, S. J. Bentley, R. W. Boyd, and J. C. Howell, Phys. Rev. Lett. **92**, 033601 (2004).
- [20] S. J. Bentley and R. W. Boyd, Opt. Express **12**, 5735 (2004); A. Pe'er, B. Dayan, M. Vucelja, Y. Silberberg, and A. A. Friesem, *ibid.* **12**, 6600 (2004); P. R. Hemmer, A. Muthukrishnan, M. O. Scully, and M. S. Zubairy, Phys. Rev. Lett. **96**, 163603 (2006).
- [21] M. Kiffner, J. Evers, and M. S. Zubairy, Phys. Rev. Lett. **100**, 073602 (2008).
- [22] V. Giovannetti, S. Lloyd, L. Maccone, and J. Shapiro, arXiv:0804.2875v1 [quant-ph].
- [23] J.-M. Wen, P. Xu, M. H. Rubin, and Y.-H. Shih, Phys. Rev. A **76**, 023828 (2007).
- [24] J.-M. Wen, M. H. Rubin, and Y.-H. Shih, Phys. Rev. A **76**, 045802 (2007).

## Appendix D Three-Photon Entangled Beams

In recent work on entangled three photon states it was shown that a protocol exists for improving resolution. The use of the protocol for sensors with large intrinsic loss is difficult because the loss entails unrealistically long counting times. To overcome this limitation it has been proposed to replace the photons that are subject to the loss by intense beams. In this paper we initiate an analysis of the protocol using beams. The model presented is chosen to make analytic calculations possible while retaining the basic physics of the protocol. As a first step, we examine the model to determine the temporal or longitudinal correlations. It is shown that in addition to the three-beam entangled state there is a term in which two entangled beams occur and a third term with no entanglement. The counting rate of each of these terms is estimated. We estimate that under ideal conditions for the model considered here, we can only get about  $5 \times 10^9 / \text{s} \cdot \text{cm}^2$ .

We consider a simple model illustrated in Fig. 58. A coherent pair of squeezed states is incident on a crystal. We assume that the crystal is cut so an idler pair, one from each beam can be up converted.

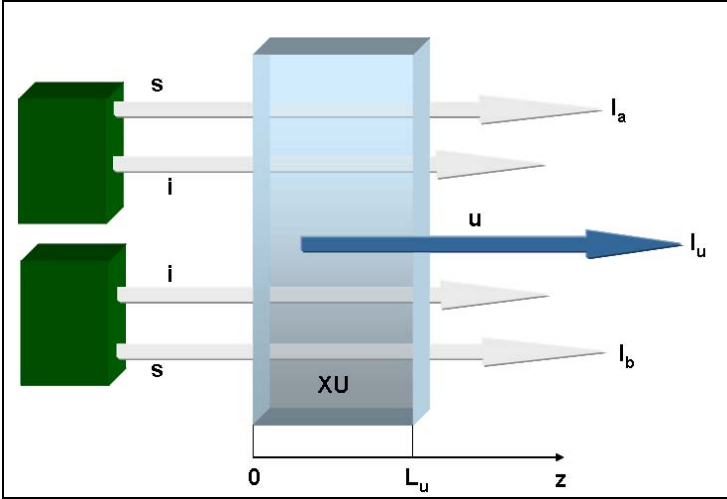


**Figure 58** Correlated beams of signals,  $s$ , and idlers,  $i$ , are produced by down-conversion. The idlers from the lower beam are frequency shifted. The crystal XU is chosen so there is phase matching that allows an idler from each beam to be up-converted to a photon.

To do this, it is necessary that the idler beams not be degenerate, this might be done by frequency shifting one of the idler beams so that  $\omega_{i1} = \omega_i + \Delta\omega$ ,  $\omega_{i2} = \omega_i$ , and  $\omega_u = \omega_{i1} + \omega_{i2}$  or, alternatively, by rotating its polarization.

This avoids the complication of an up-converted photon being produced by a pair of idlers from the same beam. The up-conversion coupling is assumed to be weak enough so that we can apply first order perturbation theory to compute the generation of the up-converted photons. The remaining idler beams are not

detected and we measure the correlation function

$$G^{(3)} = \langle \Psi | : I_a I_b I_u : | \Psi \rangle, \quad (92)$$

where  $I_j$  is the few cycle average of the photon flux of the up-converted beam for  $j=u$  and of the two signal beams,  $j=a$ , and  $b$ . The colons denote normal and time ordering, and  $|\Psi\rangle$  is the state of the system at the surface  $z = L_u$ . The Hamiltonian for the up-conversion in the interaction picture and the rotating wave approximation is

$$\begin{aligned}
H_u(t) &= \hbar \sum_{u, i1, i2} \gamma_u \left( a_u^\dagger b_{i1} b_{i2} S(\Delta k_{12} L_u) f_{i1}(\nu_{i1}) f_{i2}(\nu_{i2}) e^{-i(\omega_{i1} + \omega_{i2} - \omega_u)t} + hc \right) \\
S(x) &= e^{ix/2} \text{sinc}(x/2) \\
\Delta k_{12} &= k_u - k_{i1} - k_{i2}
\end{aligned} \tag{93}$$

where  $a_j$  and  $a_j^\dagger$  are the annihilation and creation operators for the signal modes incident of the up-conversion crystal, the  $b_j$  and  $b_j^\dagger$  are the corresponding idler operators, and  $hc$  means Hermitian conjugate. In addition, we assume that the beams are collinear and parallel to the  $z$ -axis. Note that the coupling constant  $\gamma_u$  has the dimensions of frequency.

Using perturbation theory in powers of  $\gamma_u$ ,  $|\Psi\rangle = \sum_{n=0}^{\infty} |\Psi^{(n)}\rangle$ , and the first order term is

$$|\Psi^{(1)}\rangle = \frac{1}{i\hbar} \int_0^T dt H_u(t) |\Psi^{(0)}\rangle \tag{94}$$

where the state incident on the up-conversion crystal is

$$|\Psi^{(0)}\rangle = \prod_j U_j |0\rangle \quad U_j = e^{\gamma(a_j^\dagger b_j^\dagger - a_j b_j)}, \tag{95}$$

$|0\rangle$  is the vacuum state. We have assumed perfect phase matching for each pair of modes in the squeezed states so  $\omega_{sj} + \omega_{ij} = \omega_p$ . Then taking the idler fields incident on the up-conversion crystal to be

$$E_\alpha^{(+)}(z, t) = \sum_r e_{ar} f_\alpha(\nu_{ar}) e^{-i(\omega_{ar} - k_{ar} z)} b_{ar} \quad \alpha = i1, i2 \tag{96}$$

where  $e_{ar}$  is defined in Eq. (113),  $f_\alpha(\nu_{r\alpha})$  represents a filter centered on  $\Omega_\alpha$  with  $\nu_{r\alpha} = \omega_r - \Omega_\alpha$  and  $|\nu_{r\alpha}| = \Omega_\alpha$ , we find

$$\begin{aligned}
|\Psi^{(1)}\rangle &= (-i \frac{\gamma_u c^3}{w_u w_{i1} w_{i2}} T_u \sinh^2 \gamma) \sum_{\omega_{um}, \omega_{i1}, \omega_{i2}} \delta_{\omega_{um}, \omega_{i1} + \omega_{i2}} S(\Delta k_{12} L_u) f_{i1}(\nu_{i1}) f_{i2}(\nu_{i2}) \prod_j U_j a_{um}^\dagger a_{s1}^\dagger a_{s2}^\dagger |0\rangle \\
\nu_j &= \omega_j - \Omega_j \quad j = um, i1, i2
\end{aligned} \tag{97}$$

where we have assumed that  $T_u$ , the up-conversion interaction time, is sufficiently large that the time integral can be approximated by a delta function, and the  $w$ 's are the group velocities of the beams defined in detail below in Eq. (104). In addition, we have used

$$\begin{aligned}
U_j^{-1} b_{ij} U_j &= \cosh \gamma b_{ij} + \sinh \gamma a_{si}^\dagger \\
\omega_p &= \omega_{sj} + \omega_{ij} \quad k_p = k_{sj} + k_{ij}.
\end{aligned} \tag{98}$$

Using these results, the leading order in the correlation function may be written as

$$G^{(3)}(\tau_a, \tau_b, \tau_u) = (2\varepsilon_0 c)^3 \left\| E_a^{(+)} E_b^{(+)} E_u^{(+)} |\Psi^{(1)}\rangle \right\|^2 \quad (99)$$

where the free space fields for the signal beams and the up-converted photon are

$$E_\alpha^{(+)} = \sum_r e_{ar} f_\alpha(\nu_{ar}) e^{-i\omega_a \tau_a} a_{ar} \quad (100)$$

$\alpha = a, b, u$ . It will be shown that the correlation function may be written as

$$G^{(3)} = \Gamma \left( \langle \chi_1 | \chi_1 \rangle \cosh^4 \gamma + \langle \chi_2 | \chi_2 \rangle \frac{1}{4} \sinh^2 2\gamma + \langle \chi_3 | \chi_3 \rangle \sinh^4 \gamma \right) \quad (101)$$

$$\Gamma = (2\varepsilon_0 c)^3 \left( \frac{\gamma_u c^3}{w_u w_{i1} w_{i2}} T_u \right)^2 e_a^2 e_b^2 e_c^2 \sinh^4 \gamma$$

where the three orthogonal states  $|\chi_j\rangle$  correspond to distinct processes illustrated in

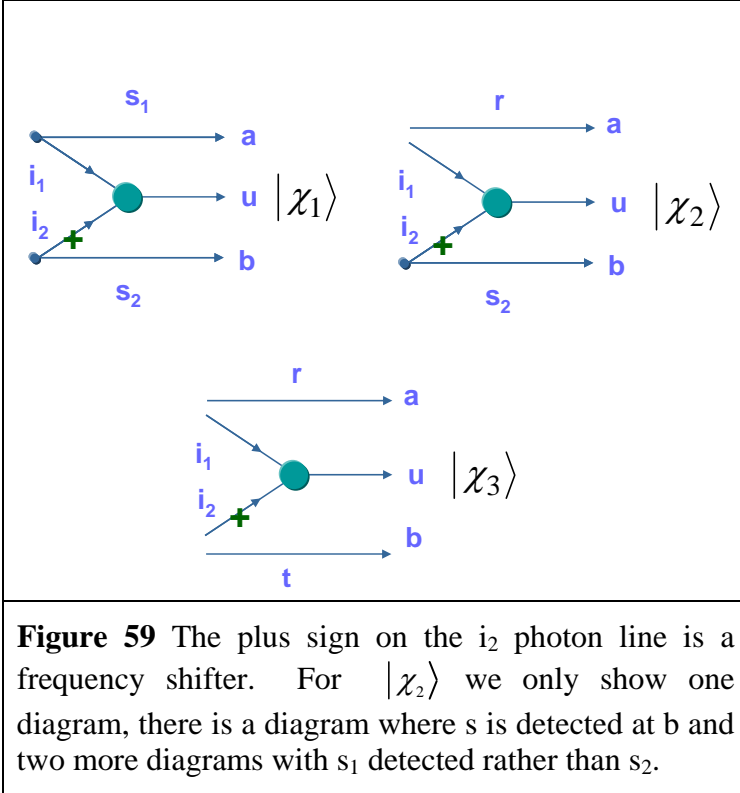


Figure. 59. In the state  $|\chi_1\rangle$  the signal photons detected at  $a$  and  $b$  are the twins of the idlers that created the up-converted photon  $u$ . This state corresponds to an entangled three-photon state and dominates in the limit of small  $\gamma$ . The state  $|\chi_2\rangle$  corresponds to four cases in which only one of the signals detected at  $a$  or  $b$  is a twin of one of the idlers that generated  $u$ . This state is a product state of a single signal photon and a two-photon entangled state. Finally, in  $|\chi_3\rangle$  neither signal detected at  $a$  or  $b$  is a twin of one of the idlers that generates  $u$ . This state is separable. The last two states decrease the visibility associated with

the three-photon entangled state.

To evaluate  $E_a^{(+)} E_b^{(+)} E_u^{(+)} |\Psi^{(1)}\rangle$  we need to compute

$$\begin{aligned}
a_{ar}a_{bt}a_{um}\prod_j U_j a_{um}^\dagger a_{s1}^\dagger a_{s2}^\dagger |0\rangle &= \prod_j U_j \delta_{umun} (a_{ar} \cosh \gamma + b_{ar}^\dagger \sinh \gamma) (a_{bt} \cosh \gamma + b_{bt}^\dagger \sinh \gamma) \times \\
&\quad a_{s1}^\dagger a_{s2}^\dagger |0\rangle \\
&= \prod_j U_j \delta_{umun} \left[ \cosh^2 \gamma (\delta_{ars1} \delta_{bts2} + ar \leftrightarrow bt) |0\rangle + \cosh \gamma \sinh \gamma \times \right. \\
&\quad \left. \{(\delta_{ars1} b_{bt}^\dagger a_{s2}^\dagger + ar \leftrightarrow bt) + 1 \leftrightarrow 2\} |0\rangle + \sinh^2 \gamma b_{ar}^\dagger b_{bt}^\dagger a_{s1}^\dagger a_{s2}^\dagger |0\rangle \right].
\end{aligned} \tag{102}$$

The three classes of states can be read off from this equation. In evaluating the delta function in Eq. (102) some care must be taken to note that

$$\begin{aligned}
\omega_{um} - \omega_{i1} - \omega_{i2} &= (\Omega_u - \Omega_{i1} - \Omega_{i2}) + \nu_{um} + \nu_{s1} + \nu_{s2} \\
&= \nu_{um} + \nu_{s1} + \nu_{s2}
\end{aligned} \tag{103}$$

using frequency phase matching for both the down-conversion and up-conversion. Similarly

$$\begin{aligned}
\Delta k_{12} &= (K_u - K_{i1} - K_{i2}) + \frac{\nu_{um}}{w_u} + \frac{\nu_{s1}}{w_{i1}} + \frac{\nu_{s1}}{w_{i2}} - +L \\
&= \frac{\nu_{um}}{w_u} + \frac{\nu_{s1}}{w_{i1}} + \frac{\nu_{s1}}{w_{i2}} + L \\
\frac{1}{w_{ij}} &= \frac{dk_i}{d\omega_i}(\Omega_{ij})
\end{aligned} \tag{104}$$

where we again use perfect phase matching and  $w_{ij}$  is the group velocity of the idler  $ij$  in the up-conversion crystal and similarly  $w_u$  is the group velocity evaluated at  $\Omega_u$  of the up-converted photon.

Using Equations (101), (102), and (104), it is not difficult to show that

$$|\chi_1\rangle = \sum_{\nu_m, \nu_r, \nu_t} \delta_{\nu_m, -\nu_r - \nu_t} f_u(\nu_m) e^{-i\nu_m \tau_u} e^{-i\phi} \left( S(\Delta k_r L_u) f_a^2(\nu_r) f_b^2(\nu_t) e^{-i(\nu_m \tau_u + \nu_r \tau_a + \nu_t \tau_b)} + r \leftrightarrow t \right) |0\rangle \tag{105}$$

where  $\phi = \Omega_u \tau_u + \Omega_s(\tau_a + \tau_b)$ , and we have assumed that  $f_{i1}(\nu) = f_a(-\nu) = f_a(\nu)$  and similarly for  $i2$  and  $b$ .

Converting the sums to integrals  $\sum_{\nu_\alpha} \rightarrow \frac{L_Q}{c} \int d\nu_\alpha$ , and using  $\nu_m = \nu_{i1} + \nu_{i2}$  and  $\nu = (\nu_{i1} + \nu_{i2})/2$ , we find

$$\begin{aligned}
\langle \chi_1 | \chi_1 \rangle &= \left( \frac{L_Q}{c} \right)^4 \left| \int d\nu_m e^{-i\nu_m \tau'} f_u(\nu_m) \int d\nu \left[ f_a^2\left(-\frac{\nu_m}{2} + \nu\right) f_b^2\left(-\frac{\nu_m}{2} - \nu\right) e^{-i\nu \tau_{ab}} \times \right. \right. \\
&\quad \left. \left. S(\Delta k_1(\nu_m, \nu) L_u) + \nu \rightarrow -\nu \right] \right|^2
\end{aligned} \tag{106a}$$

$$D_{il,i2} = \frac{1}{w_{i1}} - \frac{1}{w_{i2}} \quad (106b)$$

$$\begin{aligned} \Delta\kappa_1(\nu_m, \nu) &= D\nu_m + D_{il,i2}\nu \\ D &= \frac{1}{2}(D_{um,i1} + D_{um,i2}) = \left( \frac{1}{w_{um}} - \frac{1}{2} \left( \frac{1}{w_{i1}} + \frac{1}{w_{i2}} \right) \right) \\ D_{il,i2} &= \left( \frac{1}{w_{i1}} - \frac{1}{w_{i2}} \right) \end{aligned} \quad (106c)$$

$$\begin{aligned} \tau_{ab} &= \tau_a - \tau_b \\ \tau' &= \frac{1}{2}(\tau_{ua} + \tau_{ub}) = \tau_u - \frac{1}{2}(\tau_a + \tau_b). \end{aligned} \quad (106d)$$

This complicated expression can be understood by noting that  $\tau'$  is the difference between the time the up-converted photon and the “center of mass” of the two signal photons are at  $z = L_u$ , while  $\tau_{ab}$  is the difference in time when the two signal photons are at  $z = L_u$ .  $D_{il,i2}L_u$  is the difference in time to cross the up-converting crystal for idler wave packets with central frequencies  $\Omega_{i1}$  and  $\Omega_{i2}$

In order to get a feeling Eq. (106a), assume that the filters are Gaussians,  $f_n(\nu) = e^{-\nu^2 T_n^2/2}$ . We also assume that the function  $S(\Delta\kappa_1(\nu_m, \nu)L_u)$  is much narrower than any of the filters, then the inner product vanishes unless  $|\tau'| < |D|L_u$ ,

$$\begin{aligned} \langle \chi_1 | \chi_1 \rangle &= \frac{16\pi^4}{T^2 |D|^2 L_u^2} \left( \frac{L_Q}{c} \right)^4 e^{-\frac{(\tau_{ab} - r\tau')^2}{T^2}} \left[ H\left(1 - \frac{2\tau'}{|D|L_u}\right) - H\left(-1 - \frac{2\tau'}{|D|L_u}\right) \right] \\ T &= \sqrt{r^2 T_u^2 + (4 + r^2) T_a^2} \quad r = \frac{|D_{il,i2}|}{|D|} \end{aligned} \quad (107)$$

where  $H(x)$  is the Heaviside step function, and we have taken  $T_a = T_b$ .

The contribution to  $G^{(3)}$  of the entangled term has a magnitude that is given by

$$\begin{aligned} \left( G_1^{(3)} \right)_{\max} &= 4\sqrt{2}\pi^2 \tilde{\Gamma} \frac{h\Omega_{i1}}{A|D|L_u} \frac{T_a^2 T_N}{T^2 T_i} \cosh^4 \gamma \\ \tilde{\Gamma} &= \bar{I}_a \bar{I}_b \frac{h\Omega_u N_u}{\bar{I}_{i1}} \end{aligned} \quad (108)$$

where  $N_u$  is the average flux of u-photons detected and is defined in Equation (115) along with  $T_N$ . The parameter  $\tilde{\Gamma}$  is the product of the intensities detected at  $a$  and  $b$  times

the efficiency of producing the up-converted photons. The term following  $\tilde{\Gamma}$  in Equation (108) is the energy of a single photon idler photon divided by the area of the idler beam and the difference in time it takes the idlers to cross the up-converting crystal. The next term is of order unity.

Using Eq. (102) and referring to Figure 59, we find that

$$\begin{aligned} |\chi_2\rangle = 2 \sum_{\nu_m, \nu_i, \nu_r, \nu_{s2}} \{ & \delta_{\nu_m, -\nu_i + \nu_{s2}} f_u(\nu_m) e^{-i\phi} [ f_{i1}(\nu_i) f_b^2(\nu_{s2}) f_a(\nu_r) e^{-i(\nu_m \tau_u + \nu_r \tau_a + \nu_{s2} \tau_b)} \times \\ & S(\Delta k_{12}) + a \leftrightarrow b ] a_r^\dagger b_i^\dagger |0\rangle \} \end{aligned} \quad (109)$$

where the creation operator  $b_i^\dagger$  generates an idler which is the twin of a signal photon of frequency  $\Omega_s + \nu_i$  that is undetected, and the photon detected at  $a$  is a signal photon of frequency  $\Omega_s + \nu_{s1}$ . The second term in the square bracket is obtained by interchanging the indices  $a$  and  $b$  since the signal photons are degenerate. The remaining two terms come from the interchange of which twin of the idlers is detected. These last two terms are identical to the first two as can be seen by redefining the summation indices. It is clear that  $|\chi_1\rangle$  and  $|\chi_2\rangle$  are orthogonal.

Following the method used get Eq. (106)

$$\begin{aligned} \langle \chi_2 | \chi_2 \rangle = 2 \left( \sum_{\nu_r} f_b^2(\nu_r) \right) \sum_{\nu_{i1}} f_{i1}^2(\nu_{i1}) \left| \sum_{\nu_m} f_u(\nu_m) f_b^2(\nu_i - \nu_m) \times \right. \\ \left. S(\Delta \kappa_2 L_u) e^{-i\nu_m \tau_{ua}} + a \leftrightarrow b \right|^2 \\ \Delta \kappa_2 = D_{u,i1} \nu_m + D_{i1,i2} \nu_i \end{aligned} \quad (110)$$

This term factors into the first term in brackets which corresponds to detecting independent signal photons. In the second term there is an interference term arising from the identity of the detected signal photons.

Making the same assumptions to evaluate the integrals, we get

$$\langle \chi_2 | \chi_2 \rangle = \frac{4\sqrt{2}\pi^3}{T_a^2 |D_{u,i1}| L_u^2} \left( \frac{L_Q}{c} \right)^4 \left[ \Lambda\left( \frac{2\tau_{au}}{|D_{u,i1}| L_u} \right) + \Lambda\left( \frac{2\tau_{bu}}{|D_{u,i1}| L_u} \right) \right]. \quad (111)$$

where

$$\Lambda(x) = \begin{cases} 1 & 0 < x < 1 \\ 0 & \text{otherwise} \end{cases}.$$

The appearance of  $\tau_{au} = \tau_a - \tau_u$  is indicative of the fact that the signal detected at  $a$  and up-converted photon are partially entangled because  $\omega_u + \omega_{sa} = 2\omega_p - \omega_{sb}$ . Therefore, once the signal frequency  $\omega_b$  is determined, the other two photons are entangled in frequency. Also since we use the up-converted photon as a trigger,  $\tau_{au}$  is positive. The second term in Equation (111) corresponds to the interchange of  $a$  and  $b$ . Consequently, there is interference between the case in which the entangled pair is detected at  $(a, u)$  and



the other signal is detected at  $b$  and when the pair is measured at  $(b, u)$  and the other signal is at  $a$ .

Finally, following the same path, we find that

$$\begin{aligned} \langle \chi_3 | \chi_3 \rangle &= 2 \left( \frac{L_Q}{c} \right)^4 \left( \int d\nu_r f_a^2(\nu_r) \right) \left( \int d\nu_t f_b^2(\nu_t) \right) \int d\nu_m \int d\nu \times \\ &\quad \left| f_{i1} \left( -\frac{\nu_m}{2} + \nu \right) f_{i2} \left( -\frac{\nu_m}{2} + \nu \right) f_u(\nu_m) S(\Delta\kappa_3(\nu_m, \nu)) \right|^2 \\ &= \frac{2\pi^2}{T_a^2 T_i |D_{u,i1}| L_u} \left( \frac{L_Q}{c} \right)^4 \end{aligned} \quad (112)$$

where  $\Delta\kappa_1$  is defined in Eq. (106). This term factors into three terms corresponding to the separate detection of two signal beams that are uncorrelated with the up-conversion beam and up-converted photon.

The magnitude of the ratio of the second and first term in Eq. (100) using Equations (111) and (107) is approximately  $\frac{4\sqrt{2}}{\pi} \frac{D^2}{D_{u,i}^2} \tanh^2 \gamma$ . Using some typical numbers [Timothy E. Keller, Doctoral Thesis, UMBC (1998)], this is a factor of order  $5 \tanh^2 \gamma$  so that the contribution of the two terms is comparable when  $\gamma \approx 0.5$ . The ratio of the third term and the first term is approximately  $\frac{2}{\pi^2} \frac{|D|^2 L_u}{T_i |D_{u,i}|} \tanh^4 \gamma \approx 0.5 \tanh^4 \gamma$ . The small value of this term is mainly due to the fact that  $|D| L_u \approx 10^{-12} s$ .

Finally, we estimate the number of coincidence counts from Equation (108). Using a conversion efficiency for the up-conversion of the order  $I_u / I_i = 10^{-4}$ , and assuming that  $I_a = I_i \approx 10 \text{ W/cm}^2$  we expect that the counting rate for the up-conversion will be about  $5 \times 10^9 / s\text{-cm}^2$ . If we assume ideal conditions we can expect this to be an upper bound to the coincidence rate. This implies for the model discussed in this paper that once loss is included that the counting rate will be too low for practical sensor application. Current experiments are underway in which the rate of the up-conversion is much larger than envisioned here. In this case the single photon model of the up-conversion breaks down and an intense beam is produced. This case requires a different detection scheme.

## Appendix E

We define various quantities here in detail. The units of electric field are

$$e_{ar} = \sqrt{\frac{\hbar\omega_{ar}}{\varepsilon_\alpha AL_Q}} \approx \sqrt{\frac{\hbar\Omega_a}{\varepsilon_\alpha AL_Q}} \quad (113)$$

where  $V_Q = AL_Q$  is the quantization volume,  $\varepsilon_\alpha = \varepsilon_0 n_\alpha^2$  is the dielectric constant, and the index of refraction  $n_\alpha$  is evaluated at  $\Omega_\alpha$ . The up-conversion coupling has the dimensions of frequency and is given by

$$\gamma_u = 2\chi^{(2)}(\Omega_u; \Omega_{i1}, \Omega_{i2}) \sqrt{\frac{\hbar\Omega_u}{2\varepsilon_u V_Q}} \sqrt{\frac{\Omega_{i1}\Omega_{i2}}{4n_{i1}^2 n_{i2}^2 L_Q^2}} L_u \quad (114)$$

where  $\chi^{(2)}(\Omega_u; \Omega_{i1}, \Omega_{i2})$  is the electric susceptibility in MKS units and so has the dimensions of inverse electric field, and  $A$  is the cross-section area of the up-converted beam.

## Appendix F

We compute the average flux of the up-converted photons detected

$$\begin{aligned}
 N_u &= \frac{c}{V_Q} \sum_m |f_u(\nu_m)|^2 \langle \Psi^{(1)} | a_{um}^\dagger a_{um} | \Psi^{(+)} \rangle \\
 &= \frac{c}{V_Q} \left( \frac{\gamma_u c^3}{w_u w_{i1} w_{i2}} \right)^2 \sinh^4 \gamma T_u^2 \sum_{m,i1,i2} |f_u(\nu_m)|^2 \delta_{\omega_{um}, \omega_{i1} + \omega_{i2}} S(\Delta k_{12} L_u)^2 f_{i1}^2(\nu_{i1}) f_{i2}^2(\nu_{i2})
 \end{aligned} \tag{115}$$

Going to the continuum gives

$$\begin{aligned}
 N_u &= \frac{c}{V_Q} \left( \frac{\gamma_u c^3}{w_u w_{i1} w_{i2}} \right)^2 \sinh^4 \gamma \frac{L_Q^2 T_u^2}{c^2} \int d\nu_m |f_u(\nu_m)|^2 \int d\nu S(\Delta k_{12} L_u)^2 \times \\
 &\quad |f_{i1}(-\frac{\nu_m}{2} + \nu) f_{i2}(-\frac{\nu_m}{2} - \nu)|^2
 \end{aligned} \tag{116}$$

where we have made the change of variables  $\nu = \nu_{i1} - \nu_{i2}$  and  $\nu_+ = \frac{1}{2}(\nu_{i1} + \nu_{i2}) \rightarrow \nu_m$ .

Now assuming that the sinc function is much narrower than the idler, using Equation (106c) we replace the sinc function by

$$\begin{aligned}
 S(\Delta k_{12} L_u)^2 &\rightarrow \frac{2\pi}{DL_u} \delta(\nu_m + \frac{D_{i1,i2}}{D} \nu) \\
 r &= \frac{D_{i1,i2}}{D} \quad D = \frac{1}{2}(D_{um,i1} + D_{um,i2})
 \end{aligned} \tag{117}$$

gives

$$\begin{aligned}
 N_u &= \frac{c}{V_Q} \left( \frac{\gamma_u c^3}{w_u w_{i1} w_{i2}} \right)^2 \frac{L_Q^2 T_u^2}{c^2} \frac{2\pi}{|D| L_u} \sinh^4 \gamma \int d\nu |f_u(-r\nu) f_{i1}\left(\left(\frac{r}{2} + 1\right)\nu\right) f_{i2}\left(\left(\frac{r}{2} - 1\right)\nu\right)|^2 \\
 &= 2\pi^{3/2} \frac{c}{V_Q} \left( \frac{\gamma_u c^3}{w_u w_{i1} w_{i2}} \right)^2 \frac{L_Q^2}{c^2} \frac{T_u^2}{T_N |D| L_u} \sinh^4 \gamma \\
 T_N &= \sqrt{r^2 T_u^2 + (2 + r^2 / 2) T_i^2}
 \end{aligned} \tag{118}$$

where we have taken the filters for the idlers to be identical  $f_i(\nu) = e^{-\nu^2 T_i^2 / 2}$ . Finally, taking the group velocities to be equal to the phase velocities, using

$$\bar{I}_{i1} = \frac{cn_{i1}}{V_Q} \hbar \Omega_{i1} \frac{L_Q}{c} \frac{\sqrt{\pi}}{T_i},$$

and similarly for  $i_2$ , we have

$$N_u = \sqrt{\frac{\pi}{2}} \frac{\chi^{(2)2}}{\epsilon_0 \hbar} \bar{I}_{i1} \bar{I}_{i2} \frac{\Omega_u L_u T_u^2}{n_{i1} n_{i2} |D| c^3 \sqrt{2T_u^2 + 3T_i^2}} \left( \frac{cT_i}{L_Q} \right)^2 \quad (119)$$

Similarly intensity of the signal photons at each detector is given by

$$\bar{I}_a = c \frac{\hbar \Omega_a}{V_Q} \sqrt{\pi} \frac{L_Q}{cT_a} \sinh^2 \gamma = \frac{\hbar \Omega_a}{A} \frac{\sqrt{\pi}}{T_a} \sinh^2 \gamma \quad (120)$$

which may be interpreted as the energy per unit area times the bandwidth times the amplification factor of the down-conversion.